

2 PC (mix)

REPORT MDC A1740

IMAGE CORRELATION AND SAMPLING STUDY

D.J. Popp

D.S. McCormack

J.L. Sedwick

McDonnell Aircraft Company

Box 516, Saint Louis, Missouri 63166

June 1972

Final Report September 1971 - June 1972

Prepared for

GODDARD SPACE FLIGHT CENTER
Greenbelt, Maryland 20771

(NASA-CR-130223) IMAGE CORRELATION AND
SAMPLING STUDY Final Report, Sep. 1971
-- Jun. 1972 (McDonnell Aircraft Co.)
196 p HC \$12.00 CSCL 14E

N73-22389

Unclas
G3/14 02217

Cover only
073787
Perm Bureau

REPORT MDC A1740

1. Report No.	2. Government Accession No.	3. Recipient's Catalog No.	
4. Title and Subtitle Image Correlation and Sampling Study		5. Report Date June 1972	
		6. Performing Organization Code	
7. Author(s) D.J. Popp, Principal Investigator D.S. McCormack J.L. Sedwick, McDonnell Douglas Astronautics Co.		8. Performing Organization Report No. MDC A1740	
9. Performing Organization Name and Address McDonnell Aircraft Company Box 516 Saint Louis, Missouri 63166		10. Work Unit No.	
		11. Contract or Grant No. 2 NAS5-21662	
12. Sponsoring Agency Name and Address Goddard Space Flight Center Greenbelt, Maryland 20771 Attn: W. L. Alford, Code 563.1		13. Type of Report and Period Covered Final Report September 1971 - June 1972	
		14. Sponsoring Agency Code	
15. Supplementary Notes Portions of this report were published in the IEEE 1972 Telecommunications Conference Record, December, 1972, and presented at the E. I. A. Third Annual Symposium on Automatic Imagery Pattern Recognition, January 1973.			
16. Abstract The overall objective of this study was to develop the analytical approaches that will lead to the solution of two classical image processing problems: 1) Image correlation and 2) Image sampling. Relevant multi-spectral image statistics which are applicable to image correlation and sampling are identified and developed. Task I Image Statistics - In this task, relevant multispectral general image statistics and difference (change detected) image statistics were determined. The statistics of time sequential imagery in three spectral bands and representative of four general terrain types are presented. The general image statistics selected include intensity mean, variance, amplitude histogram, power spectral density function, and auto-correlation function. Difference image statistics presented include the intensity mean, variance, and quantized probability distribution. Task II Image Correlation - This study task considered the translation problem associated with digital image registration and developed the analytical means for comparing commonly used correlation techniques. Using suitably defined constraints, an optimum and five suboptimum image registration techniques are defined and evaluated. A computational comparison was made. Both Gaussian and real difference image statistics were used to compare the techniques in terms of radial position location error. Task III Image Sampling - In this task, general expressions for determining the reconstruction error for specific image sampling strategies are developed. The image sampling parameters considered include scanning apertures, scanning lattices, image statistics, interpolation functions, and image recorder characteristics. These analytical expressions were programmed on a digital computer and the effects of sampling parameter variation demonstrated.			
17. Key Words (Selected by Author(s)) Digital Image Registration Image Correlation Image Sampling Multispectral Image Statistics		18. Distribution Statement	
19. Security Classif (of this report) Unclassified	20. Security Classif. (of this page) Unclassified	21. No. of Pages 185	22. Price*

* For sale by the Clearinghouse for Federal Scientific and Technical Information, Springfield, Va. 22151

MCDONNELL AIRCRAFT

ACKNOWLEDGEMENT

The Image Correlation and Sampling Study was performed under Contract No. NAS5-21662 under the direction of Goddard Space Flight Center. The many contributions of Mr. William L. Alford, Technical Officer, in monitoring and reviewing the contractor's work are sincerely appreciated. The assistance of Mr. E. O. Zeitler of the Earth Resources Research Data Facility, NASA MSC, in supplying the multispectral imagery used in this study is gratefully acknowledged. In addition, the authors would like to thank the following McDonnell Douglas Corporation personnel for their many contributions to this study; P. E. Andberg who developed the software described in Sections 1 and 2, J. T. Melka who provided the image scanning and digitization discussed in Sections 1 and 2, and D. C. Torretta who developed the software described in Section 3.

**Details of illustrations in
this document may be better
studied on microfiche**

PREFACE

The objective for this study was to develop the analytical approaches that lead to the solution of two classical image processing problems, image correlation and image sampling. Relevant multispectral image statistics applicable to image correlation and sampling were identified and developed.

The study was divided into three separate but interrelated tasks. In the first task, relevant general image statistics and difference image (change detected) statistics were determined by suitable photographic processing and digital processing of multispectral imagery. The statistics of this time sequential imagery in three spectral bands (green, red, IR) and representative of four terrain types (farmland, urban, mountains, forest) were presented as numerical and graphical data. The second task considered the translation problem associated with digital image registration and developed analytical means for comparing an optimum and five commonly used correlation techniques. A digital simulation was developed to compare the techniques in terms of radial position location error using both Gaussian and real difference image statistics. In the third task, general expressions were developed for determining digital image reconstruction error for specific image sampling strategies and sensor systems. Analytical expressions were programmed on a digital computer and the effects on reconstruction error caused by image sampling parameter variation were shown.

Relevant image statistics for image correlation include the image mean, variance, autocorrelation function, and difference image histogram. Of these, the difference image histogram was found to be the most useful. From two statistical runs the tentative conclusions are:

The optimum image registration algorithm appears to be a valid means for comparing the position location performance of commonly used techniques.

On a computational basis, the mean absolute difference algorithm (using adaptive thresholding) and the cross correlation coefficient (using FFT techniques) are the most attractive correlation algorithms.

In general, image registration using hard limited (2 level) images resulted in slightly greater radial error than when using 64 level images.

Those image statistics found to be relevant for image sampling are the power spectral density functions. The analytical approach was developed to describe the effects of parametric variation of sample density, terrain type, recording device characteristics and presample filtering in terms of rms reconstruction errors. It was found that the mean squared error criterion does not restrict the choice of sampling aperture shape or size as a function of sampling lattice unless the sampling is very anisotropic. Computer image interpolation to a refinement of five recording device spots (in each direction) per pair of sensor sample values is sufficient.

Future image correlation study should be directed toward extending the digital image correlation simulation. For image sampling, sensor system noise effects and means for reducing such effects merit attention. A promising area for investigation is the development of improved image reconstruction methods.

TABLE OF CONTENTS

<u>Section</u>	<u>Title</u>	<u>Page</u>
1.	MULTISPECTRAL IMAGE STATISTICS	1-1
1.1	Introduction	1-1
1.2	Image Selection	1-1
1.3	Resolution Requirements	1-3
1.3.1	Photo Processing	1-5
1.3.2	Image Scanning and Digitization	1-6
1.4	General Multispectral Image Statistics	1-10
1.4.1	Development of Computer Program	1-11
1.4.2	Image Statistics	1-12
1.5	Difference Image Statistics	1-46
1.5.1	Development of Computer Program	1-46
1.5.2	Image Statistics	1-48
2.	IMAGE CORRELATION STUDY	2-1
2.1	Introduction	2-1
2.2	Image Registration Geometry	2-2
2.3	Position Location Analysis	2-3
2.3.1	The Optimum Position Location Technique	2-3
2.3.2	$v=1$ Correlation Technique	2-8
2.3.2	$v=2$ Correlation Technique	2-10
2.3.4	Maximum Likelihood Estimation Technique	2-11
2.3.5	Cross-Covariance Function Technique	2-12
2.3.6	Cross-Correlation Coefficient Technique	2-14
2.3.7	Position Location Optimization	2-16
2.4	Position Location Using Gaussian Difference Images	2-23
2.4.1	Development of Computer Program	2-24
2.4.2	Simulation Results	2-24
2.5	Position Location Using Multispectral Image Statistics	2-38
2.5.1	Development of Computer Program	2-38
2.5.2	Simulation Results	2-39
2.6	Conclusions	2-44

TABLE OF CONTENTS (Continued)

<u>Section</u>	<u>Title</u>	<u>Page</u>
2.7	Areas for Further Study	2-45
3.	IMAGE SAMPLING STUDY	3-1
3.1	Introduction	3-1
3.2	Image Sampling and Reconstruction Parameters	3-1
3.2.1	Sampling Lattice	3-1
3.2.2	Sampling Aperture	3-2
3.2.3	Presampling Filtering	3-4
3.2.4	Interpolation	3-4
3.2.5	Recording Device Characteristics	3-5
3.3	Method of Analysis	3-5
3.3.1	Error Criterion	3-5
3.3.2	Numerical Evaluation of Mean Square Error	3-7
3.3.3	Image Power Spectral Densities	3-11
3.4	Quantitative Results	3-14
3.4.1	Influence of Image Spatial Frequency Content	3-14
3.4.2	Sample Density	3-14
3.4.3	Sampling Lattice Effects	3-17
3.4.4	Comparison of Reconstruction Methods and Aperture Shapes	3-19
3.4.5	Effects of Continuous Scan (Video)	3-19
3.4.6	Image Recorder Effects	3-24
3.4.7	Presampling Filtering Effects	3-25
3.5	Image Sampling Strategy Specification	3-26
3.5.1	Minimum RMS Error	3-26
3.5.2	Position Location	3-27
3.5.3	Feature Extraction	3-28
3.5.4	Random Sampling	3-29
3.6	Conclusions	3-30
3.7	Areas for Further Study	3-30
REFERENCES	3-32

TABLE OF CONTENTS (Continued)

<u>Section</u>	<u>Title</u>	<u>Page</u>
APPENDIX A -	Derivation of Mean Squared Error Expressions	A-1
APPENDIX B -	Aperture Transforms	B-1
APPENDIX C -	Reconstruction Transforms	C-1
APPENDIX D -	Derivation of Mean Squared Error Expression Which Includes the Recorder Spot Characteristic	D-1
APPENDIX E -	Optimal Linear Interpolation for Non-Band Limited Functions	E-1
APPENDIX F -	Modulation Transfer Functions	F-1
APPENDIX G -	Analog Scanning and Filtering	G-1
APPENDIX H -	New Technology	H-1

LIST OF FIGURES

<u>Figure</u>	<u>Title</u>	<u>Page</u>
1-1	Effective Digital Image Processing System Scanning	
	Lattice for 8 X 8 Array	1-5
1-2	Block Diagram of Digital Image Processing System	1-7
1-3	Ideal Sampled Image Function	1-8
1-4	Plot of DIPS Scanning Aperture	1-8
1-5	Block Diagram for Generating General Image Statistics	1-11
1-6	Illustration of Zero Padding Using FFT	1-12
1-7	General Image Statistics Computer Flow Diagram	1-13
1-8	Image Statistics (Farmland Terrain - Red Spectrum - Mission 131 - 50 Meter Resolution)	1-14
1-9	Image Statistics (Farmland Terrain - Green Spectrum - Mission 131 - 50 Meter Resolution)	1-16
1-10	Image Statistics (Farmland Terrain - IR Spectrum - Mission 131 - 50 Meter Resolution)	1-18
1-11	Image Statistics (Urban Terrain - Red Spectrum - Mission 131 - 50 Meter Resolution)	1-20
1-12	Image Statistics (Urban Terrain - Green Spectrum - Mission 131 - 50 Meter Resolution)	1-22
1-13	Image Statistics (Urban Terrain - IR Spectrum - Mission 131 - 50 Meter Resolution)	1-24
1-14	Image Statistics (Mountain Terrain - Red Spectrum - Mission 131 - 50 Meter Resolution)	1-26
1-15	Image Statistics (Mountain Terrain - Green Spectrum - Mission 131 - 50 Meter Resolution)	1-28
1-16	Image Statistics (Mountain Terrain - IR Spectrum - Mission 131 - 50 Meter Resolution)	1-30
1-17	Image Statistics (Forest Terrain - Red Spectrum - Mission 131 - 50 Meter Resolution)	1-32
1-18	Image Statistics (Forest Terrain - Green Spectrum - Mission 131 - 50 Meter Resolution)	1-34

LIST OF FIGURES (Continued)

<u>Figure</u>	<u>Title</u>	<u>Page</u>
1-19	Image Statistics (Forest Terrain - IR Spectrum - Mission 131 - 50 Meter Resolution)	1-36
1-20	Image Statistics (Farmland Terrain - Red Spectrum - Mission 131 - 10 Meter Resolution)	1-38
1-21	Image Statistics (Urban Terrain - Red Spectrum - Mission 131 - 10 Meter Resolution)	1-40
1-22	Image Statistics (Mountain Terrain - Red Spectrum - Mission 131 - 10 Meter Resolution)	1-42
1-23	Image Statistics (Forest Terrain - Red Spectrum - Mission 131 - 10 Meter Resolution)	1-44
1-24	Block Diagram for Generating Difference Image Statistics .	1-46
1-25	Difference Image Statistics Computer Flow Diagram	1-47
1-26	Difference Image Statistics (Farmland Terrain - Red Spectrum - Mission 129 - 50 Meter Resolution)	1-50
1-27	Difference Image Statistics (Farmland Terrain - Green Spectrum - Mission 129 - 50 Meter Resolution)	1-52
1-28	Difference Image Statistics (Farmland Terrain - IR Spectrum - Mission 129 - 50 Meter Resolution)	1-54
1-29	Difference Image Statistics (Urban Terrain - Red Spectrum - Mission 129 - 50 Meter Resolution)	1-56
1-30	Difference Image Statistics (Urban Terrain - Green Spectrum - Mission 129 - 50 Meter Resolution)	1-58
1-31	Difference Image Statistics (Urban Terrain - IR Spectrum - Mission 129 - 50 Meter Resolution)	1-60
1-32	Difference Image Statistics (Mountain Terrain - Red Spectrum - Mission 129 - 50 Meter Resolution)	1-62
1-33	Difference Image Statistics (Mountain Terrain - Green Spectrum - Mission 129 - 50 Meter Resolution)	1-64
1-34	Difference Image Statistics (Mountain Terrain - IR Spectrum - Mission 129 - 50 Meter Resolution)	1-66

LIST OF FIGURES (Continued)

<u>Figure</u>	<u>Title</u>	<u>Page</u>
1-35	Difference Image Statistics (Forest Terrain - Red Spectrum - Mission 158 - 50 Meter Resolution)	1-68
1-36	Difference Image Statistics (Forest Terrain - Green Spectrum - Mission 158 - 50 Meter Resolution)	1-70
1-37	Difference Image Statistics (Forest Terrain - IR Spectrum - Mission 158 - 50 Meter Resolution)	1-72
1-38	Difference Image Statistics (Farmland Terrain - Red Spectrum - Mission 129 - 10 Meter Resolution)	1-74
1-39	Difference Image Statistics (Urban Terrain - Red Spectrum - Mission 129 - 10 Meter Resolution)	1-76
1-40	Difference Image Statistics (Mountain Terrain - Red Spectrum - Mission 129 - 10 Meter Resolution)	1-78
1-41	Difference Image Statistics (Forest Terrain - Red Spectrum - Mission 158 - 10 Meter Resolution)	1-80
2-1	Image Registration Geometry	2-2
2-2	Example of P_q Function	2-6
2-3	Example of Optimum Position Location Estimator	2-7
2-4	Example of $v=1$ Position Location Estimator	2-9
2-5	Example of $v=2$ Position Location Estimator	2-10
2-6	Example of Cross-Covariance Position Location Estimator	2-13
2-7	Example of Cross-Correlation Coefficient Position Location Estimator	2-15
2-8	Error Probability as a Function of Quantization Interval	2-19
2-9	Computation Comparison	2-21
2-10	Illustration of Adaptive Threshold	2-23
2-11	Comparison of Square and Circular Data Image Shape	2-25
2-12	Flow Diagram of Position Location Digital Simulation Using Gaussian Difference Images	2-26
2-13	Typical Noisy Data Images ($n=N=128$)	2-28
3-1	Image Sampling Lattices	3-3

LIST OF FIGURES (Continued)

<u>Figure</u>	<u>Title</u>	<u>Page</u>
3-2	Circular Aperture Weighting Function 	3-4
3-3	Lattice Summation Procedure	3-10
3-4	Root Mean Squared Reconstruction Error Flow Diagram	3-12
3-5	Power Spectral Density of Farmland	3-13
3-6	Effects of Image Spatial Frequency Roll-Off	3-15
3-7	Effects of Image Sample Spacing	3-16
3-8	Effects of Image Sample Spacing	3-17
3-9	Sampling Lattice Comparison	3-18
3-10	Interpolation Technique Comparison for Circular Sampling Aperture	3-20
3-11	Interpolation Technique Comparison for Hexagonal Sampling Aperture	3-20
3-12	Interpolation Technique Comparison for Square Sampling Aperture	3-21
3-13	Interpolation Technique Comparison for Gaussian Sampling Aperture	3-21
3-14	Continuous Scan Characteristics	3-22
3-15	Effects with Constant Sample Cell Area	3-23
3-16	Reconstruction Error as Function of Image Recording Device Characteristics	3-24
3-17	Effect of First Order Delay Pre-Filter	3-25
3-18	Position Location Considerations	3-27
B-1	Sampling Apertures	B-3
C-1	One Point Reconstruction Geometry	C-2
C-2	Four Point Reconstruction Geometry	C-3

LIST OF TABLES

<u>Table</u>	<u>Title</u>	<u>Page</u>
1-1	Selected Frames of Multispectral Imagery	1-2
1-2	Resolution Upper Bound as a Function of Film Type	1-4
1-3	Digital Image Processing System Intensity Compensation . .	1-9
1-4	Difference Image Identification	1-49
2-1	Optimum Position Location Algorithm Computations	2-8
2-2	Computation Formulae	2-20
2-3	Computation Comparison	2-22
2-4	Radial Error Comparison for $\sigma/\Delta=1$	2-30
2-5	Radial Error Comparison for $\sigma/\Delta=2.5$	2-31
2-6	Radial Error Comparison for $\sigma/\Delta=5$	2-32
2-7	Radial Error Comparison for $\sigma/\Delta=10$	2-33
2-8	Comparison of Estimator Values for $\sigma/\Delta=1$	2-34
2-9	Comparison of Estimator Values for $\sigma/\Delta=2.5$	2-35
2-10	Comparison of Estimator Values for $\sigma/\Delta=5$	2-36
2-11	Comparison of Estimator Values for $\sigma/\Delta=10$	2-37
2-12	Radial Error Comparison for Square Data Image	2-40
2-13	Radial Error Comparison for Circular Data Image	2-41
2-14	Radial Error Comparison as Function of Image Spectrum . . .	2-42
2-15	Radial Error Comparison as Function of Terrain Type	2-43
2-16	Radial Error Comparison as Function of Image Resolution . .	2-43

LIST OF PAGES

Title Page
ii thru xii
1-1 thru 1-81
2-1 thru 2-45
3-1 thru 3-33
A-1 thru A-8
B-1 thru B-3
C-1 thru C-3
D-1 thru D-4
E-1 thru E-3
F-1 thru F-2
G-1 thru G-2
H-1

SECTION 1

MULTISPECTRAL IMAGE STATISTICS

1.1 INTRODUCTION

In this section, multispectral imagery is selected and digitized to provide representative multispectral image data seen by an advanced spaceborne earth observation platform. General multispectral image statistics are determined which include image intensity mean, variance, amplitude histogram, power spectral density function array and autocorrelation function array. In addition, relevant difference or "noise" image statistics are generated which describe the "changes" that occur in imagery taken on sequential overflights. These statistics include the difference image intensity mean, variance, and quantized probability histogram.

The analytical use of these statistics for performing image correlation and sampling studies is discussed in Section 2 and Section 3 respectively.

1.2 IMAGE SELECTION

In recent years, much progress has been made in the observation of major geographical areas in the continental United States using a variety of multispectral sensors. The current availability of multispectral imagery taken over the same geographical area on a time sequential basis (e.g. a month apart) is quite limited, however. The objective of this portion of the study was to identify and acquire time sequential multispectral imagery in as many spectral bands and covering as many terrain types as possible.

The NASA Earth Resources Research Data Facility was used extensively for this imagery search. Multispectral imagery taken from the NASA Earth Observations Aircraft Program were found to be the most applicable. The frames of multispectral imagery selected for digitization are identified in Table 1-1 (references 1, 2, and 3). This imagery was selected because of good mission overlap in three spectral bands.

TABLE 1-1
SELECTED FRAMES OF MULTISPECTRAL IMAGERY

Mission No.	Site No.	General Location	Roll No.	Frame No.	Filter No.	Spectral Band	Terrain Category
131	210	Imperial Valley, California	14	26	25A	Red	Farmland
131	210		16	26	89B	Green	
131	210		15	26	58	IR	
131	29	City of Phoenix	14	54	25A	Red	Urban
131	29		16	54	89B	Green	
131	29		15	54	58	IR	
131	29	Vicinity of Phoenix, Ariz	14	97	25A	Red	Mountain
131	29		16	97	89B	Green	
131	29		15	97	58	IR	
131	217	Vicinity of Atlanta, Georgia	4	45	25A	Red	Forest
131	217		5	45	89B	Green	
131	217		6	45	58	IR	
129	210	Imperial Valley, California	7	16	25A	Red	Farmland
129	210		8	16	89B	Green	
129	210		9	16	58	IR	
129	29	City of Phoenix	7	51	25A	Red	Urban
129	29		8	51	89B	Green	
129	29		9	51	58	IR	
129	29	Vicinity of Phoenix, Arizona	7	57	25A	Red	Mountain
129	29		8	57	89B	Green	
129	29		9	57	58	IR	
158	217	Vicinity of Atlanta, Georgia	31	48	25	Red	Forest
158	217		34	48	89B	Green	
158	217		32	48	58	IR	

GP72-0450-80

Mission 129 was flown on 21 May 1970 at all three sites. Mission 131 was flown on 16 June 1970 for sites 210 and 29, and 8 June 1970 for site 217. Mission 158 was flown on 5 March 1970. Additional missions are available at monthly time increments for sites 29 and 210 which were not included in this study.

The terrain types selected from the available imagery are Farmland, Urban, Mountain, and Forest. Of these, the farmland terrain imagery was the easiest to identify. The forest terrain imagery was the most difficult. The selected frame for the forest terrain could, in fact, be labeled "miscellaneous", as much open land was included as well as wooded areas.

Imagery representative of the total visible spectrum (color) and the blue spectrum were not available for these missions.

1.3 RESOLUTION REQUIREMENTS

Image ground resolutions of 10 meters and 50 meters were selected as being typical requirements for advanced earth observation platforms. The imagery acquired from the NASA Earth Resources Research Data Facility was 70 mm. black and white negative transparencies. Typically, this imagery was photographed from an altitude of approximately 18,288 meters (60,000 ft.). This section discusses how the 70 mm. transparencies were photo-processed and digitized to meet the approximate 10 meter and 50 meter resolution requirements.

Without specific ground truth for the selected frames of imagery, it is impossible to determine image resolution with any degree of accuracy. By using a ground resolution formula (reference 4) however, which relates camera lens resolution, film resolution, and scale, a ground resolution upper bound for a photographic image can be determined (depending on the film type used) as follows:

$$\nabla = \frac{h}{(f) (R_{LF}) (3.28084)} \quad (1-1)$$

where:

∇ = ground resolution in meters (per line pair).

f = focal length (mm.)

R_{LF} = lens/film resolution (line pair/mm.).

Using this formula, the upper resolution bound on the acquired 70 mm. imagery can then be determined and is noted in Table 1-2.

TABLE 1-2
RESOLUTION UPPER BOUND AS A FUNCTION
OF FILM TYPE

Film Type	R_{LF} Line Pair/mm	Ground Resolution (meters)
1. 2424	80	5.72
2. 2448	80	5.72
3. 2402	100	4.57
4. 3400	160	2.86

GP72-0450-79

It is apparent (from Table 1-2) that the acquired multispectral imagery has greater resolution than is required for this study.

The MCAIR Digital Image Processing System (DIPS) (See Figure 1-2) can be used to filter the multispectral imagery as it scans and digitizes the image data. For equal vertical and horizontal resolution, a square non-overlapping scanning lattice such as is illustrated in Figure 1-1, would be utilized.

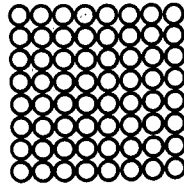


FIGURE 1-1
EFFECTIVE DIGITAL IMAGE PROCESSING SYSTEM
SCANNING LATTICE FOR 8 x 8 ARRAY

GP72-0450-6

In this scanning mode, the DIPS has a vertical and horizontal resolution of 13.1 lp/mm. If the DIPS were used to scan and digitize the 70 mm. imagery without any photo processing, the resulting ground resolution upper bound can be determined using equation (1-1) and setting $R_{LF} = 13.1$ lp/mm. Thus:

$$\nabla_{DIPS} = 34.87 \text{ meters} \quad (1-2)$$

This result implies that, if the DIPS were airborne at 18,288 meters (60,000 feet), scanning a fixed field of view, the maximum achievable resolution of the digital image data would be 34.87 meters. To increase or decrease the achievable ground resolution requires that the altitude parameter in Equation (1-1) be modified. This modification is most easily accomplished by suitable photo processing of the imagery before scanning.

1.3.1 Photo Processing

Thus, the filtering characteristic of the DIPS in the scanning mode, together with photo processing of the imagery before scanning, can be effectively used to provide digitized image data at the required resolutions.

- a) To achieve 10 meter (32.8 feet) ground resolution: Photographically enlarge the 70 mm imagery to $34.87/10 = 3.5$ times the original size before scanning.
- b) To achieve 50 meter (164 feet) ground resolution: Photographically reduce the 70 mm imagery to $34.87/50 = .7$ times the original size before scanning.

Extreme care was used in the photoprocessing of the selected multispectral image frames. In addition to the enlargement or reduction of the imagery to achieve resolution requirements, scale differences (due to minor airplane altitude variations) were minimized in the photo processing step.

1.3.2 Image Scanning and Digitization

1.3.2.1 Digital Image Processing System

The MCAIR Digital Image Processing System (DIPS) was used to scan, sample, quantize and store the selected frames of multispectral imagery on computer compatible magnetic tape. For this study, the image intensity was quantized to 6-bit accuracy (0 - 63 levels). Image intensity was scanned instead of the more commonly used image density because of the image statistics requirements for the image sampling study (Section 3).

The DIPS is a high resolution object plane image scanner and recording system. A block diagram of this system is illustrated in Figure 1-2. It has the capability of converting a photographic transparency into a rectangular or square sampling lattice of discrete image samples as defined by:

$$f_s(x_1, x_2) = |x_1| \sum_{\alpha = -\infty}^{\alpha = \infty} \delta(x_1 - \alpha a_1) \cdot |x_2| \sum_{\alpha = -\infty}^{\alpha = \infty} \delta(x_2 - \alpha a_2) \cdot f(x_1, x_2) \quad (1-3)$$

Where: $f(x_1, x_2)$ is the continuous image function

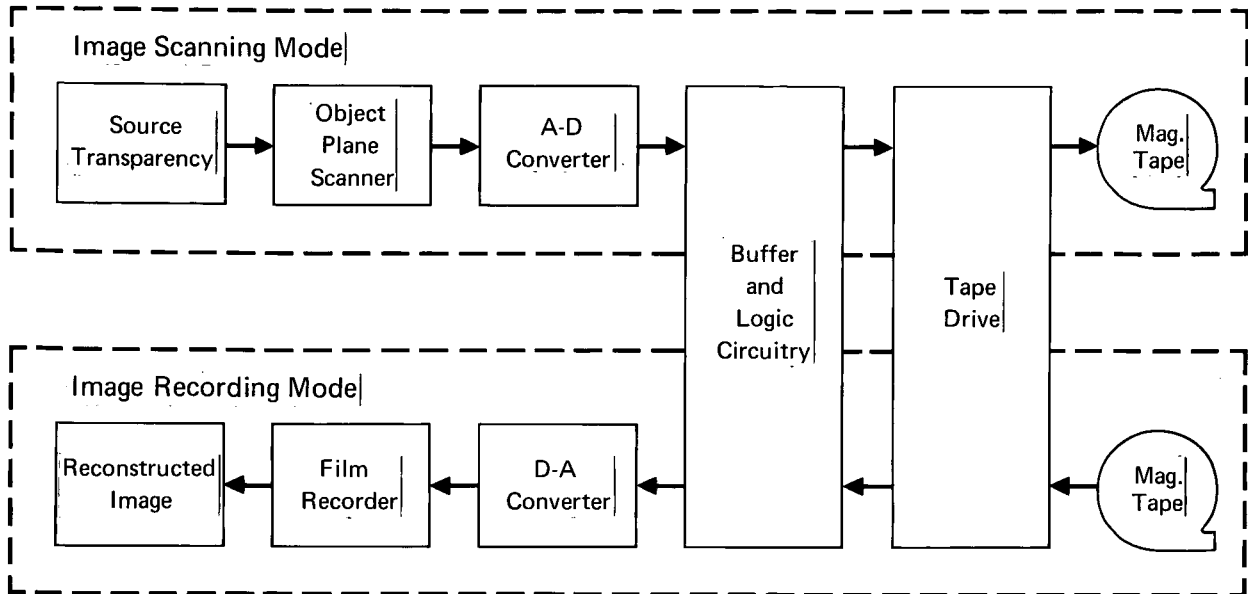


FIGURE 1-2
BLOCK DIAGRAM OF DIGITAL IMAGE PROCESSING SYSTEM

GP72-0450-5

The sampled function $f_s(x_1, x_2)$ is composed of an array of delta (δ) functions spaced at intervals of width a_1 in the x_1 direction and a_2 in the x_2 direction as shown in Figure 1-3. A value proportional to the intensity of the image area under each δ function is recorded on magnetic tape by the DIPS. Any real world image scanner does not sample an image with ideal δ functions. The measured sampling aperture of the DIPS is illustrated in two dimensional form in Figure 1-4. As can be seen, the sampling aperture is approximately Gaussian and the aperture width at half amplitude is 21 angstroms.

For the image statistics to be representative of the image data, a linear intensity response is required of the scanner. The intensity response of the DIPS in the scanning mode was measured and the required corrections are listed in Table 1-3. This intensity compensation was accomplished by table look up in the computer before the image statistics were determined (see Figures 1-7 and 1-25). As can be seen in Table 1-3, the intensity compensation causes a reduction in the number of quantized levels available. This could have been avoided by changing to 7-bit (128 levels) or 8-bit (256 levels) quantization for the image statistics computer processing. This was not done for this

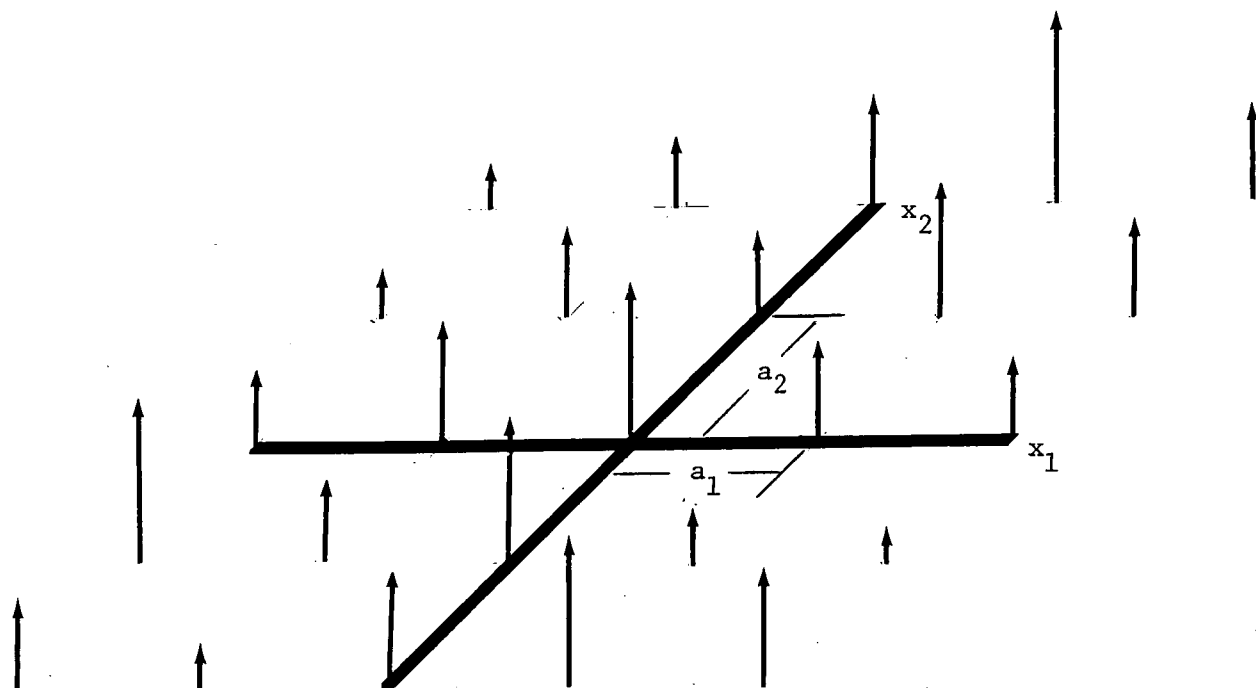


FIGURE 1-3
IDEAL SAMPLED IMAGE FUNCTION

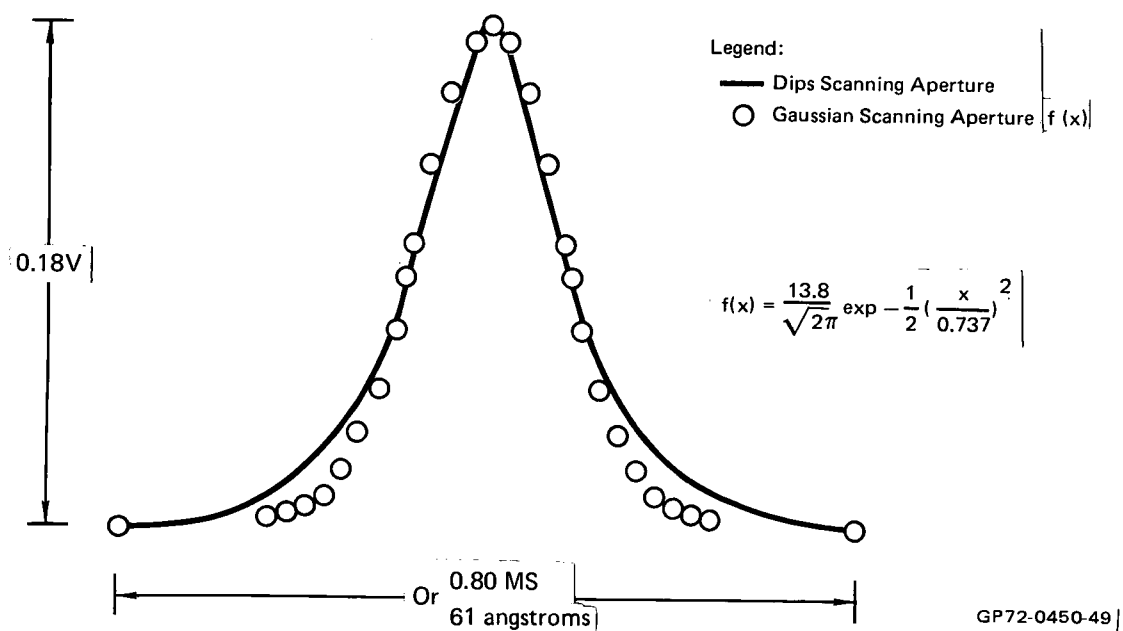


FIGURE 1-4
PLOT OF DIPS SCANNING APERTURE

TABLE 1-3
DIGITAL IMAGE PROCESSING SYSTEM INTENSITY COMPENSATION

DIPS		Corrected Quantization Level for Linear Intensity Variation
Scanned Quantization Level	Density Value	
0	1.3	0
1	1.2	2
2	1.05	4
3	0.94	6
4	0.84	7
5	0.78	9
6	0.72	10
7	0.67	11
8	0.63	12
9	0.6	13
10	0.56	14
11	0.54	14
12	0.52	15
13	0.49	16
14	0.47	17
15	0.44	18
16	0.42	18
17	0.40	19
18	0.39	20
19	0.375	20
20	0.36	21
21	0.34	22
22	0.325	22
23	0.312	23
24	0.30	24
25	0.285	25
26	0.27	25
27	0.26	26
28	0.25	27
29	0.24	27
30	0.23	28
31	0.22	29

DIPS		Corrected Quantization Level for Linear Intensity Variation
Scanned Quantization Level	Density Value	
32	0.21	29
33	0.2	30
34	0.19	31
35	0.18	32
36	0.17	33
37	0.165	33
38	0.155	34
39	0.147	35
40	0.14	36
41	0.132	37
42	0.125	38
43	0.12	38
44	0.112	39
45	0.108	40
46	0.1	41
47	0.095	42
48	0.09	43
49	0.085	44
50	0.08	45
51	0.074	46
52	0.07	47
53	0.064	48
54	0.06	49
55	0.056	50
56	0.051	52
57	0.048	53
58	0.043	54
59	0.0395	56
60	0.036	57
61	0.0325	59
62	0.029	61
63	0.025	63

GP72-0450-1

study because of time limitations and computer programming problems. The intensity compensation in Table 1-3 was used for the study.

1.3.2.2 Generation of Multispectral Image Data

One set of image data with an upper bound resolution of 50 meters was digitized from a portion of each frame of multispectral imagery listed in Table 1-1. This digital image library includes image data from three missions, and is representative of four terrain types in three spectral bands. In addition, one set of image data with an upper bound resolution of 10 meters was digitized for the red spectrum, all terrain categories, and all missions. DIPS reproduced versions of these images are displayed in Figures 1-8 through 1-23 and Figures 1-26 through 1-41. It should be noted that the reproduced image quality shown has been degraded by both the DIPS in transparency reconstruction and photo processing for publication purposes.

The DIPS was used exclusively for all image scanning and digitization. Digital image size, for all data images, was selected to be 128 x 128 samples. This choice was a compromise between the desirability of using a large image size so the image statistics are representative, and keeping the image size small to provide economical Fast Fourier Transform (FFT) computer processing.

Rotational error between sequential flight imagery was minimized by mounting a 50X microscope on the DIPS to aid in image prescanning registration. This rotational error is estimated to be within ± 4 angstroms which is \ll one scanning aperture width.

1.4 GENERAL MULTISPECTRAL IMAGE STATISTICS

Figure 1-5 is a block diagram of the procedure used for generating the general multispectral image statistics. It is not clear what the best statistical descriptors for multispectral imagery are. Those selected for this study include the image intensity mean, variance, amplitude histogram, power spectral density function and autocorrelation function. It was anticipated that the image mean, variance, and autocorrelation statistics would be used in Section 2 and the power spectral density used in Section 3.

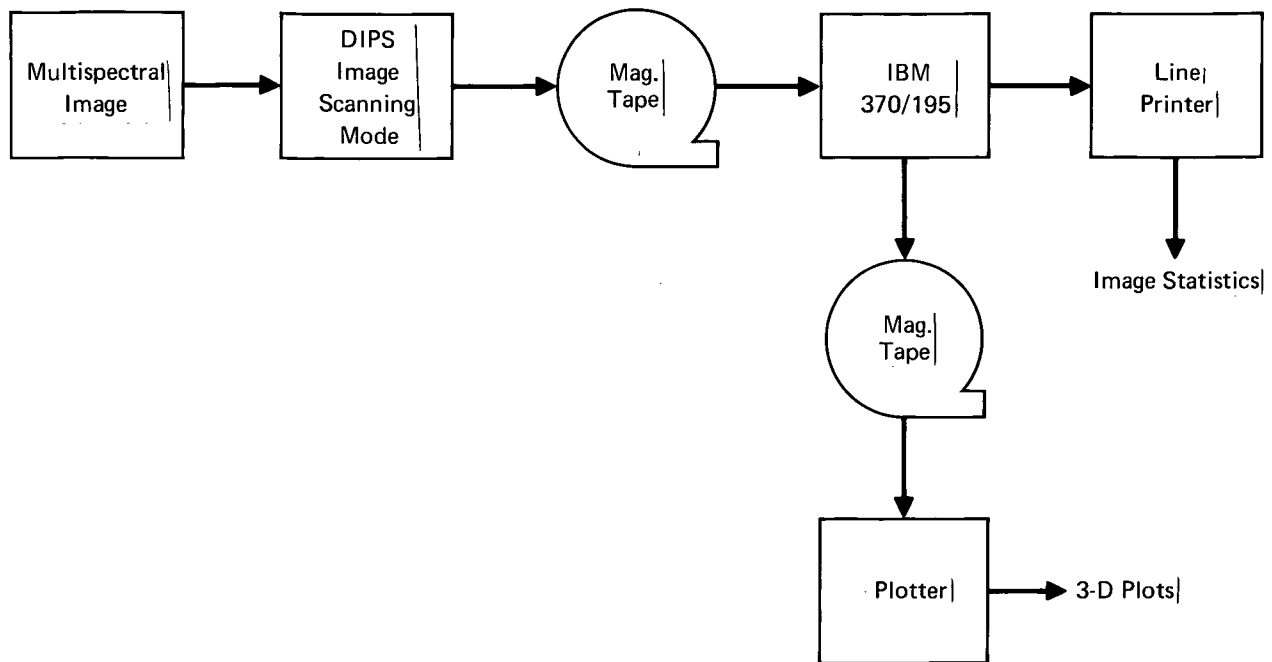


FIGURE 1-5
BLOCK DIAGRAM FOR GENERATING
GENERAL IMAGE STATISTICS

GP72-0450-7

1.4.1 Development of Computer Program

The power spectral density $\phi(\omega)$ of an image can be defined as follows:

$$\phi(\omega) = X(\omega) \cdot X^*(\omega) \quad (1-4)$$

where

$X(\omega)$ is the two dimensional Fourier transform of the spatial image function.

$X^*(\omega)$ is the complex conjugate of the Fourier transform

The autocorrelation function $R(x_1, x_2)$ of an image can then be defined:

$$R(x_1, x_2) = F^{-1} \left\{ X(\omega) \cdot X^*(\omega) \right\} \quad (1-5)$$

where:

F^{-1} denotes the inverse two dimensional Fourier transform.

Direct application of Equations (1-4) and (1-5) to numerical computation using the discrete Fourier transform must be performed with care (references 5, 6, 7). Cyclical correlation and "leakage" computational problems associated with the

discrete Fourier transform must be minimized before computational efficiencies using the Fast Fourier Transform (FFT) can be realized. According to Anuta (Reference 5), the cyclical correlation problem is eliminated by padding the digitized image array with zeros (as shown in Figure 1-6) before transform computer processing. This padding greatly increases the size of the image data array and, hence, the computational cost. The leakage problem was minimized by first subtracting the image mean intensity from the data, and then multiplying the outer 10% of the 128 x 128 image array by the cosine bell function (References 6 and 7).

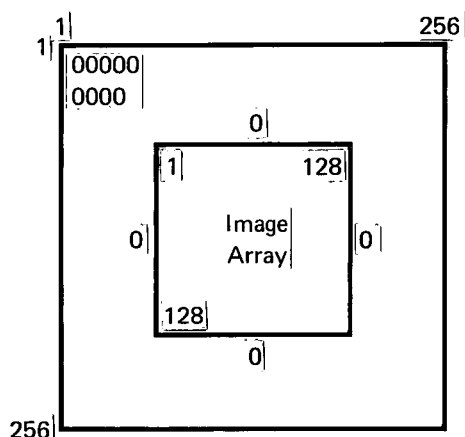


FIGURE 1-6
ILLUSTRATION OF ZERO PADDING USING FFT

GP72-0450-72

The computer program for generating the general image statistics is outlined in Figure 1-7. The power spectral density function and autocorrelation function arrays were determined using Equations (1-4) and (1-5) with zero padding of the image data and "leakage" minimization being accomplished. It should be noted that $\phi(\omega)$ and $R(x_1, x_2)$ are now 256 x 256 arrays because of the zero padding operation.

1.4.2 Image Statistics

General image statistics were determined for the 50 meter resolution and 10 meter resolution digital images of Mission 131. These statistics are illustrated in Figures 1-8 through 1-23. The three dimensional illustrations for the power spectral density and autocorrelation function arrays are plots of every eighth value in the array.

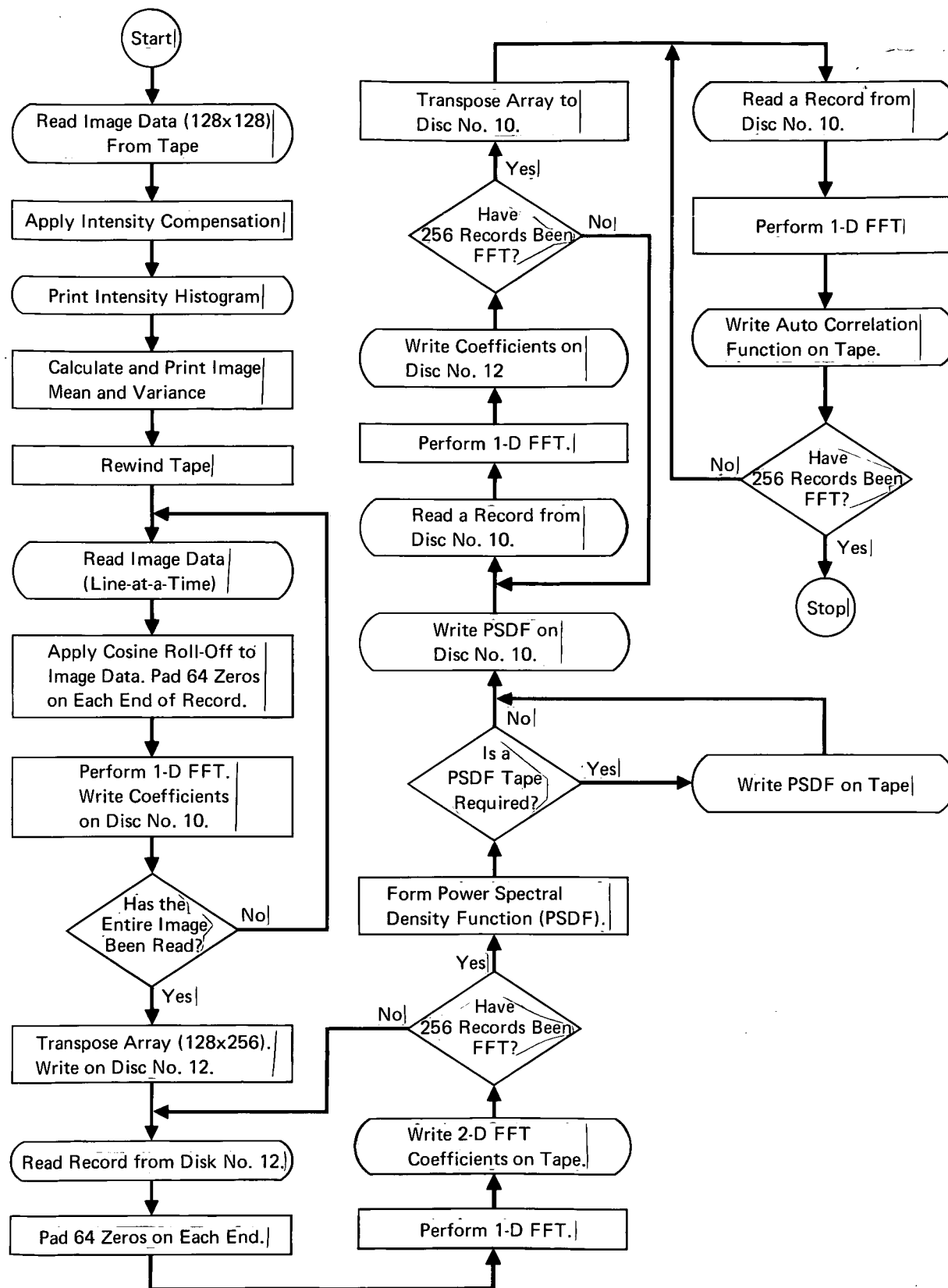


FIGURE 1-7
GENERAL IMAGE STATISTICS COMPUTER FLOW DIAGRAM

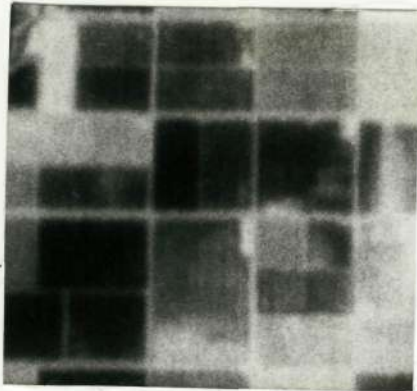
GP72-0450-29

Reproduced from
best available copy.

Centered At: $32^{\circ} 08' 30''$ N. Latitude
 $115^{\circ} 28' 00''$ W. Longitude

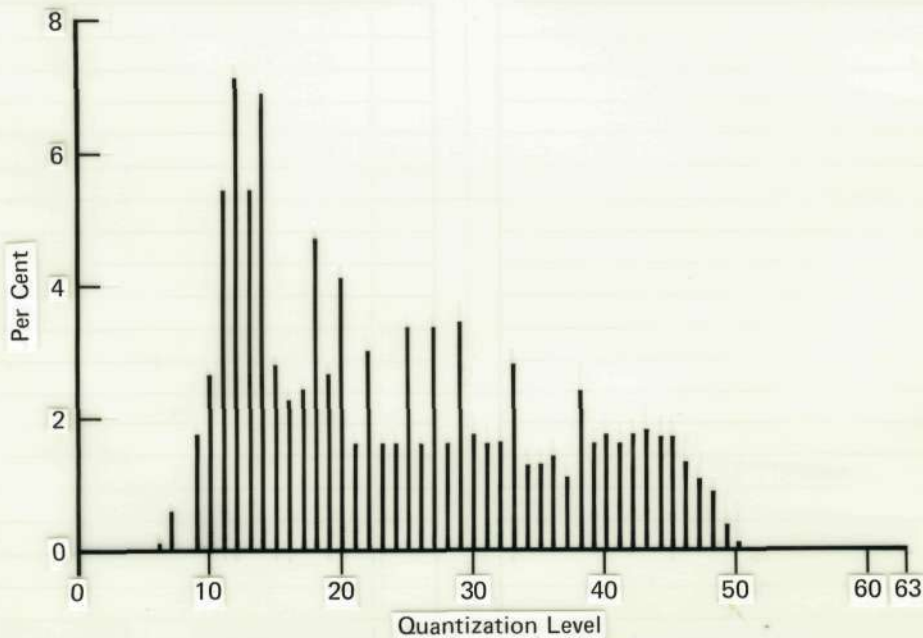
Image Mean: 24.016

Image Variance: 127.66



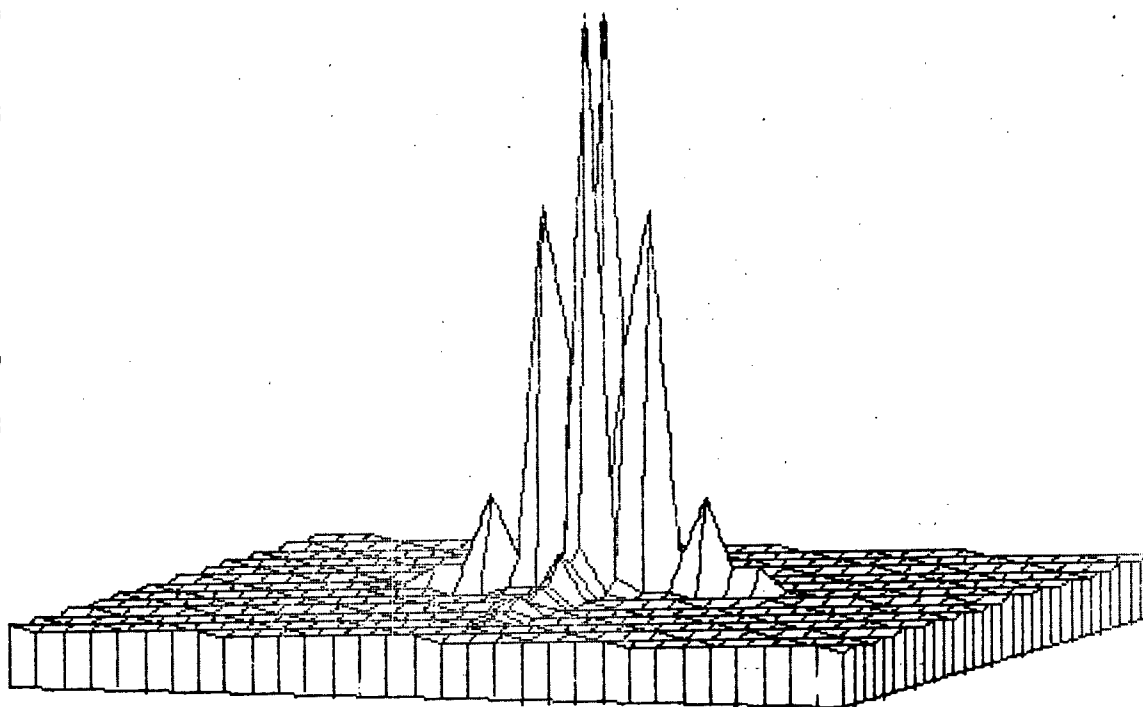
128 x 128 Image Array

a. Reference Image

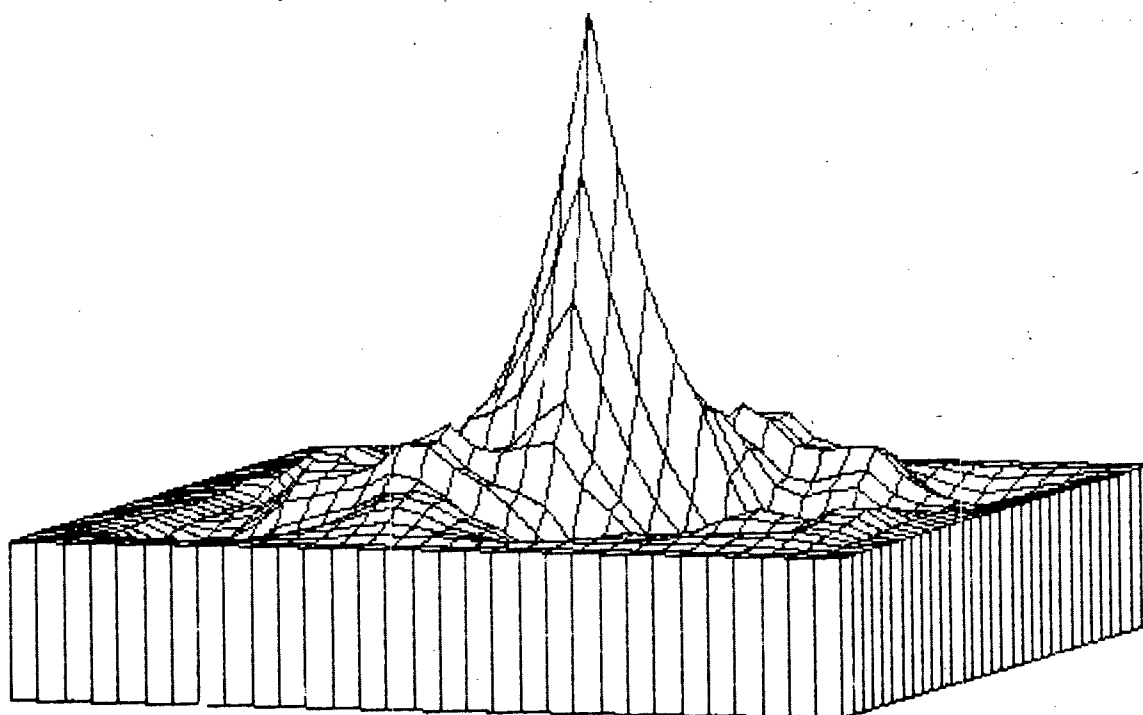


b. Image Intensity Histogram

FIGURE 1-8
IMAGE STATISTICS (FARMLAND TERRAIN - RED SPECTRUM -
MISSION 131 - 50 METER RESOLUTION)



c. Power Spectral Density Function



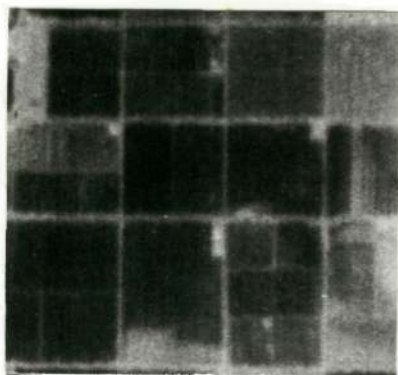
d. Autocorrelation Function

FIGURE 1-8 (Continued)
IMAGE STATISTICS (FARMLAND TERRAIN - RED SPECTRUM -
MISSION 131 - 50 METER RESOLUTION)

MCDONNELL AIRCRAFT

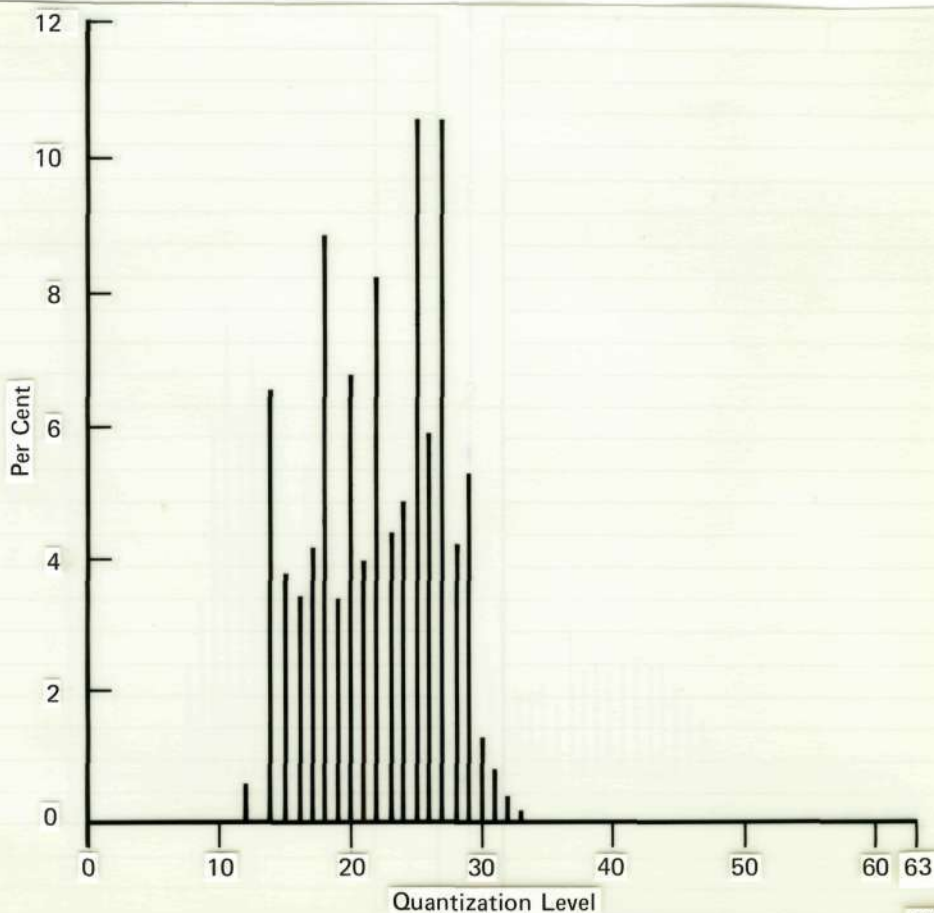
Reproduced from
best available copy.

Centered At: 32° 08'30" N. Latitude
115° 28'00" W. Longitude
Image Mean: 22.04
Image Variance: 23.7482



128 x 128 Image Array

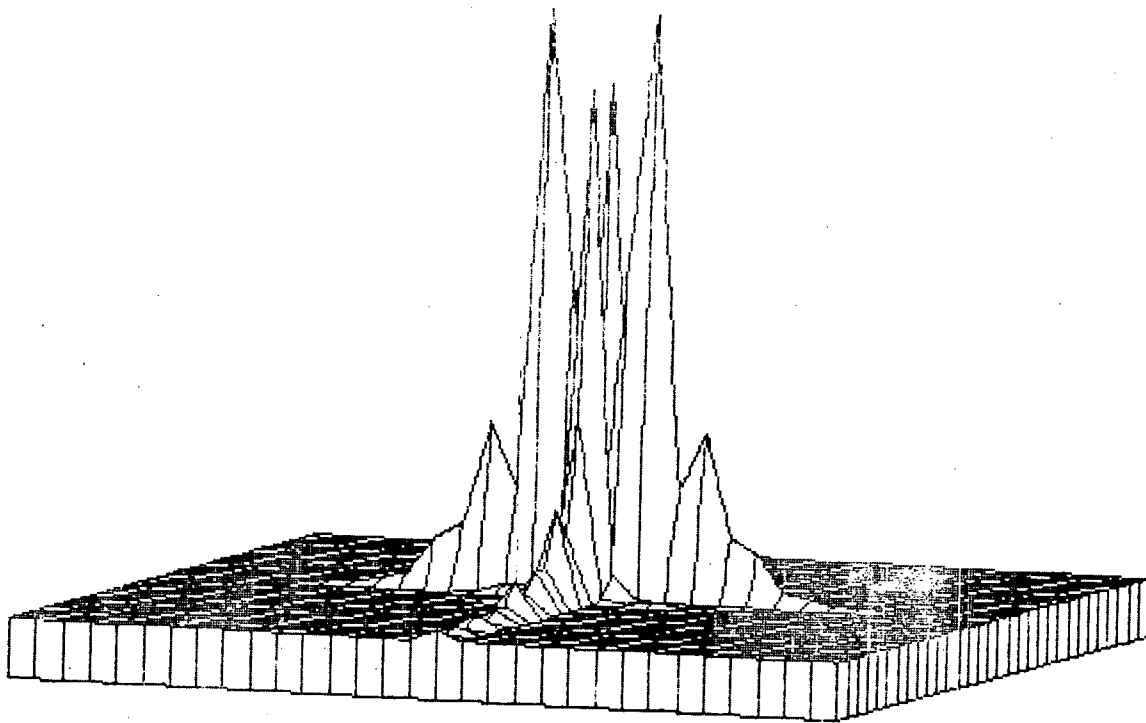
a. Reference Image



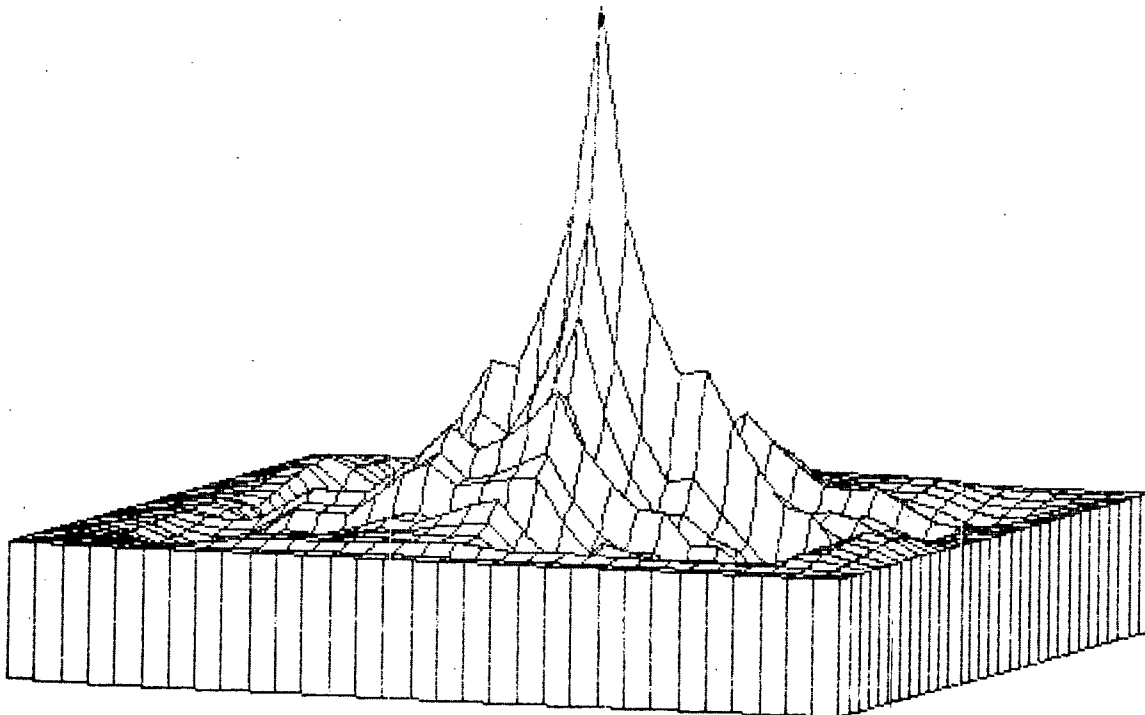
b. Image Intensity Histogram

FIGURE 1-9
IMAGE STATISTICS (FARMLAND TERRAIN - GREEN SPECTRUM -
MISSION 131 - 50 METER RESOLUTION)

035619



c. Power Spectral Density Function

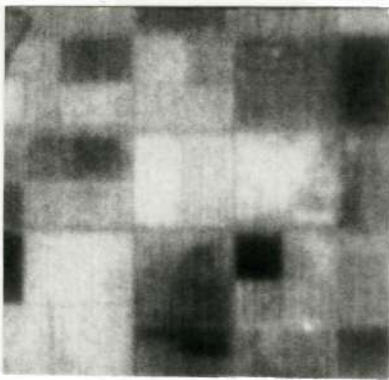


d. Autocorrelation Function

FIGURE 1-9 (Continued)
IMAGE STATISTICS (FARMLAND TERRAIN - GREEN SPECTRUM -
MISSION 131 - 50-METER RESOLUTION)

MCDONNELL AIRCRAFT

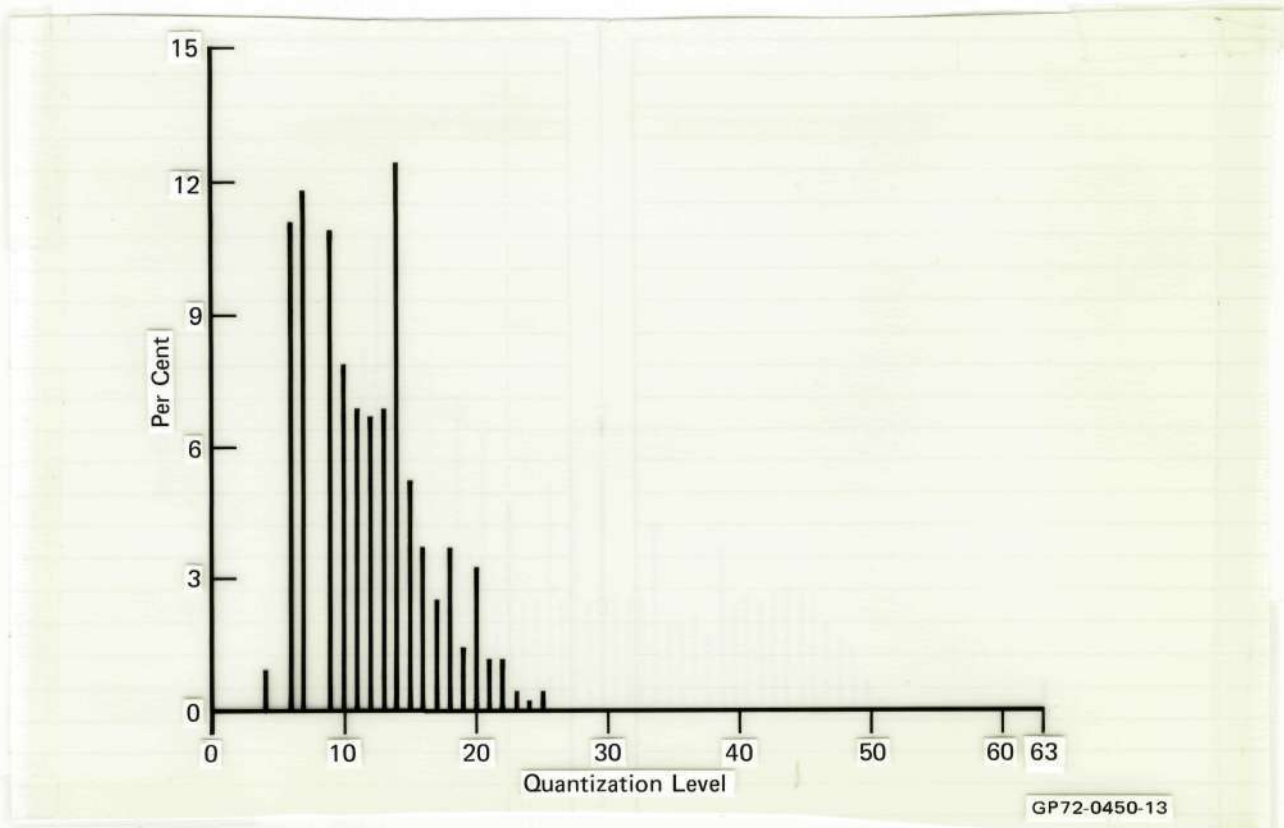
1-18



Centered At: 32° 08'30" N. Latitude
115° 28'00" W. Longitude
Image Mean: 11.8873
Image Variance: 20.5854

128 x 128 Image Array

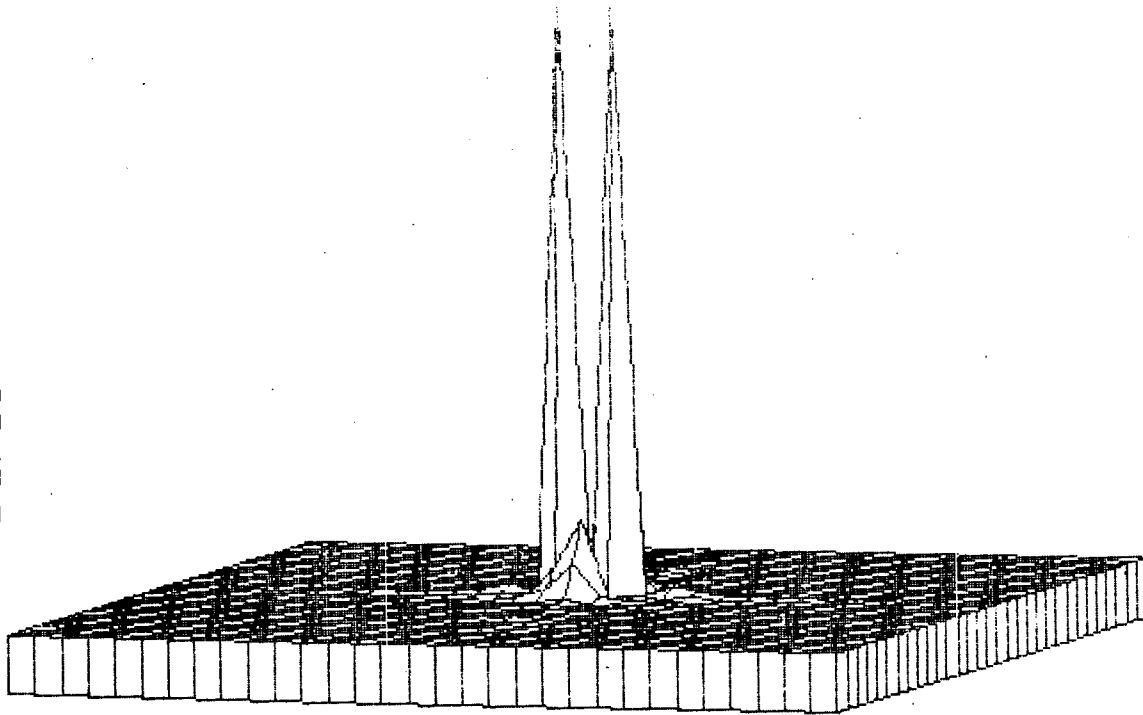
a. Reference Image



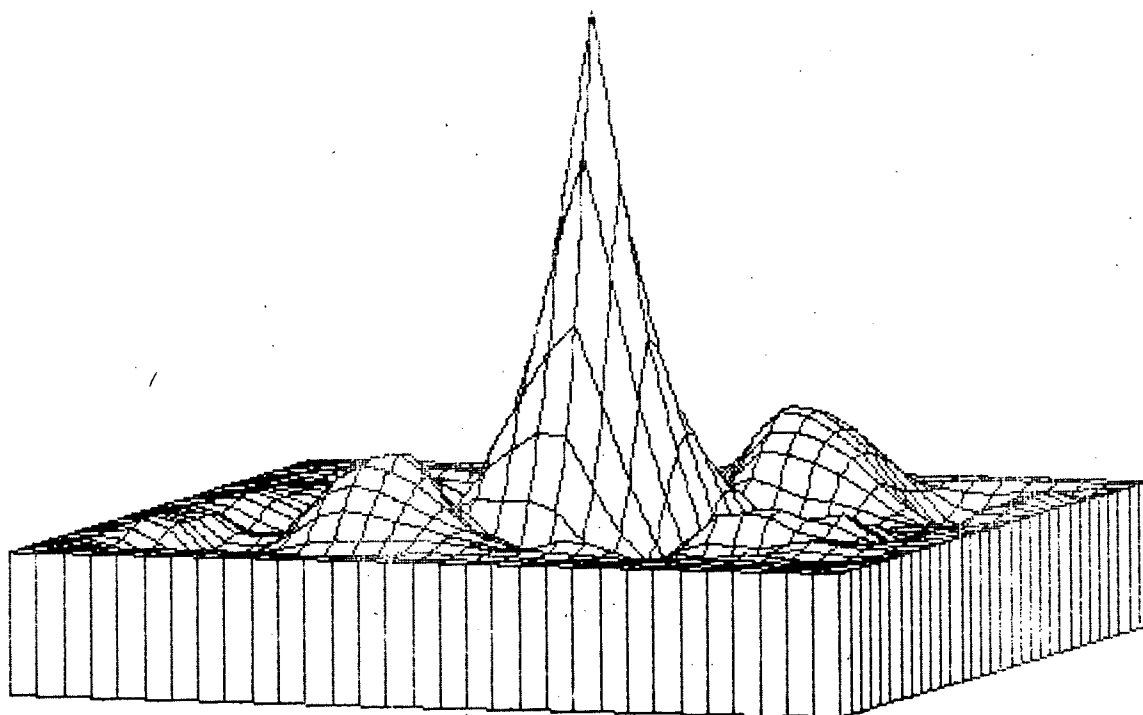
b. Image Intensity Histogram

FIGURE 1-10
IMAGE STATISTICS (FARMLAND TERRAIN - IR SPECTRUM -
MISSION 131 - 50 METER RESOLUTION)

035619



c. Power Spectral Density Function

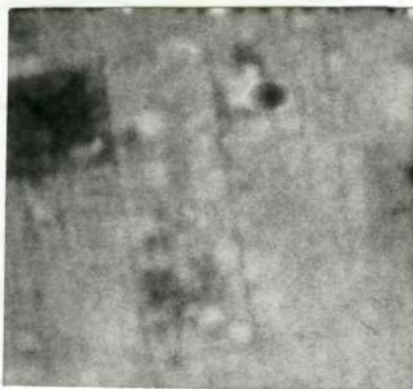


d. Autocorrelation Function

FIGURE 1-10 (Continued)
IMAGE STATISTICS (FARMLAND TERRAIN - IR SPECTRUM -
MISSION 131 - 50 METER RESOLUTION)

MCDONNELL AIRCRAFT

1-20

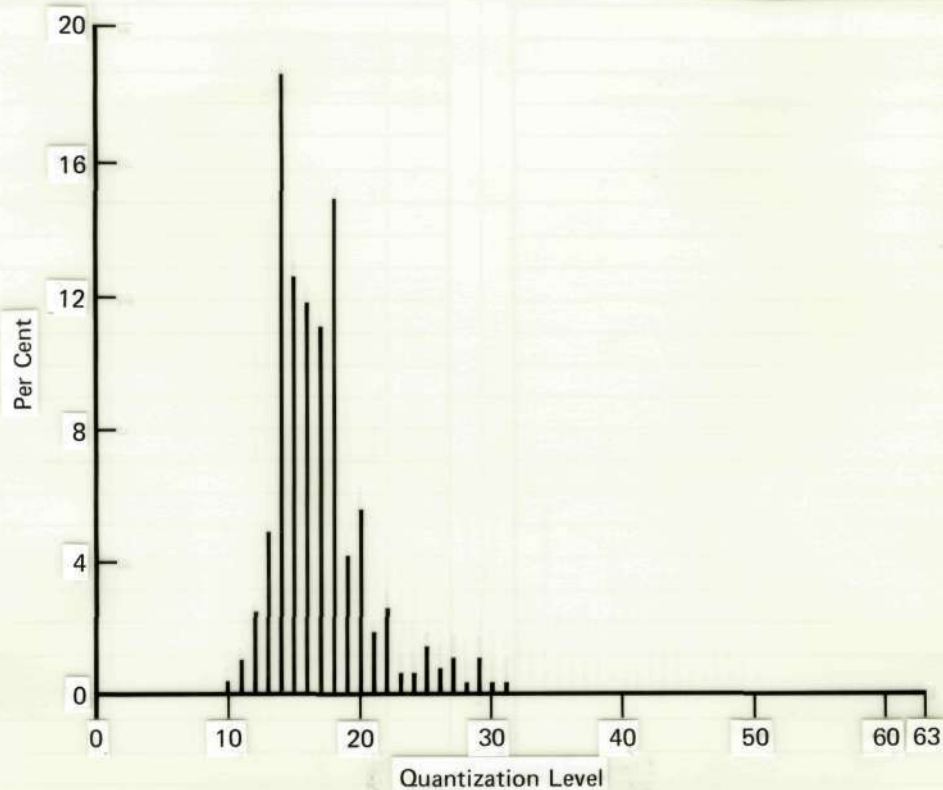


Reproduced from
best available copy.

Centered At: 33° 28'45" N. Latitude
112° 04'45" W. Longitude
Image Mean: 17.1965
Image Variance: 22.2811

128 x 128 Image Array

a. Reference Image

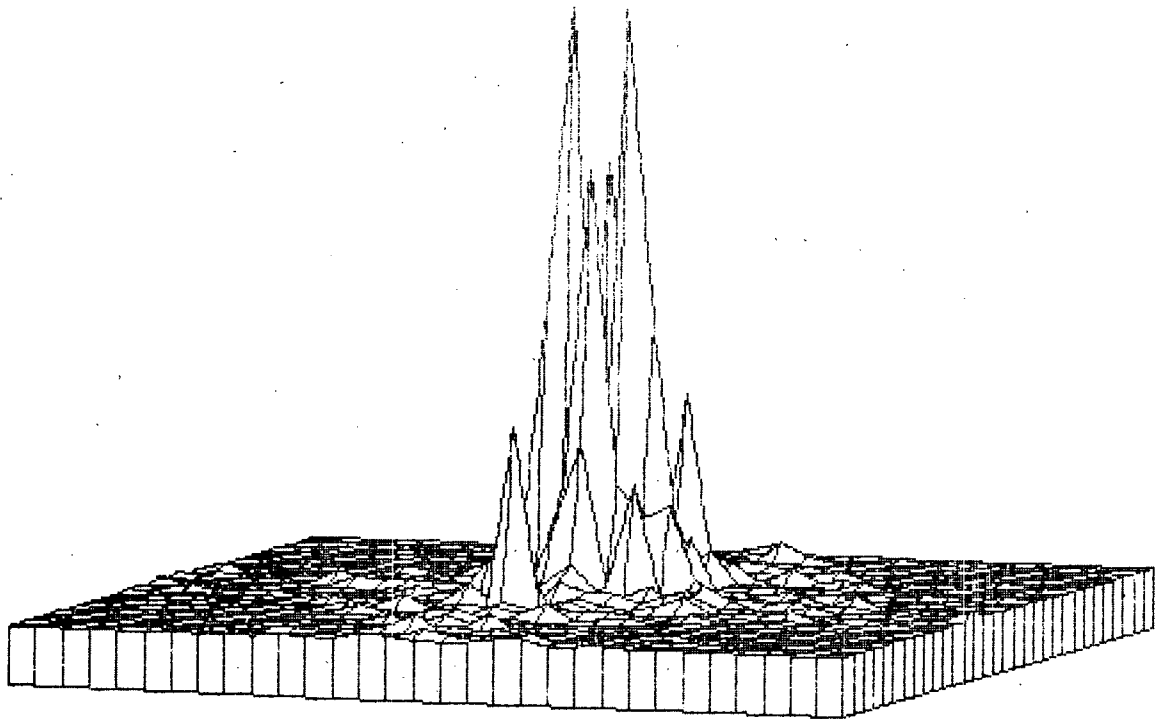


b. Image Intensity Histogram

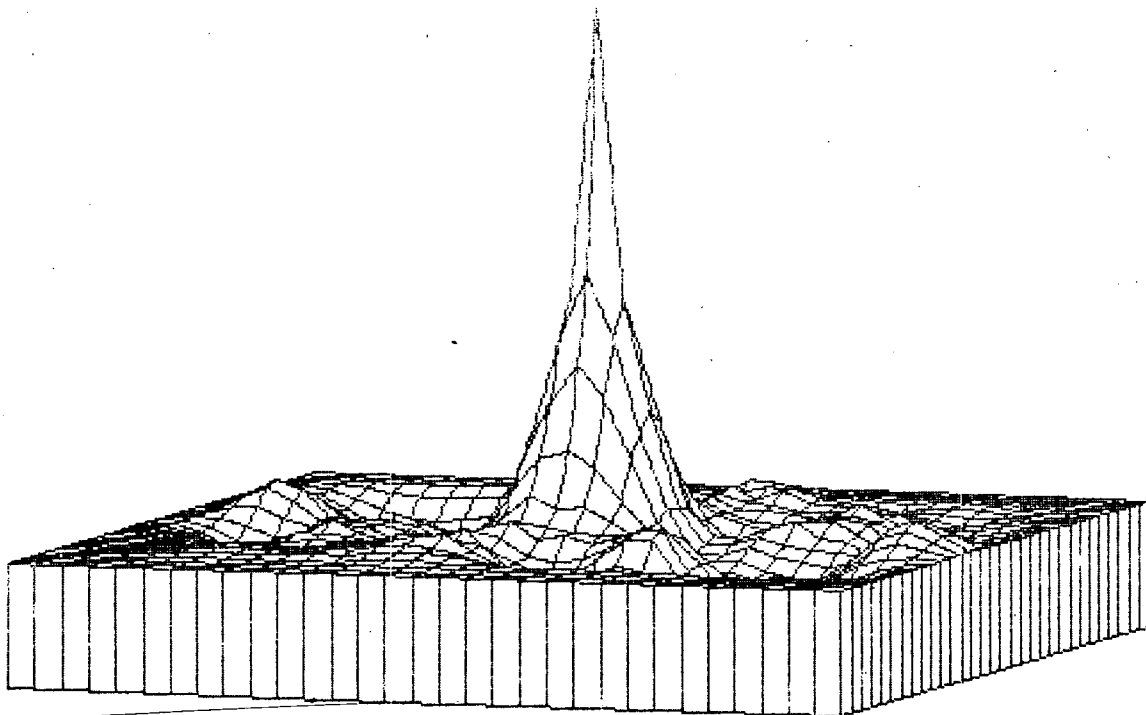
GP72-0450-25

FIGURE 1-11
IMAGE STATISTICS (URBAN TERRAIN - RED SPECTRUM -
MISSION 131 - 50 METER RESOLUTION)

035619



c. Power Spectral Density Function



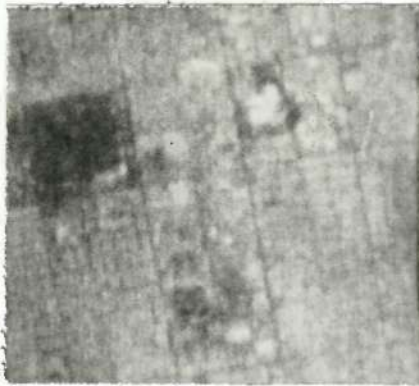
d. Autocorrelation Function

FIGURE 1-11 (Continued)
IMAGE STATISTICS (URBAN TERRAIN - RED SPECTRUM -
MISSION 131 - 50 METER RESOLUTION)

MCDONNELL AIRCRAFT

Reproduced from
best available copy.

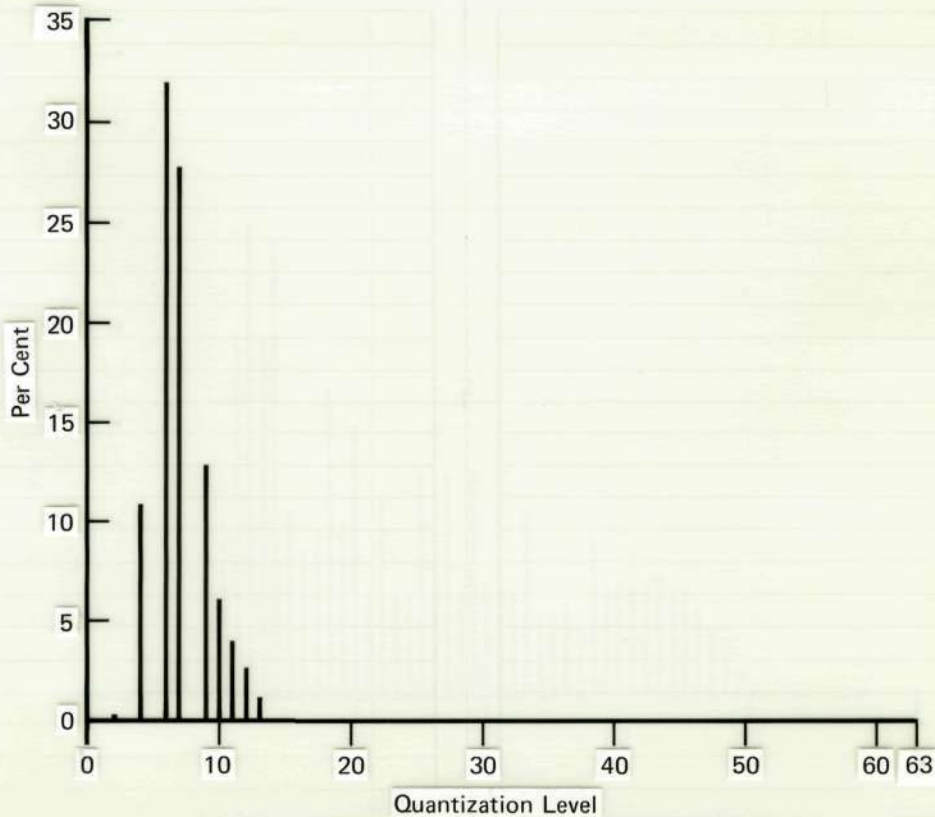
1-22



Centered At: 33° 28'45" N. Latitude
112° 04'45" W. Longitude
Image Mean: 7.15179
Image Variance: 4.98433

128 x 128 Image Array

a. Reference Image

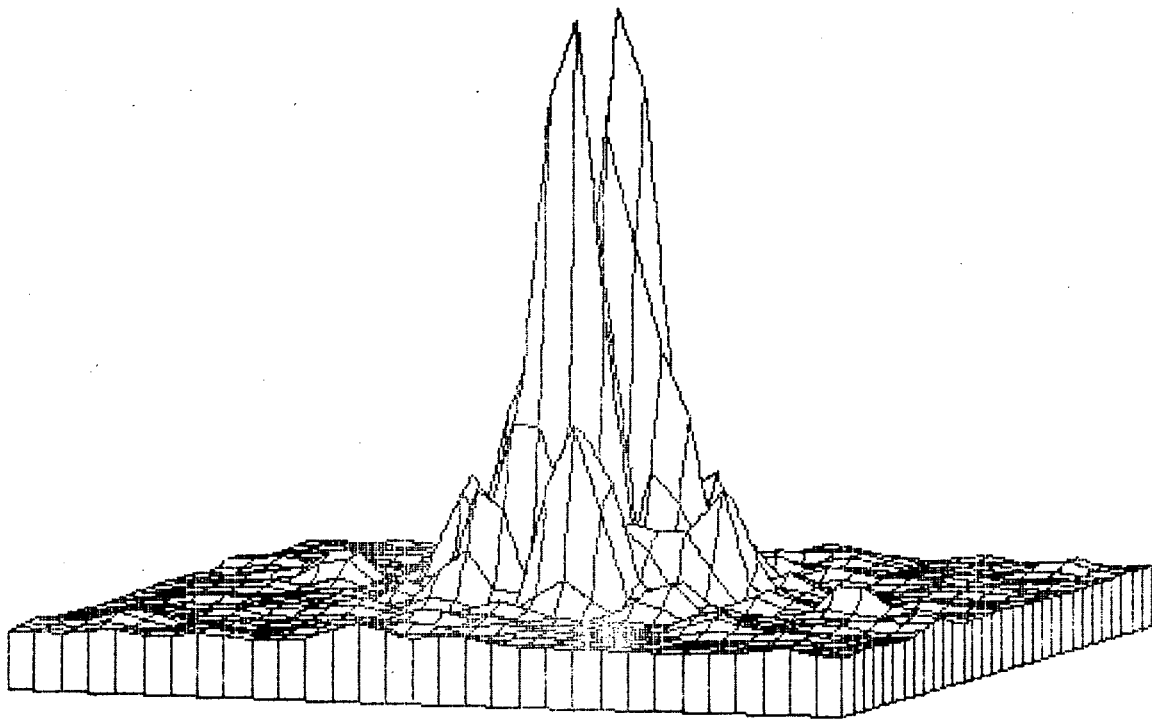


GP72-0450-24

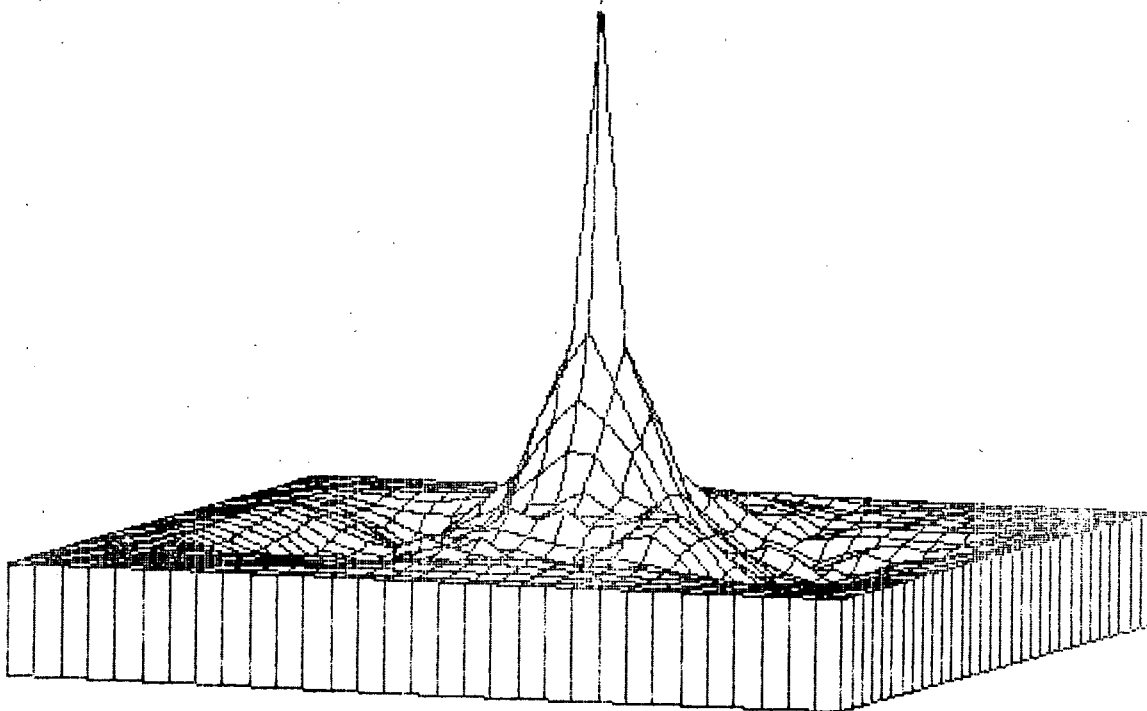
b. Image Intensity Histogram

FIGURE 1-12
IMAGE STATISTICS (URBAN TERRAIN - GREEN SPECTRUM -
MISSION 131 - 50 METER RESOLUTION)

035-619



c. Power Spectral Density Function

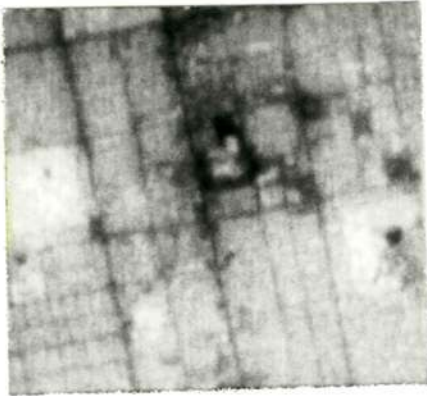


d. Autocorrelation Function

FIGURE 1-12 (Continued)
IMAGE STATISTICS (URBAN TERRAIN - GREEN SPECTRUM -
MISSION 131 - 50 METER RESOLUTION)

MCDONNELL AIRCRAFT

1-24



Centered At: 33° 28'45" N. Latitude
112° 04'45" W. Longitude
Image Mean: 8.58197
Image Variance: 12.6391

128 x 128 Image Array

a. Reference Image

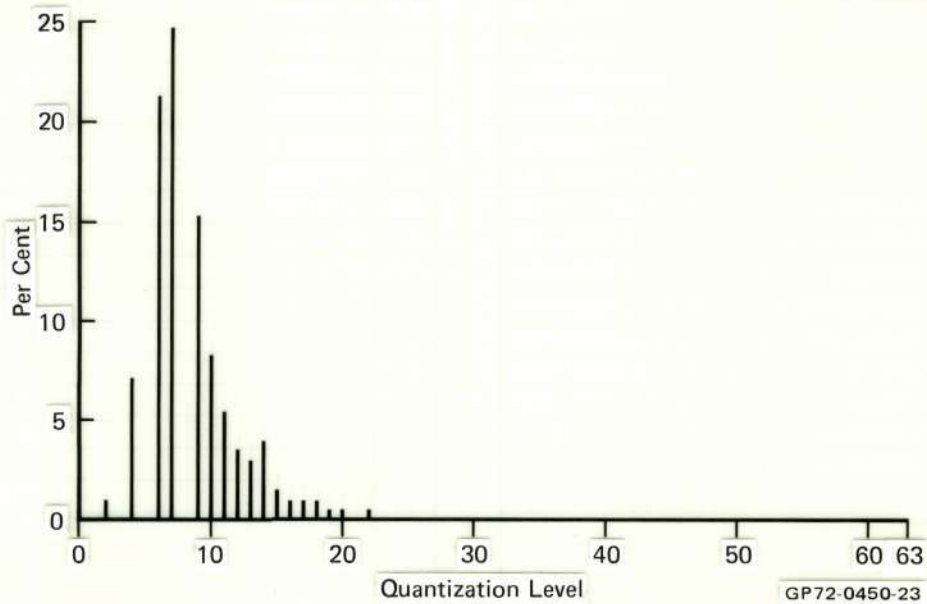
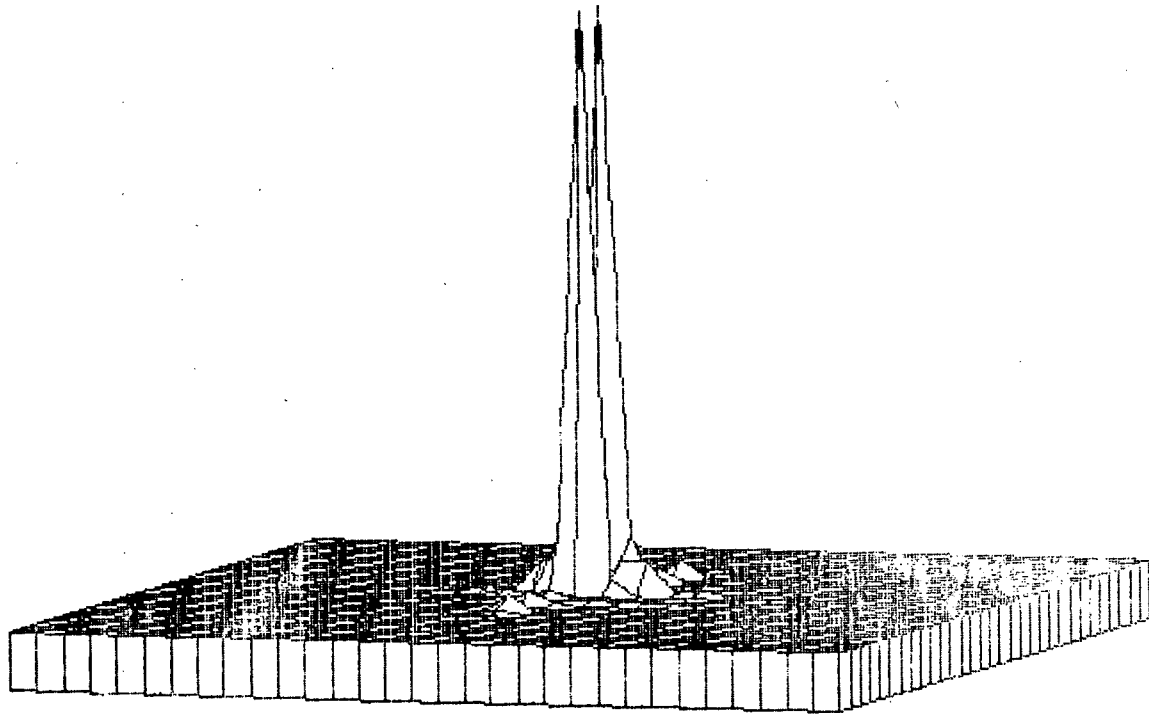
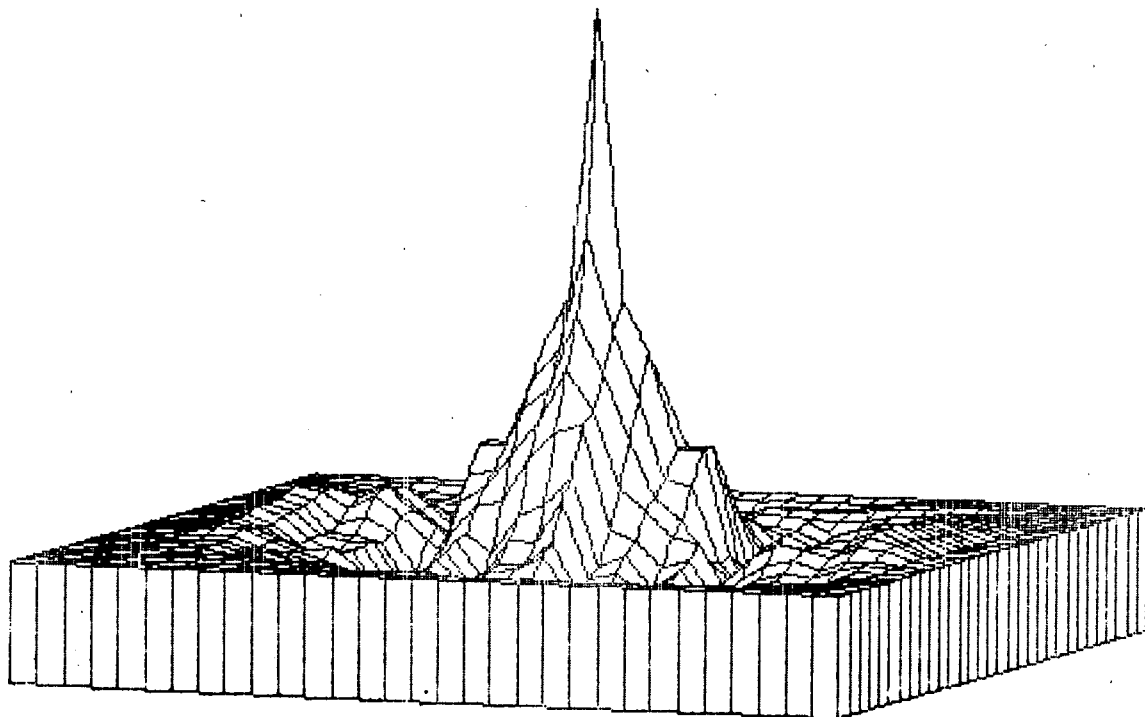


FIGURE 1-13
IMAGE STATISTICS (URBAN TERRAIN - IR SPECTRUM -
MISSION 131 - 50 METER RESOLUTION)

035-619



c. Power Spectral Density Function



d. Autocorrelation Function

FIGURE 1-13 (Continued)
IMAGE STATISTICS (URBAN TERRAIN - IR SPECTRUM -
MISSION 131 - 50 METER RESOLUTION)

Reproduced from
best available copy.



1-26



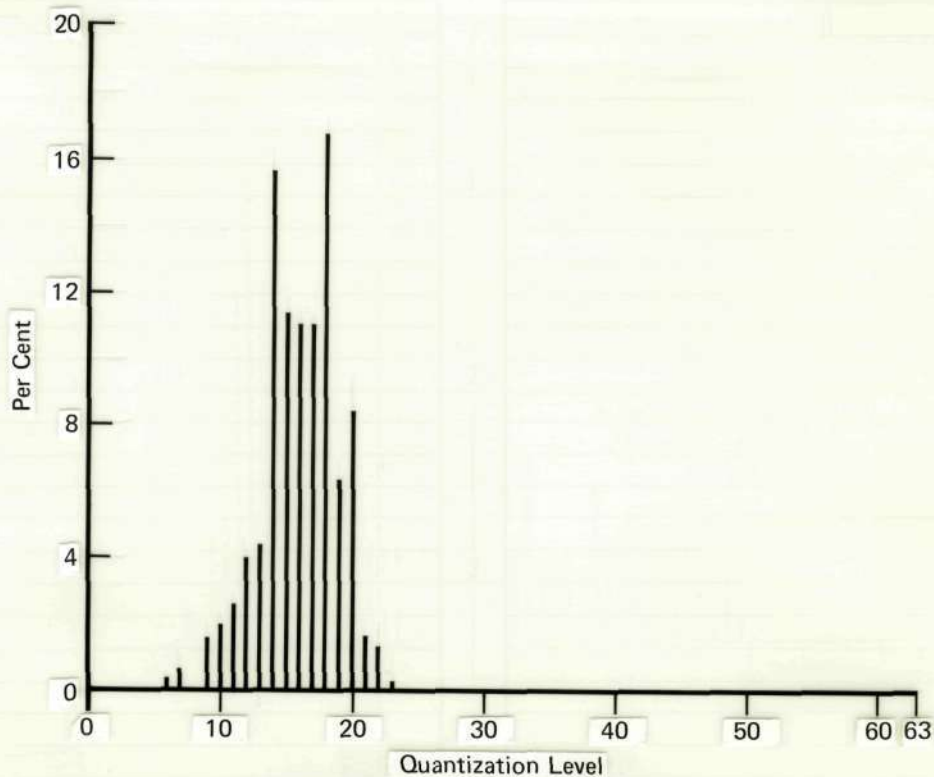
Centered At: $33^{\circ} 30' 45''$ N. Latitude
 $111^{\circ} 31' 45''$ W. Longitude

Image Mean: 15.9868

Image Variance: 9.04295

128 x 128 Image Array

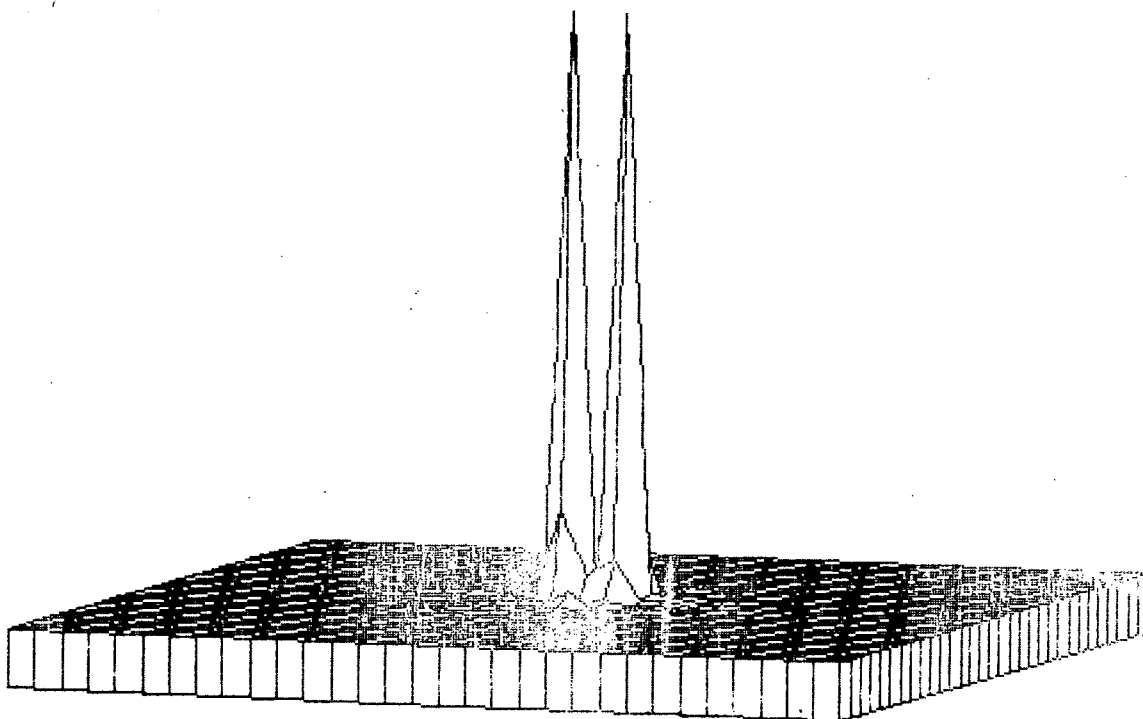
a. Reference Image



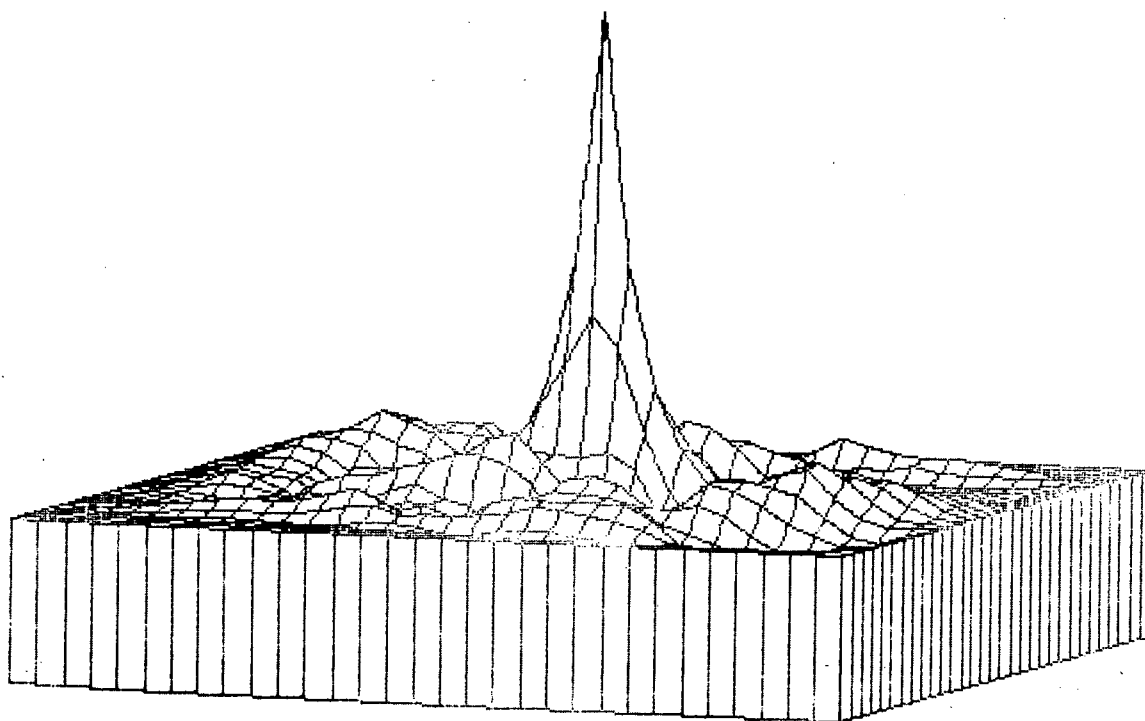
b. Image Intensity Histogram

GP72-0450-22

FIGURE 1-14
IMAGE STATISTICS (MOUNTAIN TERRAIN - RED SPECTRUM -
MISSION 131 - 50 METER RESOLUTION)



c. Power Spectral Density Function



d. Autocorrelation Function

FIGURE 1-14 (Continued)
IMAGE STATISTICS (MOUNTAIN TERRAIN - RED SPECTRUM -
MISSION 131 - 50 METER RESOLUTION)

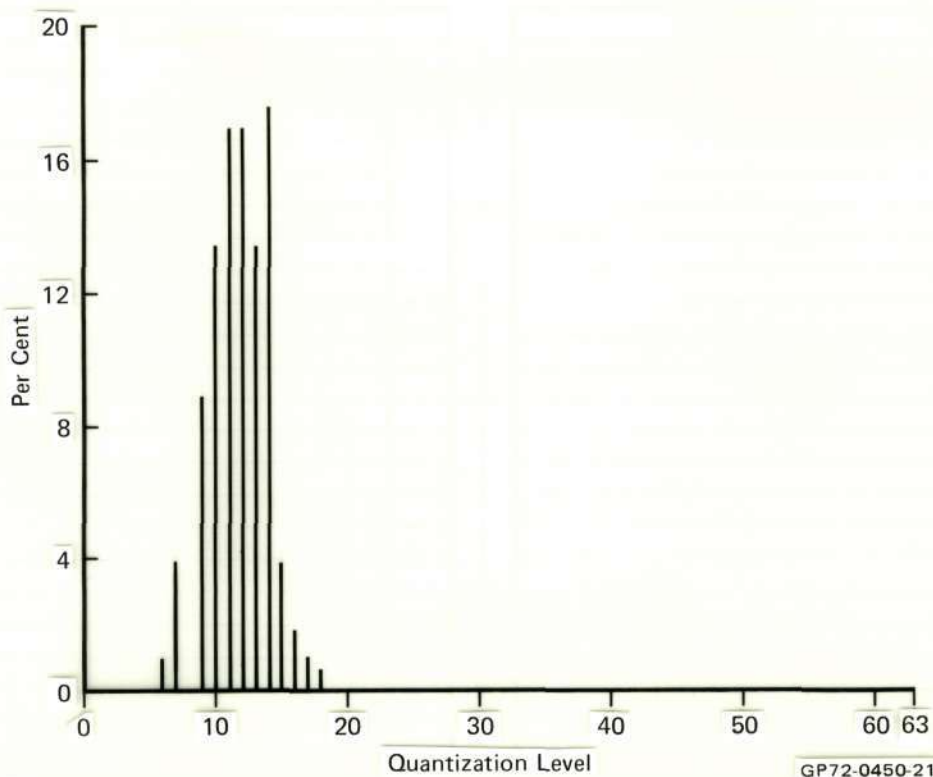
MCDONNELL AIRCRAFT



128 x 128 Image Array

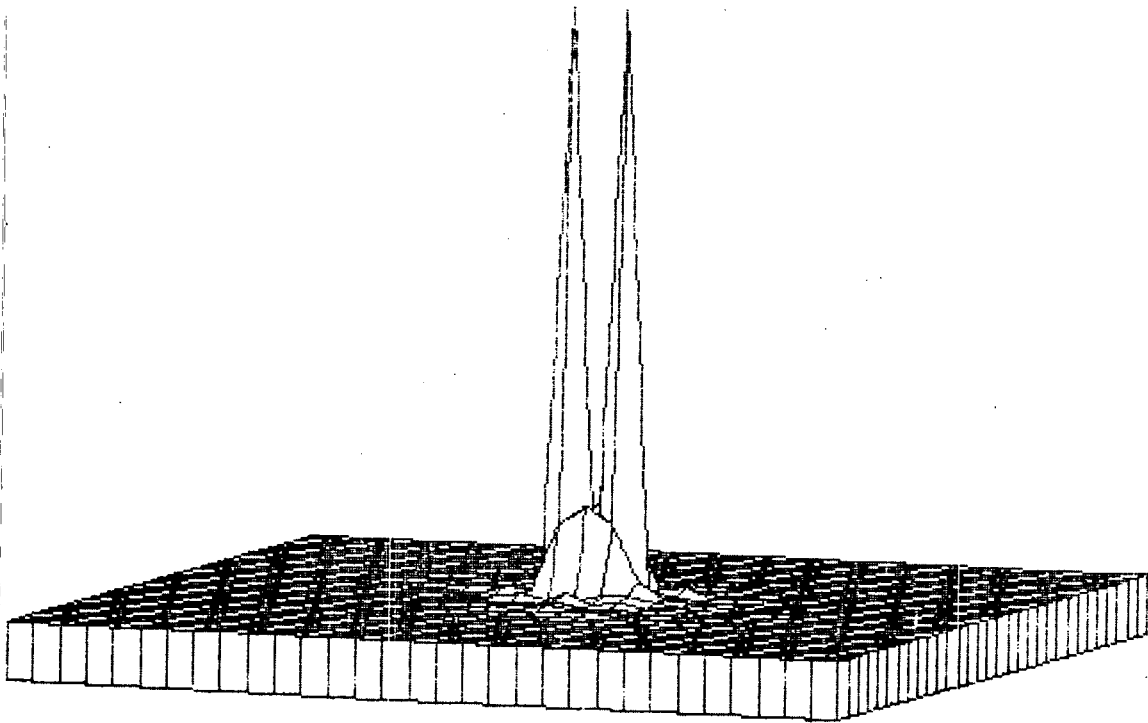
Centered At: 33° 30'45" N. Latitude
 111° 31'45" W. Longitude
 Image Mean: 11.801
 Image Variance: 5.13853

a. Reference Image

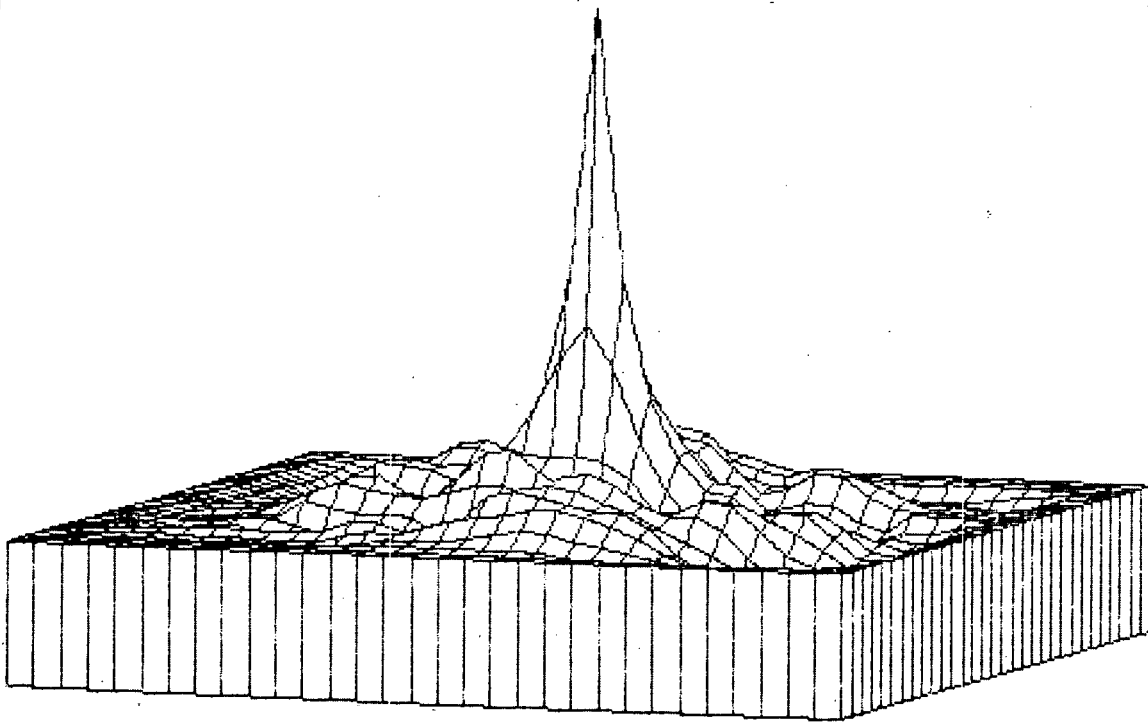


b. Image Intensity Histogram

FIGURE 1-15
IMAGE STATISTICS (MOUNTAIN TERRAIN - GREEN SPECTRUM -
MISSION 131 - 50 METER RESOLUTION)



c. Power Spectral Density Function



d. Autocorrelation Function

FIGURE 1-15 (Continued)
IMAGE STATISTICS (MOUNTAIN TERRAIN - GREEN SPECTRUM -
MISSION 131 - 50 METER RESOLUTION)

MCDONNELL AIRCRAFT

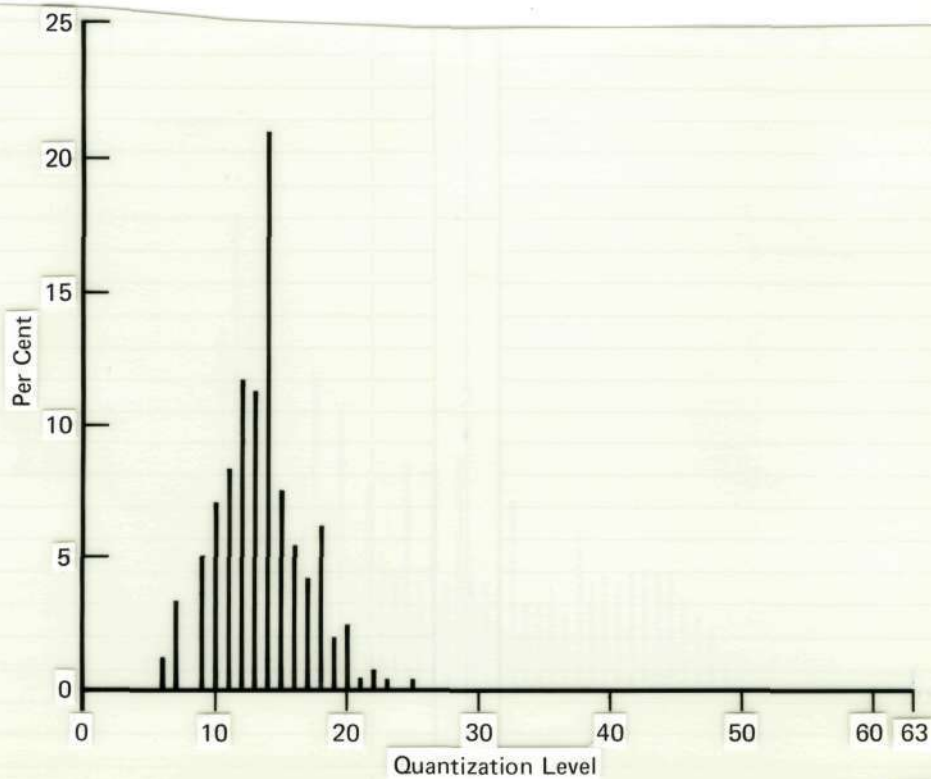
Reproduced from
best available copy.



128 x 128 Image Array

Centered At: 33° 30'45" N. Latitude
111° 31'45" W. Longitude
Image Mean: 13.55
Image Variance: 11.0946

a. Reference Image

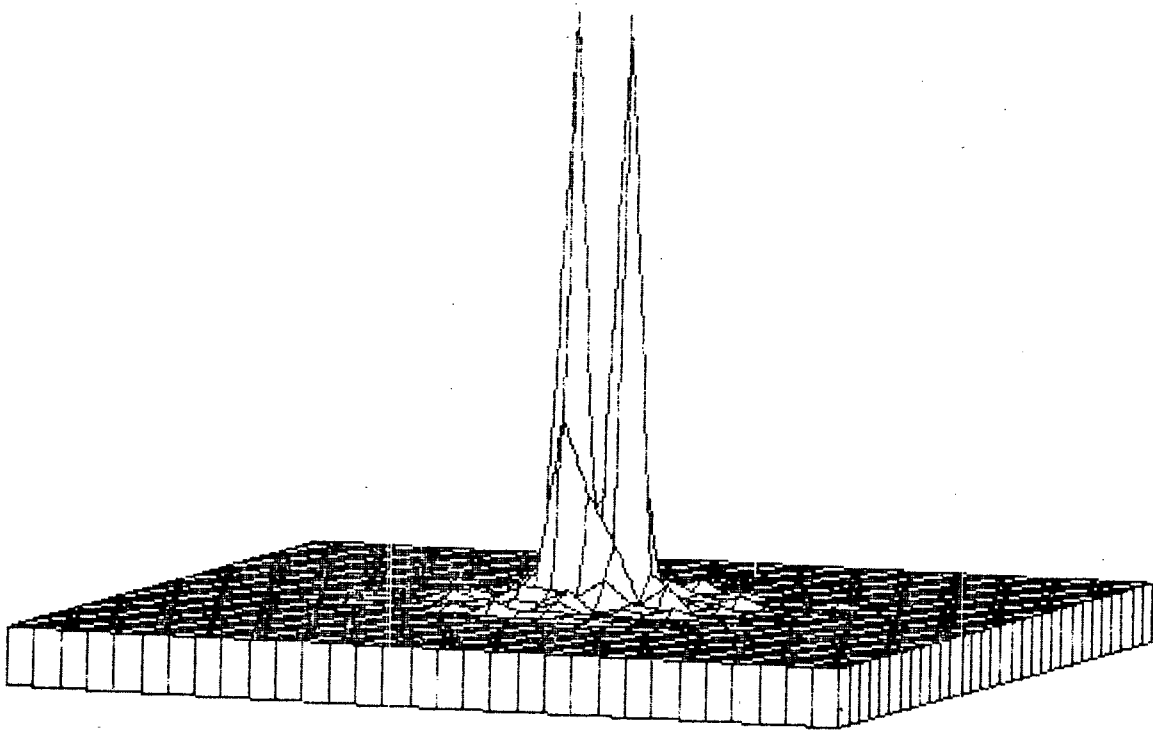


GP72-0450-20

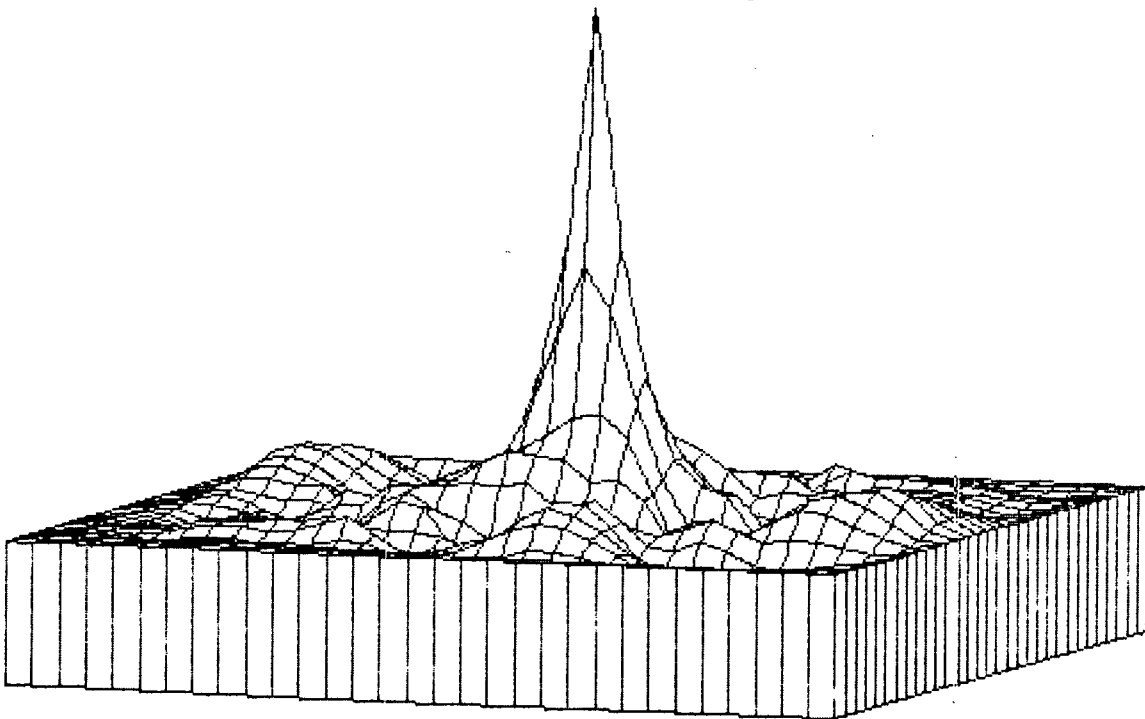
b. Image Intensity Histogram

FIGURE 1-16
IMAGE STATISTICS (MOUNTAIN TERRAIN - IR SPECTRUM -
MISSION 131 - 50 METER RESOLUTION)

035619



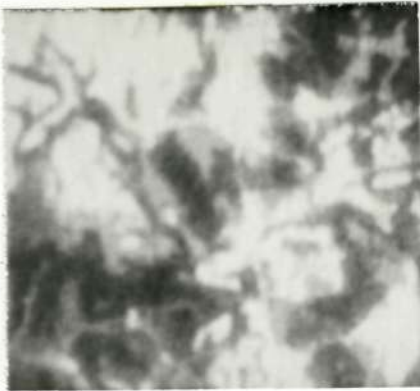
c. Power Spectral Density Function



d. Autocorrelation Function

FIGURE 1-16 (Continued)
 IMAGE STATISTICS (MOUNTAIN TERRAIN - IR SPECTRUM -
 MISSION 131 - 50 METER RESOLUTION)

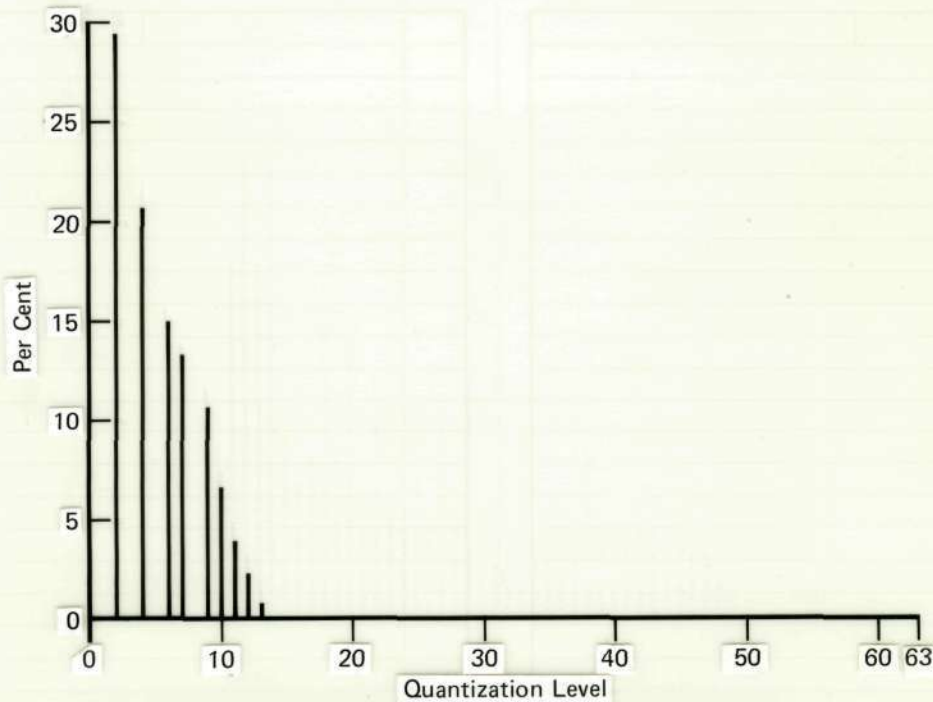
MCDONNELL AIRCRAFT



128 x 128 Image Array

Centered At: 33° 42'30" N. Latitude
85° 15'00" W. Longitude
Image Mean: 5.528
Image Variance: 9.19487

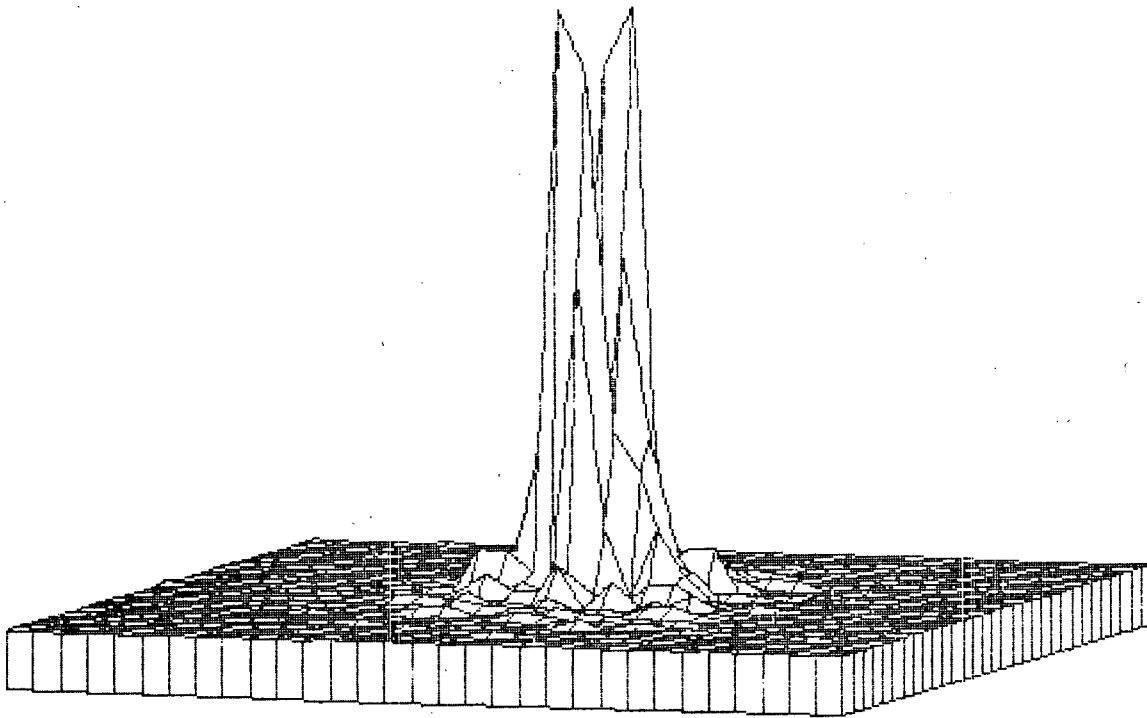
a. Reference Image



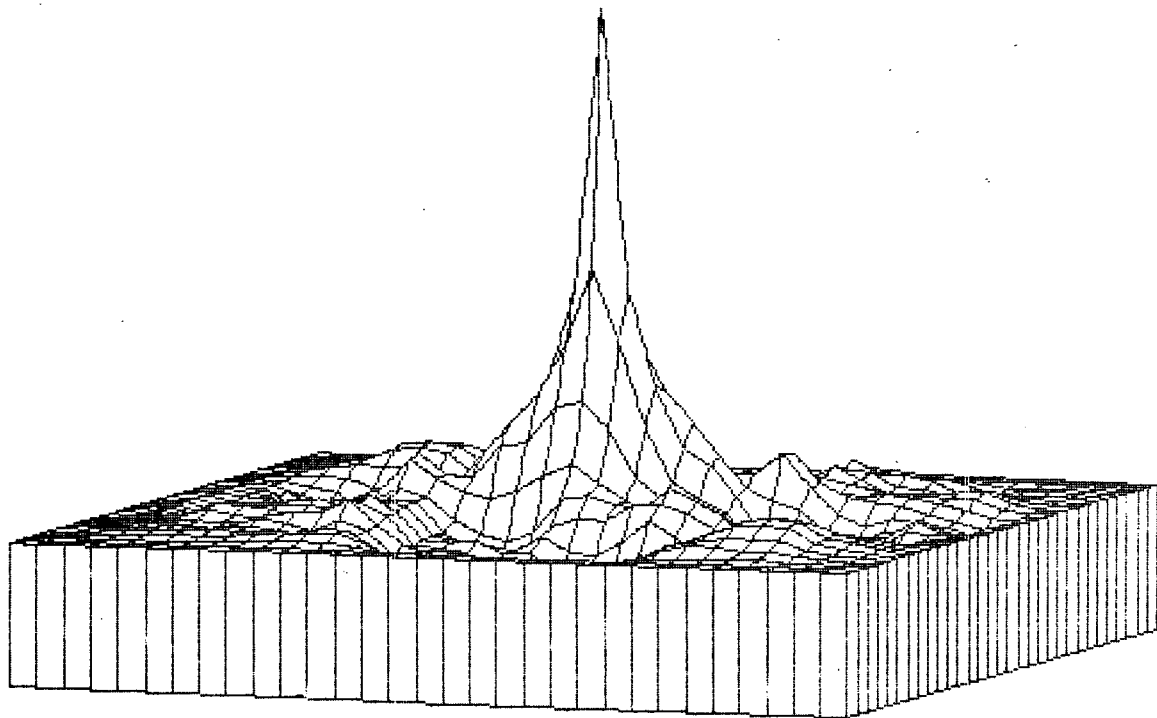
b. Image Intensity Histogram

GP72-0450-19

FIGURE 1-17
IMAGE STATISTICS (FOREST TERRAIN - RED SPECTRUM -
MISSION 131 - 50 METER RESOLUTION)



c. Power Spectral Density Function

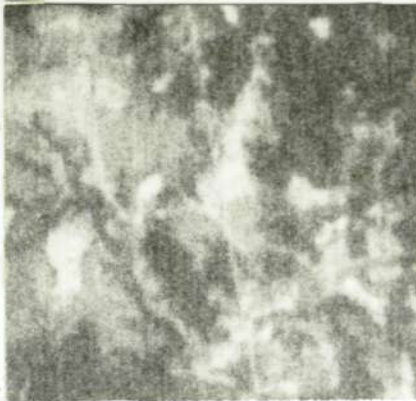


d. Autocorrelation Function

FIGURE 1-17 (Continued)
IMAGE STATISTICS (FOREST TERRAIN - RED SPECTRUM -
MISSION 131 - 50 METER RESOLUTION)

MCDONNELL AIRCRAFT

1-34

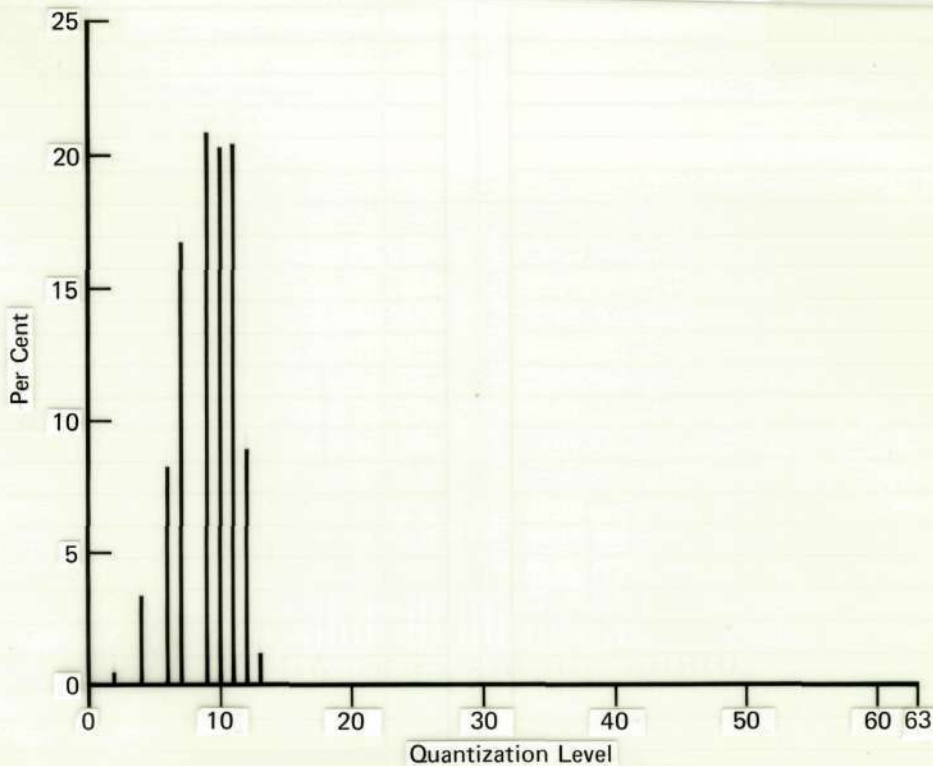


Reproduced from
best available copy.

Centered At: 33°42'30" N. Latitude
85° 15'00" W. Longitude
Image Mean: 9.15808
Image Variance: 4.52321

128 x 128 Image Array

a. Reference Image



GP72-0450-18

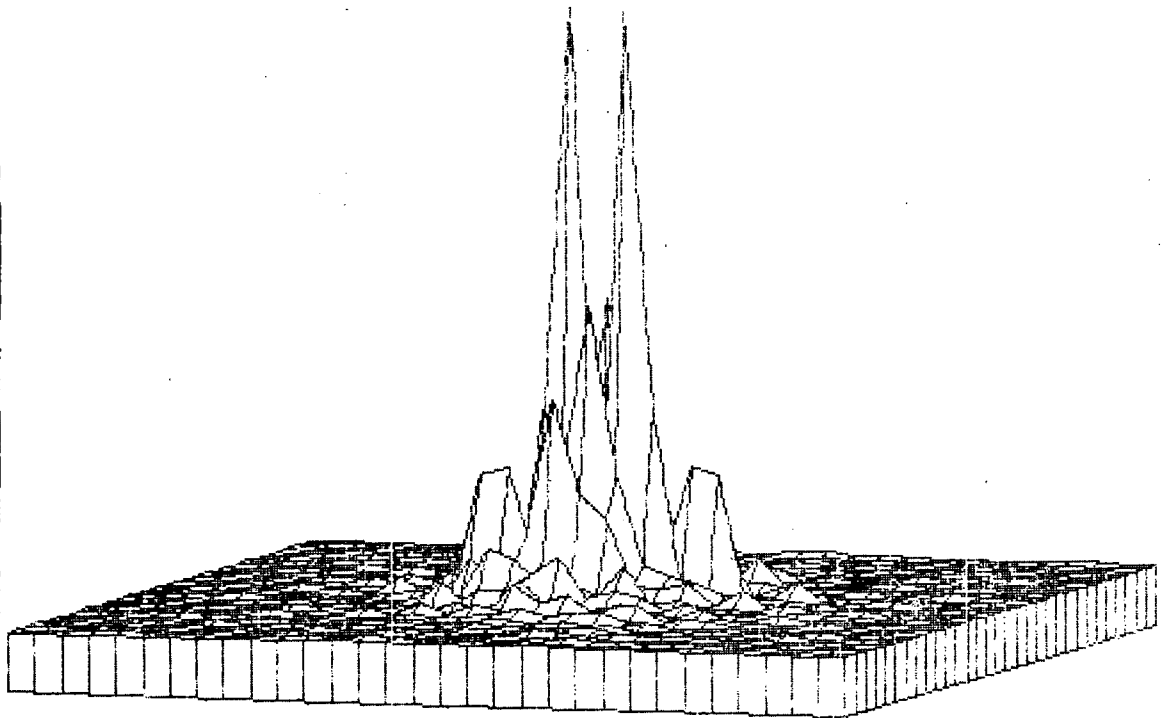
b. Image Intensity Histogram

FIGURE 1-18
IMAGE STATISTICS (FOREST TERRAIN - GREEN SPECTRUM -
MISSION 131 - 50 METER RESOLUTION)

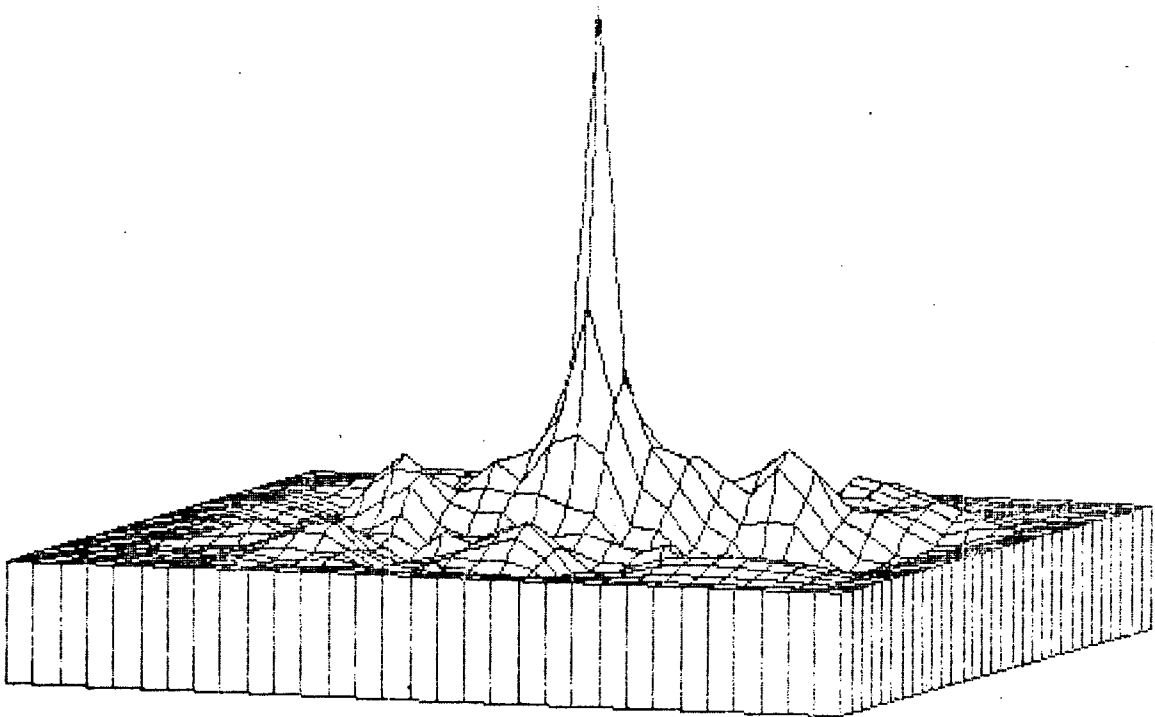
MCDONNELL AIRCRAFT

1-34

035619



c. Power Spectral Density Function



d. Autocorrelation Function

FIGURE 1-18 (Continued)
IMAGE STATISTICS (FOREST TERRAIN - GREEN SPECTRUM -
MISSION 131 - 50 METER RESOLUTION)

MCDONNELL AIRCRAFT

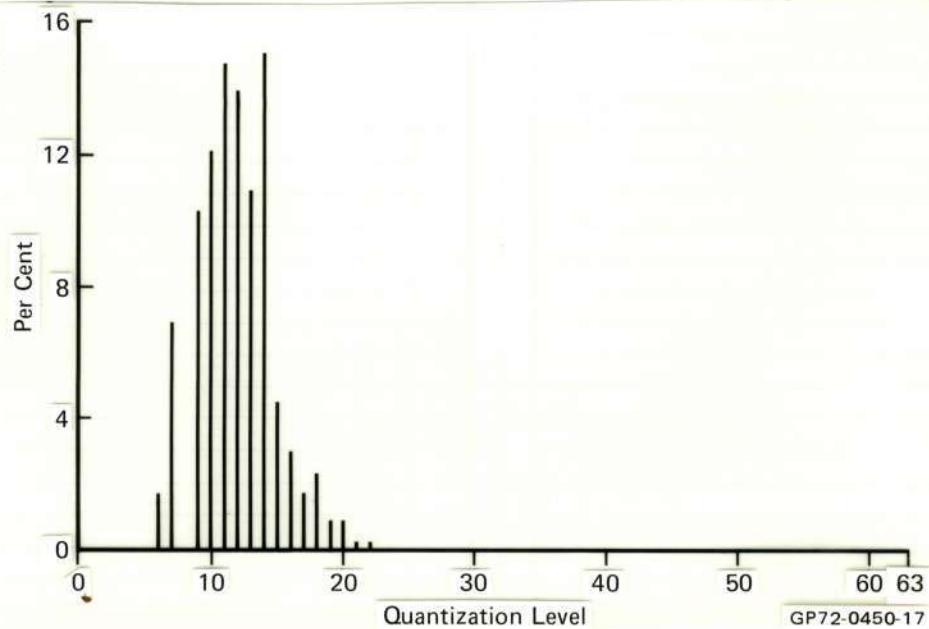
1-36



128 x 128 Image Array

Centered At: 33° 42'30" N. Latitude
85° 15'00" W. Longitude
Image Mean: 11.9337
Image Variance: 8.649

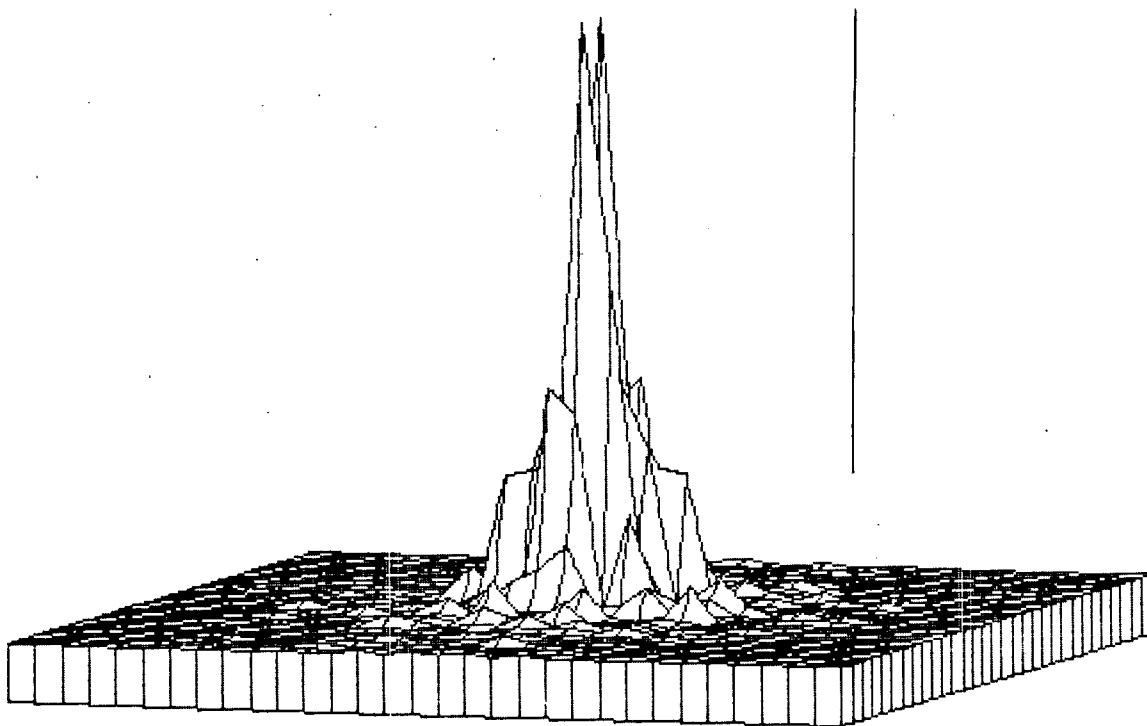
a. Reference Image



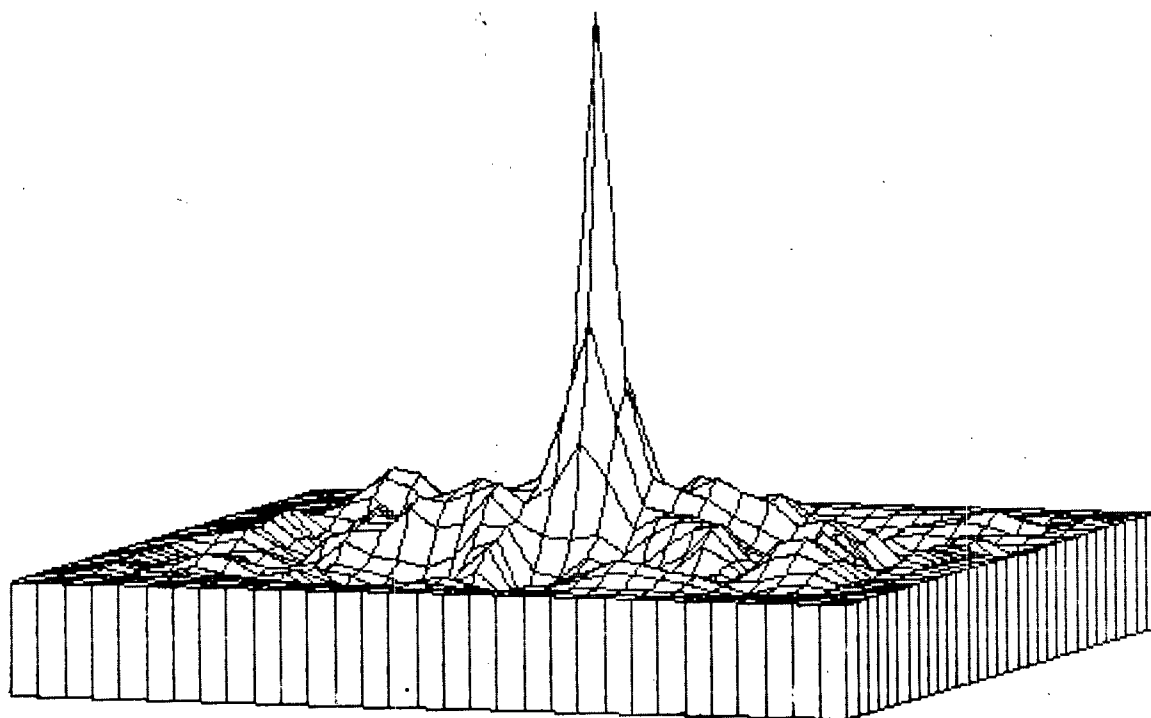
b. Image Intensity Histogram

FIGURE 1-19
IMAGE STATISTICS (FOREST TERRAIN - IR SPECTRUM -
MISSION 131 - 50 METER RESOLUTION)

035619



c. Power Spectral Density Function



d. Autocorrelation Function

FIGURE 1-19 (Continued)
IMAGE STATISTICS (FOREST TERRAIN - IR SPECTRUM -
MISSION 131 - 50 METER RESOLUTION)

MCDONNELL AIRCRAFT

Reproduced from
best available copy.

1-38

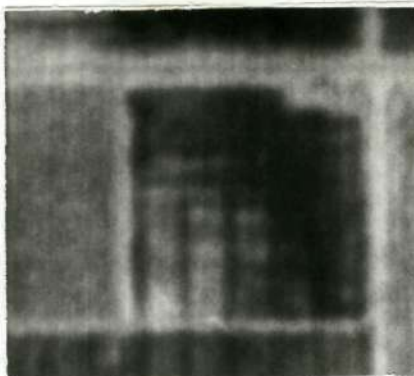
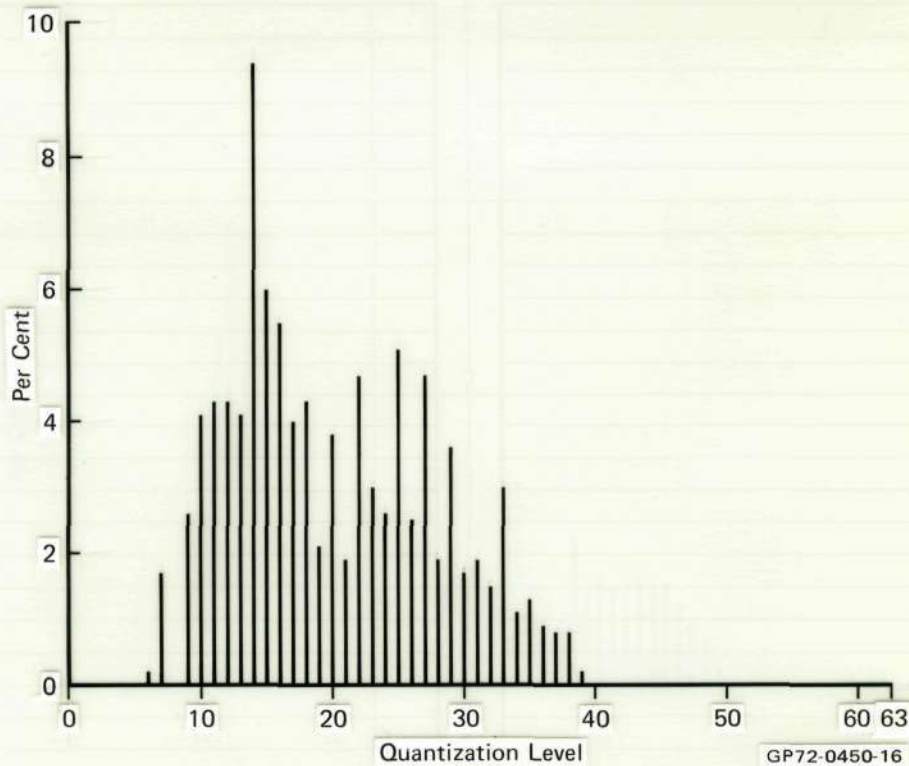


Image Mean: 20.0235
Image Variance: 59.6 858

128 x 128 Image Array

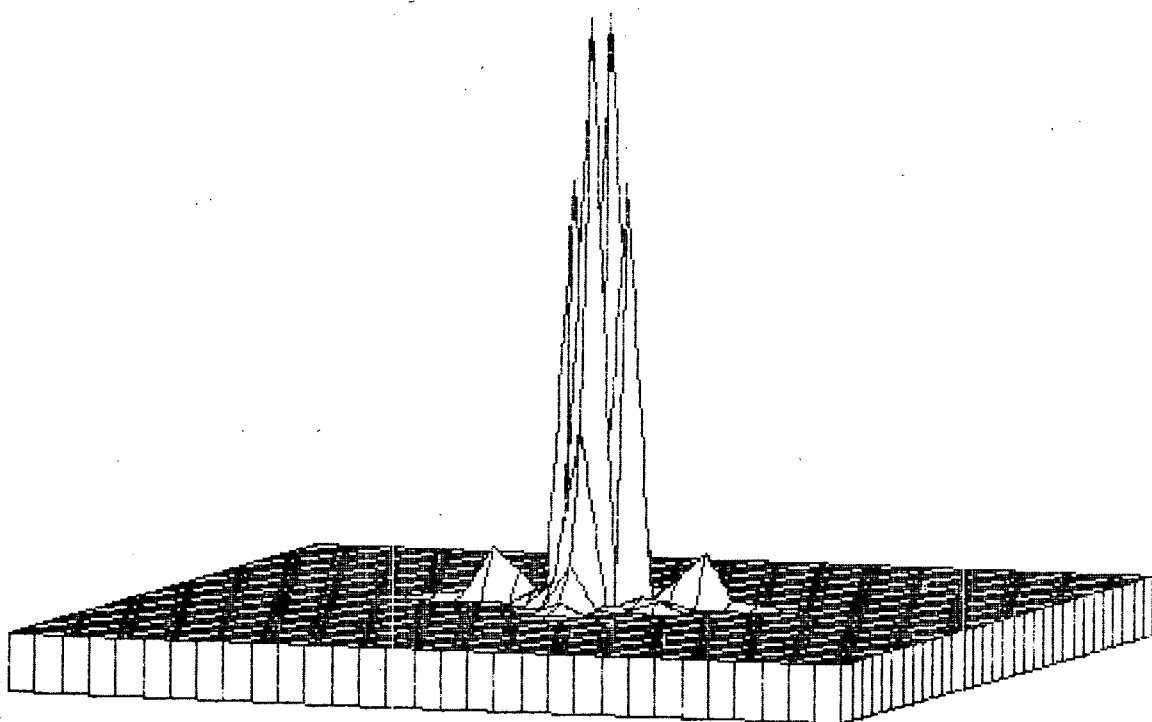
a. Reference Image



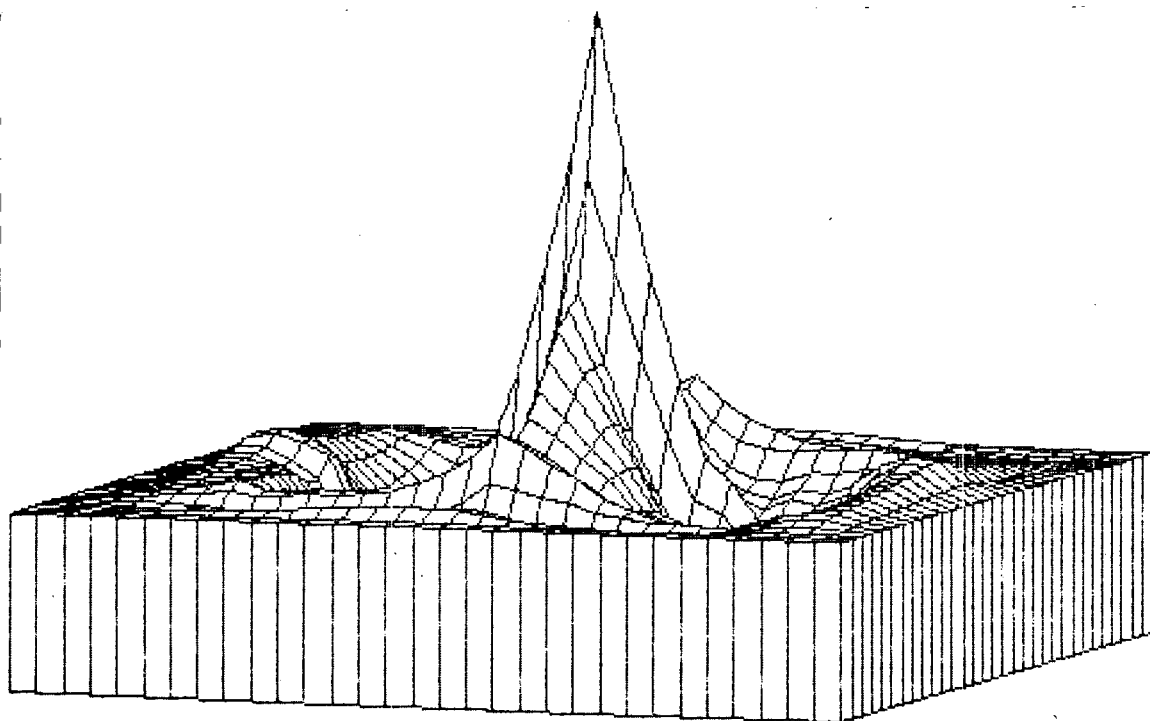
b. Image Intensity Histogram

FIGURE 1-20
IMAGE STATISTICS (FARMLAND TERRAIN - RED SPECTRUM -
MISSION 131 - 10 METER RESOLUTION)

035619



c. Power Spectral Density Function



d. Autocorrelation Function

FIGURE 1-20 (Continued)
IMAGE STATISTICS (FARMLAND TERRAIN - RED SPECTRUM -
MISSION 131 - 10 METER RESOLUTION)

MCDONNELL AIRCRAFT

1-40



Image Mean: 12.7518
Image Variance: 8.16483

128 x 128 Image Array

a. Reference Image

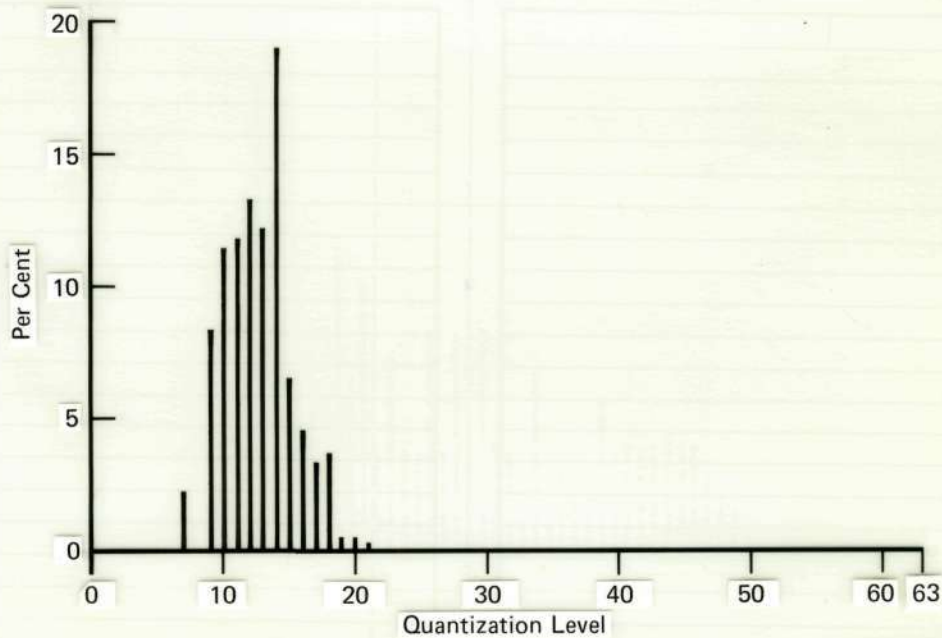
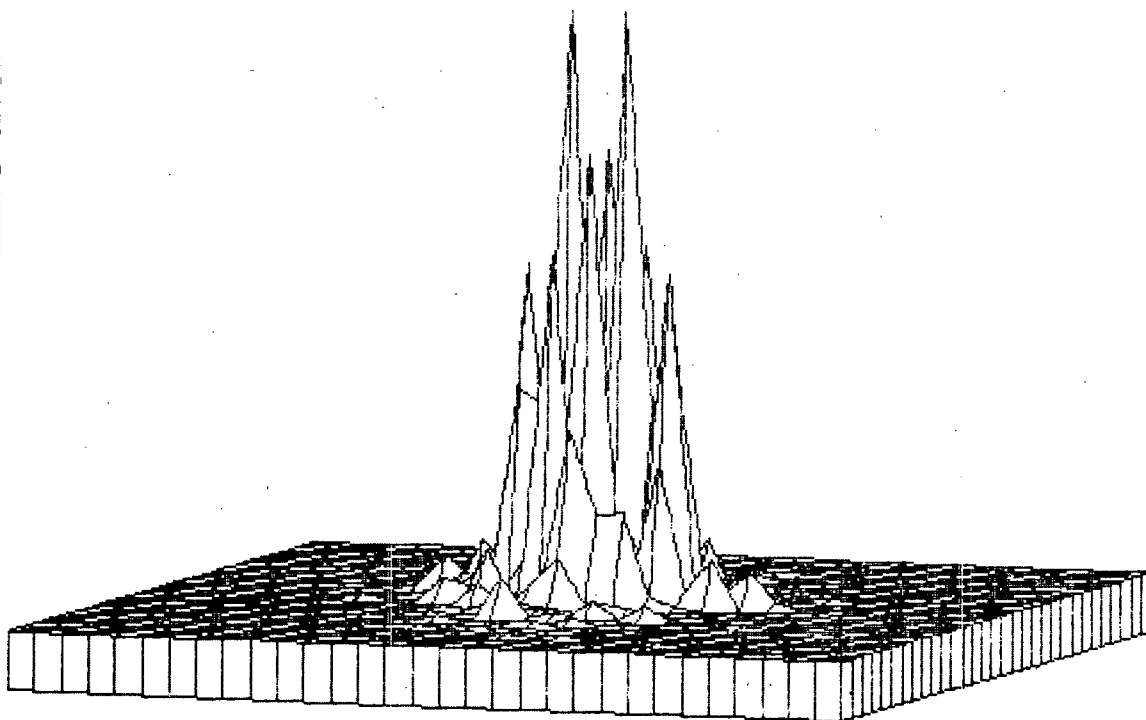


FIGURE 1-21b

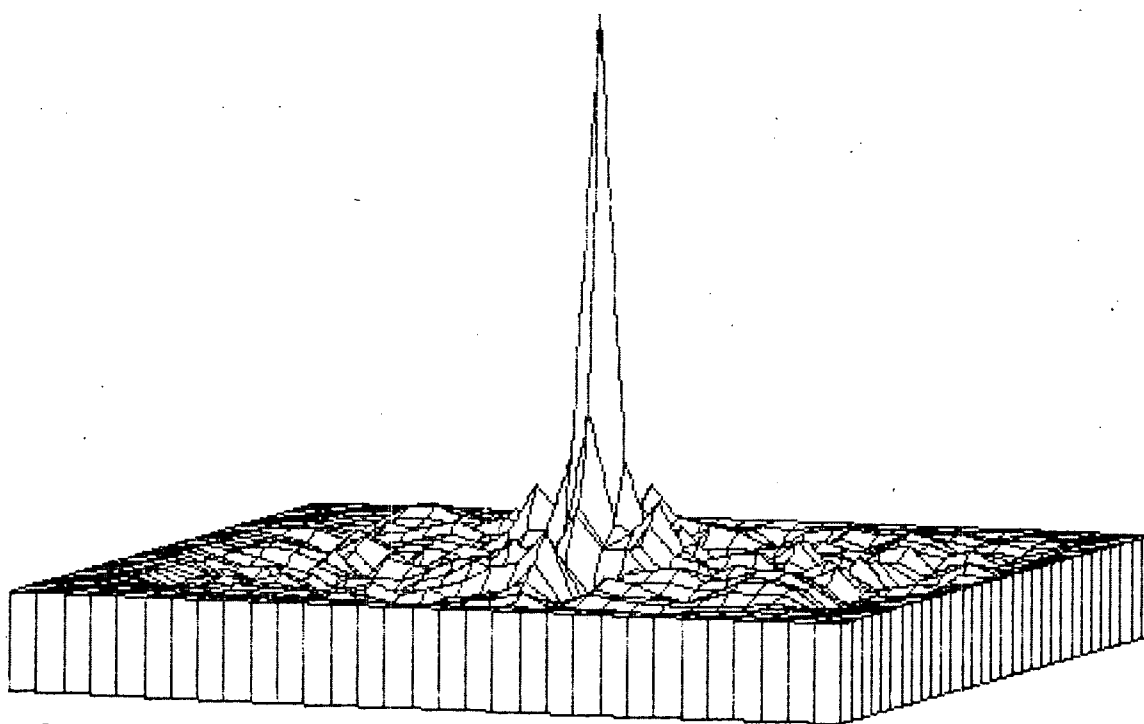
GP72-0450-15

FIGURE 1-21
IMAGE STATISTICS (URBAN TERRAIN - RED SPECTRUM -
MISSION 131 - 10 METER RESOLUTION)

035619



c. Power Spectral Density Function



d. Autocorrelation Function

FIGURE 1-21 (Continued)
IMAGE STATISTICS (URBAN TERRAIN - RED SPECTRUM -
MISSION 131 - 10 METER RESOLUTION)

MCDONNELL AIRCRAFT

1-42



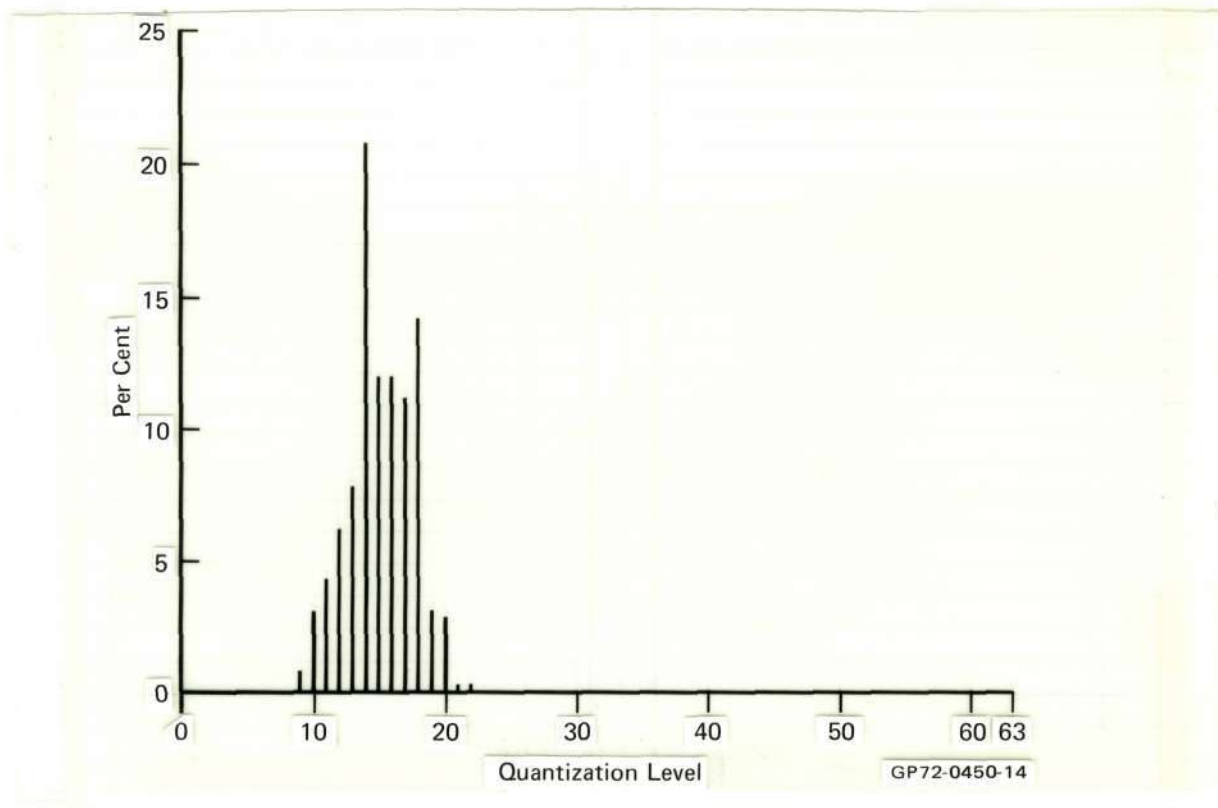
Reproduced from
best available copy.

Image Mean: 15.1554

Image Variance: 6.88269

128 x 128 Image Array

a. Reference Image



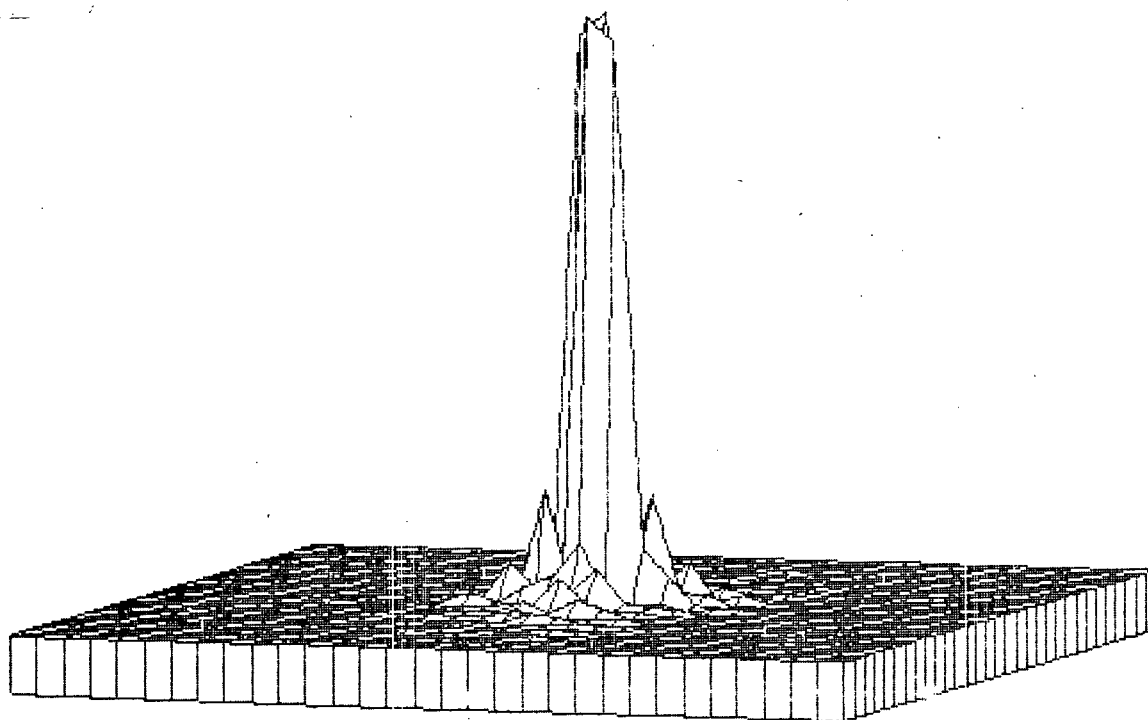
b. Image Intensity Histogram

FIGURE 1-22
IMAGE STATISTICS (MOUNTAIN TERRAIN - RED SPECTRUM -
MISSION 131 - 10 METER RESOLUTION)

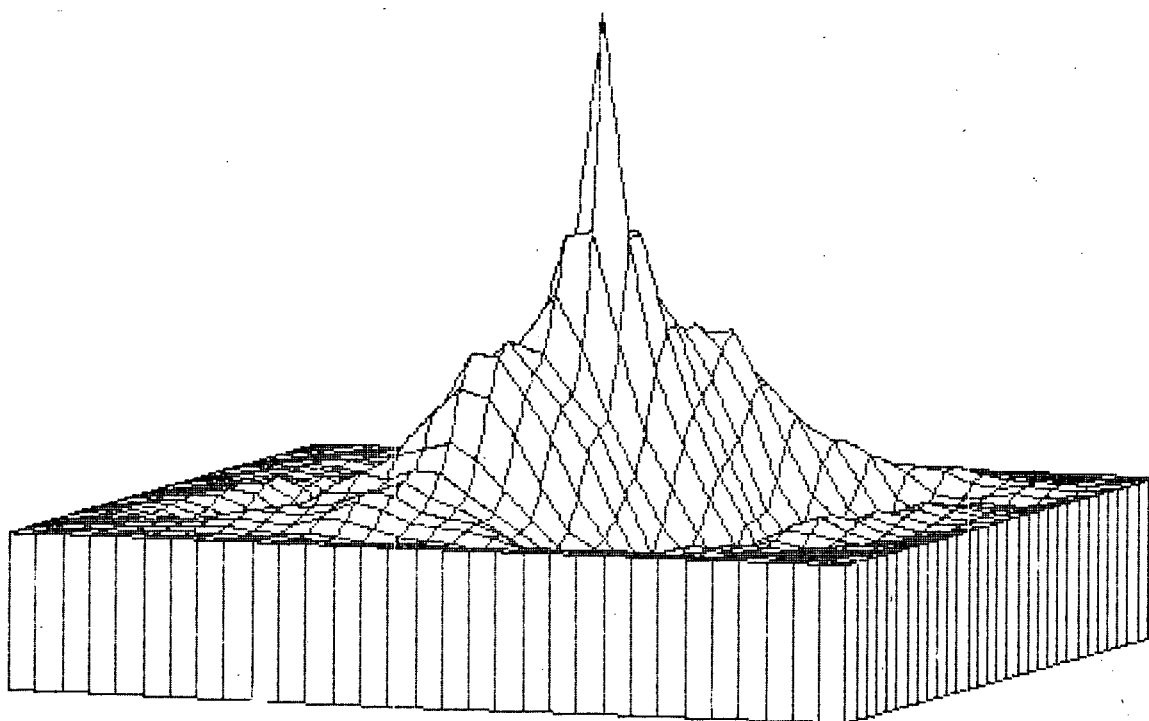
MCDONNELL AIRCRAFT

1-42

035619



c. Power Spectral Density Function



d. Autocorrelation Function

FIGURE 1-22 (Continued)
IMAGE STATISTICS (MOUNTAIN TERRAIN - RED SPECTRUM -
MISSION 131 - 10 METER RESOLUTION)

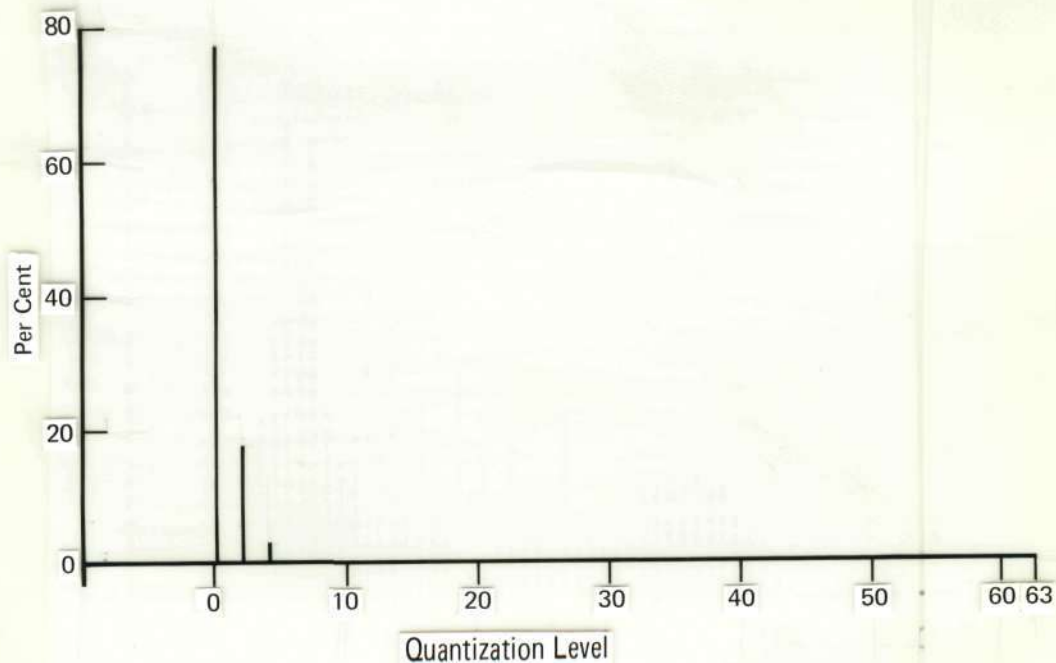
MCDONNELL AIRCRAFT



Image Mean: 64
Image Variance: 10.5

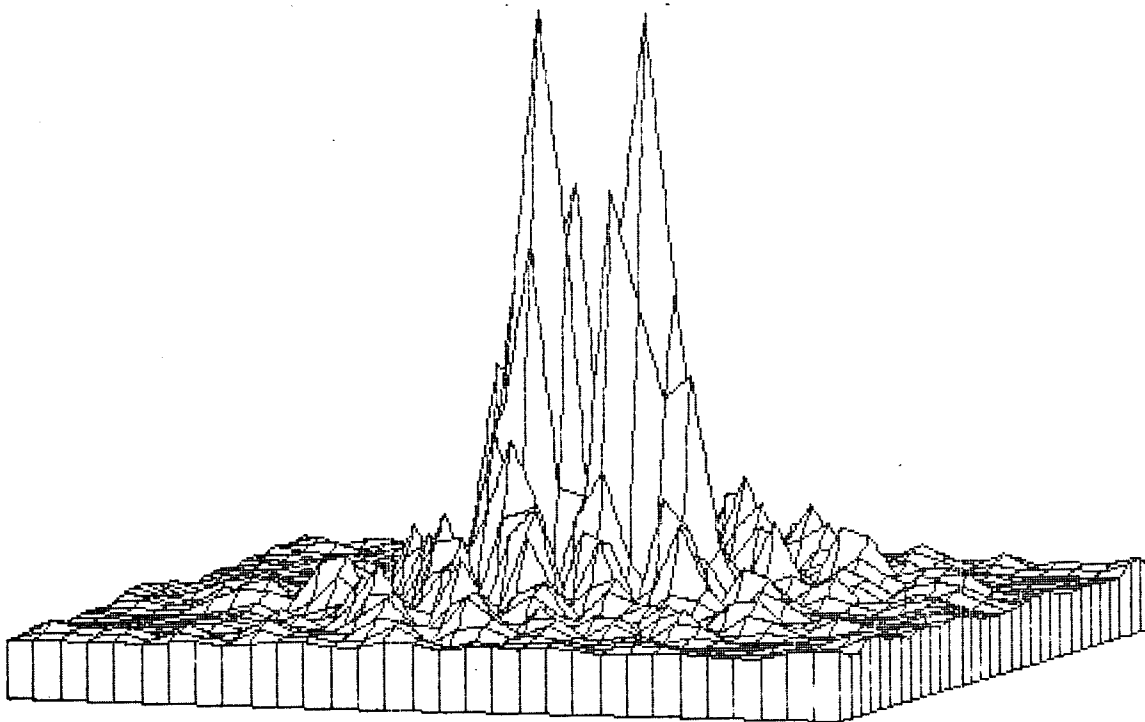
128 x 128 Image Array

a. Reference Image

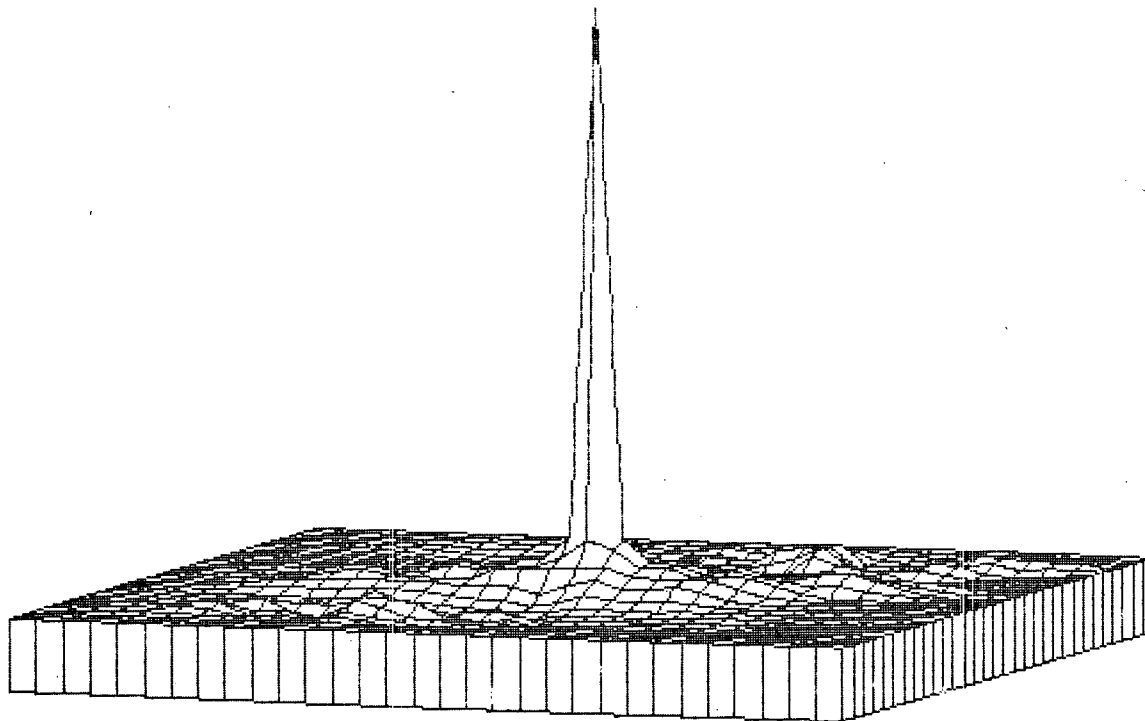


b. Image Intensity Histogram

FIGURE 1-23
IMAGE STATISTICS (FOREST TERRAIN - RED SPECTRUM -
MISSION 131 - 10 METER RESOLUTION)



c. Power Spectral Density Function



d. Autocorrelation Function

FIGURE 1-23 (Continued)
IMAGE STATISTICS (FOREST TERRAIN - RED SPECTRUM -
MISSION 131 - 10 METER RESOLUTION)

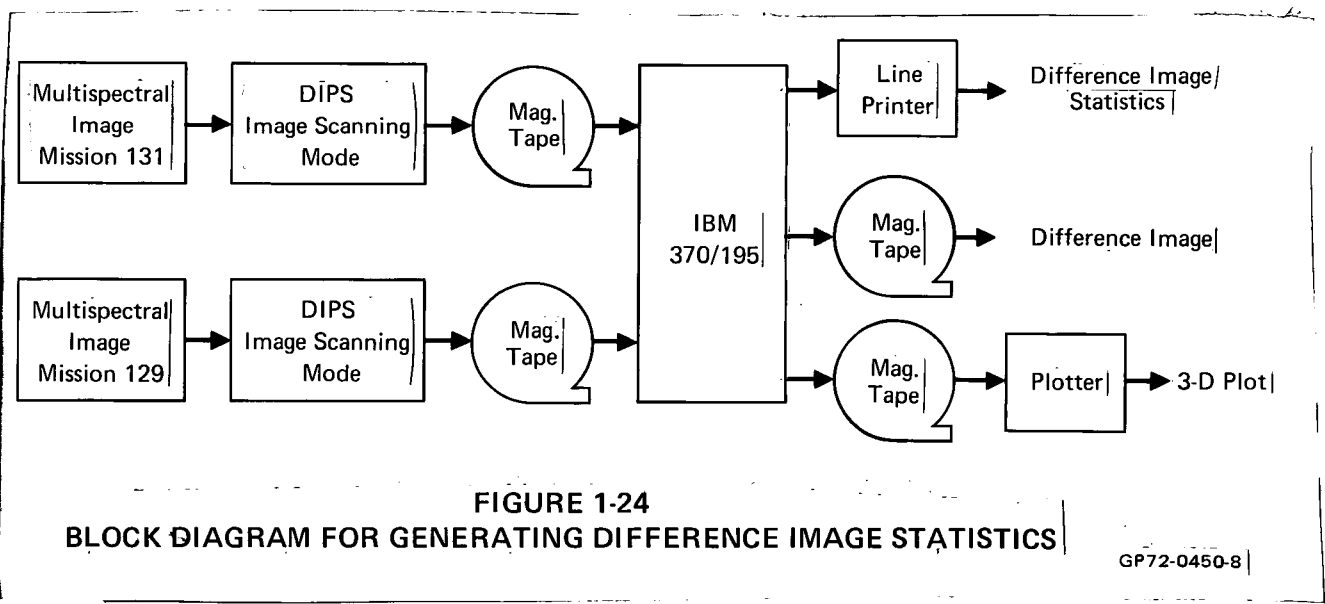
MCDONNELL AIRCRAFT

1.5 DIFFERENCE IMAGE STATISTICS

When properly generated, a difference image contains any change information between two images of the same geographical area at two separate observation times. This change information is a result of the following:

- a) Different sun angles (shadows)
- b) Different viewing angles
- c) Seasonal changes
- d) Sampling
- e) Random sensing and data processing system phenomenon

Figure 1-24 is a block diagram of the procedure used for generating the difference image statistics.



1.5.1 Development of Computer Program

The flow diagram for the computer program used to generate the difference image and its relevant statistics is illustrated in Figure 1-25.

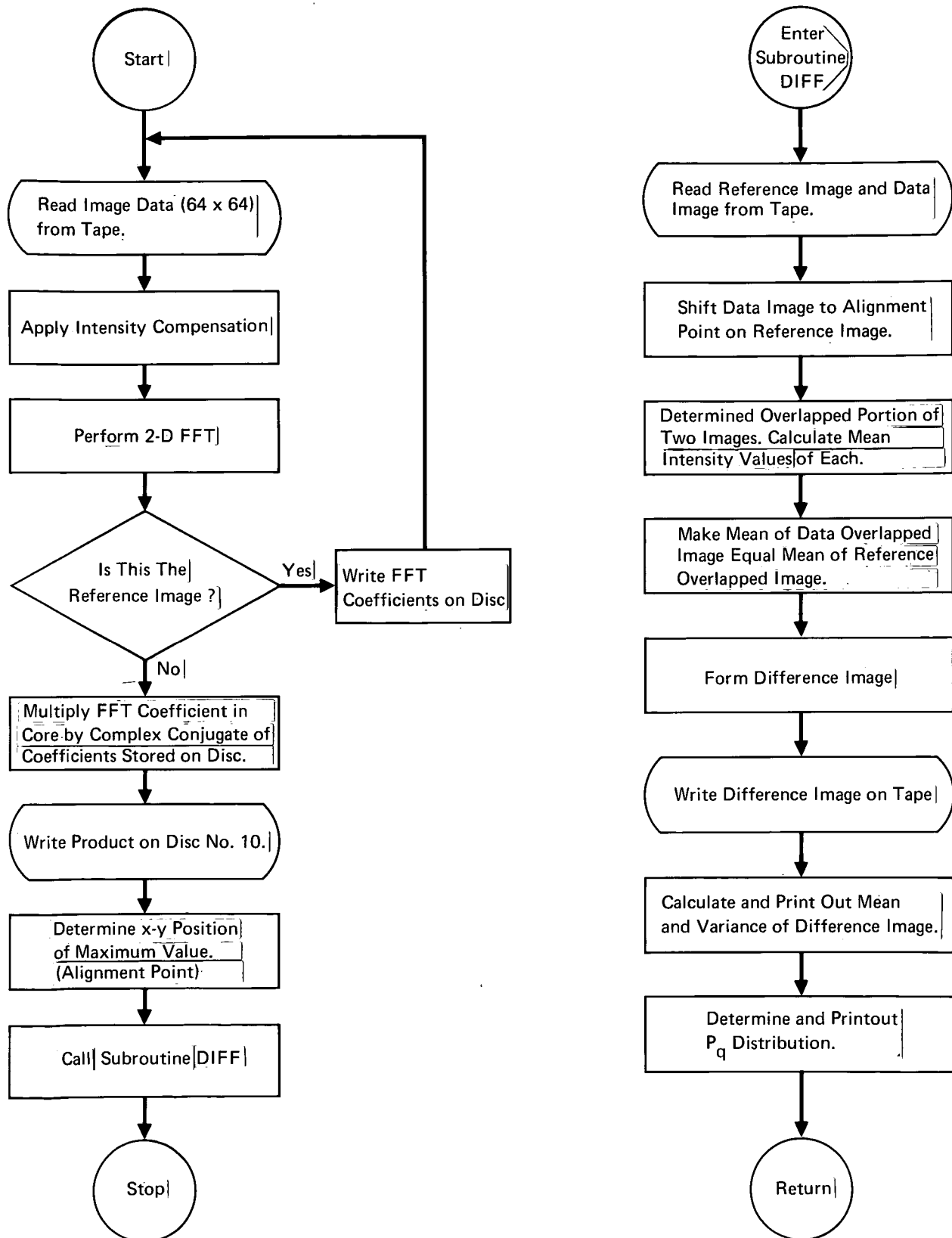


FIGURE 1-25
DIFFERENCE IMAGE STATISTICS COMPUTER FLOW DIAGRAM

GP72-0450-44

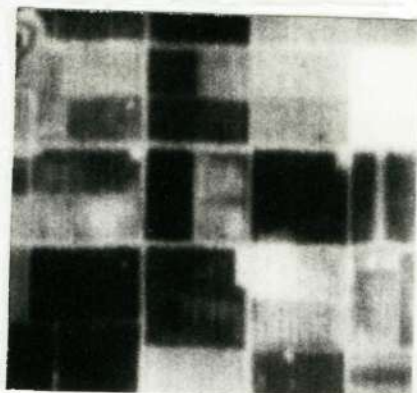
The program input consists of two digital image arrays from magnetic tape. The (x_1, x_2) displacement between the two images is determined by utilizing the cross-correlation coefficient image registration algorithm. Computationally, this was accomplished using two dimension FFT techniques. Figures 1-26b through 1-41b are three dimensional plots of the center (32 x 32) points for this image registration estimator. (In some cases, the image alignment point is not shown in these plots.) Following determination of the (x_1, x_2) displacement, the data image is forced to register with the reference image. The overlapped portions of the two images are then identified and the mean intensity value of the overlapped images are made equal. The difference image is then formed and the relevant difference image statistics printed out.

1.5.2 Image Statistics

Difference image statistics were determined for the 50 meter resolution and 10 meter resolution digital images scanned in Section 1.3.2.2. The difference images are defined and identified in Table 1-4. The relevant statistics determined were the difference image mean, variance, and the quantized probability P_q distribution discussed more fully in Section 2.3.1.2. These statistics are illustrated in Figures 1-26c and d through Figures 1-41c and d.

TABLE 1-4
DIFFERENCE IMAGE IDENTIFICATION

DIFFERENCE IMAGE (Reference Image - Data Image)		
<u>Figure No.</u>		<u>Figure No.</u>
1-8a	Minus	1-26a
1-9a	"	1-27a
1-10a	"	1-28a
1-11a	"	1-29a
1-12a	"	1-30a
1-13a	"	1-31a
1-14a	"	1-32a
1-15a	"	1-33a
1-16a	"	1-34a
1-17a	"	1-35a
1-18a	"	1-36a
1-19a	"	1-37a
1-20a	"	1-38a
1-21a	"	1-39a
1-22a	"	1-40a
1-23a	"	1-41a



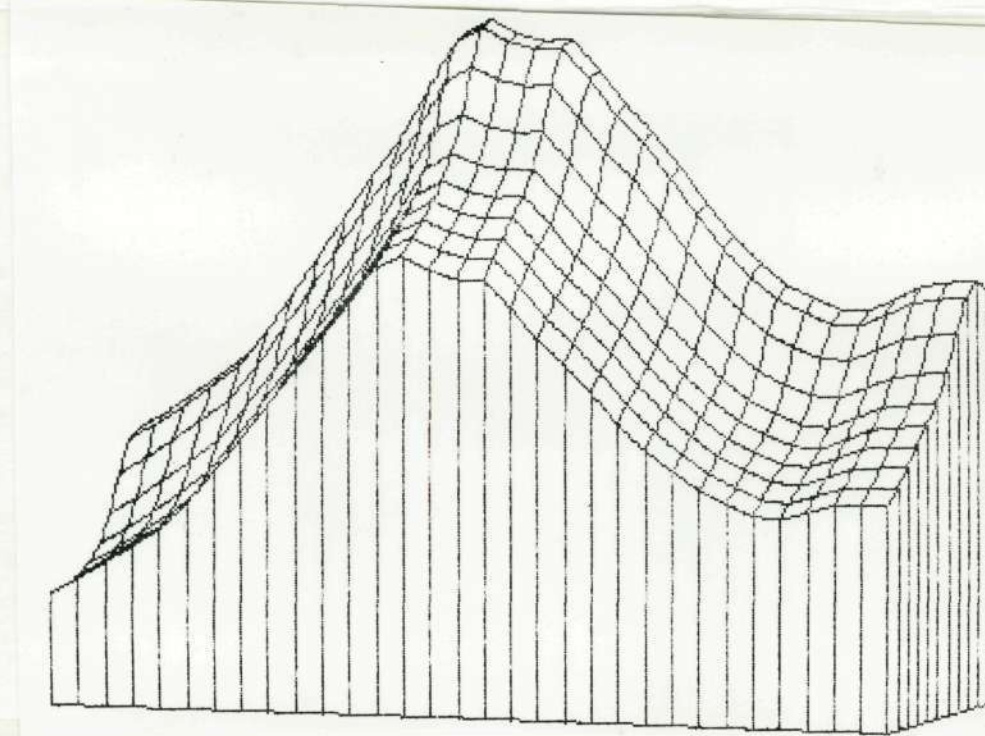
Reproduced from
best available copy.

Difference Image Mean: -0.217
Difference Image Variance: 63.1

128 x 128 Image Array

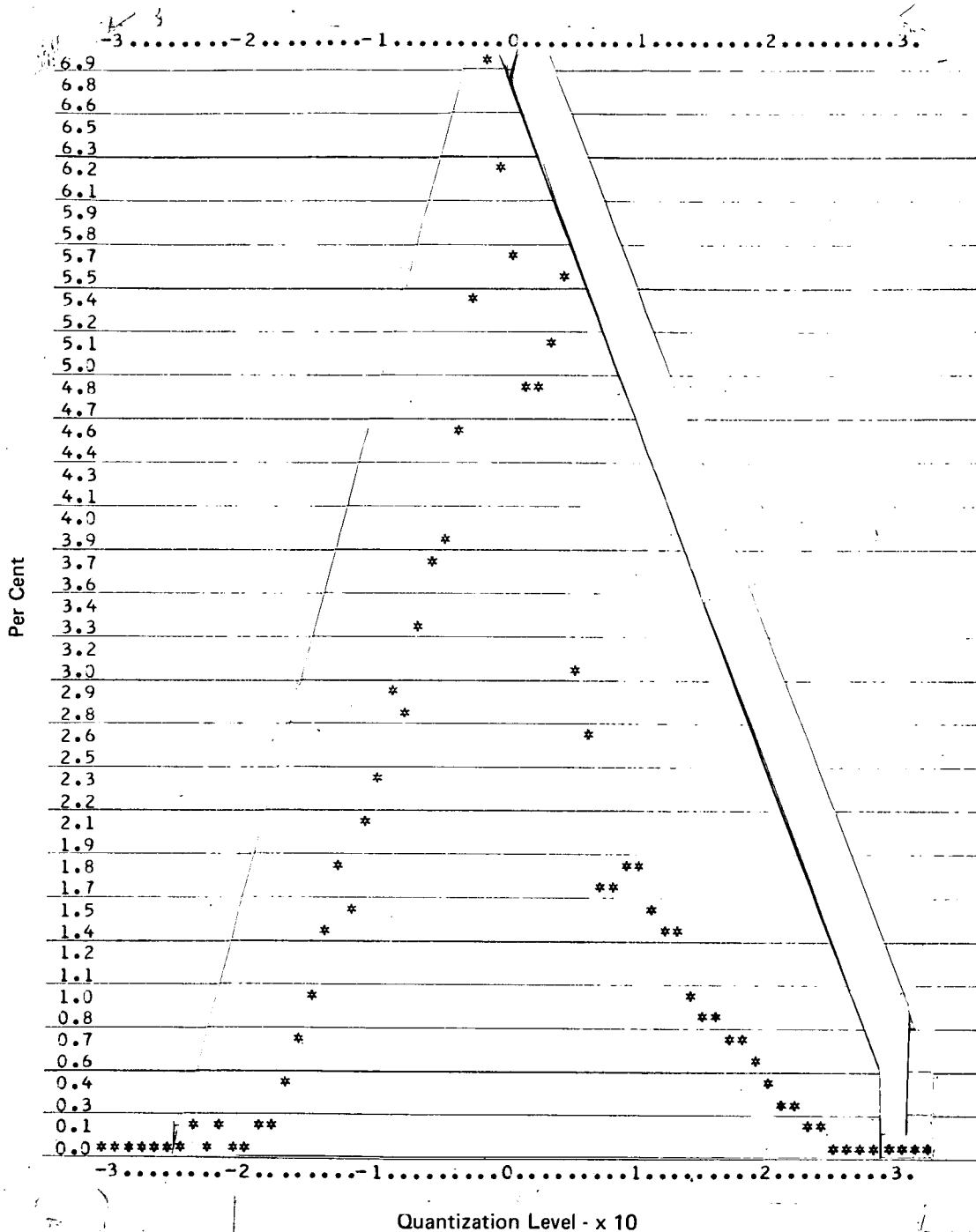
a. Data Image

c. Difference Image Statistics
(Reference Image - Data Image)



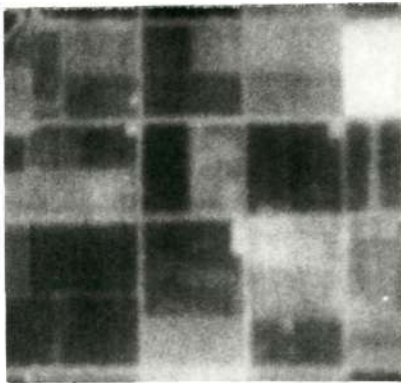
b. Image Registration Estimator

FIGURE 1-26
DIFFERENCE IMAGE STATISTICS (FARMLAND TERRAIN - RED SPECTRUM -
MISSION 129 - 50 METER RESOLUTION)



d. Difference Image Histogram

FIGURE 1-26 (Continued)
DIFFERENCE IMAGE STATISTICS (FARMLAND TERRAIN - RED SPECTRUM -
MISSION 129 - 50 METER RESOLUTION)



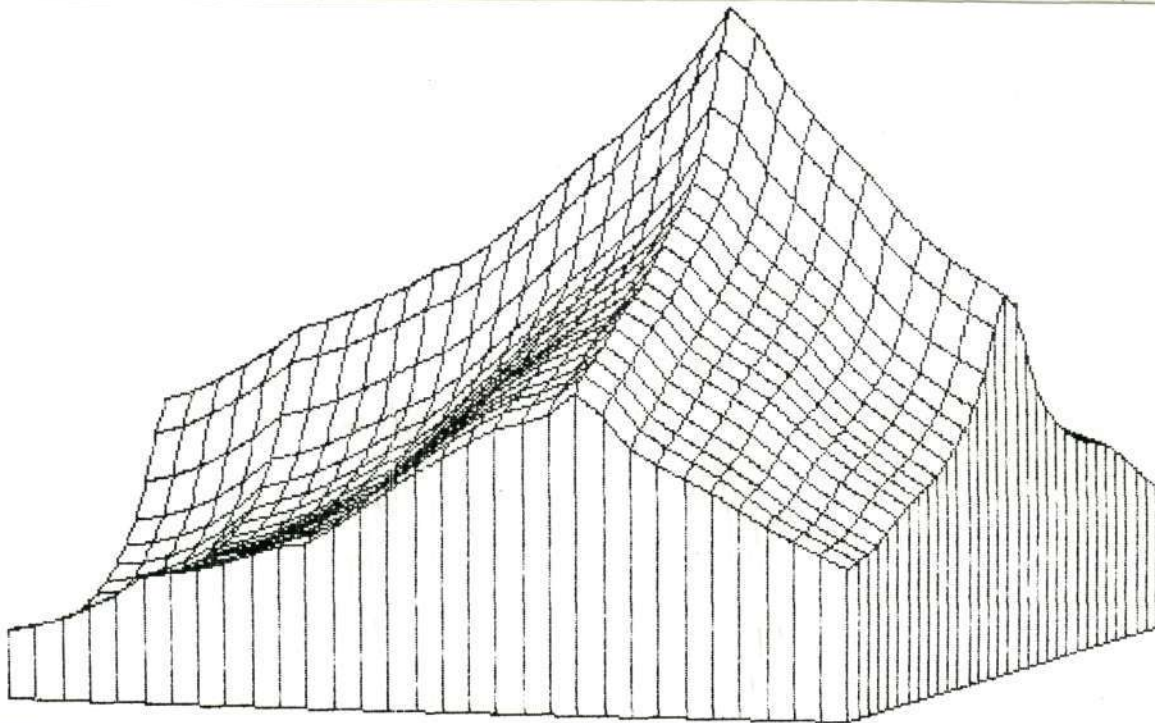
128 x 128 Image Array

a. Data Image

Difference Image Mean: 0.326

Difference Image Variance: 17.1

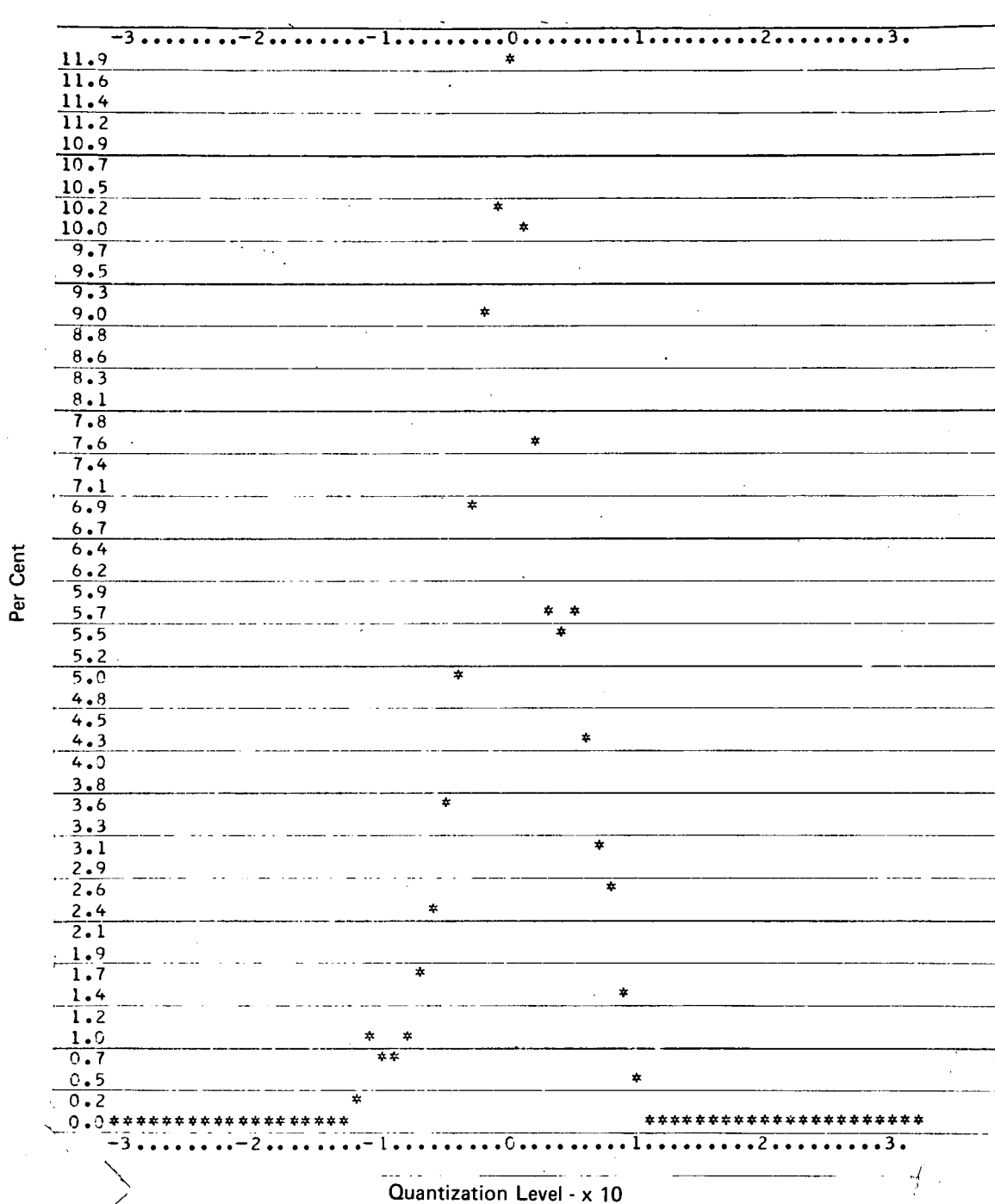
c. Difference Image Statistics
(Reference Image - Data Image)



b. Image Registration Estimator

FIGURE 1-27
DIFFERENCE IMAGE STATISTICS (FARMLAND TERRAIN - GREEN SPECTRUM -
MISSION 129 - 50 METER RESOLUTION)

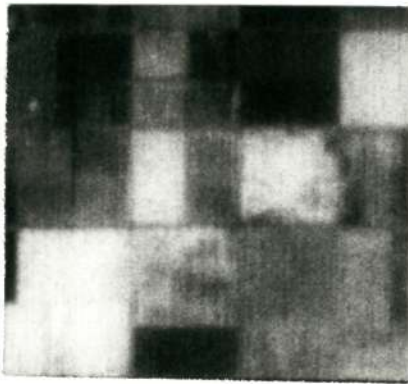
MCDONNELL AIRCRAFT



d. Difference Image Histogram

FIGURE 1-27 (Continued)
DIFFERENCE IMAGE STATISTICS (FARMLAND TERRAIN - GREEN SPECTRUM -
MISSION 129 - 50 METER RESOLUTION)

1-54



Reproduced from
best available copy.

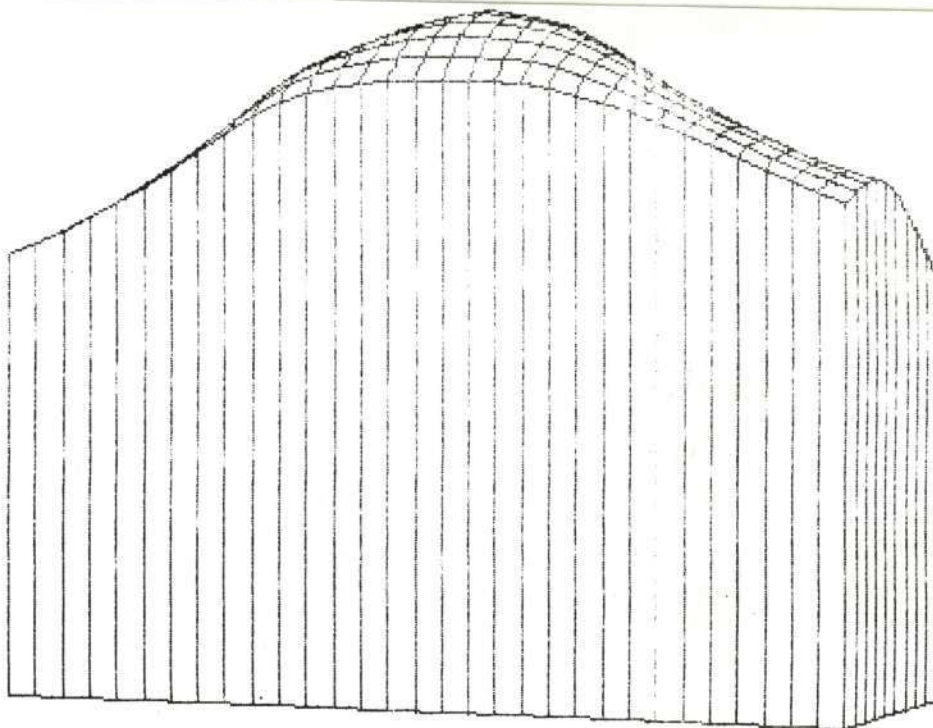
Difference Image Mean: -0.095

Difference Image Variance: 40.3

128 x 128 Image Array

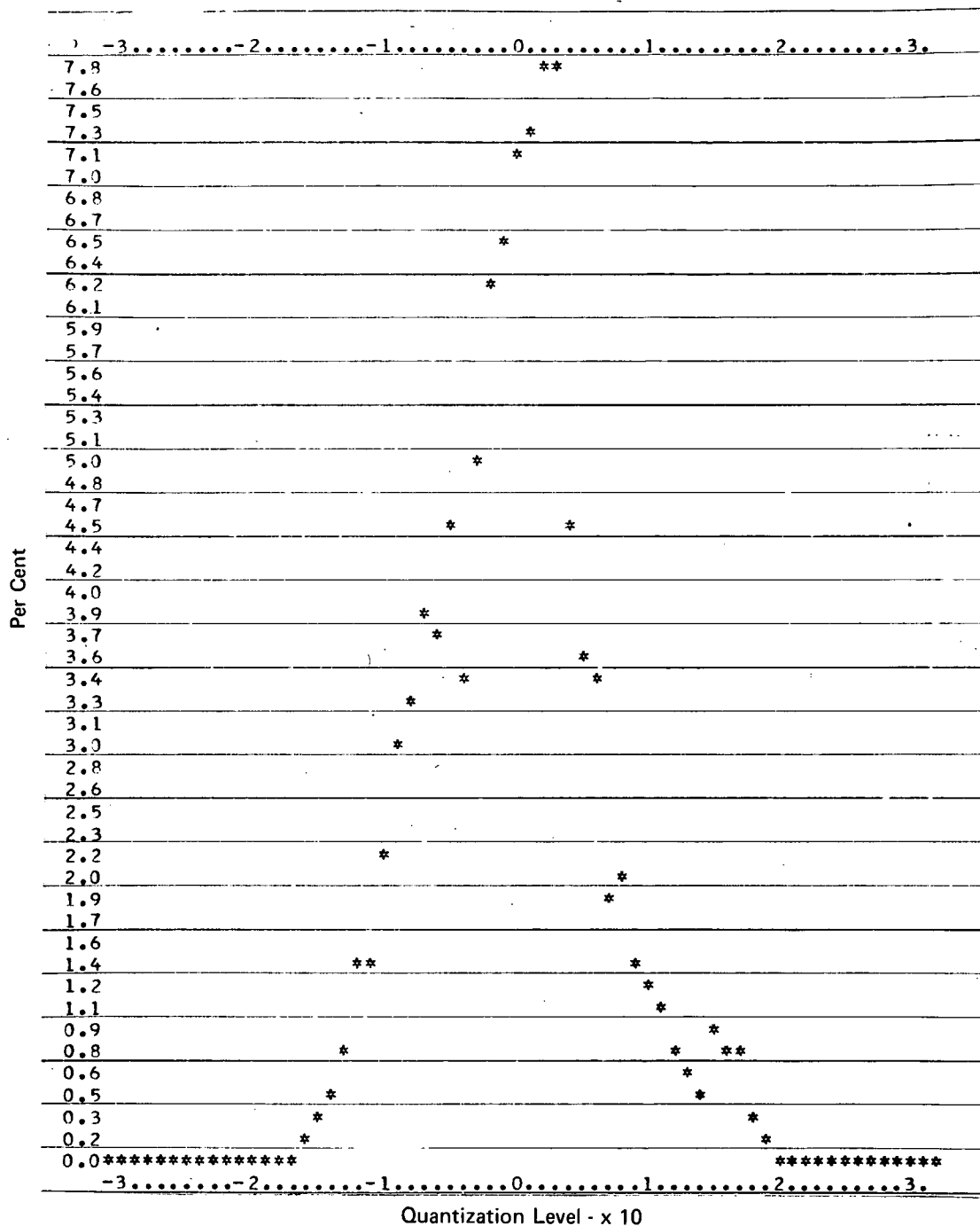
a. Data Image

c. Difference Image Statistics
(Reference Image - Data Image)



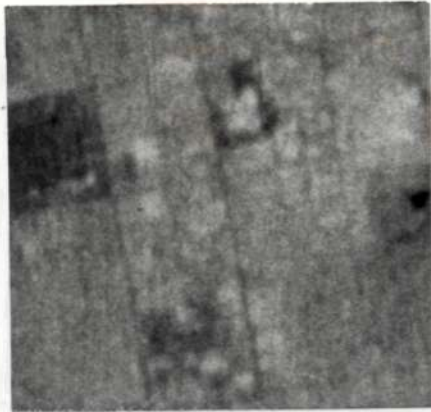
b. Image Registration Estimator

FIGURE 1-28
DIFFERENCE IMAGE STATISTICS (FARMLAND TERRAIN - IR SPECTRUM -
MISSION 129 - 50 METER RESOLUTION)



d. Difference Image Histogram

FIGURE 1-28 (Continued)
DIFFERENCE IMAGE STATISTICS (FARMLAND TERRAIN - IR SPECTRUM -
MISSION 129 - 50 METER RESOLUTION)

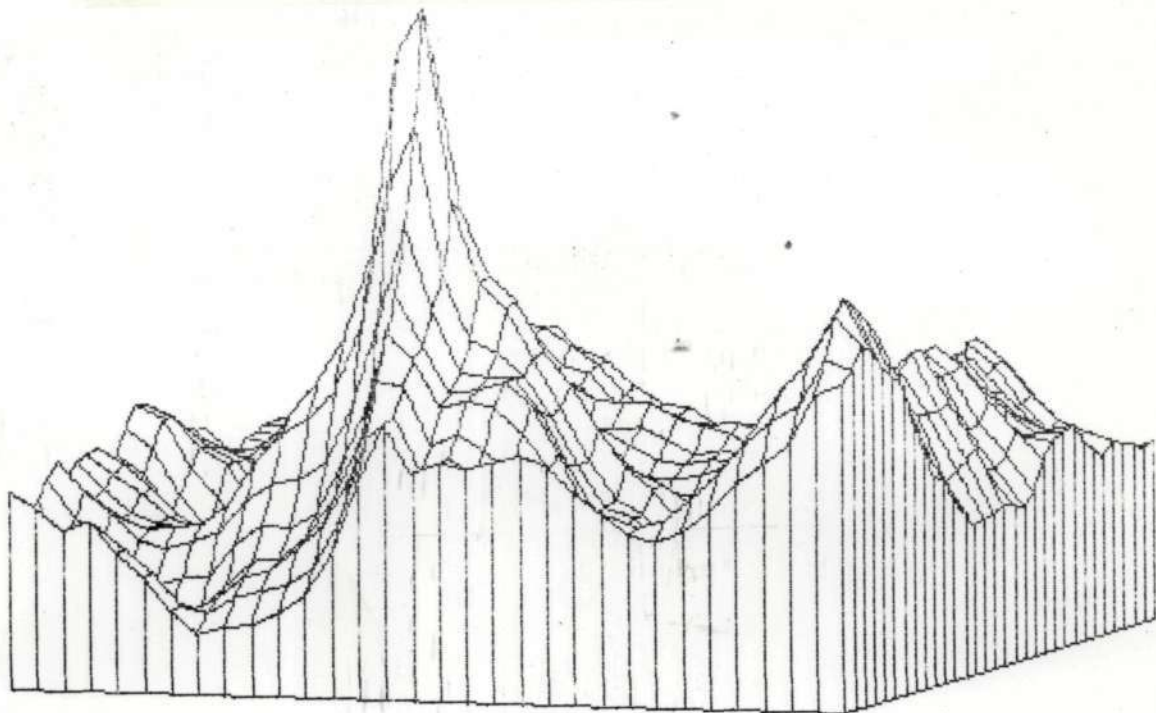


128 x 128 Image Array

a. Data Image

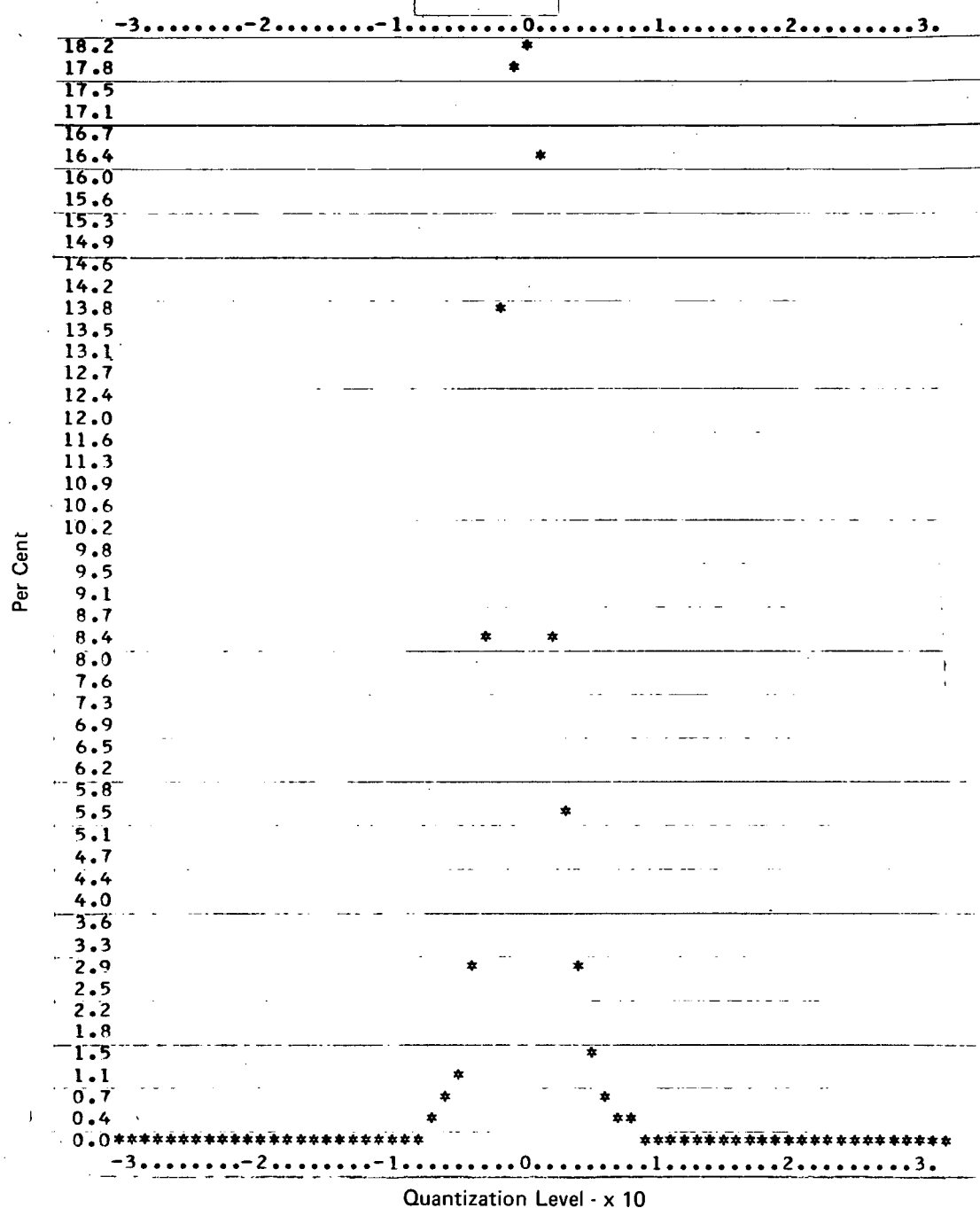
Difference Image Mean: 0.087
Difference Image Variance: 6.07

c. Difference Image Statistics
(Reference Image - Data Image)



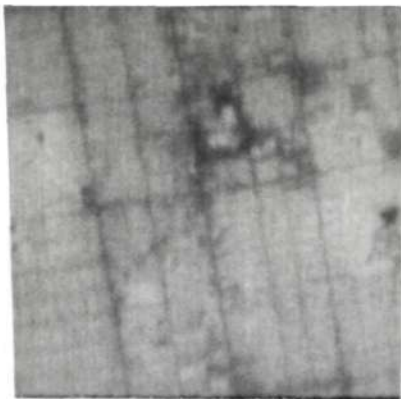
b. Image Registration Estimator

FIGURE 1-29
DIFFERENCE IMAGE STATISTICS (URBAN TERRAIN - RED SPECTRUM -
MISSION 129 - 50 METER RESOLUTION)



d. Difference Image Histogram

FIGURE 1-29 (Continued)
DIFFERENCE IMAGE STATISTICS (URBAN TERRAIN - RED SPECTRUM -
MISSION 129 - 50 METER RESOLUTION



128 x 128 Image Array

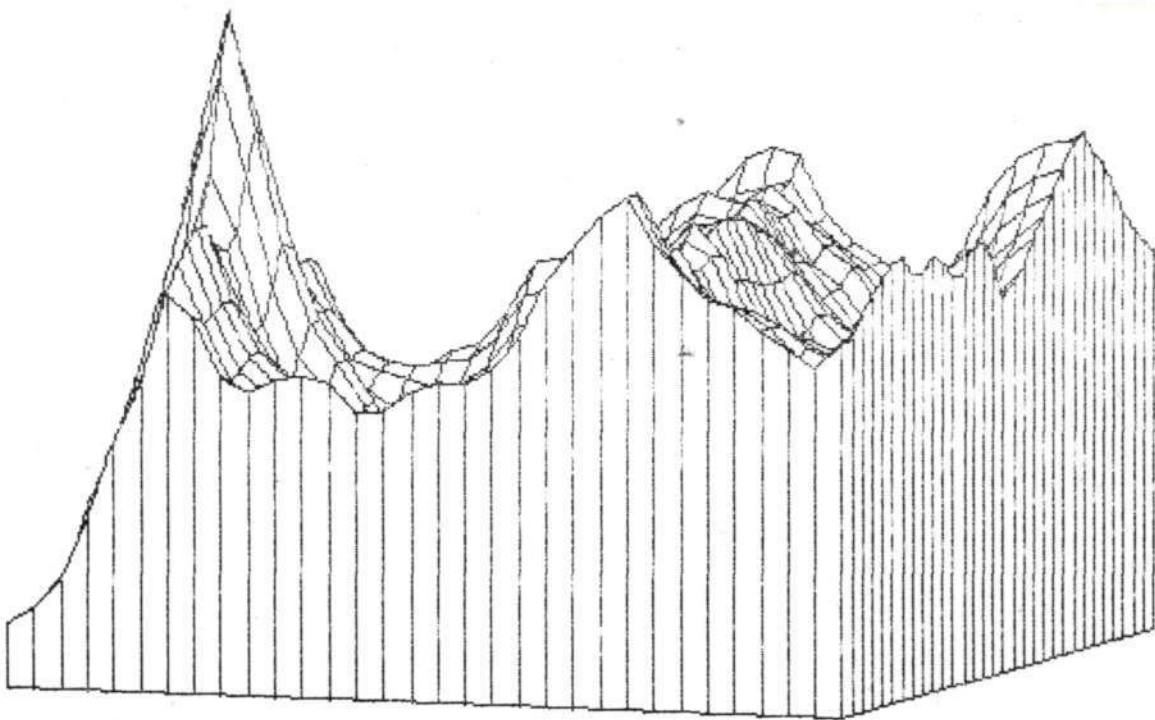
Reproduced from
best available copy.

Difference Image Mean: 0.48

Difference Image Variance: 17.2

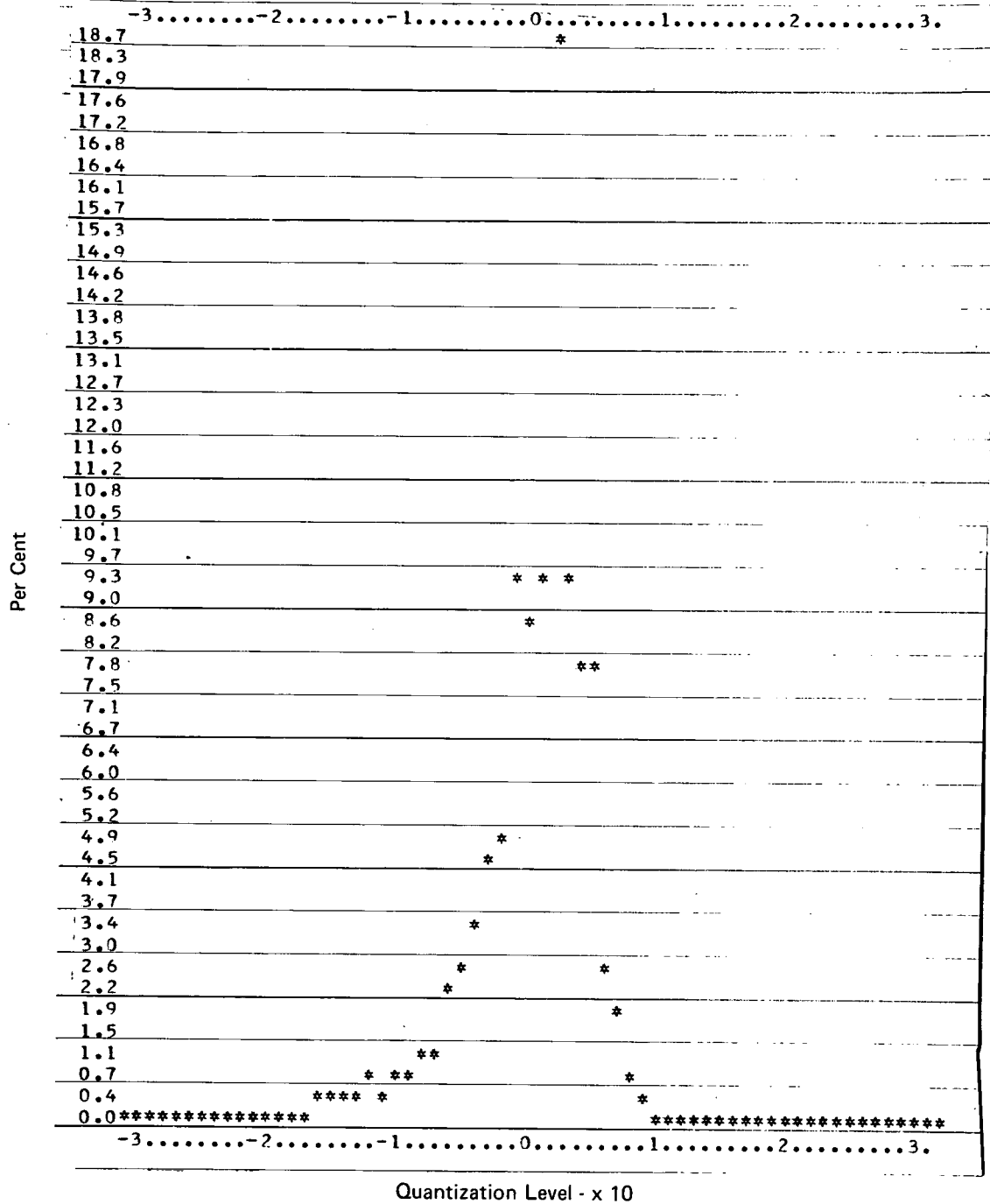
a. Data Image

c. Difference Image Statistics
(Reference Image - Data Image)



b. Image Registration Estimator

FIGURE 1-30
DIFFERENCE IMAGE STATISTICS (URBAN TERRAIN - GREEN SPECTRUM -
MISSION 129 - 50 METER RESOLUTION)



d. Difference Image Histogram

FIGURE 1-30 (Continued)
DIFFERENCE IMAGE STATISTICS (URBAN TERRAIN - GREEN SPECTRUM -
MISSION 129 - 50 METER RESOLUTION)

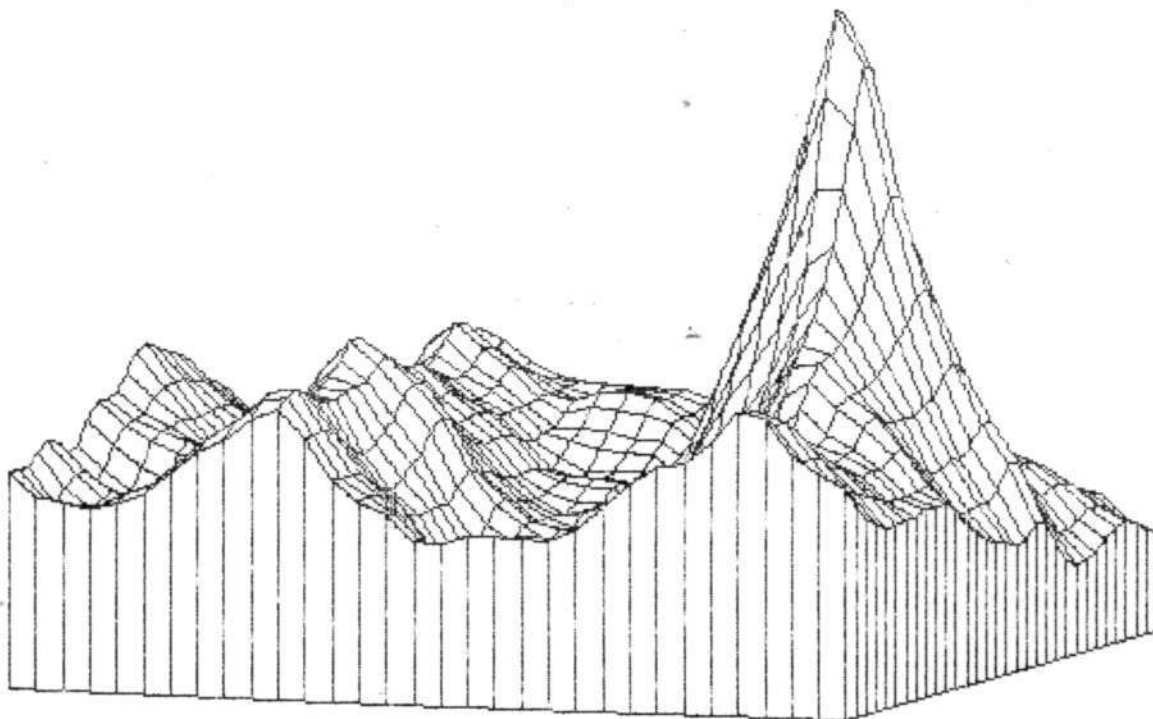


128 x 128 Image Array

a. Data Image

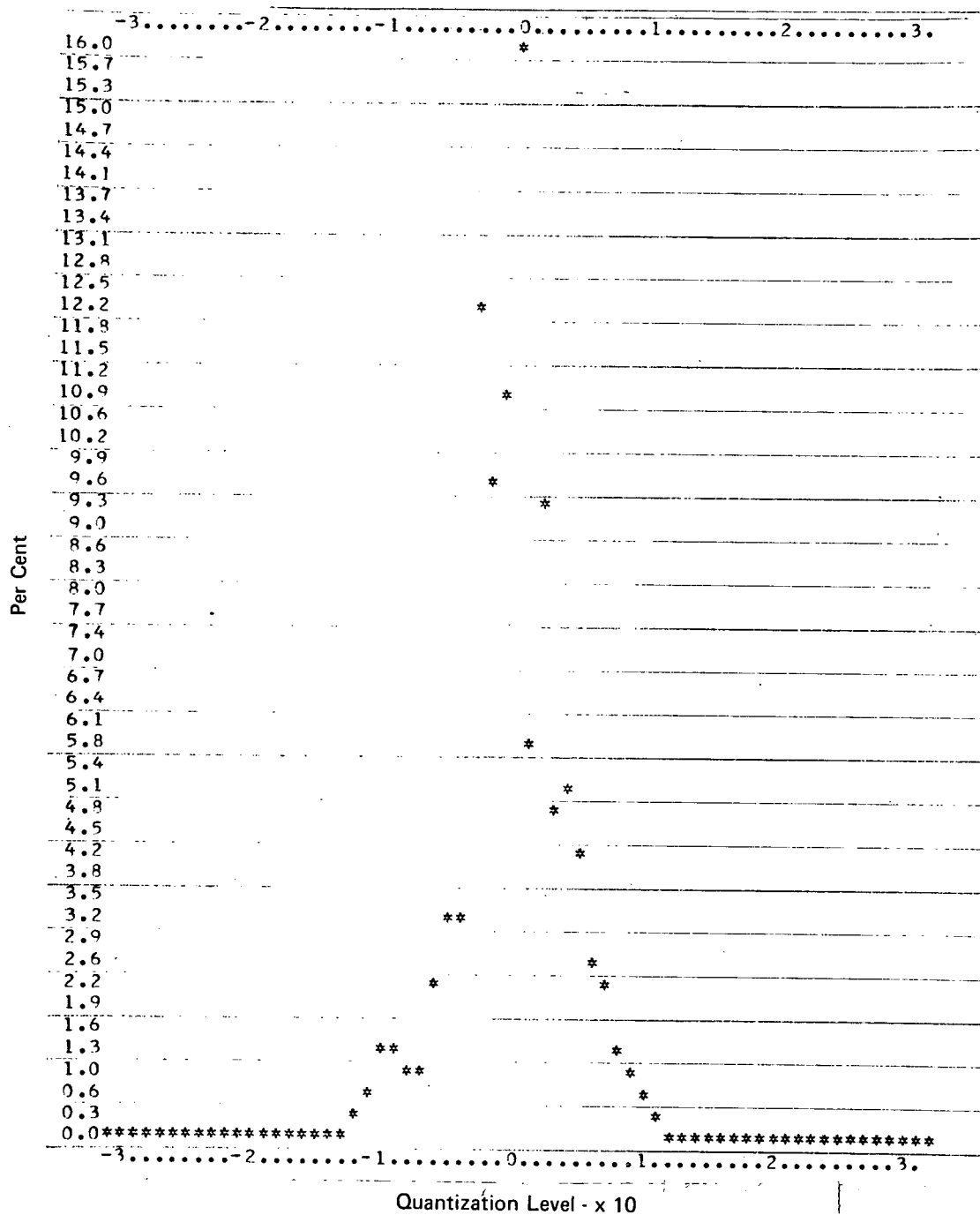
Difference Image Mean: -0.12
 Difference Image Variance: 16.3

c. Difference Image Statistics
 (Reference Image - Data Image)



b. Image Registration Estimator

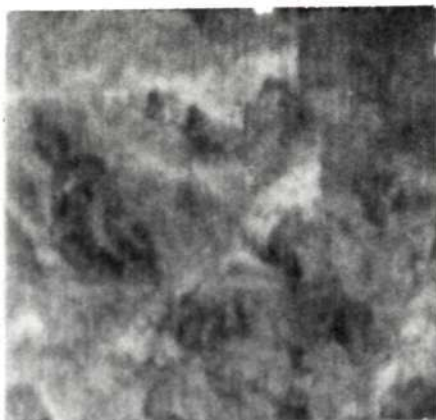
FIGURE 1-31
 DIFFERENCE IMAGE STATISTICS (URBAN TERRAIN - IR SPECTRUM -
 MISSION 129 - 50 METER RESOLUTION)



d. Difference Image Histogram

FIGURE 1-31 (Continued)
DIFFERENCE IMAGE STATISTICS (URBAN TERRAIN - IR SPECTRUM -
MISSION 129 - 50 METER RESOLUTION)

1-62



128 x 128 Image Array

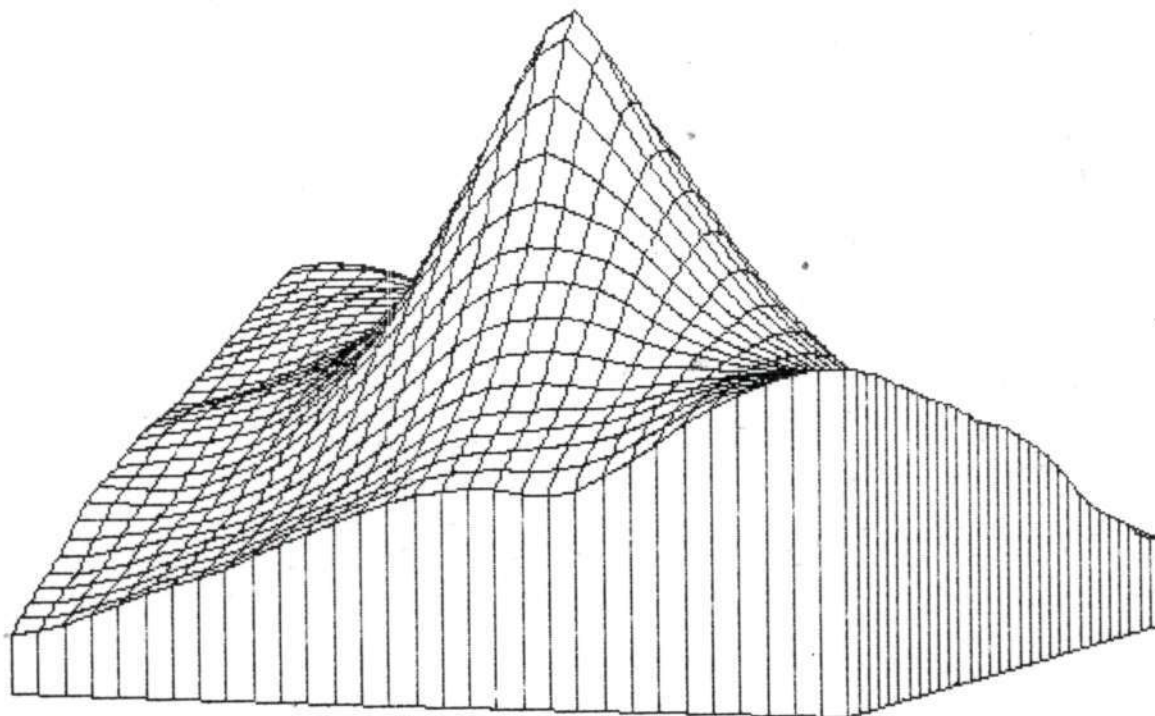
a. Data Image

Reproduced from
best available copy.

Difference Image Mean: -0.21

Difference Image Variance: 4.15

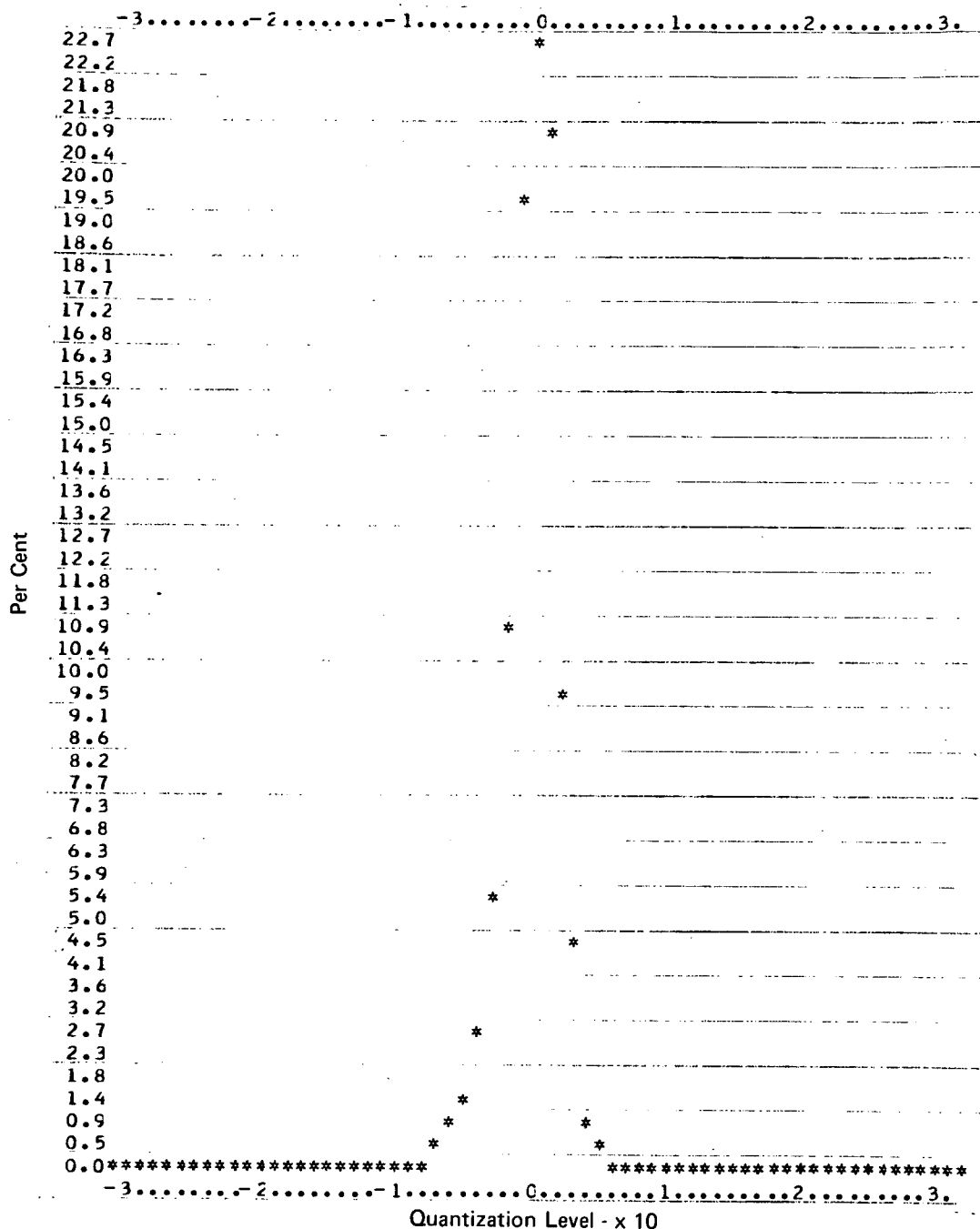
c. Difference Image Statistics
(Reference Image - Data Image)



b. Image Registration Estimator

FIGURE 1-32
DIFFERENCE IMAGE STATISTICS (MOUNTAIN TERRAIN - RED SPECTRUM -
MISSION 129 - 50 METER RESOLUTION)

035619



d. Difference Image Histogram

FIGURE 1-32 (Continued)
DIFFERENCE IMAGE STATISTICS (MOUNTAIN TERRAIN - RED SPECTRUM -
MISSION 129 - 50 METER RESOLUTION)



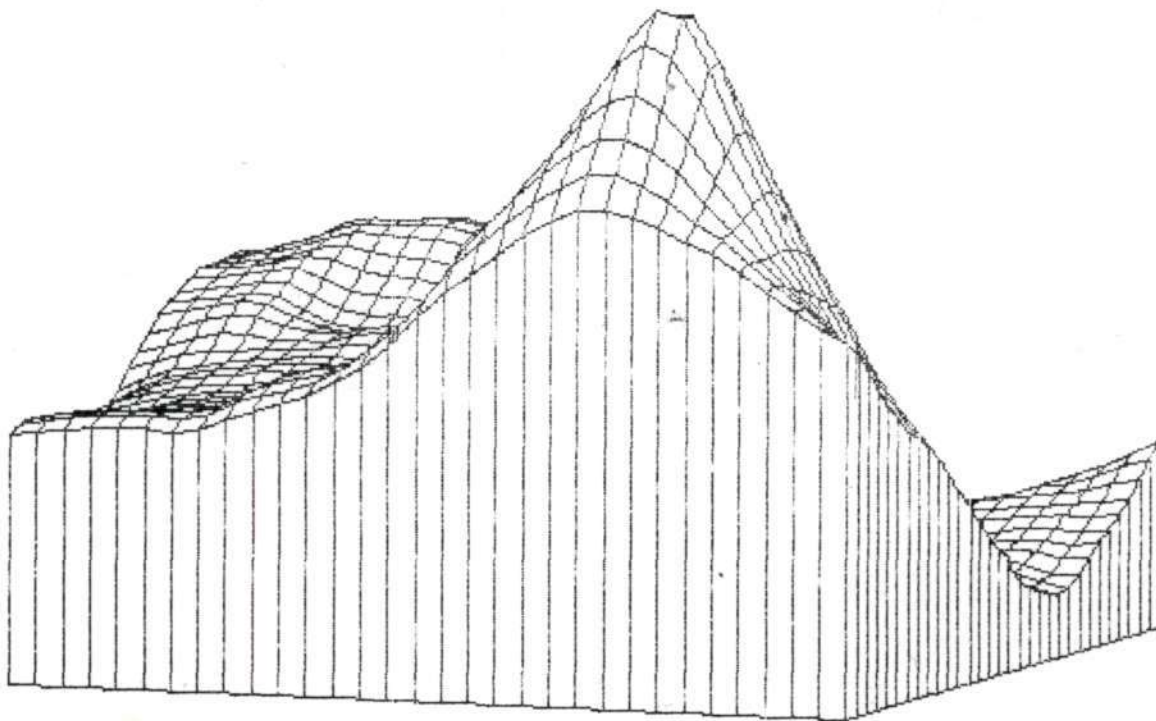
128 x 128 Image Array

a. Data Image

Difference Image Mean: 0.459

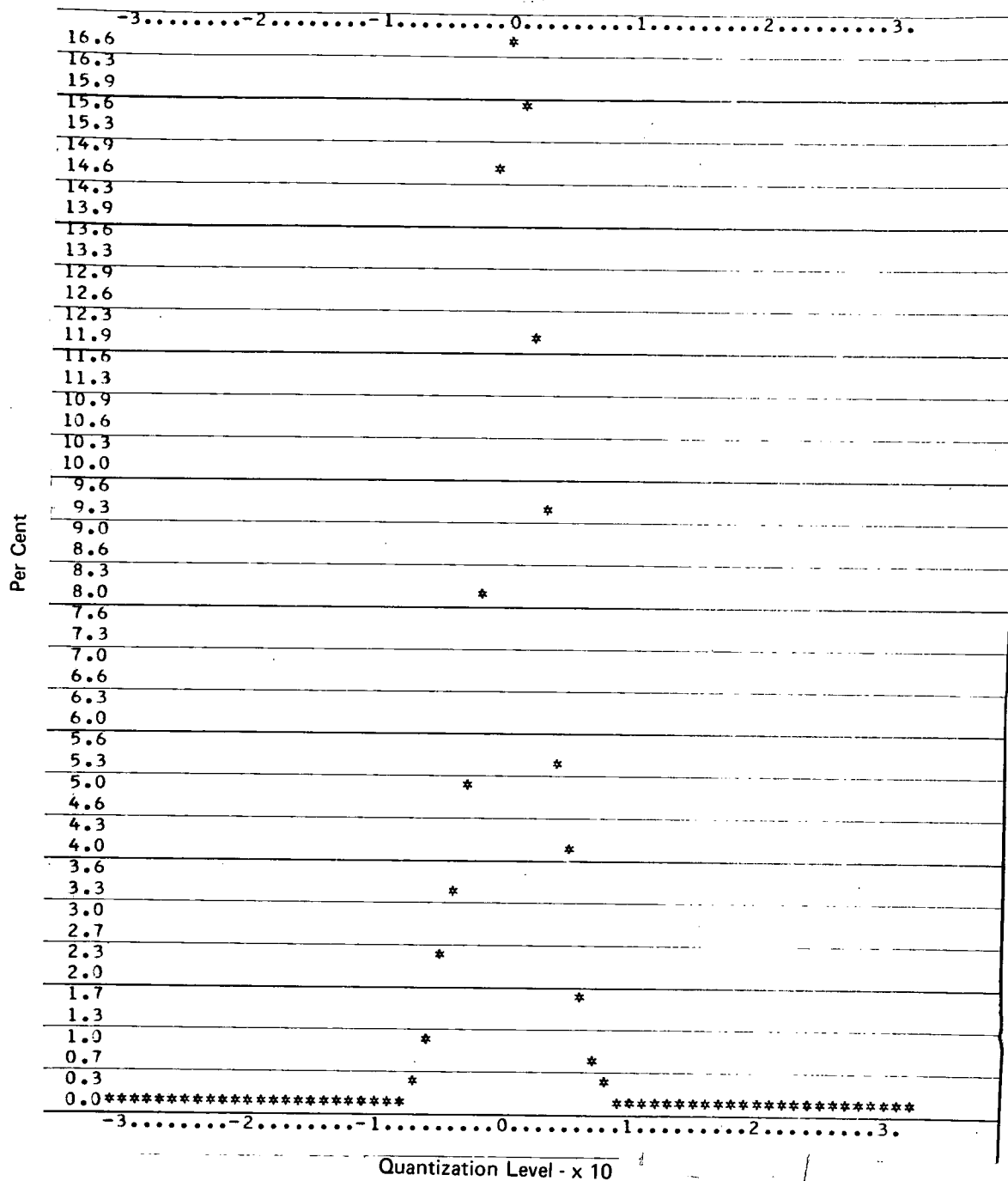
Difference Image Variance: 7.13

c. Difference Image Statistics
(Reference Image - Data Image)



b. Image Registration Estimator

FIGURE 1-33
DIFFERENCE IMAGE STATISTICS (MOUNTAIN TERRAIN - GREEN SPECTRUM -
MISSION 129 - 50 METER RESOLUTION)



d. Difference Image Histogram

FIGURE 1-33 (Continued)
DIFFERENCE IMAGE STATISTICS (MOUNTAIN TERRAIN - GREEN SPECTRUM -
MISSION 129 - 50 METER RESOLUTION)

Reproduced from
best available copy.

1-66

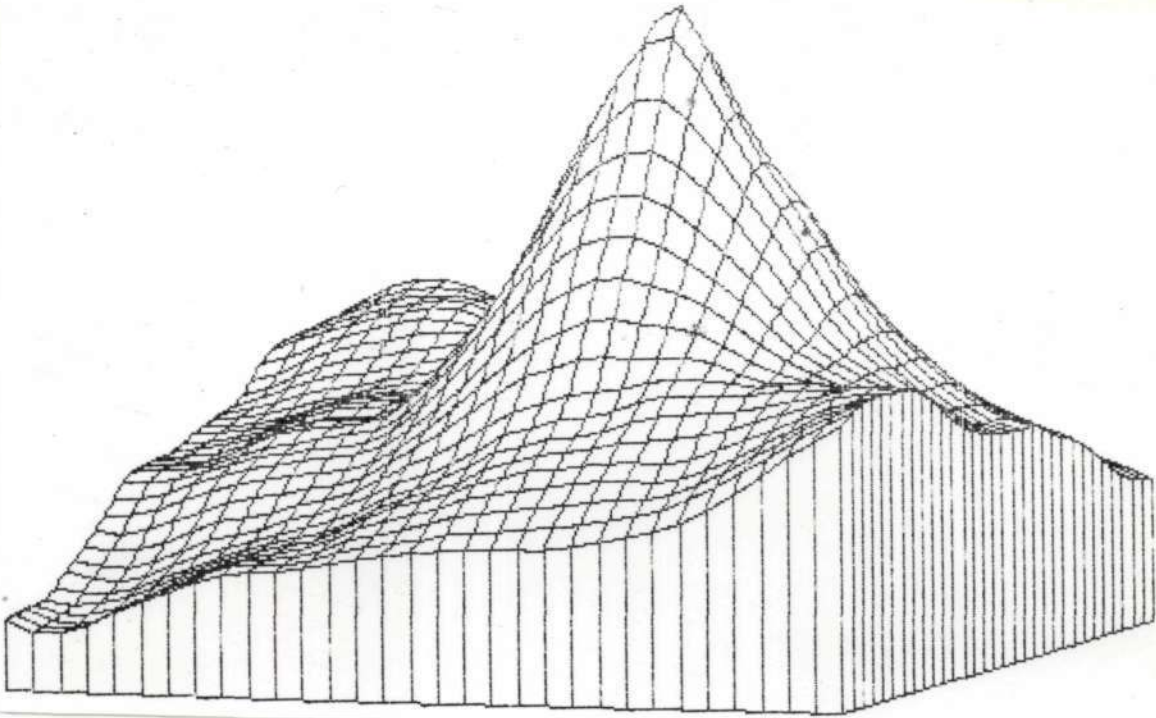


128 x 128 Image Array

a. Data Image

Difference Image Mean: 0.37
Difference Image Variance: 6.03

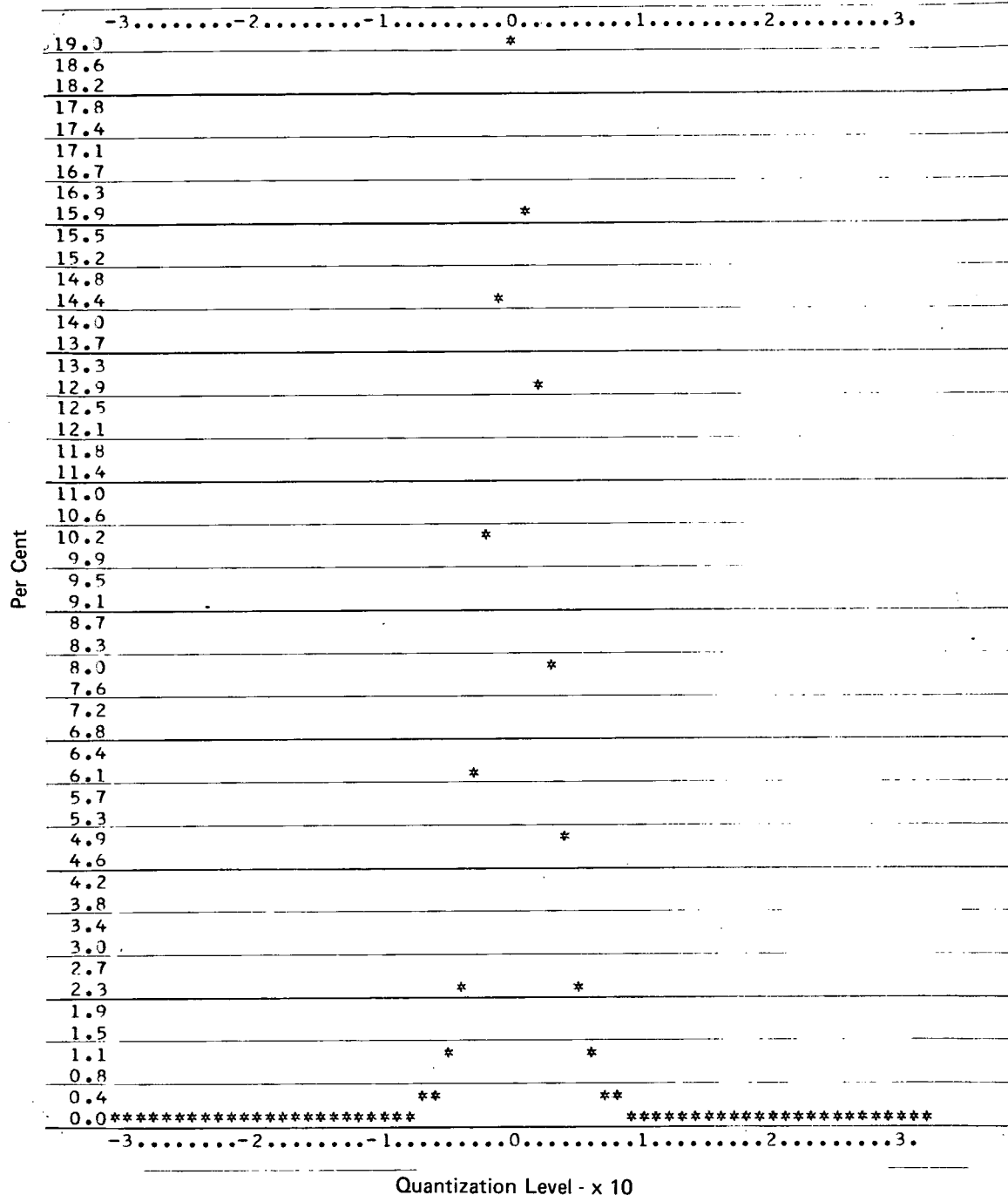
c. Difference Image Statistics
(Reference Image - Data Image)



b. Image Registration Estimator

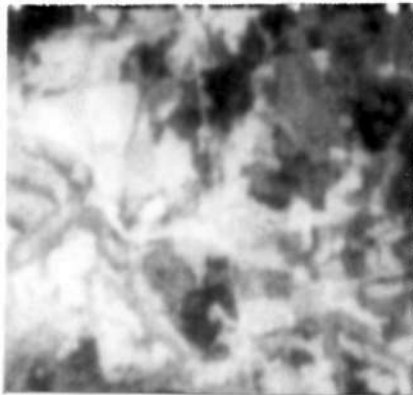
FIGURE 1-34
DIFFERENCE IMAGE STATISTICS (MOUNTAIN TERRAIN - IR SPECTRUM -
MISSION 129 - 50 METER RESOLUTION)

035619



d. Difference Image Histogram

FIGURE 1-34 (Continued)
 DIFFERENCE IMAGE STATISTICS (MOUNTAIN TERRAIN - IR SPECTRUM -
 MISSION 129 - 50 METER RESOLUTION)



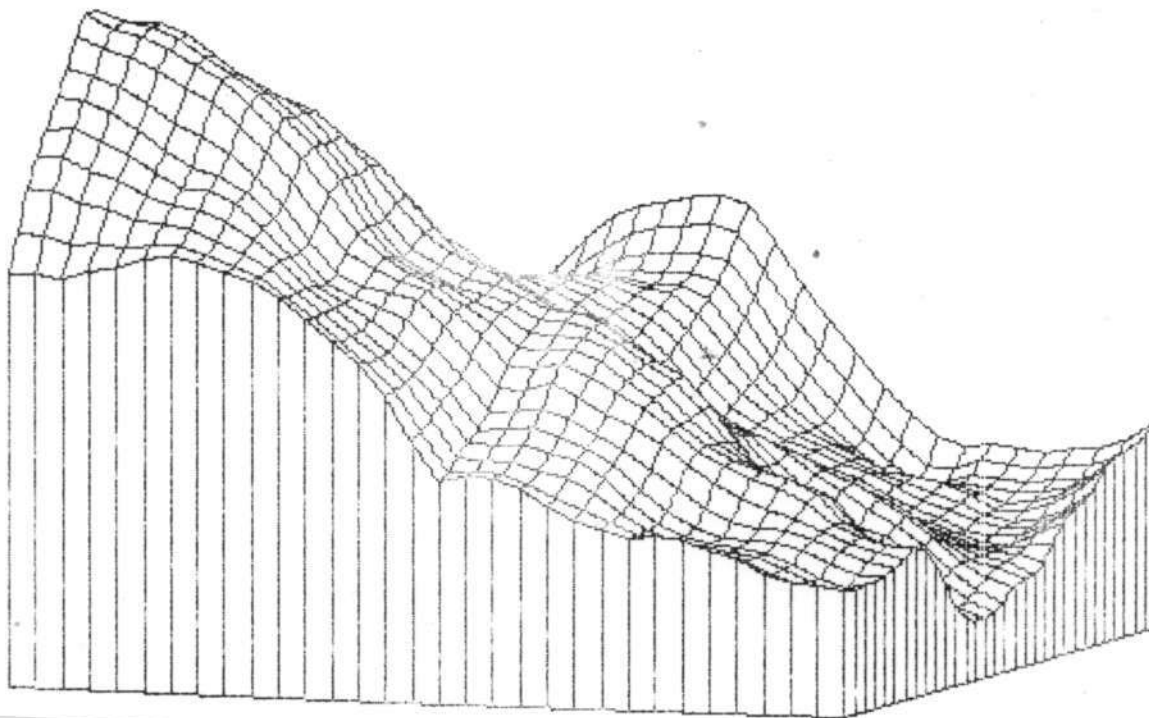
128 x 128 Image Array

a. Data Image

Difference Image Mean: 0.44

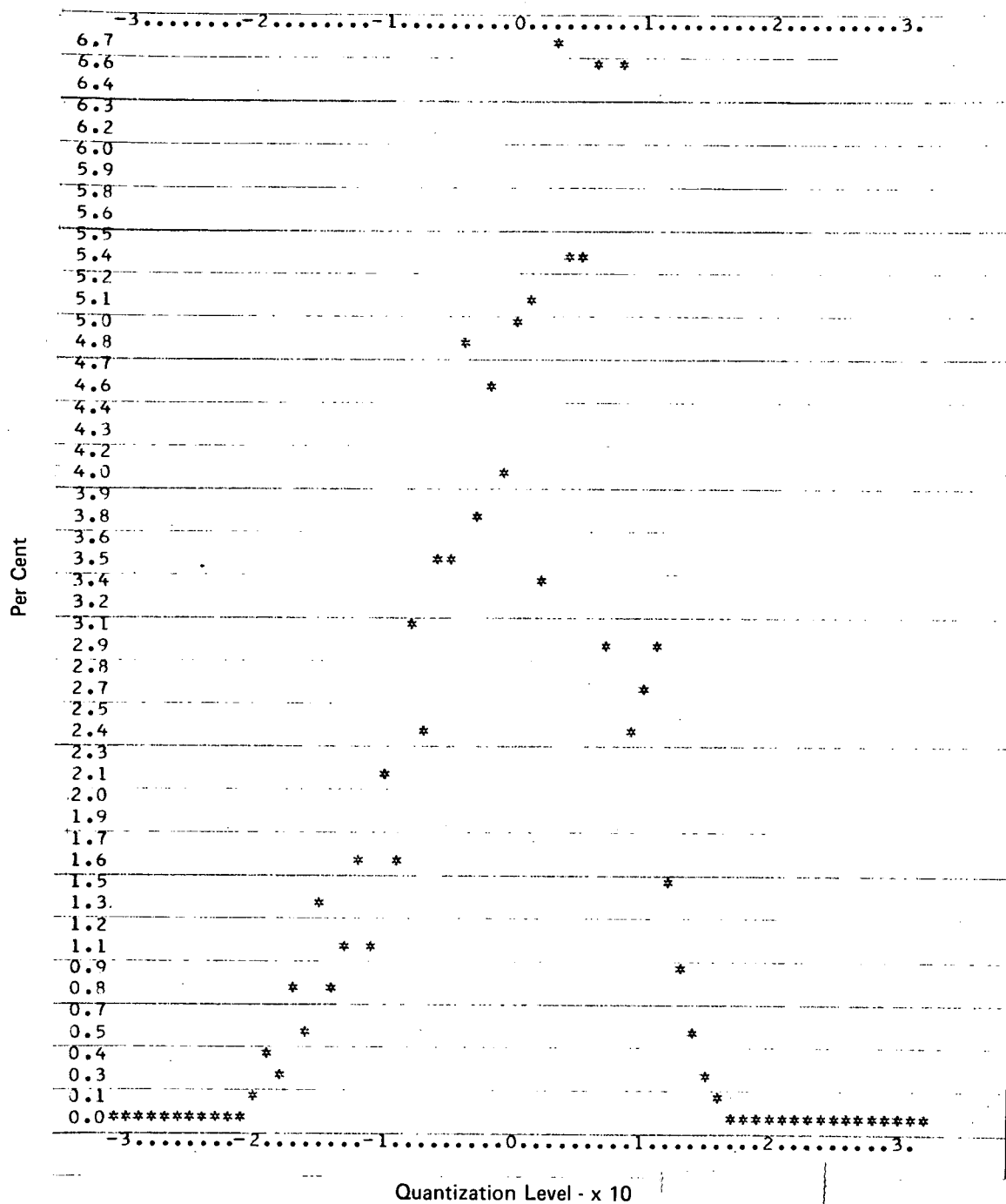
Difference Image Variance: 52.2

c. Difference Image Statistics
(Reference Image - Data Image)



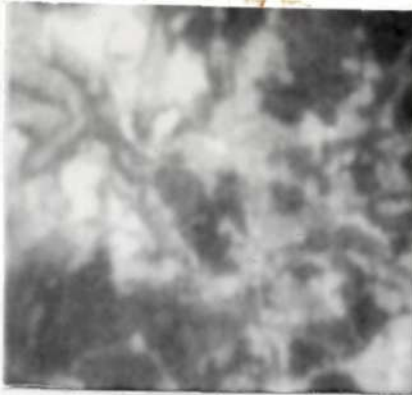
b. Image Registration Estimator

FIGURE 1-35
DIFFERENCE IMAGE STATISTICS (FOREST TERRAIN - RED SPECTRUM -
MISSION 158 - 50 METER RESOLUTION)



d. Difference Image Histogram

FIGURE 1-35 (Continued)
DIFFERENCE IMAGE STATISTICS (FOREST TERRAIN - RED SPECTRUM -
MISSION 158 - 50 METER RESOLUTION)



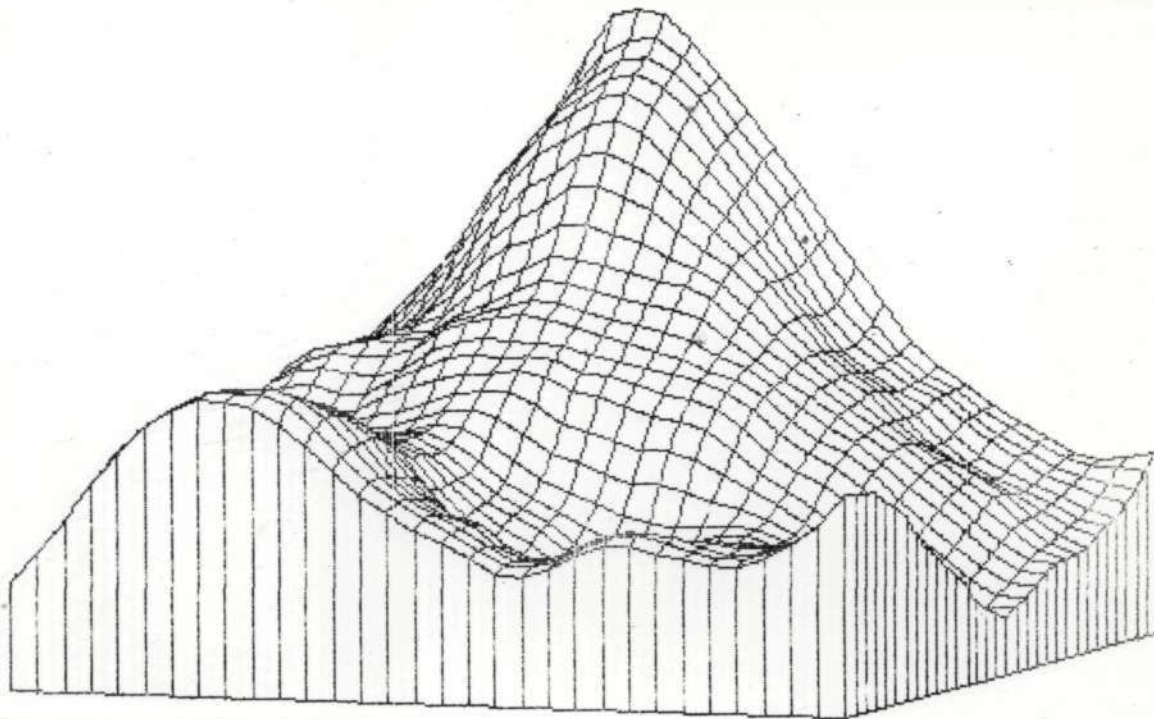
128 x 128 Image Array

a. Data Image

Reproduced from
best available copy.

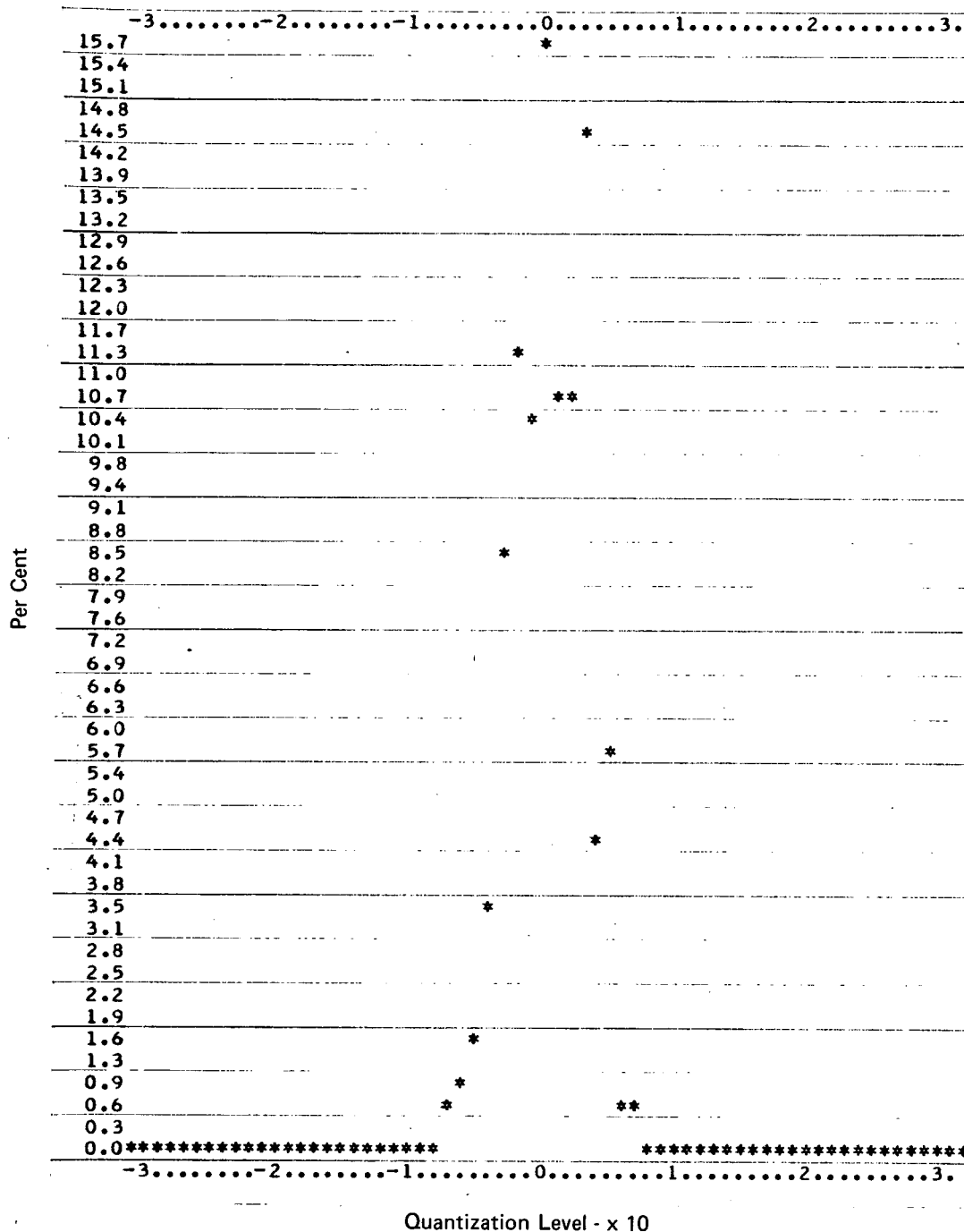
Difference Image Mean: 0.4
Difference Image Variance: 8.23

c. Difference Image Statistics
(Reference Image - Data Image)



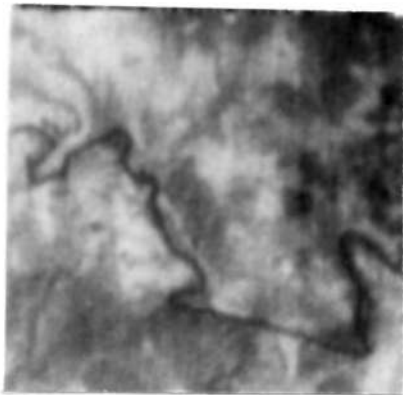
b. Image Registration Estimator

FIGURE 1-36
DIFFERENCE IMAGE STATISTICS (FOREST TERRAIN - GREEN SPECTRUM -
MISSION 158 - 50 METER RESOLUTION)



d. Difference Image Histogram

FIGURE 1-36 (Continued)
DIFFERENCE IMAGE STATISTICS (FOREST TERRAIN - GREEN SPECTRUM -
MISSION 158 - 50 METER RESOLUTION)

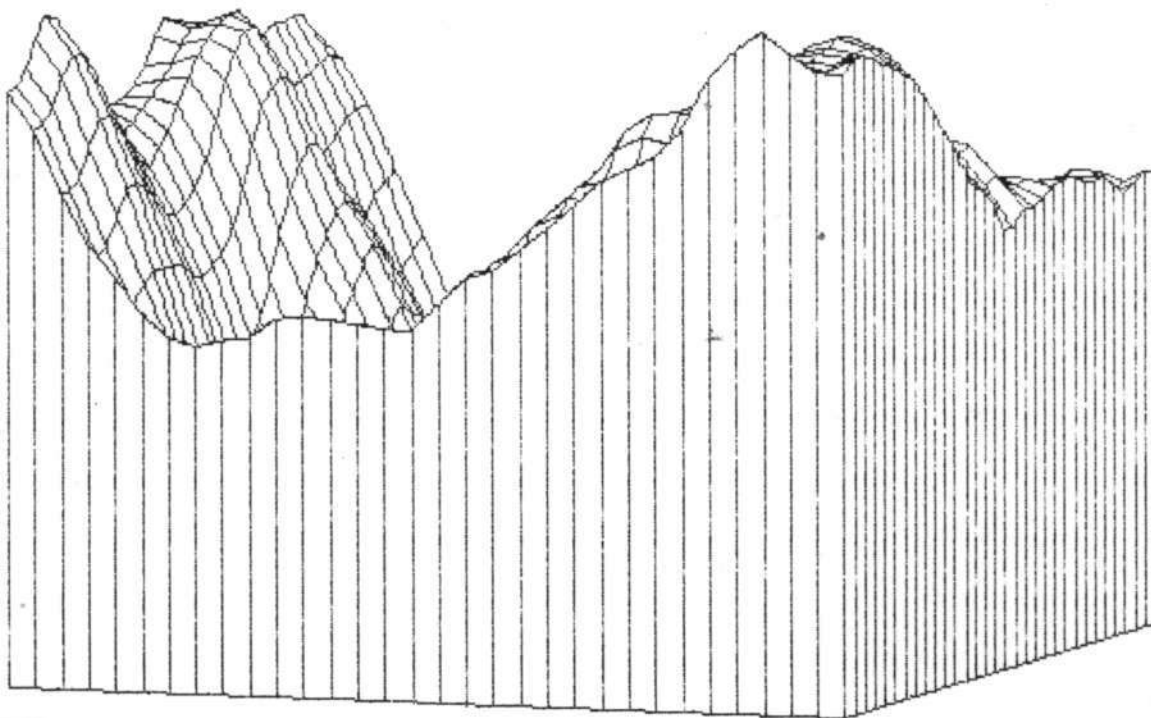


128 x 128 Image Array

a. Data Image

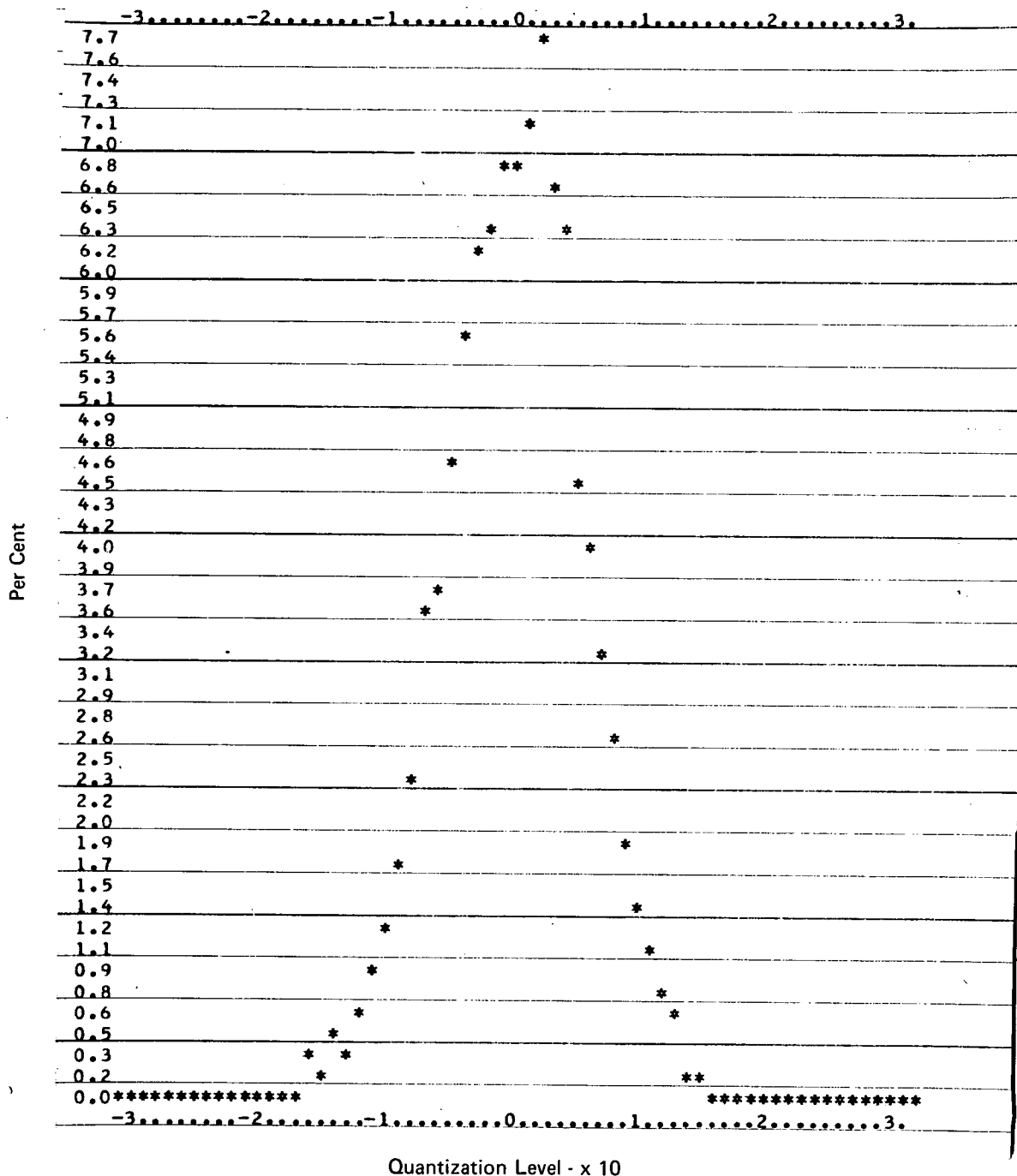
Difference Image Mean: 0.082
Difference Image Variance: 30.5

c. Difference Image Statistics
(Reference Image - Data Image)



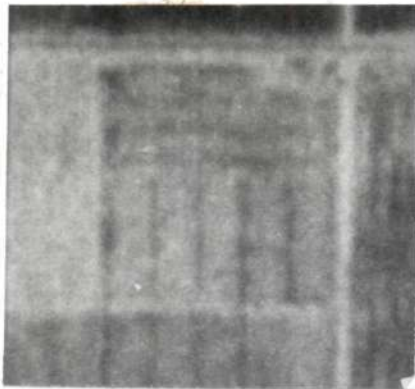
b. Image Registration Estimator

FIGURE 1-37
DIFFERENCE IMAGE STATISTICS (FOREST TERRAIN - IR SPECTRUM -
MISSION 158 - 50 METER RESOLUTION)



d. Difference Image Histogram

FIGURE 1-37 (Continued)
DIFFERENCE IMAGE STATISTICS (FOREST TERRAIN - IR SPECTRUM -
MISSION 158 - 50 METER RESOLUTION)



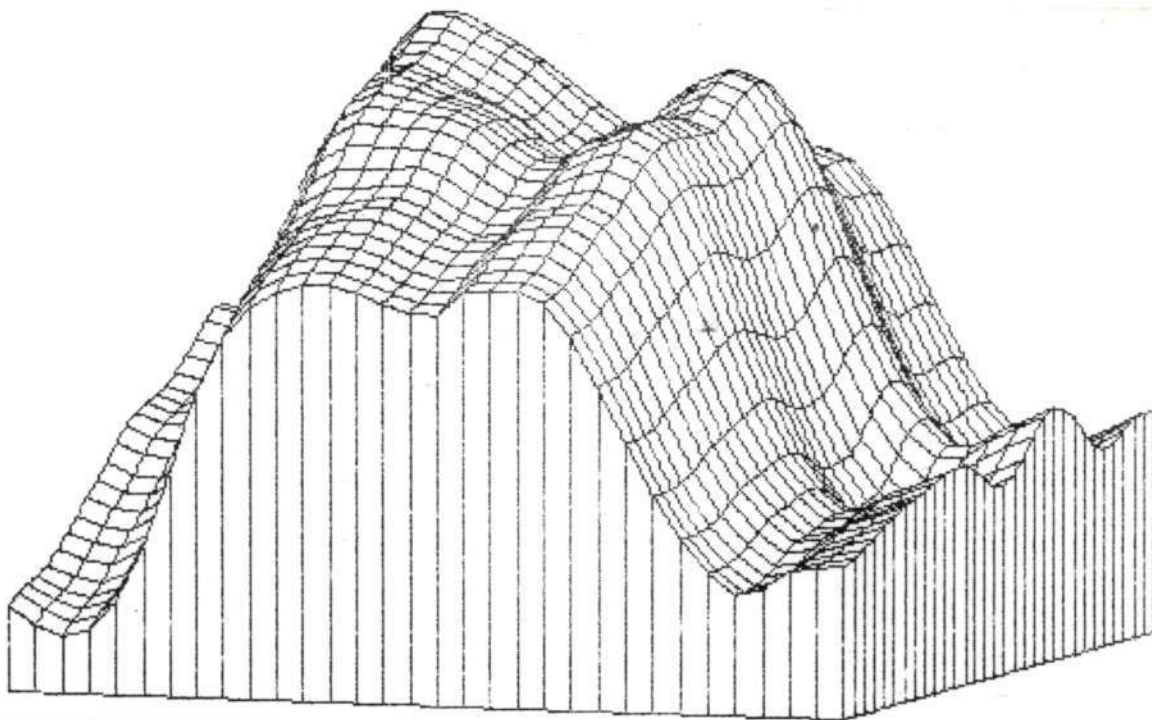
128 x 128 Image Array

a. Data Image

Difference Image Mean: 0.211

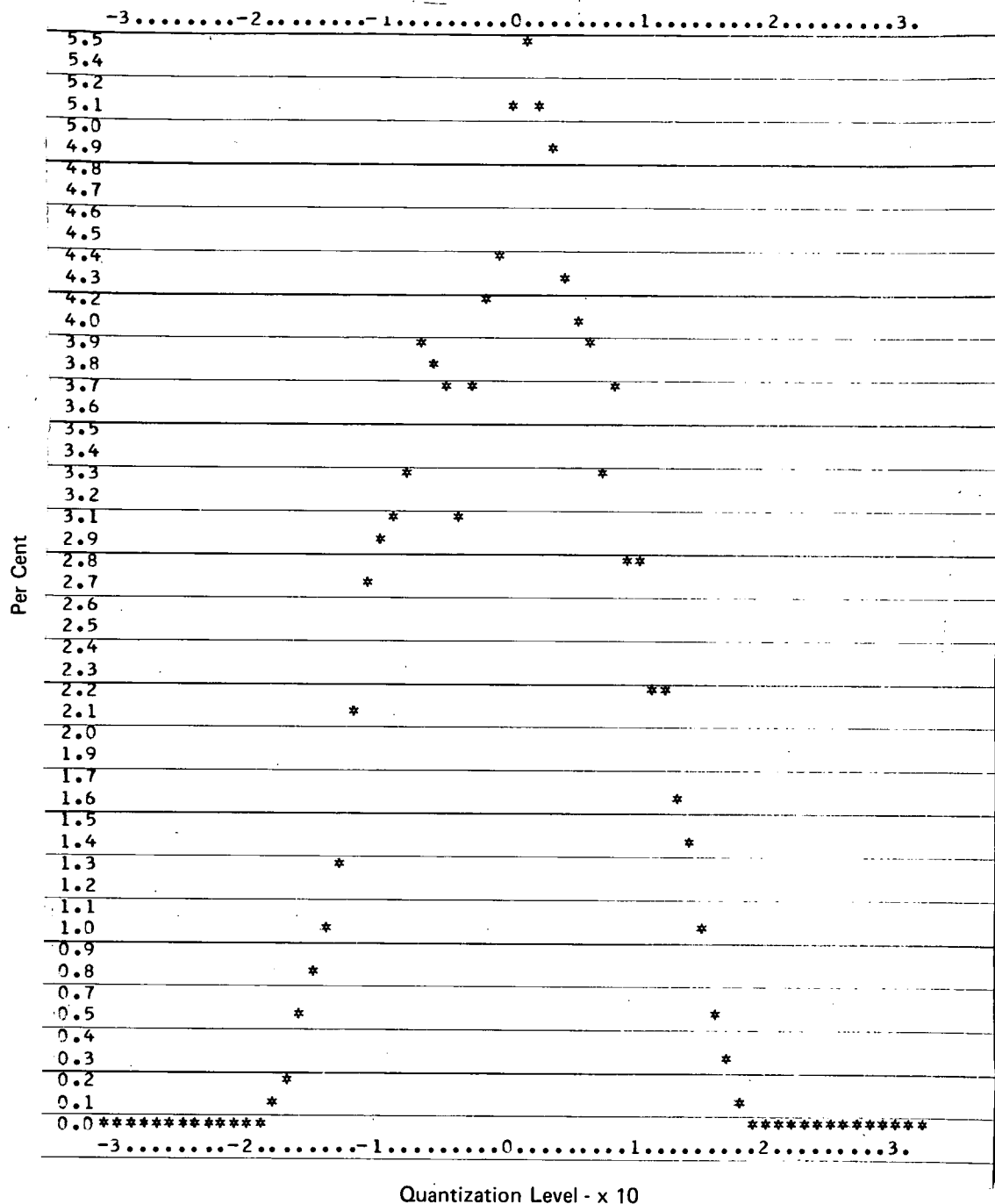
Difference Image Variance: 57.6

c. Difference Image Statistics
(Reference Image - Data Image)



b. Image Registration Estimator

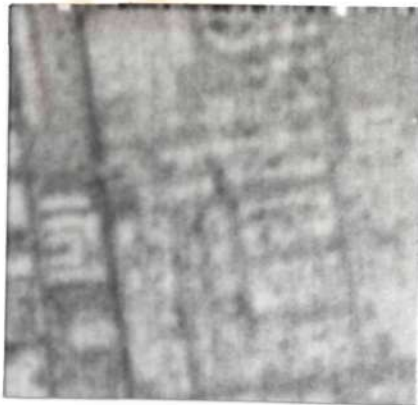
FIGURE 1-38
DIFFERENCE IMAGE STATISTICS (FARMLAND TERRAIN - RED SPECTRUM -
MISSION 129 - 10 METER RESOLUTION)



d. Difference Image Histogram

FIGURE 1-38 (Continued)
DIFFERENCE IMAGE STATISTICS (FARMLAND TERRAIN - RED SPECTRUM -
MISSION 129 - 10 METER RESOLUTION)

1-76



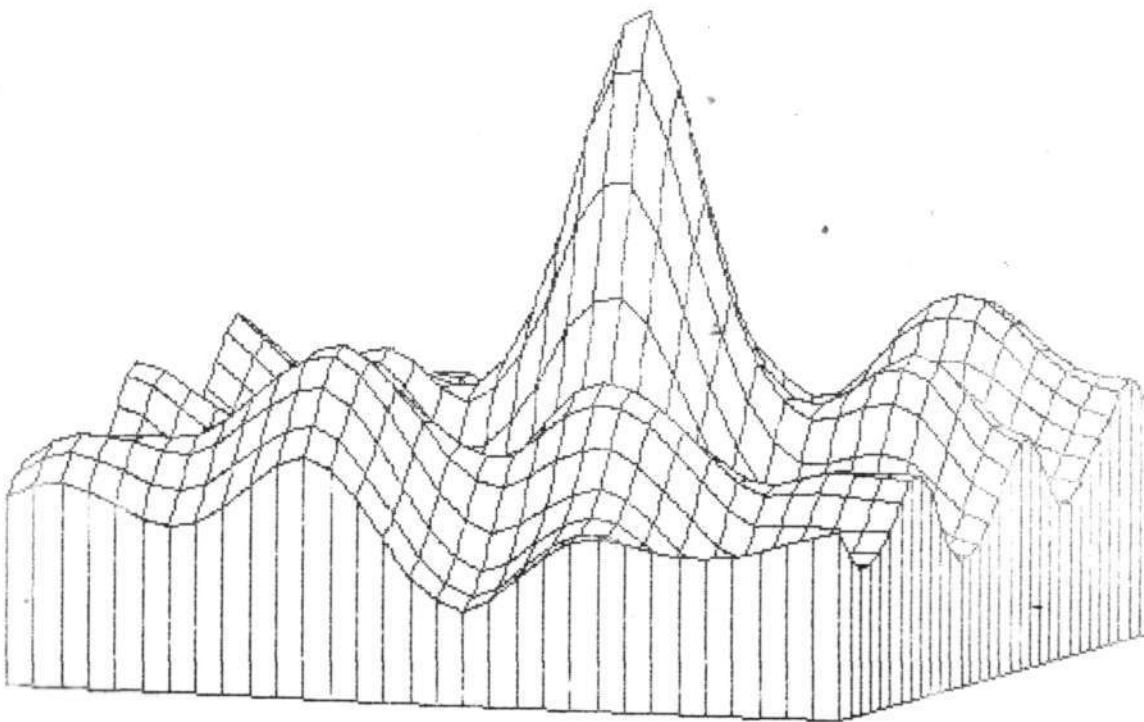
Reproduced from
best available copy.

Difference Image Mean: 0.359
Difference Image Variance: 3.59

128 x 128 Image Array

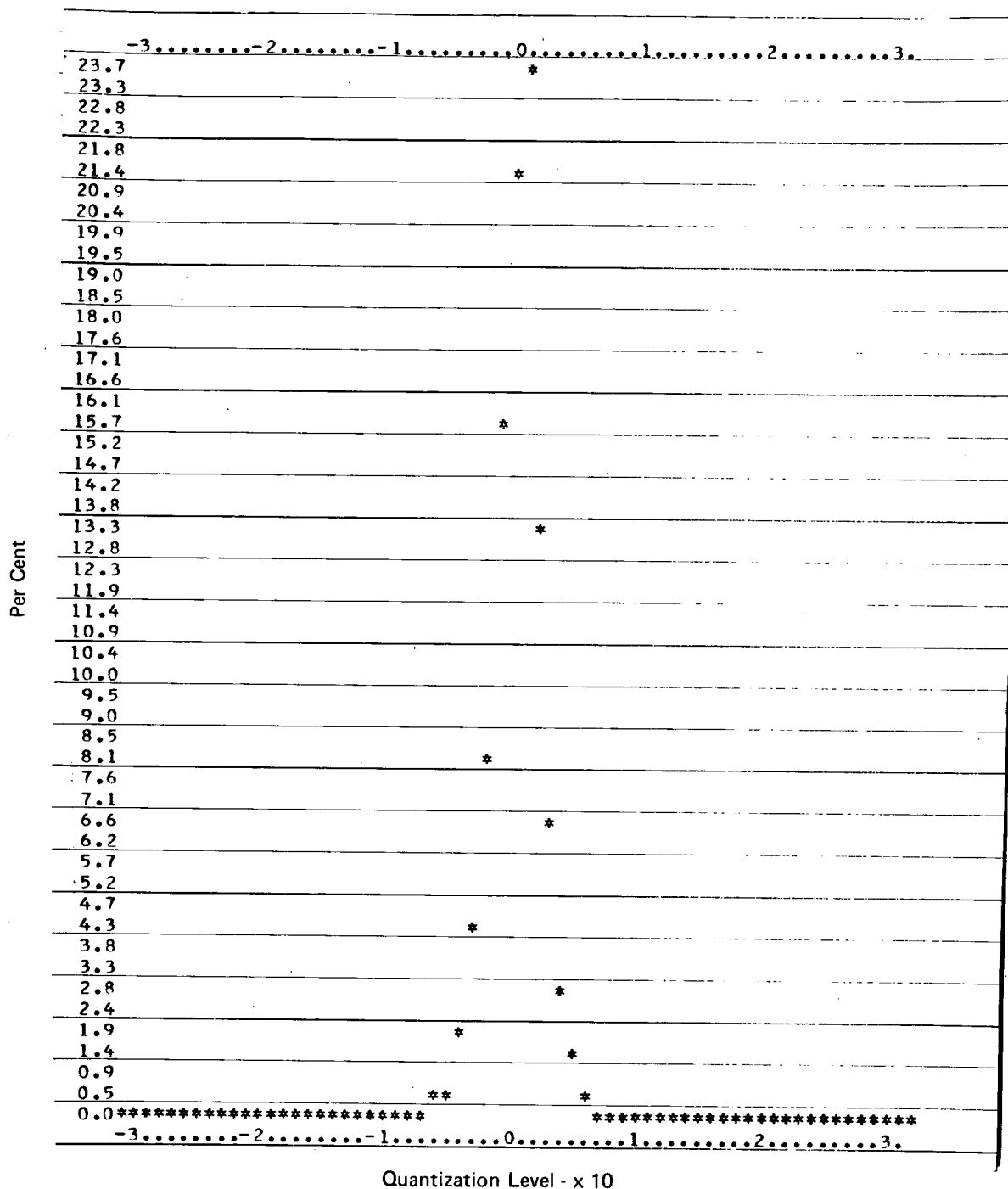
a. Data Image

c. Difference Image Statistics
(Reference Image - Data Image)



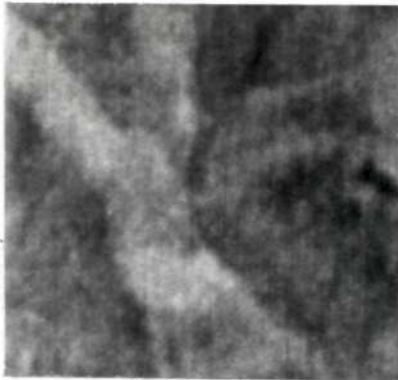
b. Image Registration Estimator

FIGURE 1-39
DIFFERENCE IMAGE STATISTICS (URBAN TERRAIN - RED SPECTRUM -
MISSION 129 - 10 METER RESOLUTION)



d. Difference Image Histogram

FIGURE 1-39 (Continued)
DIFFERENCE IMAGE STATISTICS (URBAN TERRAIN - RED SPECTRUM -
MISSION 129 - 10 METER RESOLUTION)



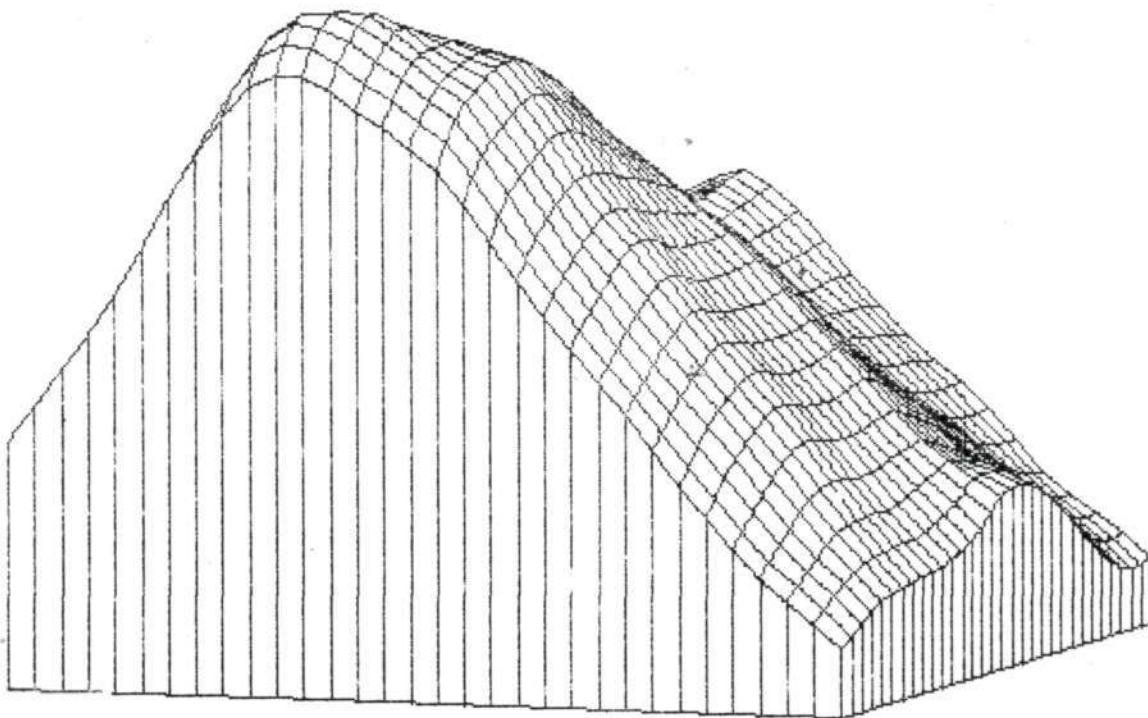
128 x 128 Image Array

a. Data Image

Difference Image Mean: 0.072

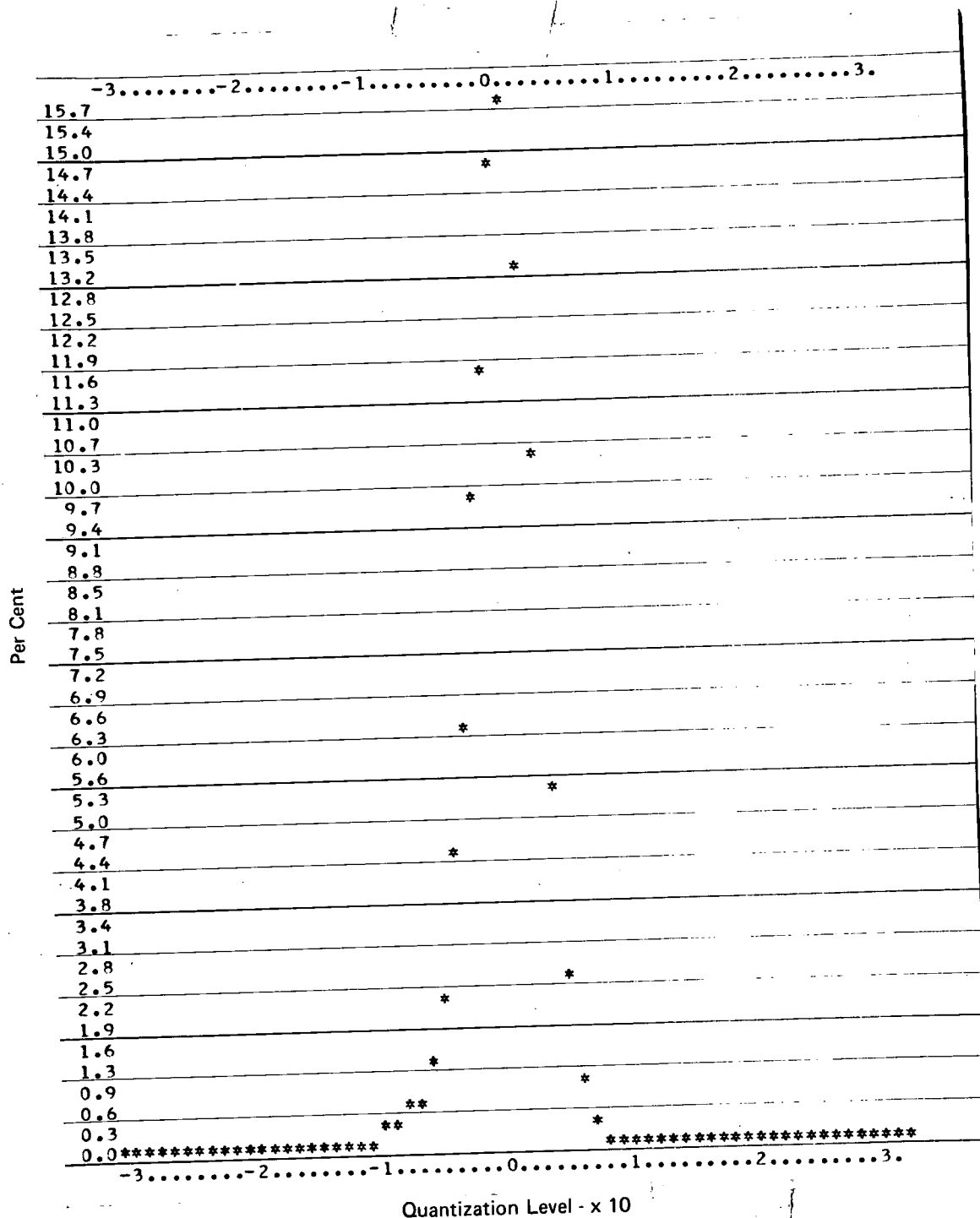
Difference Image Variance: 8.16

c. Difference Image Statistics
(Reference Image - Data Image)



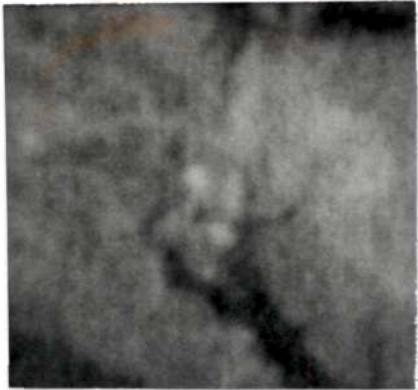
b. Image Registration Estimator

FIGURE 1-40
DIFFERENCE IMAGE STATISTICS (MOUNTAIN TERRAIN - RED SPECTRUM -
MISSION 129 - 10 METER RESOLUTION)



d. Difference Image Histogram

FIGURE 1-40 (Continued)
DIFFERENCE IMAGE STATISTICS (MOUNTAIN TERRAIN - RED SPECTRUM -
MISSION 129 - 10 METER RESOLUTION)



128 x 128 Image Array

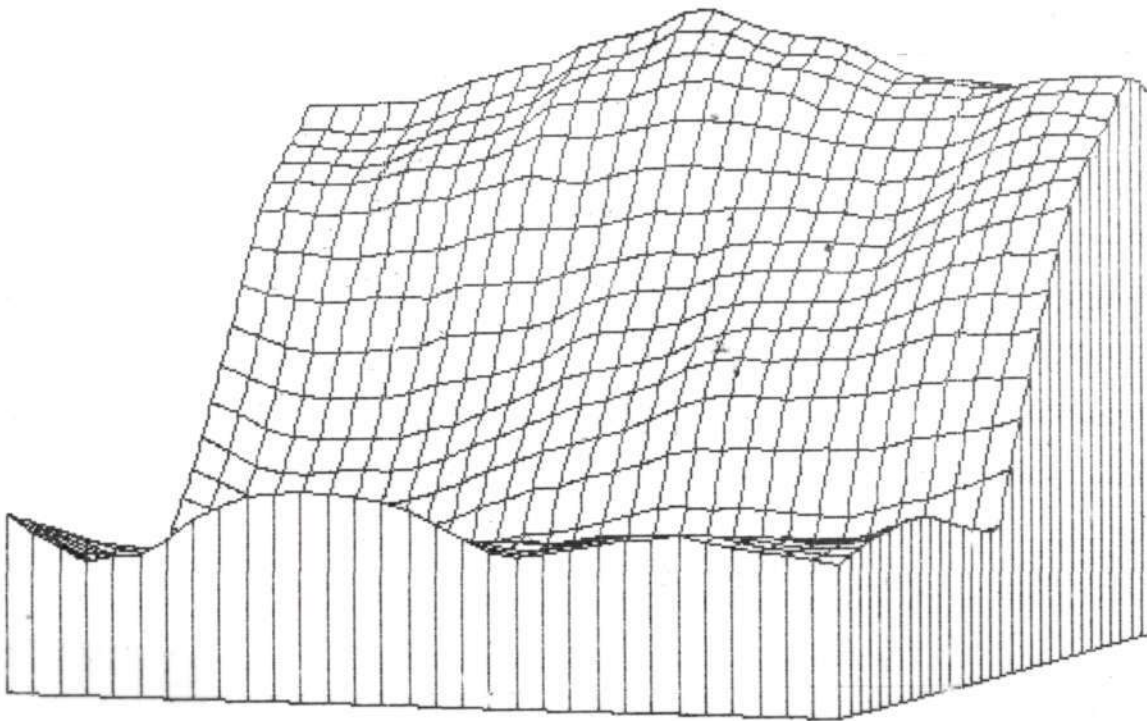
a. Data Image



Difference Image Mean: -0.5

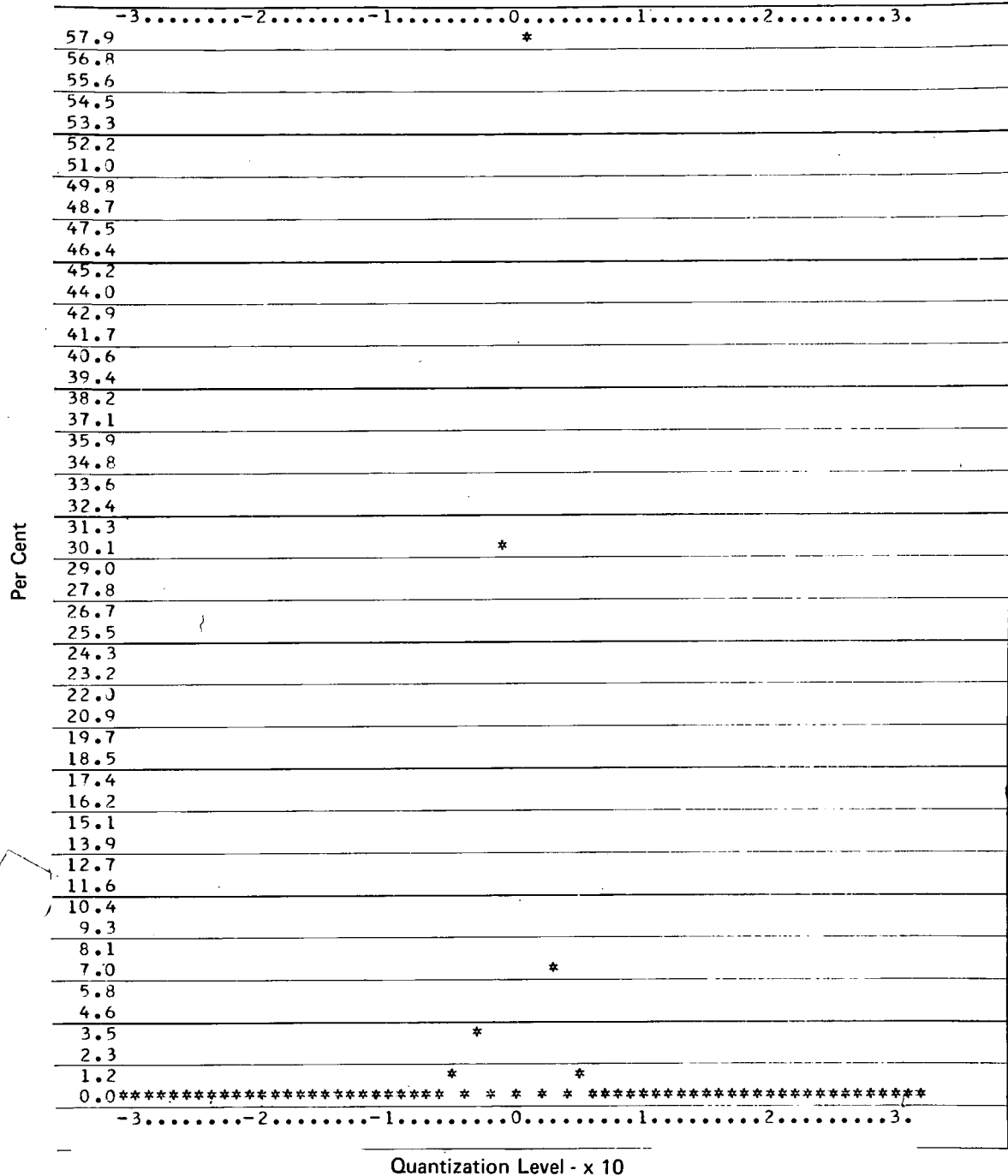
Difference Image Variance: 8

c. Difference Image Statistics
(Reference Image - Data Image)



b. Image Registration Estimator

FIGURE 1-41
DIFFERENCE IMAGE STATISTICS (FOREST TERRAIN - RED SPECTRUM -
MISSION 158 - 10 METER RESOLUTION)



d. Difference Image Histogram

FIGURE 1-41 (Continued)
DIFFERENCE IMAGE STATISTICS (FOREST TERRAIN - RED SPECTRUM -
MISSION 158 - 10 METER RESOLUTION)

SECTION 2

IMAGE CORRELATION STUDY

2.1 INTRODUCTION

In this study, digital techniques for the two-dimensional spatial registration of multispectral imagery are developed and evaluated. As the imagery from successive flights shown in Section 1 has demonstrated, there are two basic reasons why spatial registration is a serious problem for potential users of multispectral imagery.

- 1) The Fields of View (FOV) are not precisely aligned.
- 2) The images are sensed at different times from different sensor locations.

These factors cause translation, rotation, scale, geometric distortion, and brightness/contrast differences between images to be registered. User applications of earth resources imagery require accurate spatial alignment so that multidimensional analysis can be performed on image data from different spectral bands, or from successive overflights, or both.

This study considers the translation problem associated with digital image registration and develops a means for comparing commonly used digital algorithms. Using suitably defined constraints, an optimum and five suboptimum position location (registration) techniques are developed and evaluated. Both Gaussian and image derived statistics are used to compare the various techniques as functions of radial error (in image sample distances) and computational cost.

2.2 IMAGE REGISTRATION GEOMETRY

This section describes the image geometry, nomenclature and assumptions used to examine the image translational registration problem.

Two digital picture element arrays are defined as follows:

$$S = \text{Reference Image } (m \times M) \quad (2-1)$$

$$d = \text{Data Image } (n \times N) \quad (2-2)$$

where d is considered to be a subset of S and $(n \times N)$ is smaller than $(m \times M)$. These arrays are illustrated in Figure 2.1 where the $(n \times N)$ data image is referenced to its equivalent position on the reference image, that is, the potential alignment point (ℓ, L) is the position on the reference image of the $(1, 1)$ position on the data image.

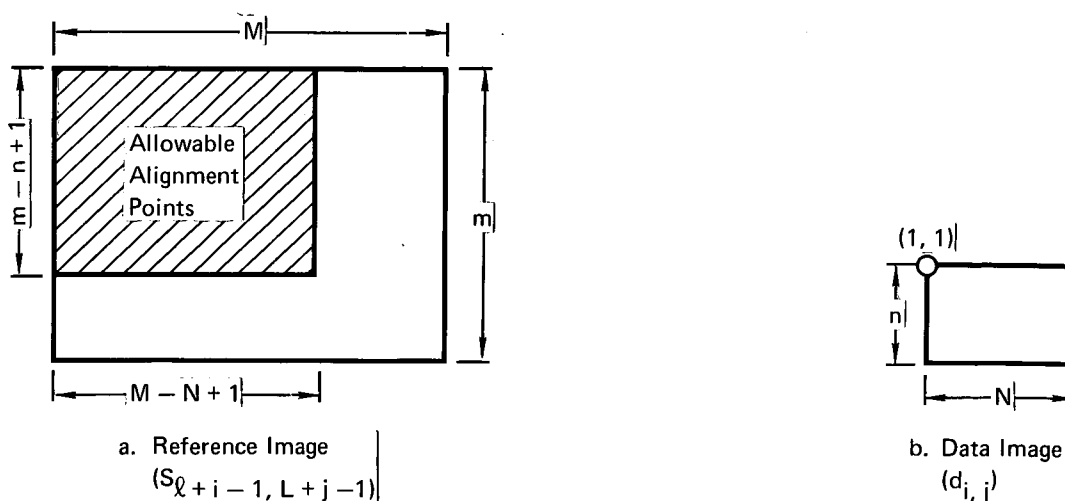


FIGURE 2-1
IMAGE REGISTRATION GEOMETRY

GP72-0450-48

In the usual image registration search procedure, the data image is systematically stepped in two dimensions around the reference image. This procedure implies that the position location alignment point (ℓ°, L°) must lie within the range $1 \leq i \leq M-N+1$ and $1 \leq j \leq m-n+1$ on the reference image

The difference image, formed by subtracting S from d , is sometimes called the "noise" or "change detected" image. These image changes are caused by varying sun angles, different viewing angles, seasonal changes and other random phenomena associated with the sensing system. For this study, the difference image ζ is defined as follows:

$$\zeta_{i,j}(\ell, L) = (d_{i,j} - S_{\ell+i-1, L+j-1}) \quad (2-3)$$

where $\zeta_{i,j}$ represents additive sample-to-sample independent noise. This assumption makes it possible to derive the optimum position location technique discussed in Section 2.3.1.

2.3 POSITION LOCATION ANALYSIS

In the following sections, an optimum position location algorithm based on minimum mean square radial error (SRE) estimation is derived and its computational complexity discussed. In addition, five suboptimum position location algorithms commonly used for image registration are defined together with their computational requirements.

2.3.1 The Optimum Position Location Technique

The conditional probability of alignment on the reference image S (assuming no angular misalignment) shown in Figure 2-1 is given by Equation (2-4).

$$P(\ell, L) = CP_A(\ell, L) \prod_{i=1}^n \prod_{j=1}^N P_{\zeta} \{ \zeta_{i,j}(\ell, L) \} \quad (2-4)$$

Where: C = normalization parameter.

$P_A(\ell, L)$ = a priori probability of alignment for any given point in S .

$\zeta_{i,j}(\ell, L)$ = defined in Equation (2-3).

$\prod_{i=1}^n \prod_{j=1}^N P_{\zeta} \{ \zeta_{i,j}(\ell, L) \}$ = joint probability of the difference image ζ .

For this study, no a priori knowledge about the alignment point (ℓ°, L°) is known, therefore, $P_A(\ell, L)$ is assumed $1/(m-n+1)(M-N+1)$. The probability of alignment $P(\ell, L)$ can be determined for each allowable point within S for any given difference image ζ . Allowable points (ℓ, L) consist of all points within the set $\{ 1 \leq \ell \leq m-n+1, 1 \leq L \leq M-N+1 \}$. Assume that the alignment point (ℓ°, L°) is within the allowable point set. The normalization parameter C is then specified as:

$$C = \left[\sum_{\ell=1}^{m-n+1} \sum_{L=1}^{M-N+1} P_A(\ell, L) \prod_{i=1}^n \prod_{j=1}^N P_{\zeta} \{ \zeta_{i,j}(\ell, L) \} \right]^{-1} \quad (2-5)$$

Since:

$$\sum_{\ell=1}^{m-n+1} \sum_{L=1}^{M-N+1} P(\ell, L) \underline{\underline{= 1}} \quad (2-6)$$

2.3.1.1 Mean Square Radial Error

The mean square radial error (MSRE) estimate for the alignment point is determined for that position of (ℓ, L) which minimizes:

$$\overline{r^2(\ell_1, L_1)} = \sum_{\ell=1}^{m-n+1} \sum_{L=1}^{M-N+1} P(\ell, L) [(\ell_1 - \ell)^2 + (L_1 - L)^2] \quad (2-7)$$

Where: $\overline{r^2(\ell, L)}$ = mean square radial error.

$P(\ell, L)$ = defined in Equation (2-4).

(ℓ_1, L_1) = alignment point being examined.

The implementation of this optimum position location estimator for image registration applications requires a tractable expression for $P_{\zeta}\{\zeta_{i,j}(\ell,L)\}$ to solve for $P(\ell,L)$ in Equation (2-4). In the following section, an approach for implementation of this estimator is described.

2.3.1.2 Implementation

One attractive approach for implementation of the optimum position location estimator is to determine $P_{\zeta}\{\zeta_{i,j}(\ell,L)\}$ experimentally using histograms of real difference image data and then perform a minimization of $r^2(\ell,L)$ (Equation 2-7) using the digital computer. Unfortunately, when this approach is implemented using reference images of useful size, the digital storage and computational cost of using this estimator becomes prohibitive. An alternate approach and the one determining $P_{\zeta}\{ \}$ in a straightforward manner used in this study is to form the following equivalent expression. Let:

$$\prod_{\text{all } i} \prod_{\text{all } j} P_{\zeta}(\zeta_{i,j}(\ell,L)) \equiv \prod_{\text{all } q} P_q^{b_q(\ell,L)} \quad (2-8)$$

Where: $b_q(\ell,L)$ = the number of difference image samples that lie in the q th quantization level.

P_q = the probability that a difference image sample is in the q th quantization level.

Using the right half of Equation (2-8) instead of the left to determine $P(\ell,L)$ allows a substantial savings in both image statistic storage and estimator computations. A typical quantized difference image probability P_q function is illustrated in Figure 2-2.

For any given difference image then, (assuming the constraints of Sections 2.2 and 2.3.1) the optimum position location algorithm can be digitally implemented for image registration using the following steps:

- a) Form P_q histogram for given $\zeta_{i,j}(\ell,L)$.
- b) Solve for $\prod_{\text{all } i} \prod_{\text{all } j} P_{\zeta}\{\zeta_{i,j}(\ell,L)\}$ using Equation (2-8).

- c) Solve for normalization constant C using Equation (2-5).
- d) Determine $P(\ell, L)$ using Equation (2-4).
- e) Solve for the alignment point (ℓ^*, L^*) where $\overline{r^2}(\ell, L)$ is minimum.

Note that the only a priori image statistic required is the P_q histogram of the difference image.

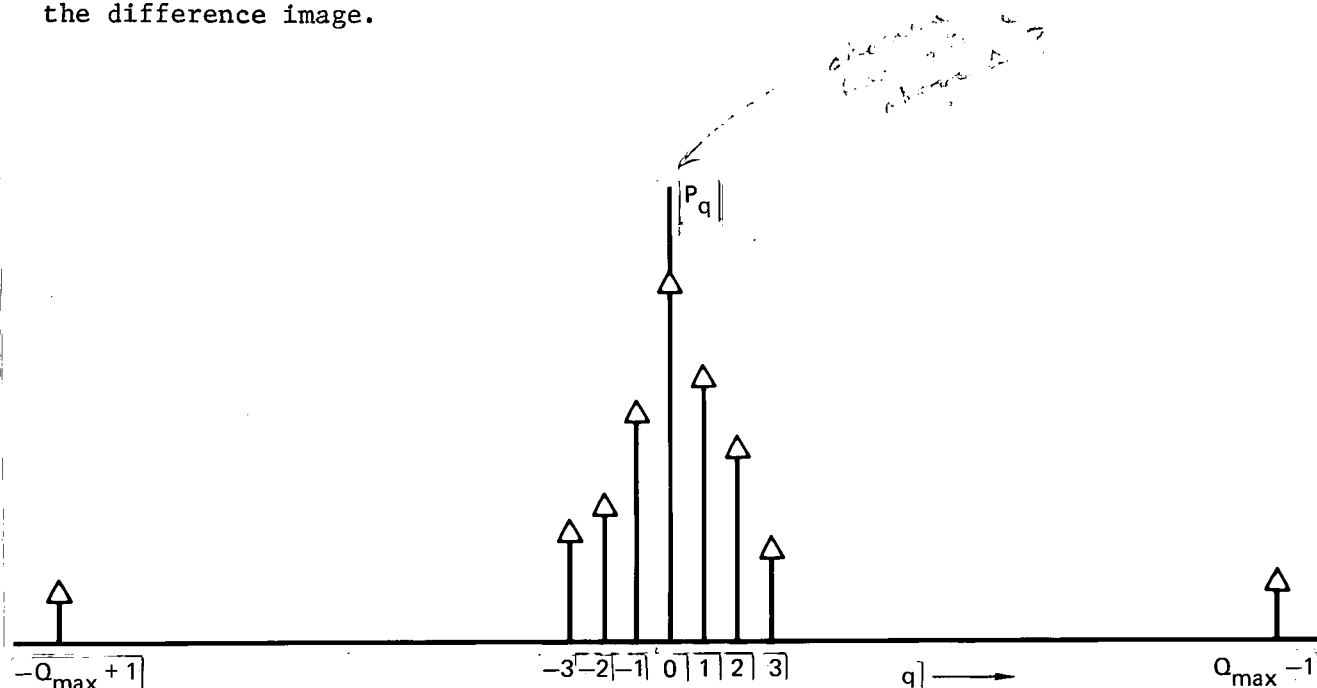


FIGURE 2-2
EXAMPLE OF P_q FUNCTION

2.3.1.3 Estimator

The optimum position location estimator was described mathematically in Equation (2-7). For image registration, the alignment point is that value of (ℓ, L) where $\overline{r^2}(\ell, L)$ is a minimum. Figure 2-3 is a 3-D plot illustrating the behavior of this estimator for a specific difference image. For the example of Figure 2-3, $n=N=5$, $m=M=50$, and a difference image with a Gaussian P_q histogram ($\sigma = 10$) was assumed.

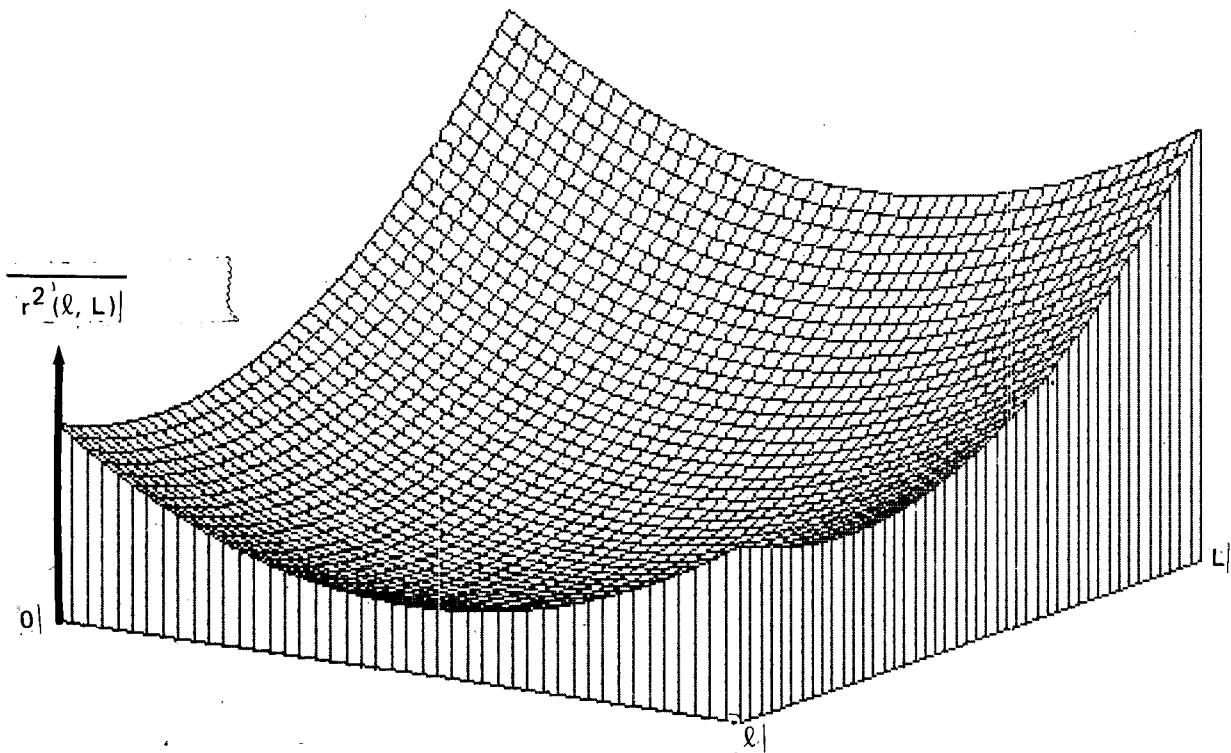


FIGURE 2-3
EXAMPLE OF OPTIMUM POSITION LOCATION ESTIMATOR

2.3.1.4 Computations

The optimum position location algorithm requires a specific number of computations for any given reference and data image size. These computations have been listed parametrically in Table 2-1. In this tabulation, a subtraction and division were made equivalent to an addition and multiplication respectively.

TABLE 2-1
OPTIMUM POSITION LOCATION ALGORITHM COMPUTATIONS

Parameter	Additions	Multiplications
1. $\prod_{i=1}^n \prod_{j=1}^N P_{\xi} \left\{ \xi_{i,j}(\ell, L) \right\}$	$nN, \forall (\ell, L)$	$(nN-1), \forall (\ell, L)$
2. C, Store Value	$(m-n+1)(M-N+1)$	0
3. P(ℓ, L), Store Each Value	$nN, \forall (\ell, L)$	$nN, \forall (\ell, L)$
4. $\overline{r^2}(\ell, L)$	$4(m-n+1)(M-N+1) - 1,$ $\forall (\ell, L)$	$3(m-n+1)(M-N+1),$ $\forall (\ell, L)$
5. All $\overline{r^2}(\ell, L)$	$4(m-n+1)^2(M-N+1)^2 +$ $+ nN(m-n+1)(M-N+1)$	$3(m-n+1)^2(M-N+1)^2$ $+ nN(m-n+1)(M-N+1)$

GP72-0450-37

2.3.2 $v = 1$ Correlation Techniques

The v -law correlation algorithms are based on the minimization of the absolute difference between S and d . For example, if S and d are identical (at alignment), the sum of the absolute values of the difference image samples are zero. The difference image at other potential alignment points would have non-zero samples yielding the separating property of the v -law correlation algorithm. Alignment for the general v -law correlation algorithm occurs for that point (ℓ^*, L^*) where:

$$C_v = \sum_{i=1}^n \sum_{j=1}^N |d_{i,j} - s_{\ell+i-1, L+j-1}|^v \quad (2-9)$$

is a minimum. For $v=1$, this becomes:

$$C_1 = \sum_{i=1}^n \sum_{j=1}^N |d_{i,j} - s_{\ell+i-1, L+j-1}| \quad (2-10)$$

2.3.2.1 Estimator

The $\nu=1$ position location estimator described in Equation (2-10) can best be illustrated by a specific examples. Figure 2-4 is a 3-D plot of the estimator using a Gaussian difference image ($\sigma/\Delta=10$), $n=N=5$, $m=M=50$ (See Section 2.4).

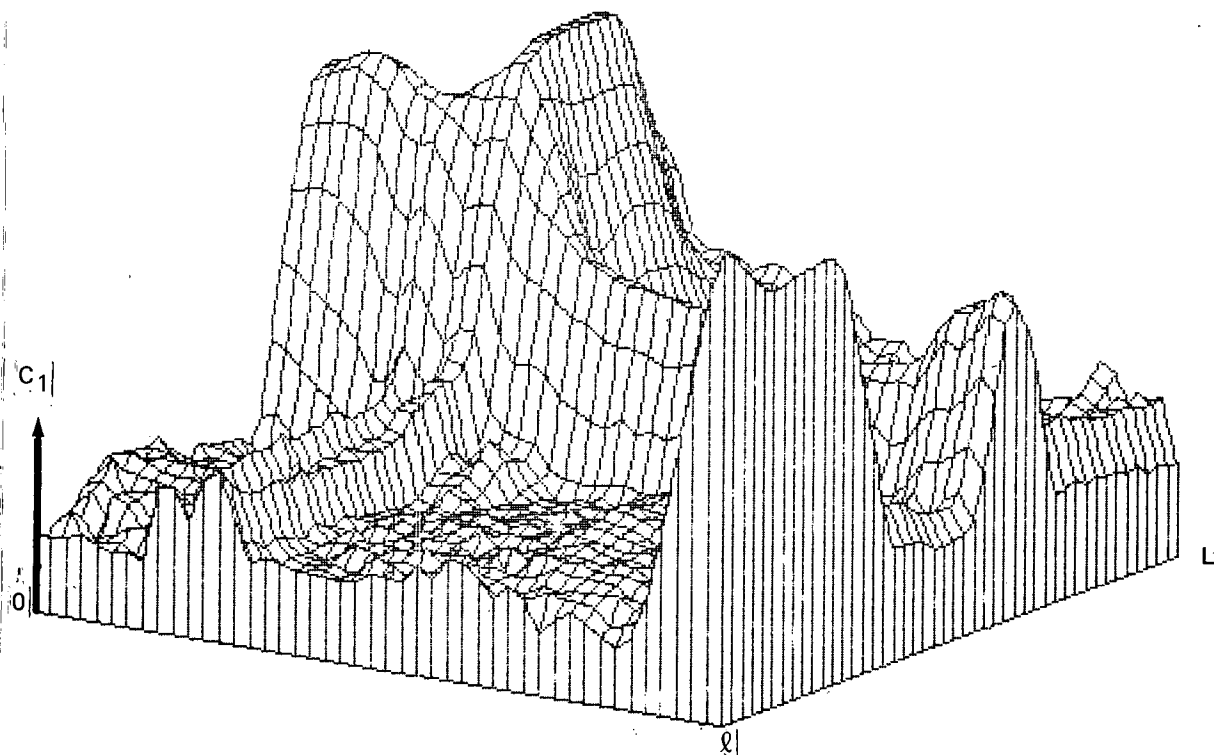


FIGURE 2-4
EXAMPLE OF $\nu=1$ POSITION LOCATION ESTIMATOR

2.3.2.2 Computations

For any given set of S and d images, a finite number of computations are required using the $\nu=1$ position location estimator. No multiplications are required, only additions. These are:

$$\left. \begin{array}{l} \text{Number of Additions} \\ \text{For one } (l, L) \end{array} \right\} = 2nN-1 \quad (2-11)$$

$$\left. \begin{array}{l} \text{Total Number of Additions} \\ \text{For All Allowable } (l, L) \end{array} \right\} = (2nN-1) (m-n+1) (M-N+1) \quad (2-12)$$

2.3.2 $\nu = 2$ Correlation Technique

Another attractive suboptimum position location technique involves using Equation (2-9) with $\nu=2$.

$$C_2 = \sum_{i=1}^n \sum_{j=1}^N |d_{i,j} - s_{\ell+i-1, L+j-1}|^2 \quad (2-13)$$

2.3.3.1 Estimator

Alignment occurs for that point (ℓ^*, L^*) where C_2 is a minimum. A 3-D plot of a representative $\nu=2$ position location estimator is shown in Figure 2-5. As with the previous estimators, this example assumes a Gaussian difference image ($\sigma/\Delta=10$), $n=N=5$, $m=M=50$ (See Section 2.4).

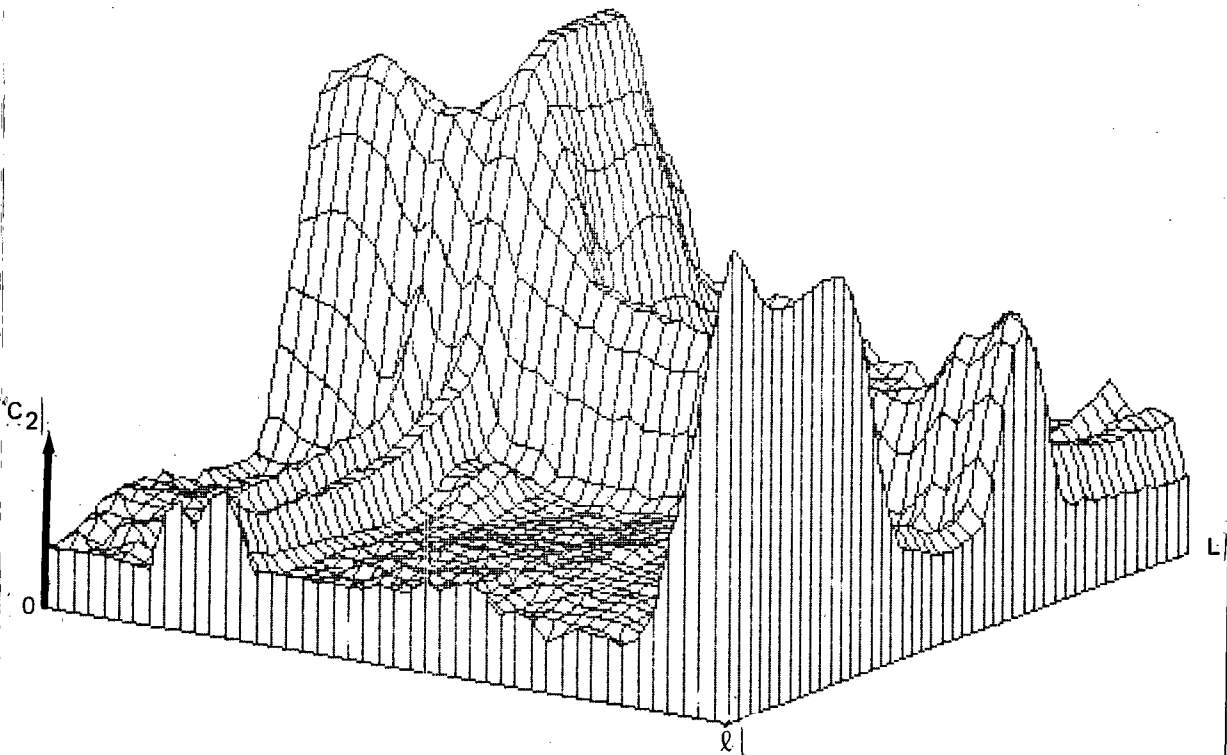


FIGURE 2-5
EXAMPLE OF $\nu = 2$ POSITION LOCATION ESTIMATOR

2.3.3.2 Computations

For any given set of S and d images, a finite number of computations are required using the $v=2$ position location estimator. These are:

$$\left. \begin{array}{l} \text{Total Number of Additions} \\ \text{For All Allowable } (\ell, L) \end{array} \right\} = (2nN-1) (m-n+1) (M-N+1) \quad (2-14)$$

$$\left. \begin{array}{l} \text{Total Number of Multiplications} \\ \text{For All Allowable } (\ell, L) \end{array} \right\} = nN (m-n+1) (M-N+1) \quad (2-15)$$

2.3.4 Maximum Likelihood Estimation Technique

The maximum likelihood estimator is, perhaps, the most utilized decision algorithm. Applying this estimation technique to the image registration problem, the maximum likelihood position location algorithm would compute the probability of alignment at all allowable points in S . The potential alignment point (ℓ^*, L^*) having the maximum probability value would be selected as the alignment point. The expression for computing these alignment probabilities was given previously in Section 2.3.1, Equation (2-4).

$$P(\ell, L) = C \prod_{i=1}^n \prod_{j=1}^N P_{\zeta} \{ \zeta_{i,j}(\ell, L) \} \quad (2-16)$$

When the difference image ζ is Gaussian with zero mean, the maximum likelihood estimator becomes identical to the $v=2$ law position location algorithm. This can be shown as follows:

Let:

$$\prod_{i=1}^n \prod_{j=1}^N P_{\zeta} \{ \zeta_{i,j}(\ell, L) \} = \frac{C}{(2\pi\sigma^2)^{\frac{nN}{2}}} \exp \left(-\frac{\zeta^2}{2\sigma^2} \right) \quad (2-17)$$

Where: C = normalization constant discussed in Equation (2-5).

$$\zeta^2 = \left[\sum_{i=1}^n \sum_{j=1}^N (d_{i,j} - s_{\ell+i-1, L+j-1}) \right]^2 \quad (2-18)$$

Using maximum likelihood estimation, the point (ℓ^*, L^*) would be selected as the alignment point which maximizes $P(\ell, L)$ in Equation (2-16). This procedure is equivalent to minimizing ζ^2 as defined in Equation (2-18) which is seen to correspond with Equation (2-13) for the $v=2$ algorithm. Thus, for Gaussian zero mean ζ , the maximum likelihood and $v=2$ are equivalent position location algorithms. This equivalence will be noted in Section 2.4.

2.3.4.1 Estimator

Due to the equivalence of the maximum likelihood and $v=2$ algorithms when ζ is a zero mean Gaussian difference image, Figure 2-5 illustrates a representative maximum likelihood position location estimator.

2.3.4.2 Computations

The finite number of computations required by the maximum likelihood position location technique is determined from Table 2-1 to be;

$$\left. \begin{array}{l} \text{Total Number of} \\ \text{Additions For all} \\ \text{Allowable } (\ell, L) \end{array} \right\} = (nN+1) (m-n+1) (M-N+1) \quad (2-19)$$

$$\left. \begin{array}{l} \text{Total Number of} \\ \text{Multiplications for} \\ \text{All Allowable } (\ell, L) \end{array} \right\} = (nN+1) (m-n+1) (M-N+1) \quad (2-20)$$

2.3.5 Cross-Covariance Function Techniques

The cross covariance position location estimator is defined as:

$$C_{xy} = \sum_{i=1}^n \sum_{j=1}^N (d_{i,j} - \bar{d}) (S_{\ell+i-1, L+j-1} - \bar{S}_{\ell, L}) \quad (2-21)$$

Where: \bar{d} = mean Value of $d_{i,j}$

$\bar{S}_{\ell, L}$ = Mean Value of $S_{\ell+i-1, L+j-1}$, summed over all i and j

The algorithm alignment point estimate occurs for that point (ℓ^*, L^*) where C_{xy} has its maximum value.

2.3.5.1 Estimator

A 3-D plot of a representative cross-covariance position location estimator is shown in Figure 2-7. This example assumed a Gaussian difference image ($\sigma/\Delta=10$), $n=N=5$, $m=M=50$ (See Section 2.4)

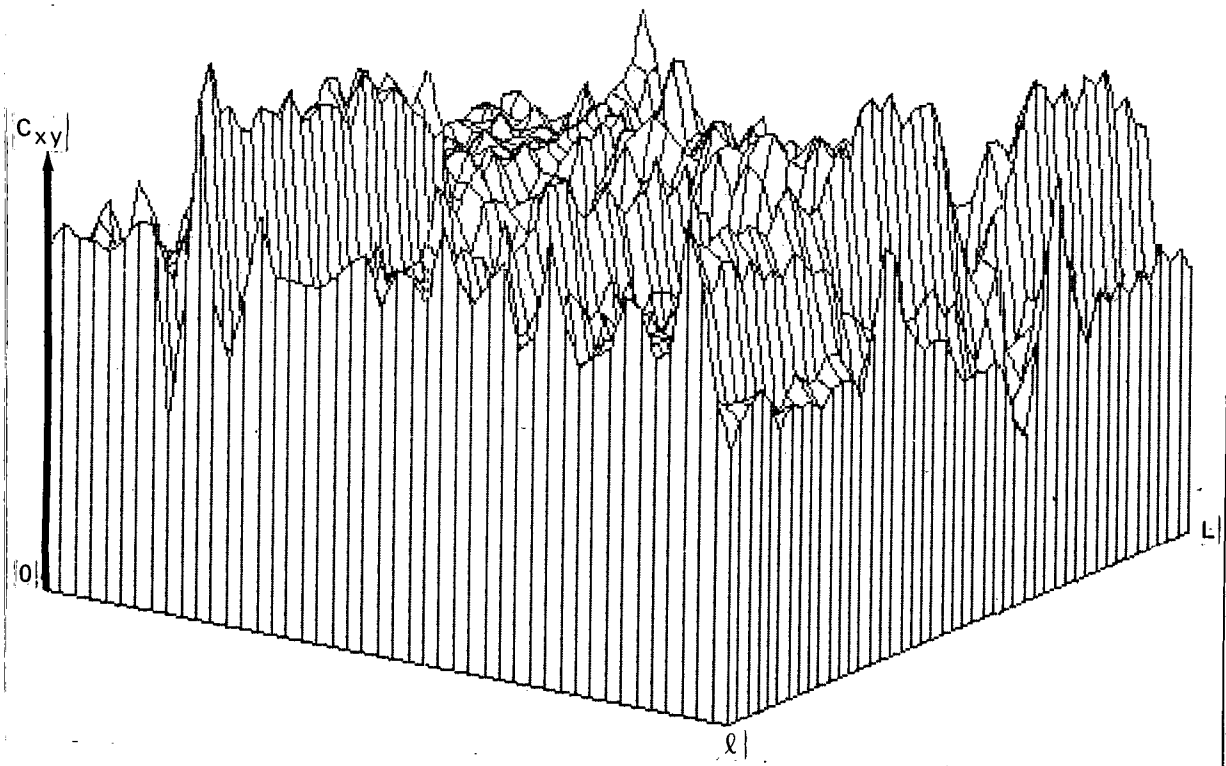


FIGURE 2-6
EXAMPLE OF CROSS-COVARIANCE POSITION LOCATION ESTIMATOR

2.3.5.2 Computations

The expression for the cross-variance position location estimator can be re-written as follows:

$$C_{xy} = \left(\sum_{i=1}^n \sum_{j=1}^N d_{i,j} \cdot s_{\ell+i-1, L+j-1} \right) - nN \bar{d} \bar{s}_{\ell, L} \quad (2-22)$$

Equation (2-22) can be computed with fewer additions and multiplications than Equation (2-21) and will be used to determine computational requirements. (A subtraction is equivalent to an addition.)

$$\left. \begin{array}{l} \text{Total Number of Additions} \\ \text{For All Allowable } (\ell, L) \end{array} \right\} = (m-n+1) (M-N+1) (2nN-1) + nN-1 \quad (2-23)$$

$$\left. \begin{array}{l} \text{Total Number of} \\ \text{Multiplications for} \\ \text{All Allowable } (\ell, L) \end{array} \right\} = (m-n+1) (M-N+1) (nN+4) + 1 \quad (2-24)$$

2.3.6 Cross Correlation Coefficient Technique

The most widely used digital position location algorithm is that of the cross-correlation coefficient (Reference 5). This estimator is defined in Equation (2-25) in terms of two dimensional image samples.

$$\rho_{xy} = \frac{C_{xy}}{\left[\left[\sum_{i=1}^n \sum_{j=1}^N (d_{i,j} - \bar{d}) \right] \left[\sum_{i=1}^n \sum_{j=1}^N (S_{\ell+i-1, L+j-1} - \bar{S}_{\ell, L}) \right] \right]^{1/2}} \quad (2-25)$$

Where: C_{xy} is defined by Equation (2-22)

\bar{d} = Mean value of $d_{i,j}$

$\bar{S}_{\ell, L}$ = Mean Value of $S_{\ell+i-1, L+j-1}$

Alignment occurs at that point (ℓ^*, L^*) where ρ_{xy} has its maximum value.

2.3.6.1 Estimator

A 3-D plot of a representative cross-correlation coefficient position location estimator is shown in Figure 2-8. This example assumed a Gaussian difference image ($\sigma/\Delta = 10$), $n=N=5$, and $m=M=50$ (See Section 2.4).

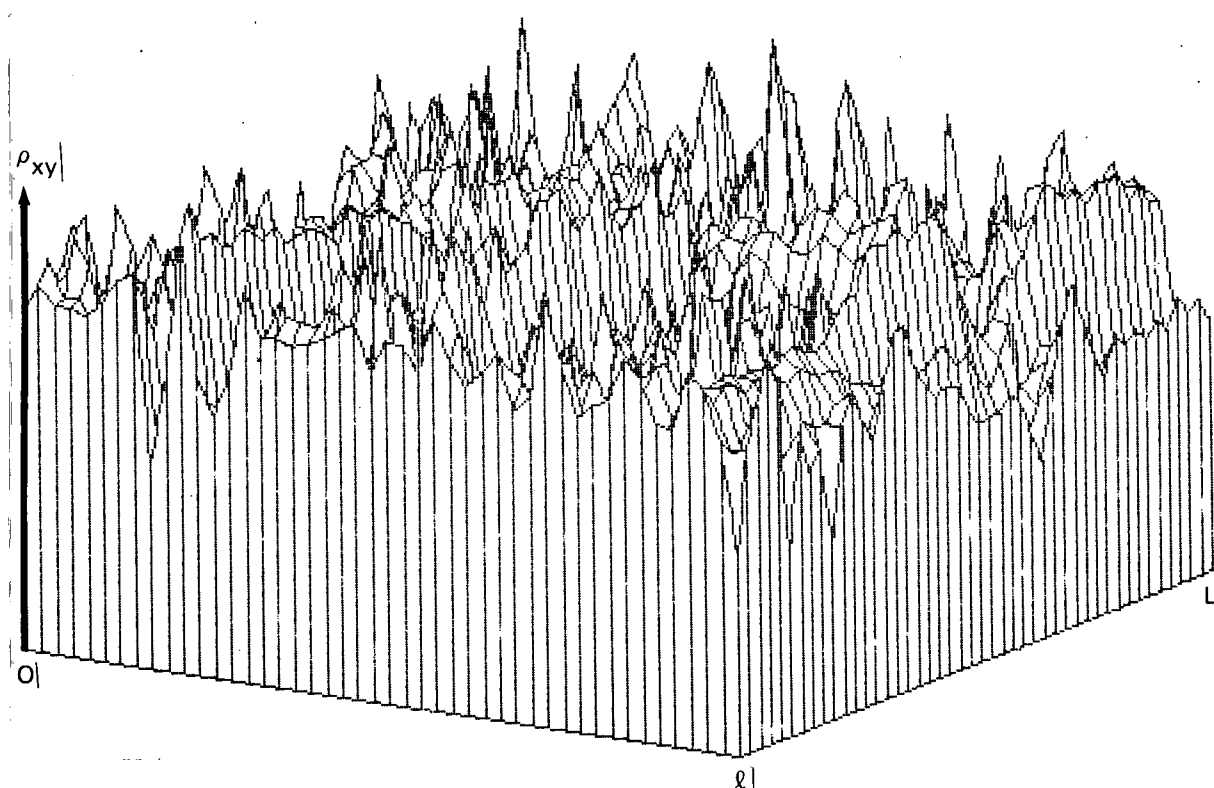


FIGURE 2-7
EXAMPLE OF CROSS-CORRELATION COEFFICIENT POSITION
LOCATION ESTIMATOR

2.3.6.2 Computations

Using conventional numerical methods, the computational requirements for the cross-correlation coefficient position location technique are listed as follows. A subtraction and division are equivalent to an addition and multiplication, respectively.

$$\left. \begin{array}{l} \text{Total Number of} \\ \text{Additions For} \\ \text{All Allowable Points} \end{array} \right\} = (4nN-1) (m-N+1) (M-N+1)+2nN \quad (2-26)$$

$$\left. \begin{array}{l} \text{Total Number of} \\ \text{Multiplications for} \\ \text{All Allowable Points} \end{array} \right\} = (2nN+6) (m-n+1) (M-N+1)+17N+3 \quad (2-27)$$

In addition, Fast Fourier Transform (FFT) computational methods can be utilized for correlation. Such usage however, must be exercised with care. Aliasing errors require the d image be padded with zeros to form an $m \times M$ image. An additional constraint is that m and M must be powers of 2. For determining computational requirements using the FFT, it is convenient to assume $n=N$ and $m=M$. Then:

$$\left. \begin{array}{l} \text{Total Number of} \\ \text{Additions} \end{array} \right\} = 6M^2 \log_2 M + 2M^2 \quad (2-28)$$

$$\left. \begin{array}{l} \text{Total Number of} \\ \text{Complex Multiplications} \end{array} \right\} = 3M^2 \log_2 M + (M-N+1)^2 + M^2 + 1 \quad (2-29)$$

2.3.7 Position Location Optimization

This section discusses various parameters which affect both the accuracy and efficiency of position location techniques.

2.3.7.1 Preprocessing

Preprocessing is defined as any refinement of the image data S and d which will reduce the system error in the ζ image. This includes any photo-processing and image normalization which make ζ representative only of terrain "change detected" or difference information.

Preprocessing is very important to the optimum, $v=1$, $v=2$, and maximum likelihood position location techniques. These estimators, basically, all search for minimum values of the ζ image. At alignment, any error due either to dynamic range limitation or intensity mean value offset will seriously degrade performance of these position location techniques. The cross-correlation position location techniques have some normalization inherent in the algorithms which reduce their susceptibility to these errors.

2.3.7.2 Quantization

The optimization of image quantization for image registration applications has a twofold purpose: 1) reduce the error probability and 2) reduce the computational complexity. Examination of each position location algorithm discussed in the preceding sections will show that each is based on a set of

sums of random variables. The sum accuracy for each algorithm is a direct function of the quantization range for that random variable. For example, the estimator for the optimum position location technique (Equation 2-7) is seen to be a set of sums whose accuracy depends on the quantization error present in the ζ image (Equation 2-3).

The error probability for a sum of random variables can be approximated by invoking the central limit theorem: this error probability is:

$$P_{\epsilon}(\alpha) = P \left\{ \left| \sum_{i=1}^n \sum_{j=1}^N (d_{i,j}^* - d_{i,j}) \right| > \alpha \right\} \quad (2-30)$$

where: $d_{i,j}$ = unquantized data image

$d_{i,j}^*$ = quantized data image

$(d_{i,j}^* - d_{i,j})$ = quantization error $\epsilon_{i,j}$ (d) is uniformly distributed

$P_{\epsilon}(\alpha)$ = probability that the sum is outside the confidence interval $[-\alpha, \alpha]$.

Consider the normalized random variable:

$$y = \frac{\sum_{i=1}^n \sum_{j=1}^N \epsilon_{i,j}(d) / -E \left\{ \sum_{i=1}^n \sum_{j=1}^N \epsilon_{i,j}(d) \right\}}{\left[v \left\{ \sum_{i=1}^n \sum_{j=1}^N \epsilon_{i,j}(d) \right\} \right]^{1/2}} \quad (2-31)$$

Which has a limiting distribution that is normal with zero mean and unity variance. In other words, as "nN" becomes larger, the probability density function for y is approximately a zero mean unity variance normal. Thus, the probability that $|y|$ is greater than some δ is:

$$P(|y| > \delta) = P \left\{ \left| \sum_{i=1}^n \sum_{j=1}^N \epsilon_{i,j}(x) \right| > \delta \Delta \left(\frac{nN}{12} \right)^{\frac{1}{2}} \right\} \quad (2-32)$$

Where: $\frac{\Delta^2}{12}$ = variance of uniformly distributed quantization error
(reference 8)

$\frac{\Delta^2 nN}{12}$ = Variance of a sum of uniformly distributed independent quantization error random variables.

Δ = quantization interval

$$P(|y| > \delta) \approx \frac{2}{\sqrt{2\pi}} \int_{\delta}^{\infty} \exp \left\{ -\frac{y^2}{2} \right\} dy \quad (2-33)$$

Equation (2-33) and (2-31) are now equivalent and are plotted in Figure 2-8. It is obvious from Figure 2-8 that, for a fixed α , increasingly fine quantization will decrease the error probability. This implies that increasingly fine quantization should provide image registration with increasing position location accuracy. A trade off of registration accuracy as a function of quantization probably exists for each algorithm, however, a digital simulation would be needed to provide quantitative evaluation.

2.3.7.3 Data Image Size and Shape

In general, an optimum data image size and shape should exist for each of the position location techniques. Intuitively, those position location estimations that depend on the correlation present between two images (such as the C_{xy} and ρ_{xy} algorithms) should benefit from using maximum sample compactness in the sampling lattice. This would imply that a rhombic sampling lattice (as discussed in Section 3.4.3) should be used for these algorithms. It is felt that the improvement over using a square sampling lattice would only be slight, however. Quantitative data is lacking concerning the trade off of data image size and shape as a function of position location error performance. In the digital simulations of Section 2-4 and 2-5, an attempt is made to determine if square or circular data images should be used.

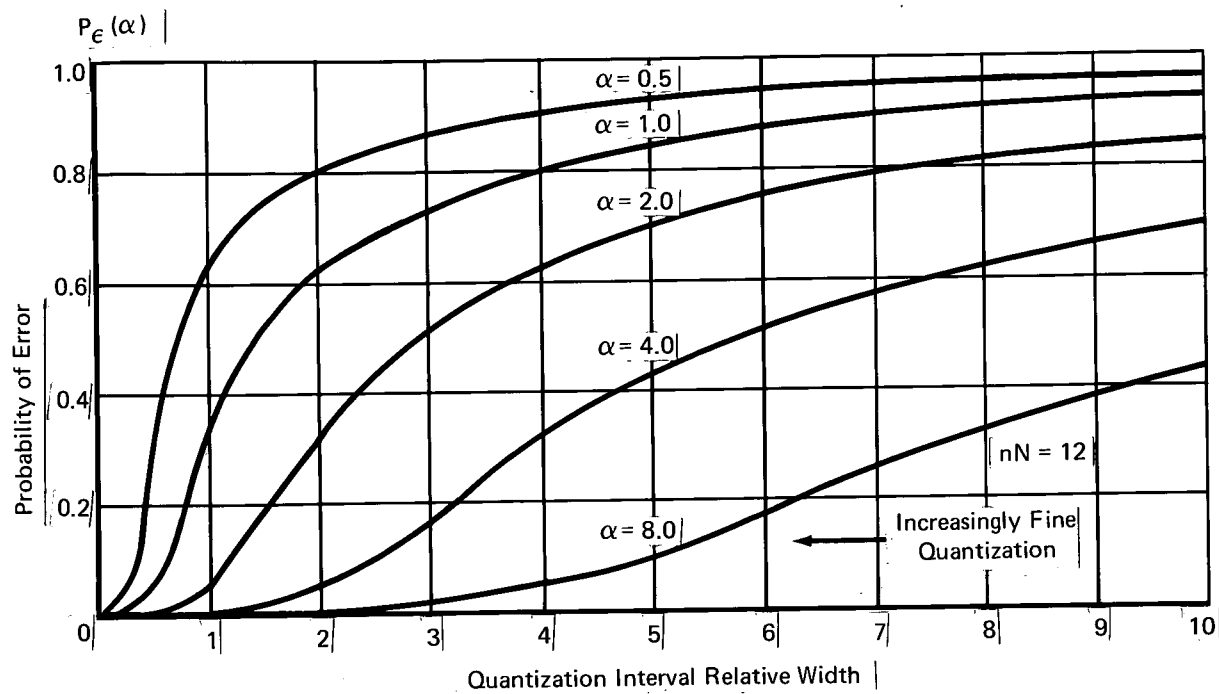


FIGURE 2-8
ERROR PROBABILITY AS A FUNCTION OF QUANTIZATION INTERVAL

GP72-0450-69

2.3.7.4 Computations

In this section, a comparison of computational requirements for the position location techniques is presented. This computational comparison assumes that "brute force" numerical techniques are used as specified in the previous sections. Table 2-2 is a collection of the required computation formulae.

TABLE 2-2
COMPUTATION FORMULAE

Position Location Algorithm	Computation Operations	
	Equivalent Additions	Equivalent Multiplications
1. Optimum	$4\Delta_1^2 \Delta_2^2 + nN \Delta_1 \Delta_2$	$3\Delta_1^2 \Delta_2^2 + nN \Delta_1 \Delta_2$
2. $\nu = 1$	$(2nN - 1) \Delta_1 \Delta_2$	
3. $\nu = 2$	$(2nN - 1) \Delta_1 \Delta_2$	$nN \Delta_1 \Delta_2$
4. Maximum Likelihood	$(nN + 1) \Delta_1 \Delta_2$	$(nN + 1) \Delta_1 \Delta_2$
5. C_{xy}	$(2nN - 1) \Delta_1 \Delta_2 + nN - 1$	$(nN + 4) \Delta_1 \Delta_2 + 1$
6. ρ_{xy} (Conventional)	$(4nN - 1) \Delta_1 \Delta_2 + 2nN$	$(2nN + 6) \Delta_1 \Delta_2 + nN + 3$
7. ρ_{xy} (FFT)	$6M^2 \log_2 M + 2M^2$	$3M^2 \log_2 M + \Delta_2^2 + M^2 + 1$
where: $\Delta_1 = m - n + 1$ $\Delta_2 = M - N + 1$		

GP72-0450-71

For a straightforward comparison, the computation "cost" for a multiplication has been set at 3 times that required for an addition. Other assumptions include the use of square reference and data images. The curves of Figure 2-9 demonstrate this comparison as a function of data image size for a reference image $m=M=50$.

It is apparent from these curves that the optimum position location technique requires the largest number of computations and the $\nu=1$ technique requires the least number. $\nu = 2$ and C_{xy} are almost identical.

To compare ρ_{xy} using the FFT with the other algorithms, it is necessary to use a reference image size of a power of 2. Table 2-3 is such a comparison using $m=M=64$ and varying $n=N=8, 16$ and 32 . Because of the zero padding

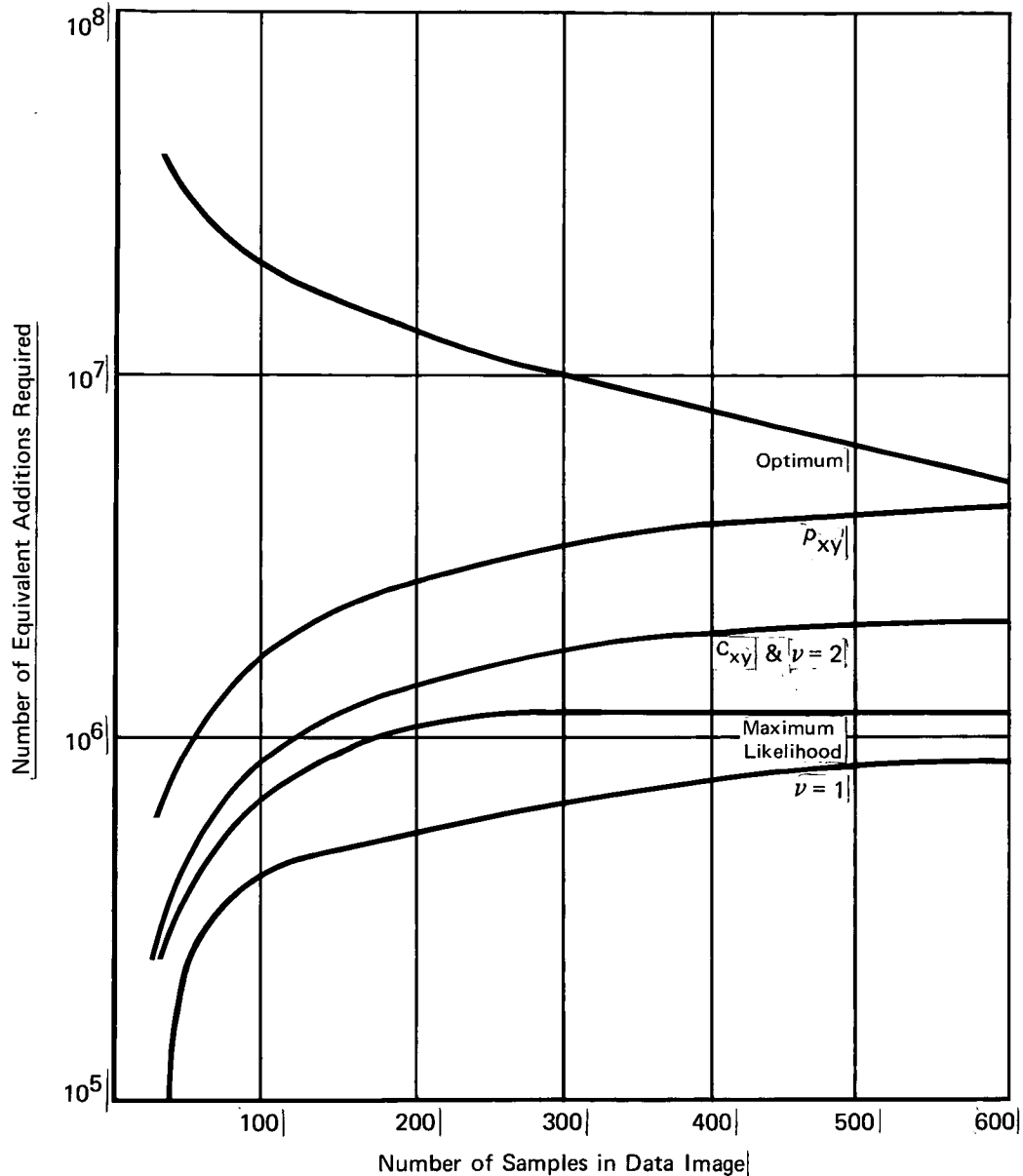


FIGURE 2-9
COMPUTATION COMPARISON
 (Reference Image $m = M - 50$)

requirement for the data image, the number of computations for ρ_{xy} using the FFT is basically due to the size of the reference image and does not vary appreciably with data image size. For large data images (e.g. $n=N=32$), the ρ_{xy} estimator using the FFT is seen to require far less computations than the other position location techniques.

TABLE 2-3
COMPUTATION COMPARISON
(Reference Image $m = M = 64$)

$n = N$	Number of Samples in Data Image	Number of Additional Operations Required						
		Optimum	$\nu = 1$	$\nu = 2$	Maximum Likelihood	ρ_{xy}	ρ_{xy} FFT	C_{xy}
8	64	0.138×10^9	0.413×10^6	0.104×10^7	0.845×10^6	0.213×10^7	0.4×10^6	0.108×10^7
16	256	0.774×10^8	0.123×10^7	0.307×10^7	0.247×10^7	0.619×10^7	0.398×10^6	0.31×10^7
32	1024	0.199×10^8	0.223×10^7	0.557×10^7	0.446×10^7	0.101×10^8	0.394×10^6	0.559×10^7

GP72-0450-73

2.3.7.5 Thresholds

Various thresholds can be employed in certain position location algorithms to reduce computational effort. The adaptive threshold shown in Figure 2-10 could be employed for those position location estimators that look for a minimum value (such as the optimum, $\nu=1$, and $\nu=2$ techniques). An additional requirement is that the estimators should be well behaved functions (e.g., compare the estimators of Figures 2-3, 2-4 and 2-5 with those of Figures 2-6 and 2-7). The adaptive threshold is based on the comparison of each new estimator value against the previously computed minimum value. Computations for a position location estimator would terminate when the threshold is exceeded. For the case where the estimator has a final value which is less than the threshold, the adaptive threshold would assume the minimum computed value. The computational savings achieved by use of the adaptive threshold can only be determined through simulation. The simulations in Section 2-4 and 2-5 used such a threshold and results are reported there.

In addition, variable threshold schemes can be used to reduce computational effort. Reference [9] is an example of this kind of approach. It should be noted however, that the use of a variable threshold has the potential for increasing the probability of error.

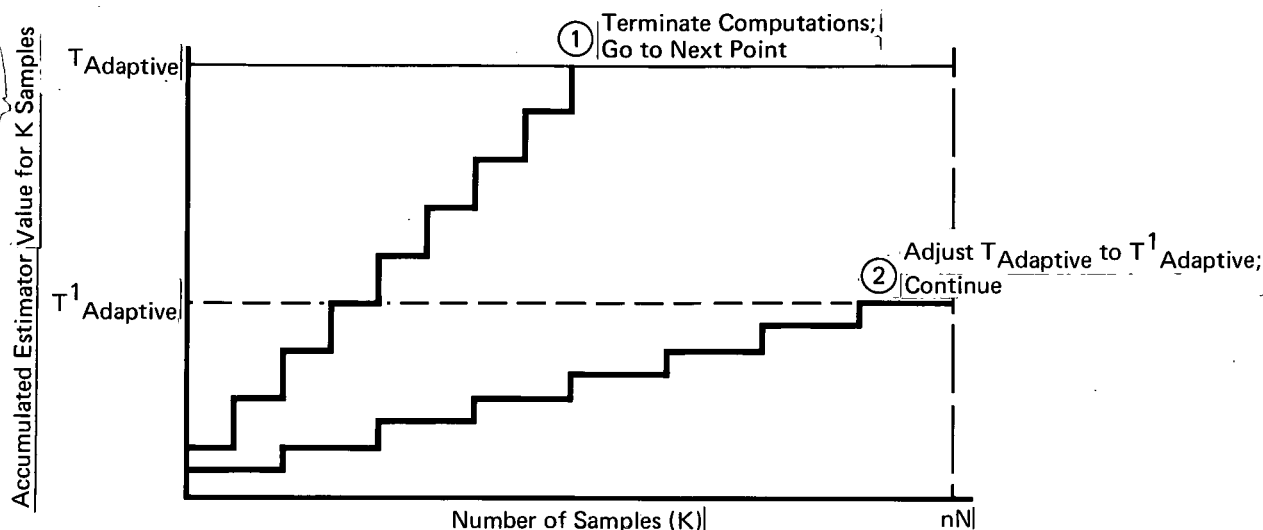


FIGURE 2-10
ILLUSTRATION OF ADAPTIVE THRESHOLD

GP72-0450-75

2.3.7.6 Search Scanning Philosophy

The optimum starting point for any of the position location estimators is the center of the allowable points in S . There are several searching algorithms that can be utilized to speed the searching process. For example a coarse/fine algorithm can be easily implemented for the C_{xy} and ρ_{xy} estimators. Such searching algorithms were not investigated in this study since their use would lead to an increase in the probability of position location error.

2.4 POSITION LOCATION USING GAUSSIAN DIFFERENCE IMAGES

As real difference image statistics did not become available until the latter part of this study, a digital simulation was developed to compare the position location techniques using Gaussian computer generated difference images. Trade offs of data image size and shape were examined as a function of radial error performance and estimator value for difference image noise levels of $\sigma/\Delta = 1, 2.5, 5$, and 10 . Reference image size was selected to be 50×50 and is the center 50×50 subimage of the reference image illustrated in Figure 1-8a.

Both square and circular data images were evaluated. Figure 2-11 illustrates the lattice used for the $d_{i,j}$ images when $n=N=15$ and Δ (diameter)=15.

2.4.1 Development of Computer Program

The flow diagram for the position location simulation is presented in Figure 2-12. This computer program determines position location performance as a function of radial error (in image sample distances) for 64 level and 2 level (hardlimited) quantized images.

The Gaussian P_q distribution was machine generated using the NOISE SUBROUTINE to form difference images having noise levels of $\sigma/\Delta = 1, 2.5, 5, \text{ and } 10$ quantization intervals. Statistically, these ζ images can be compared to real world difference images having variances $\sigma^2 = 1, 6.25, 25, \text{ and } 100$. The data image d is formed by adding the difference image ζ to the reference image S (shown in Figure 1.8a). Subjectively, d resembles the images illustrated in Figure 2-13 for $\sigma/\Delta = 1, 2.5, 5, \text{ and } 10$. To reduce computation requirements, only the center 50×50 image samples were used in this simulation.

It should be noted that, for statistically reliable results using this simulation, a large number of different noise images should be run at each specified σ/Δ level. Such large numbers of simulation runs, however, were beyond the scope of the current effort. For the results presented in the following three sections, only one such machine generated noise image was utilized. These results demonstrate that the computer program is operational and can be used to perform trade off studies for the indicated image registration parameters. In this simulation, the maximim likelihood estimator was not included due to its similarity with the $\nu = 2$ estimator as discussed in Section 2.3.4.

2.4.2 Simulation Results

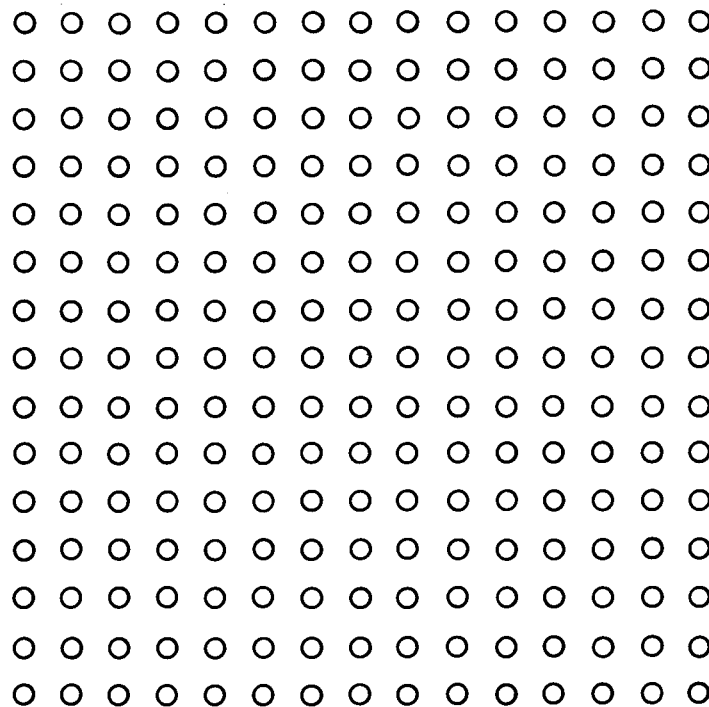
2.4.2.1 Radial Error

Position Location Radial Error is defined as:

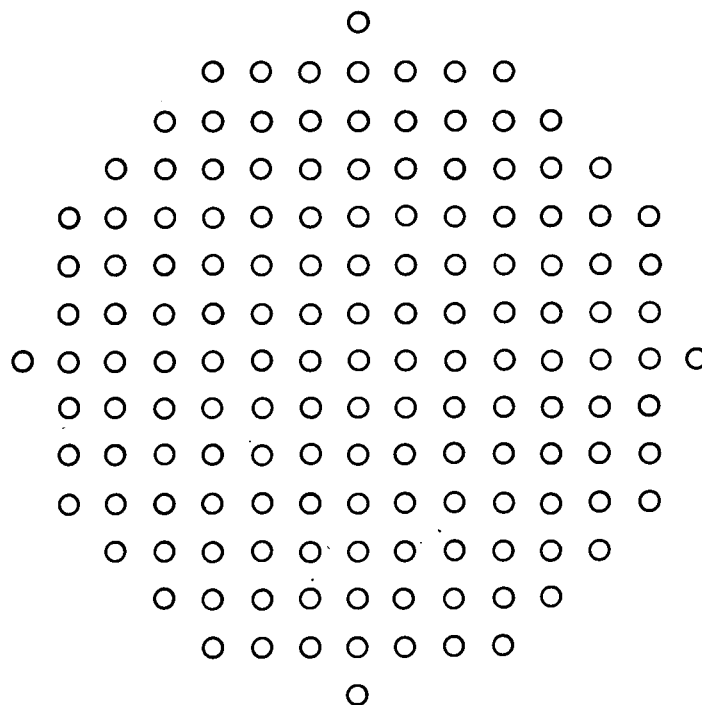
$$\text{Radial Error} = \left[(\ell^\circ - \ell^*)^2 + (L^\circ - L^*)^2 \right]^{1/2} \quad (2-34)$$

(ℓ°, L°) is the alignment point

(ℓ^*, L^*) is the alignment point selected by the estimator



a. Square Lattice ($n = N = 15$)
Total Samples = 225



b. Circular Lattice ($\Lambda = 15$)
Total Samples = 149

FIGURE 2-11.
COMPARISON OF SQUARE AND CIRCULAR DATA IMAGE SHAPE

GP72-0450-42

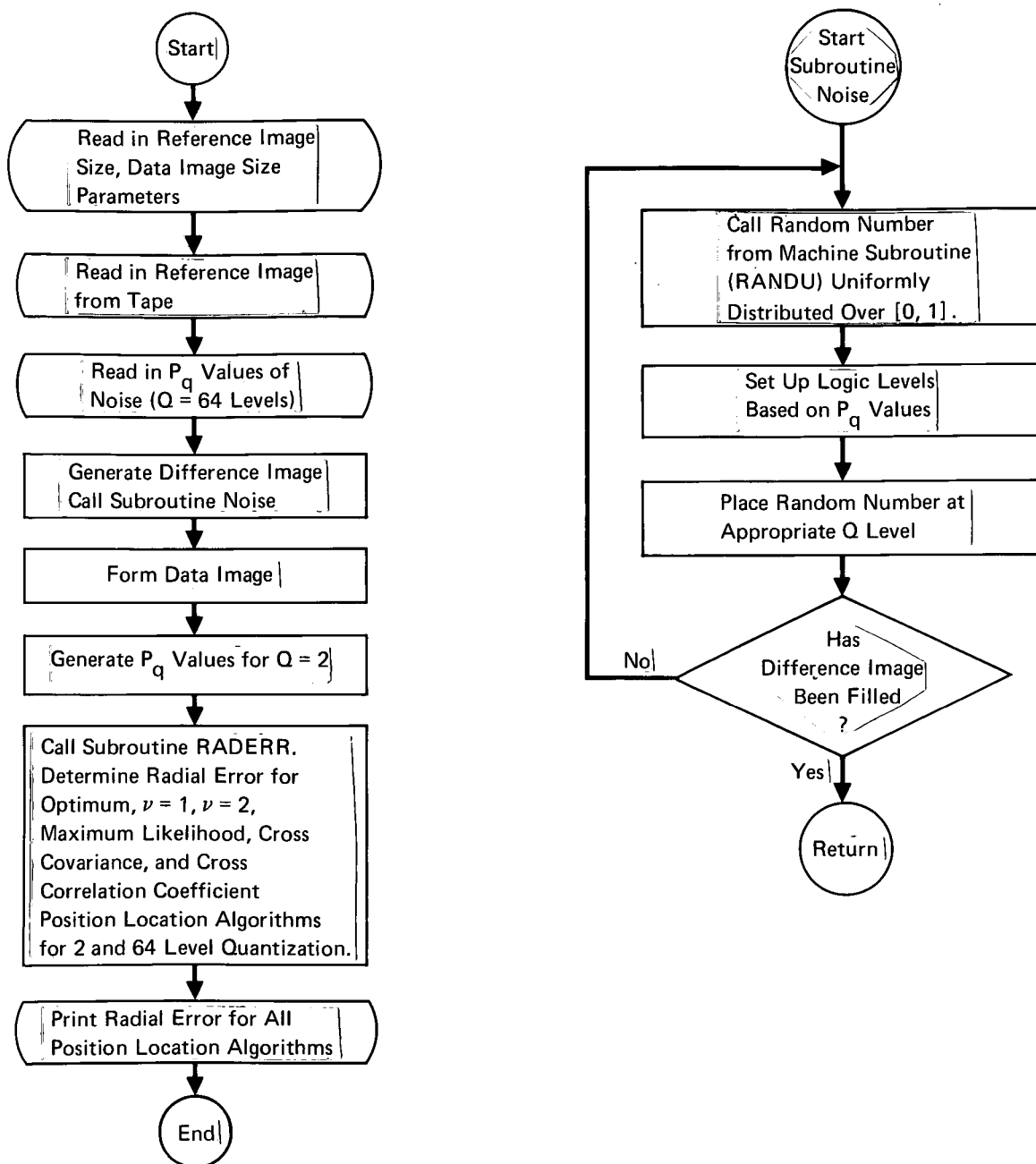


FIGURE 2-12
FLOW DIAGRAM OF POSITION LOCATION DIGITAL SIMULATION
USING GAUSSIAN DIFFERENCE IMAGES

GP72-0450-38

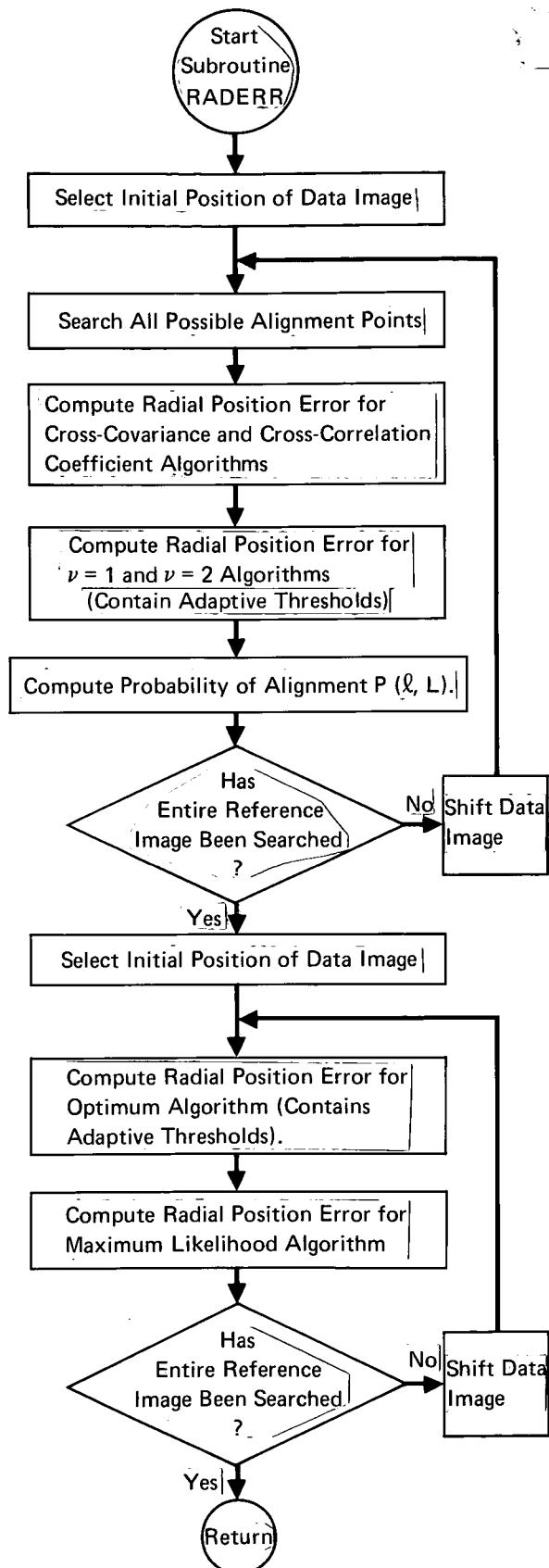


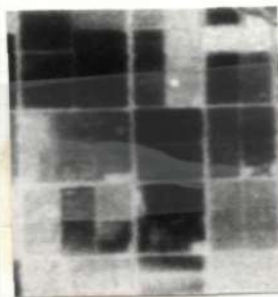
FIGURE 2-12 (Continued)
FLOW DIAGRAM OF POSITION LOCATION DIGITAL SIMULATION
USING GAUSSIAN DIFFERENCE IMAGES

GP72-0450-39

Reproduced from
best available copy.

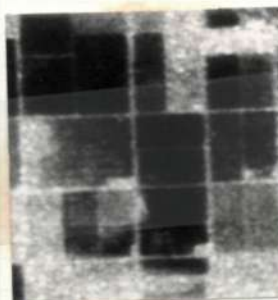


a. $\sigma/\Delta = 1$

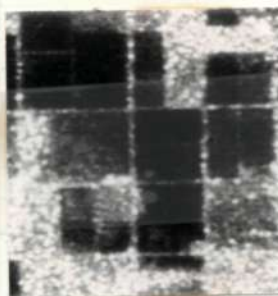


2-28

b. $\sigma/\Delta = 2.5$



c. $\sigma/\Delta = 5$



d. $\sigma/\Delta = 10$



FIGURE 2-13
TYPICAL NOISY DATA IMAGES ($n = N = 128$)

GP72-0450-77

The computer program outlined in Figure 2-12 determines the radial error for the optimum and suboptimum position location algorithms for a specified difference image. Using a single computer generated difference image, data image parameters of size and shape were examined as functions of σ/Δ , where:

$$\frac{\sigma}{\Delta} = \frac{1 \text{ sigma value of } \zeta}{\text{quantization interval}} \quad (2-35)$$

For this simulation, $\Delta = 1$; therefore, σ and σ/Δ were varied from 1, 2.5, 5, and 10.

Radial error simulation results are illustrated in Tables 2-4, 2-5, 2-6, and 2-7. Although it is difficult to draw conclusions from using only a single difference image, a few general observations can be made.

- a) The optimum position location estimator did not always provide the least radial error.
- b) Except for the $\sigma/\Delta = 1$ case, radial error did not seem to be a function of σ/Δ .
- c) The C_{xy} position location algorithm is the suboptimum technique most likely to provide registration error.
- d) In many cases, 2-level quantization provided similar radial error performance to 64-level quantization (but not all cases! e.g., see $\sigma/\Delta = 10$).
- e) A data image size of less than 150 samples appears to be adequate for image registration.

These comments apply to the Gaussian difference image simulation only.

2.4.2.2. Estimator Values

The estimator values at alignment are given in Tables 2-8, 2-9, 2-10, and 2-11. This information is of value in establishing typical thresholds for determining image registration versus no registration. For those cases in the tables where 0 radial error resulted, the following observations can be made:

- a) An estimator value of less than .5 appears to provide image registration with 0 radial error for the optimum algorithm. Probably an estimator value of less than .1 would be a better choice.

TABLE 2-4
RADIAL ERROR COMPARISON FOR $\sigma/\Delta = 1$

POSITION LOCATION ALGORITHM	SQUARE DATA IMAGE				CIRCULAR DATA IMAGE			
	n = N	Data Image Size	RADIAL ERROR (In Sample Distances)		Δ Diameter	Data Image Size	RADIAL ERROR (In Sample Distances)	
			64 Level	2 Level			64 Level	2 Level
$r^2(l, L)$	5	25	0	0	5	13	2.24	17.26
$v = 1$		25	0	0		13	2.24	22.09
$v = 2$		25	0	0		13	2.24	22.09
C_{xy}		25	0	0		13	2.24	22.09
ρ_{xy}		25	11.7	22		13	18.44	0
		25	0	7		13	14.14	7
$r^2(l, L)$	15	225	0	0	15	149	0	0
$v = 1$		225	0	0		149	0	0
$v = 2$		225	0	0		149	0	0
C_{xy}		225	0	0		149	0	0
ρ_{xy}		225	0	13		194	11.05	0
		225	0	13		149	0	17
$r^2(l, L)$	25	625	0	0	25	441	0	0
$v = 1$		625	0	0		441	0	0
$v = 2$		625	0	0		441	0	0
C_{xy}		625	0	0		441	0	0
ρ_{xy}		625	0	0		441	0	0
		625	0	0		441	0	11

TABLE 2-5
RADIAL ERROR COMPARISON FOR $\sigma/\Delta = 2.5$

POSITION LOCATION ALGORITHM	SQUARE DATA IMAGE				CIRCULAR DATA IMAGE			
	n = N	Data Image Size	RADIAL ERROR (In Sample Distances)		Λ Diameter	Data Image Size	RADIAL ERROR (In Sample Distances)	
			64 Level	2 Level			64 Level	2 Level
$r^2(\ell, L)$ $v = 1$ $v = 2$ C_{xy} ρ_{xy}	5	25	19.24	18.44	5	13	18.75	7.07
		25	19.42	19.24		13	19.24	19.24
		25	19.24	19.24		13	19.24	19.24
		25	19.24	19.42		13	19.24	19.24
		25	15.81	19.42		13	15.3	0
		25	19.24	7		13	11.05	2
$r^2(\ell, L)$ $v = 1$ $v = 2$ C_{xy} ρ_{xy}	15	225	0	0	15	149	0	0
		225	0	0		149	0	0
		225	0	0		149	0	0
		225	0	0		149	0	0
		225	0	13		149	17	0
		225	0	13		149	0	9
$r^2(\ell, L)$ $v = 1$ $v = 2$ C_{xy} ρ_{xy}	25	625	0	0	25	441	0	0
		625	00	0		441	0	0
		625	0	0		441	0	0
		625	0	0		441	0	0
		625	0	0		441	0	0
		625	0	0		441	0	12

TABLE 2-6
RADIAL ERROR COMPARISON FOR $\sigma/\Delta = 5$

POSITION LOCATION ALGORITHM	SQUARE DATA IMAGE				CIRCULAR DATA IMAGE			
	n = N	Data Image Size	RADIAL ERROR (In Sample Distances)		Λ Diameter	Data Image Size	RADIAL ERROR (In Sample Distances)	
			64 Level	2 Level			64 Level	2 Level
$r^2(\ell, L)$	5	25	15.30	5.39	5	13	11.66	4.47
$v = 1$		25	14.14	0		13	22.36	25.46
$v = 2$		25	21.1	0		13	18.68	25.46
C_{xy}		25	21.1	16.03		13	18.68	27.66
ρ_{xy}		25	11.7	14.87		13	22.47	0
ρ_{xy}		25	7.28	7		13	20.22	9
$r^2(\ell, L)$	15	225	0	0	15	149	0	0
$v = 1$		225	0	0		149	0	0
$v = 2$		225	0	0		149	0	0
C_{xy}		225	0	0		149	0	0
ρ_{xy}		225	17.03	13.15		149	10.05	0
ρ_{xy}		225	0	13		149	0	5
$r^2(\ell, L)$	25	625	0	0	25	441	0	0
$v = 1$		625	0	0		441	0	0
$v = 2$		625	0	0		441	0	0
C_{xy}		625	0	0		441	0	0
ρ_{xy}		625	0	0		441	0	0
ρ_{xy}		625	0	0		441	0	0

TABLE 2-7
RADIAL ERROR COMPARISON FOR $\sigma/\Delta = 10$

POSITION LOCATION ALGORITHM	SQUARE DATA IMAGE				CIRCULAR DATA IMAGE			
	n = N	Data Image Size	RADIAL ERROR (In Sample Distances)		Λ Diameter	Data Image Size	RADIAL ERROR (In Sample Distances)	
			64 Level	2 Level			64 Level	2 Level
$r^2(\ell, L)$	5	25	12	11	5	13	13.34	6.0
$v = 1$		25	12.4	29.7		13	24.04	24.04
$v = 2$		25	13.3	29.7		13	13.34	24.04
C_{xy}		25	13.3	15.26		13	13.34	24.04
ρ_{xy}		25	23.02	28.6		13	23.77	0
		25	17.12	7		13	18.11	7
$r^2(\ell, L)$	15	225	0	1.41	15	149	0	12.17
$v = 1$		225	0	4.12		149	0	12.17
$v = 2$		225	0	4.12		149	0	12.17
C_{xy}		225	0	1.41		149	0	12.17
ρ_{xy}		225	17	13.04		149	0	0
		225	0	0		149	0	2
$r^2(\ell, L)$	25	625	0	1	25	441	0	1
$v = 1$		625	0	0		441	0	1
$v = 2$		625	0	0		441	0	1
C_{xy}		625	0	1		441	0	1
ρ_{xy}		625	0	0		441	0	0
		625	0	0		441	0	9

TABLE 2-8
COMPARISON OF ESTIMATOR VALUES FOR $\sigma/\Delta = 1$

POSITION LOCATION ALGORITHM	SQUARE DATA IMAGE				CIRCULAR DATA IMAGE			
	n = N	Data Image Size	ESTIMATOR VALUES		Λ Diameter	Data Image Size	ESTIMATOR VALUES	
			64 Level	2 Level			64 Level	2 Level
$r^2(\ell, L)$	5	25	$.22 \times 10^{-14}$.03	5	13	.61	144
$v = 1$		25	29	1		13	18	0
$v = 2$		25	61	1		13	44	0
C_{xy}		25	1	.999		13	.939	.717
ρ_{xy}		25	571	6.2		13	244	6
		25	.78	.14		13	.792	.926
$r^2(\ell, L)$	15	225	0	$.73 \times 10^{-16}$	15	149	0	$.53 \times 10^{-12}$
$v = 1$		225	221	11		149	142	7
$v = 2$		225	371	11		149	228	7
C_{xy}		225	1	1		149	1	1
ρ_{xy}		225	31000	46		149	15600	99
		225	.994	.627		149	.992	.147
$r^2(\ell, L)$	25	625	0	0	25	441	0	$.11 \times 10^{-43}$
$v = 1$		625	630	17		441	439	13
$v = 2$		625	1130	17		441	777	13
C_{xy}		625	1	1		441	1	1
ρ_{xy}		625	97200	145		441	55300	203
		626	.994	.976		441	.993	.116

TABLE 2-9
COMPARISON OF ESTIMATOR VALUES FOR $\sigma/\Delta = 2.5$

POSITION LOCATION ALGORITHM	SQUARE DATA IMAGE				CIRCULAR DATA IMAGE			
	n = N	Data Image Size	ESTIMATOR VALUES		Λ Diameter	Data Image Size	ESTIMATOR VALUES	
			64 Level	2 Level			64 Level	2 Level
$r^2(l, L)$	5	25	1.54	18	5	13	17.2	275
$v = 1$		25	58	3		13	32	1
$v = 2$		25	234	3		13	116	1
C_{xy}		25	.685	.835		13	.91	.014
ρ_{xy}		25	686	4.8		13	314	3
		25	.707	.109		13	.819	.79
$r^2(l, L)$	15	225	0	.002	15	149	0	.0028
$v = 1$		225	551	27		149	348	19
$v = 2$		225	2180	27		149	1300	19
C_{xy}		225	1	.999		149	1	.999
ρ_{xy}		225	31100	43		149	15500	91
		225	.967	.569		149	.958	.139
$r^2(l, L)$	25	625	0	$.195 \times 10^{-38}$	25	441	0	$.31 \times 10^{-31}$
$v = 1$		625	1620	49		441	1130	38
$v = 2$		625	6860	49		441	4710	38
C_{xy}		625	1	1		441	1	1
ρ_{xy}		625	97400	129		441	54600	189
		625	.967	.547		441	.959	.114

TABLE 2-10
COMPARISON OF ESTIMATOR VALUES FOR $\sigma/\Delta = 5$

POSITION LOCATION ALGORITHM	SQUARE DATA IMAGE				CIRCULAR DATA IMAGE			
	n = N	Data Image Size	ESTIMATOR VALUES		Λ Diameter	Data Image Size	ESTIMATOR VALUES	
			64 Level	2 Level			64 Level	2 Level
$r^2(\ell, L)$	5	25	98	169	5	13	165	351
$v = 1$		25	124	6		13	52	2
$v = 2$		25	971	6		13	319	2
C_{xy}		25	.216	.22		13	.0964	.0121
ρ_{xy}		25	1800	4.68		13	671	3
		25	.713	.14		13	.8128	.1080
$r^2(\ell, L)$	15	225	$.36 \times 10^{-22}$	$.8 \times 10^{-5}$	15	149	$.3647 \times 10^{-18}$	5.123
$v = 1$		225	1160	33		149	766	30
$v = 2$		225	9100	33		149	5942	30
C_{xy}		225	1	.999		149	1	.9609
ρ_{xy}		225	31100	38.3		149	15505	80
		225	.878	.509		149	.84	.11845
$r^2(\ell, L)$	25	625	0	$.13 \times 10^{-25}$	25	441	$.596 \times 10^{-45}$	$.23 \times 10^{-17}$
$v = 1$		625	3290	87		441	2305	69
$v = 2$		625	26800	87		441	18211	69
C_{xy}		625	1	1		441	1	1
ρ_{xy}		625	98100	111		441	56563	171
		625	.888	.44		441	.87128	.4458

TABLE 2-11
COMPARISON OF ESTIMATOR VALUES FOR $\sigma/\Delta = 10$

POSITION LOCATION ALGORITHM	SQUARE DATA IMAGE				CIRCULAR DATA IMAGE			
	n = N	Data Image Size	ESTIMATOR VALUES		Λ Diameter	Data Image Size	ESTIMATOR VALUES	
			64 Level	2 Level			64 Level	2 Level
$r^2(\ell, L)$	5	25	80.7	208	5	13	176.5	313
$v = 1$		25	201	8		13	103	2
$v = 2$		25	2470	8		13	154	2
C_{xy}		25	.075	.00313		13	.02446	.006158
ρ_{xy}		25	1310	3.6		13	867	3
		25	.547	.11		13	.696	.926
$r^2(\ell, L)$	15	225	.0235	1.519	15	149	.02855	.09654
$v = 1$		225	2130	57		149	1395	41
$v = 2$		225	31500	57		149	19725	41
C_{xy}		225	.994	.88900		149	.9926	.9786
ρ_{xy}		225	30100	32.15		149	15097	60
		225	.687	.284		149	.6133	.1020
$r^2(\ell, L)$	25	625	$.73 \times 10^{-16}$.153	25	441	181	$.49 \times 10^{-1}$
$v = 1$		625	6150	165		441	4281	118
$v = 2$		625	95600	165		441	65981	118
C_{xy}		625	1	.85		441	1	.99972
ρ_{xy}		625	101,000	74.3		441	56297	142
		625	.726	.317		441	.68	.105

- b) There does not seem to be a well-defined image registration reject threshold for the $v = 1$ and $v = 2$ algorithms.
- c) An estimator value of greater than 31,000 appears to provide image registration with 0 radial error for the cross-covariance algorithm.
- d) A well-defined image registration reject threshold was not demonstrated for the cross-correlation coefficient algorithm. Further runs would probably indicate an estimator value in the .8 to .9 range.

Several additional simulation runs are needed to develop statistically reliable results.

2.4.2.3 Computational Savings

Adaptive thresholds were implemented in the simulation for the optimum, $v = 1$, and $v = 2$ position location estimators. These thresholds reduce the number of computations required for alignment without increasing the probability of error. Using results from the simulation for the single difference image, averaged computational savings were determined based on the numerical techniques discussed in Section 2.3.7.4. On the average, the optimum position location algorithm required only 23% ($Q = 64$) and 26% ($Q = 2$) of the equivalent addition computations indicated in Figure 2-10 and Table 2-3. The $v = 1$ algorithm required 31% (for $Q = 64$ and $Q = 2$), and the $v = 2$ algorithm required 19% ($Q = 64$) and 31% ($Q = 2$). It should be noted (from Table 2-3) that use of the adaptive threshold makes the $v = 1$ position location estimator competitive with the ρ_{xy} (FFT) estimator on a computational basis.

2.5 POSITION LOCATION USING MULTISPECTRAL IMAGE STATISTICS

This section examines estimator position location performance using difference image statistics taken from real multispectral imagery. These statistics (illustrated in Section 1.5) became available for use late in the study.

2.5.1 Development of Computer Program

The position location digital simulation of Section 2.4 can be used to accept statistics from real difference images. The difference image histograms determined in Section 1.5.2 for the selected multispectral imagery can be

entered directly into the computer program of Figure 2-13. It should be emphasized that, for statistically reliable results, several noise images should be generated for each P_q distribution. Limitations of scope and time, however, allowed only one such noise image to be generated for the simulation results reported in the next several sections.

2.5.2 Simulation Results

As in Section 2.4, trade offs of algorithm performance as a function of data image size and shape were accomplished. In addition, one run was made to determine algorithm radial error as a function of terrain category, image spectrum, and image resolution.

2.5.2.1 Radial Error As Function of Data Image Size and Shape

Circular and square data images were evaluated using the P_q histogram illustrated in Figure 1-26d. The variance of this difference image (Figure 1-26c) is 63.1 and is approximately comparable to the Gaussian $\sigma/\Delta = 10$ noise simulation. The reference image was taken to be the center 50 x 50 samples of Figure 1-26a. A comparison of radial error performance for the various position location algorithms is given in Tables 2-12 and 2-13.

Again, it is difficult to draw any substantive conclusions from the use of only one noise image. The radial errors recorded for the estimators are not unreasonable if the difference image is considered to be "worst case". It can be seen from examination of the difference image variances (Figures 1-26c through 1-41c), that this indeed is the situation. Comparison can be made between these results and the $\sigma/\Delta = 10$ Gaussian noise simulation of Section 2.4.1 (Table 2-7). Again, the optimum position location estimator did not always provide the least amount of registration error. In general (but not always), the radial error was greater for $Q = 2$ quantization than for $Q = 64$ for all algorithms except C_{xy} . For C_{xy} , radial error became less than that for $Q = 64$ with increasing data image size.

2.5.2.2 Radial Error As Function of Image Spectrum

One run of the simulation was made to compare radial error performance as a function of image spectrum. Farmland terrain was assumed together with a square $N = n = 7$ data image. These results are given in Table 2-14.

TABLE 2-12
RADIAL ERROR COMPARISON FOR SQUARE DATA IMAGE

DATA IMAGE SIZE	RADIAL POSITION LOCATION ERROR					
	Optimum	$v = 1$	$v = 2$	Max Likelihood	ρ_{xy}	C_{xy}
	Quantization = 64 Levels					
16	2.24	10.05	0	10.2	17	9.06
36	19.1	11	12	3.16	14.04	10
49	8.06	0	0	10	25	14.87
64	2.83	0	1.41	8	18.44	14.21
81	23.71	1	1	10.44	1	17.49
100	2.24	1	1	1	0	17.12
225	0	2	0	0	0	13.89
Quantization = 2 Levels						
16	1	19.24	19.24	19.24	19	17.72
36	0	20.59	20.59	0	13	29.07
49	9.9	14.21	14.21	24.17	8	14.14
64	10.05	14.14	14.14	11.18	16	12.73
81	0	17.49	17.49	0	13	11.4
100	13.89	15.03	15.03	22.63	18	11.4
225	7	13.15	13.15	7	8	13.04

TABLE 2-13
RADIAL ERROR COMPARISON FOR CIRCULAR DATA IMAGE

DATA IMAGE SIZE	RADIAL POSITION LOCATION ERROR					
	Optimum	$v = 1$	$v = 2$	Max Likelihood	ρ_{xy}	C_{xy}
	Quantization = 64 Levels					
13	4.12	14.04	14.04	13.04	11.05	14.21
29	5.1	3.61	3.61	10.44	18.44	15.56
49	1.41	1	1	10.44	16.55	15.56
81	4.	13.04	13.04	21.4	10.44	21.10
149	25.46	2.0	14.	15.03	0	13.04
253	19.85	0	0	19.85	0	14.76
	Quantization = 2 Levels					
13	5.1	14.04	14.04	14.04	11.	14.04
29	8.49	3.61	3.61	3.	11.	21.47
49	6.71	15.56	15.56	17.	17.	0
81	8.94	16.28	16.28	1.41	4.	13.45
149	9.85	13.6	13.6	8.54	10.	12.21
253	19.85	0	0	19.85	16.	0

TABLE 2-14
RADIAL ERROR COMPARISON AS FUNCTION OF IMAGE SPECTRUM

Image Spectrum	RADIAL POSITION LOCATION ERROR					
	Optimum	$v = 1$	$v = 2$	Max. Likelihood	ρ_{xy}	C_{xy}
Quantization = 64 Levels						
Red	8.06	0	0	10	25	14.87
Green	7.28	14.14	3.61	15.03	29	28.43
IR	5	24.19	24.19	24.19	24.19	14.21
Quantization = 2 Levels						
Red	9.9	14.21	14.21	24.17	8	14.14
Green	1.41	23.09	23.09	18	21	10.20
IR	8.6	20.81	20.81	8.49	17	20.59

P_q histograms from Figures 1-26d, 1-27d, and 1-28d were used. It should be noted (from Figures 1-26c, 1-27c, and 1-28c) that the variance of the difference images are 63.1 for the Red spectrum, 17.1 for the Green spectrum, and 40.3 for the IR spectrum.

2.5.2.3 Radial Error As Function of Terrain Type

One run of the simulation was made to compare radial error performance as a function of image terrain type. The Red spectrum was selected for registration together with a square $n = N = 7$ data image. These results are presented in Table 2-15. P_q histograms from Figures 1-26d, 1-29d, 1-32d, and 1-35d were used. The variances for these difference images are 63.1 for the Farmland terrain, 6.07 for the Urban terrain, 4.15 for the Mountain terrain, and 52.2 for the Forest terrain.

2.5.2.4 Radial Error as Function of Image Resolution

One run of the simulation was made to compare radial error performance as a function of image resolution. Again Farmland terrain was assumed together with a square $n = N = 7$ data image. The digital simulation, up to this point,

TABLE 2-15
RADIAL ERROR COMPARISON AS FUNCTION OF TERRAIN TYPE

Terrain Type	Radial Position Location Error					
	Optimum	$\nu = 1$	$\nu = 2$	Maximum Likelihood	ρ_{xy}	C_{xy}
	Quantization = 64 Levels					
Farmland	8.06	0	0	10	25	14.87
Urban	26.25	27.66	27.66	26.25	0	0
Mountain	26.25	0	0	26.25	0	16.28
Forest	1	17.03	8.06	8.06	8.06	17
	Quantization = 2 Levels					
	Optimum	$\nu = 1$	$\nu = 2$	Maximum Likelihood	ρ_{xy}	C_{xy}
	Quantization = 2 Levels					
Farmland	9.9	14.21	14.21	24.17	8	14.14
Urban	1	29.70	29.70	31.11	0	0
Mountain	12.04	18.97	18.97	18.97	0	20.52
Forest	5	19.34	19.42	14.42	1	19.42

had used only 50 meter resolution image data. The 10 meter image data of Figure 1-38 is compared with the 50 meter image data of Figure 1-26 in Table 2-16. The variances for the difference images are 63.1 for the 50 meter resolution, and 57.6 for the 10 meter resolution image data.

TABLE 2-16
RADIAL ERROR COMPARISON AS FUNCTION OF IMAGE RESOLUTION

Image Resolution (Meters)	Radial Position Location Error					
	Optimum	$\nu = 1$	$\nu = 2$	Maximum Likelihood	ρ_{xy}	C_{xy}
	Quantization = 64 Levels					
50	8.09	0	0	10	25	14.87
10	12.81	23.6	11	11	11	20.59
	Quantization = 2 Levels					
	Optimum	$\nu = 1$	$\nu = 2$	Maximum Likelihood	ρ_{xy}	C_{xy}
	Quantization = 2 Levels					
50	9.9	14.21	14.21	24.17	8	14.14
10	5	23.60	23.60	9.22	13	23.02

2.6 CONCLUSIONS

This study has derived a suitably defined optimum (on the basis of minimum squared radial error estimation) image registration algorithm. It has developed and provided the computational means for the quantitative comparison of the optimum and five suboptimum image registration techniques using both machine generated and real multispectral difference image statistics. Computational requirements for the six image registration algorithms were determined and illustrated. Radial error performance of the algorithms was determined and illustrated using one run of machine generated and one run of real multispectral difference image statistics. Parametric trade offs of image quantization, and data image size and shape were demonstrated.

On the basis of two statistical runs however, it is impossible to make major conclusions. Some general comments that can be made are:

- a) The optimum image registration algorithm appears to be a valid means for comparing the performance of suboptimum techniques. Further refinements can be made to improve its performance.
- b) On a computational basis, the $v=1$ (using adaptive thresholding) and the ρ_{xy} (using FFT techniques) image registration estimators are the most attractive suboptimum techniques for small data image sizes (less than $n=N=16$). For large data image sizes, the ρ_{xy} (using FFT techniques) has computational advantages.
- c) In general, the radial error performance of the most widely used image registration estimator, ρ_{xy} , was not as good as that obtained with the $v=1$ and $v=2$ estimators.
- d) In general, image registration using hard limited (2 level) images provided greater radial error than that achieved using 64 level imagery.
- e) To determine the best parameters for data image size and shape or to determine which spectrum, terrain type, or image resolution is best for multispectral image registration will require a large number of runs to establish reliable statistical averages.

2.7 AREAS FOR FURTHER STUDY

This initial study of digital image correlation techniques has suggested several interesting areas for further investigation. For example, there are two constraints on the optimum position location estimator which should be relaxed to make it more applicable to real world image registration problems. These are: 1) the assumption that the difference image samples are statistically independent, and 2) the assumption of a uniform a priori probability of alignment. The removal of these constraints should be examined and their computational cost and effect on position location performance determined. This can be accomplished by extending the present optimum position location technique formulation.

In addition, new position location techniques have been developed which have potential for becoming the "best" suboptimum technique. These recently developed techniques should be examined and included in the simulation for comparisons of computational efficiency and radial error performance.

Finally, the most obvious area for further work is to perform a sufficient number of simulation runs to provide statistically reliable results. Image registration parameters such as data image size, shape, and quantization should be optimized for computational efficiency. Simulation results should then be obtained to determine radial error performance as functions of position location technique, multispectral image spectrum, terrain category, and image resolution. Fast search algorithms should be examined to determine their effectiveness at reducing computational cost.

SECTION 3

IMAGE SAMPLING STUDY

3.1 INTRODUCTION

Previous studies have developed theories for image sampling and image reconstruction (References 10 and 11). Little has been provided to date, however, which presents a quantitative comparison of techniques or which relates to actual image statistics. The purpose of this study is to provide a quantitative evaluation of several image sampling strategies and methods of image reconstruction.

Two sample densities are considered in this study: (1) One sample for each 58.06 square meters (625 square feet), and (2) One sample for each 3,716 square meters (40,000 square feet). These densities bound the range of sampling densities encountered in practice. Image statistics based upon actual aerial imagery are utilized. These statistics were obtained in Section 1.4. Parametric studies based upon an average mean squared error of reconstruction are presented which show the effect of varying sample densities, terrain types, aperture sizes and shapes, and sample lattices. Also included is a measure of the errors introduced by presample filtering and image recording device characteristics.

This study is confined to the accuracy of reconstruction for an image based on samples obtained through a sensing device which has an undistorted view of a scene. No image distortion correction is involved nor any time dependency considered. For purposes of the analysis, an infinite scene having specified spatial statistical properties is considered.

3.2 IMAGE SAMPLING AND RECONSTRUCTION PARAMETERS

Relevant parameters relating to image sampling and reconstruction are discussed in the following sections.

3.2.1 Sampling Lattice

The sampling lattice is defined as the set of points (denoted by A) in the spatial domain (image plane denoted by X) which defines the centers of the

instantaneous fields of view of a sensor at the instant a particular sample is observed. Each of these points has a sample value of image intensity. This collection of samples is the data from which the image is to be reconstructed. Sample lattices in this study are usually sets of discrete points in two dimensions. They can form a square lattice, a rectangular lattice, or a rhombic lattice. These are defined in Figure 3-1, a, b, and c respectively. The spatial coordinates are (x_1, x_2) denoted by \underline{x} . The names of the lattices refer to the shapes of a basic cell in the lattice. Even more general sampling strategies are possible as candidates but usually the strategy is determined by the shape of the sensor instantaneous field of view (IFOV) and these generally lead to the lattices mentioned above.

Since continuously scanned images (video) are also of interest, we can include this possibility in the category of a sample lattice which is infinitely dense in the scan (x_1) direction so that the set A in this case is a family of parallel lines.

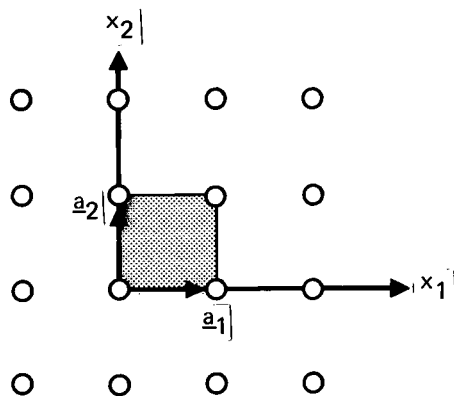
In connection with the sample lattice, there is another point set, B. This is a point set in the spatial frequency plane (Ω) which is "dual" to the set A in the sense that if $(\underline{a}_1, \underline{a}_2)$ are the basis vectors (see Figure 3-1) for set A, then vectors $(\underline{b}_1, \underline{b}_2)$ in Ω satisfying

$$\underline{a}_i \cdot \underline{b}_j = 2\pi \delta_{i,j} \quad (3-1)$$

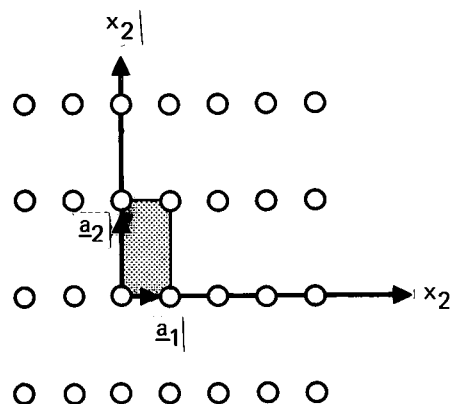
determine a set B in Ω . This is the two dimensional set of folding frequencies introduced by the sampling procedure and is more fully explained in Reference 10 and in Appendix A of this report.

3.2.2 Sampling Aperture

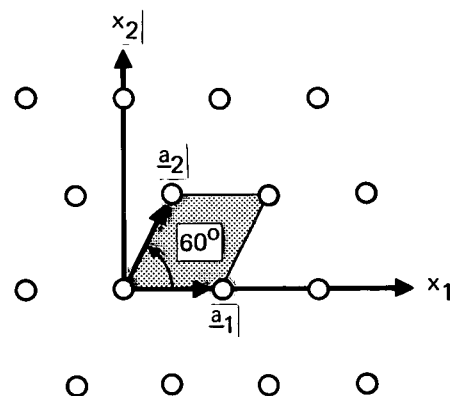
In general, a sensor will not be able to determine the image intensity at a single point, but will give some average value of intensities in the neighborhood of the point. This can be described by convolving the image with a weighting function $\gamma(x)$ corresponding to the sensor IFOV. For example, if the aperture is a uniform disk (that is, the sensing device senses every point in a circle with equal intensity and nothing outside the circle), then the aperture function is as shown in Figure 3-2. Usually the volume under the surface



a. Square Lattice



b. Rectangular Lattice



c. Rhombic Lattice

FIGURE 3-1
IMAGE SAMPLING LATTICES

GP72-0450-3

defined by this function is taken as unity.

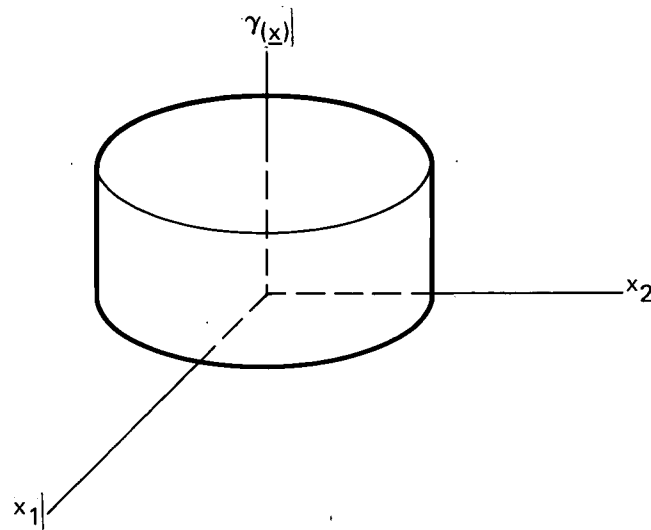


FIGURE 3-2
CIRCULAR APERTURE WEIGHTING FUNCTION

Other apertures of interest include square, rectangular, hexagonal and gaussian. The weighting functions for these are given in Appendix B, together with their two dimensional Fourier transforms, which will be of interest in the subsequent analysis.

The size and shape of the aperture selected for best performance may depend on the sample lattice used, since too much overlap will smear the reconstructed image, and too small an aperture will omit information present in the image.

3.2.3 Presampling Filtering

Electronic or optical filtering can be performed on the signal representing the image before it is digitized and transmitted over the communication channel. In this study the effect of real time filtering of a video image is investigated. This is represented as a first order lag on the order of a fraction of a sample interval.

3.2.4 Interpolation

Image reconstruction by means of interpolation between sample values is studied by comparing three different interpolation methods. The simplest of

these and indeed the simplest of any interpolation scheme is one-point or step interpolation in which the reconstructed image at any point depends only on one sample value. Actually the reconstructed value is the value of the sample which is nearest in some sense. This is discussed in more explicit detail in Appendix C, as is the following method.

An intermediate reconstruction method is a four point scheme which performs an interpolation on a sample cell determined by four surrounding points. This interpolation is a two dimensional generalization of common linear interpolation of one dimension.

Also an interpolation is studied which is optimal in a least square error sense. This method for image reconstruction is theoretically the best that can be achieved with a particular aperture and sample lattice. This least squares estimate is best described as a two dimensional Wiener filter with no noise and no causality constraint and which depends on sampling aperture, sampling lattice and image statistics. It is derived in Appendix E.

3.2.5 Recording Device Characteristics

The output of the sampling and reconstruction procedure is not usually the (piecewise) continuous function determined by the interpolation method, but rather, a superposition of spots arrayed in a recording lattice. The shape of the spots depends on the recording device while their magnitude depends on the interpolated value at the spot center. The degradation in image reconstruction introduced is examined in this study for two recording spot characteristics, a gaussian and a rectangular spot. The printing lattice is considered to be a refinement of the sampling lattice for analytical tractability in the study (that is, the sample lattice is a sublattice of the recording lattice).

3.3 METHOD OF ANALYSIS

3.3.1 Error Criterion

The frequency or wave number space formulation of Peterson and Middleton (Reference 10), which has been specialized to two dimensions, forms the basis for most of the analysis in this study. The band limited condition has been

eliminated since the actual scene power spectral densities to which this study is directed do not exhibit this characteristic. An expression for the averaged mean square error of image reconstruction has been derived in Appendix A and is as follows (Equation A-31).

$$E\{[f(\underline{x}) - \hat{f}(\underline{x})]^2\} = \frac{1}{(2\pi)^2} \int_{\Omega} \Phi(\underline{\omega}) \left[1 - \frac{2}{Q} \Gamma(-\underline{\omega}) G(\underline{\omega}) + \frac{1}{Q^2} \Gamma(\underline{\omega}) \Gamma(-\underline{\omega}) \sum_{\underline{u} \in B} G(\underline{\omega} + \underline{u}) G(-\underline{\omega} - \underline{u}) \right] d\underline{\omega} \quad (3-2)$$

where

$\Phi(\underline{\omega})$ = scene spatial power spectral density,

$\Gamma(\underline{\omega})$ = Fourier transform of aperture function,

$G(\underline{\omega})$ = Fourier transform of interpolation function,

Q = area of sample lattice cell,

Ω = two dimensional spatial frequency space,

B = lattice in Ω dual to sample lattice,

$\underline{\omega} = (\omega_1, \omega_2)$ - spatial frequency (radians per meter)

These quantities were more fully explained in Section 3.2. This expression is generalized to include filtering (Appendix G) and recording device characteristics (Appendix D). It is this mean square error of image reconstruction which forms the primary basis for comparison of sampling strategies, apertures, filtering, and recording characteristics in this study. The procedure for numerically evaluating these expressions is discussed in the next section.

It should be kept in mind that averaged mean squared error is not the only possible basis which may be used for evaluation of sampling strategies. For particular applications (boundary detection, for example) one may wish to weigh certain spatial frequencies more than others. This can easily be accommodated by restricting the region of integration to a desired subset of Ω or more generally by inserting a frequency dependent weighting function

into the integrand. Another technique which may be used is a two dimensional generalization of the modulation transfer function approach discussed in Appendix F. Results from these other approaches are, for the most part, beyond the scope of this study, but are not intrinsically difficult to incorporate.

3.3.2 Numerical Evaluation of Mean Square Error

Evaluation of the expressions for mean squared error (Equation 3-2) must be done numerically. One-dimensional studies of sampling and reconstruction such as the study of Reference 12 are much simpler to perform as integration over the real line is required rather than over the entire plane. If in a one-dimensional case, the integrand functions are rational algebraic, then the theory of residues can be used for evaluation, greatly simplifying the procedure at no loss in accuracy. In two dimensions, however, this is not possible. The roll-off characteristics of the integrand functions are of primary concern in influencing the value of the mean squared error. This effect is much more pronounced in two dimensions, necessitating great care in the numerical integration procedures.

Mean squared error computation requires numerical quadrature in which the integrand is a fairly complicated expression involving power spectral densities, aperture and reconstruction functions, and lattice sums. Furthermore, the integration is over an infinite two-dimensional domain. Since the expressions involved are of a somewhat arbitrary nature, techniques such as gaussian quadrature are not applicable, and, since the expressions are of great complexity, high order methods involving partial derivatives are not practical. Because of this, the selected method is a trapezoidal rule using Romberg quadrature (Reference 13). Because the integrand is the difference between two comparable quantities, numerical integration error must be monitored.

Romberg's method is a scheme by which higher order integration techniques can be generated by a linear combination of the trapezoidal sums with decreasing step size (h). For the one-dimensional case, the trapezoidal integration T is an h^2 process so that the value of the integration (y) is in error by an amount ϵh^2 .

$$y = T(h) + \epsilon h^2 \quad (3-3)$$

If the integration step size is doubled, the error increases by 2^2 or

$$y = T(2h) + \epsilon (2h)^2 \quad (3-4)$$

Using the correct combination of Equation 3-3 and 3-4, the error term can be subtracted out.

$$\begin{aligned} 4y &= 4T(h) + 4\epsilon h^2 \\ - \quad y &= T(2h) + \epsilon (2h)^2 \\ \hline 3y &= 4T(h) - T(2h) \end{aligned} \quad (3-5)$$

$$y = \frac{4T(h) - T(2h)}{3} = S(h) \quad (3-6)$$

which is Simpsons rule. But Simpsons rule is an h^4 process; therefore:

$$\begin{aligned} y &= S(h) + \epsilon h^4 \\ y &= S(2h) + \epsilon (2h)^4 \end{aligned} \quad (3-7)$$

Continuing as before

$$\begin{aligned} 2^4 y &= 2^4 S(h) + \epsilon (2h)^4 \\ - \quad y &= S(2h) + \epsilon (2h)^4 \\ \hline (2^4 - 1)y &= 2^4 S(h) - S(2h) \end{aligned} \quad (3-8)$$

$$y = \frac{2^4 S(h) - S(2h)}{2^4 - 1} = N(h) \quad (3-9)$$

This yields a Newton-Cotes technique, which is an h^6 process. Therefore, a general expression for the Romberg T-table can be developed.

$$T_m^k = \frac{4^m T_{m-1}^{(k+1)} - T_{m-1}^{(k)}}{4^m - 1} \quad m \neq 0 \quad (3-10)$$

which gives the T-table

$$\begin{array}{cccc}
 T_0^0 & & & \\
 T_0^1 & T_1^0 & & \\
 T_0^2 & T_1^1 & T_2^0 & \\
 T_0^3 & T_1^2 & T_2^1 & T_3^0
 \end{array} \tag{3-11}$$

where $m = 0$; Trapezoidal rule
 $m = 1$; Simpson's rule
 $m = 2$; Newton-Cotes rule
 $m \geq 2$; higher order Romberg methods

Looking at the two-dimension cases, the h in Equation (3-3) is replaced by Δx^2 .

$$\begin{aligned}
 y &= T(\Delta x) + \epsilon \Delta x^4 \\
 y &= T(2\Delta x) + \epsilon 2^4 x^4 \\
 S(x) &= 2^4 \frac{T(\Delta x) - T(2\Delta x)}{2^4 - 1}
 \end{aligned} \tag{3-12}$$

Therefore, the general expression for the T function is simply modified by a power of two.

$$T_m^k = \frac{4^{2m} T_{m-1}^{(k+1)} - T_{m-1}^{(k)}}{4^{2m} - 1} \tag{3-13}$$

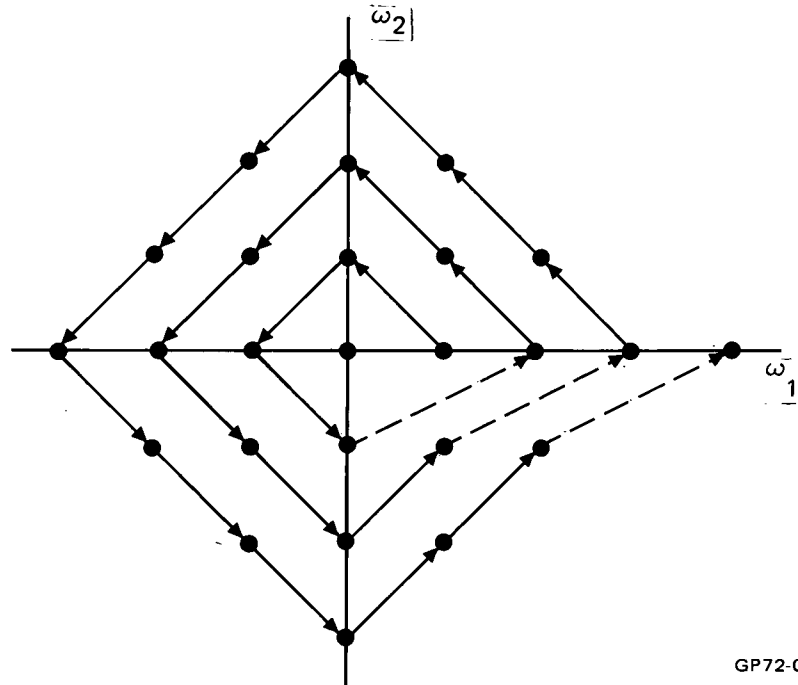
The above scheme has been used extensively to evaluate the average root mean square error expression of Equation (3-2).

In the evaluation of the integrand, several lattice summations must be performed which are of the form:

$$\sum_{\underline{u}_m \in B} F(\underline{\omega} + \underline{u}_m) \tag{3-14}$$

$$\underline{u}_m = m_1 \underline{b}_1 + m_2 \underline{b}_2 \tag{3-15}$$

where m_1 and m_2 are integers and \underline{b}_1 and \underline{b}_2 are the dual basis vectors. The function is then summed by incrementing m_1 and m_2 in a sequence as shown in the Figure 3-3.



GP72-0450-41

FIGURE 3-3
LATTICE SUMMATION PROCEDURE

This allows a finite number of lattice rings to be calculated which constitute a great savings in computer run time. The number of rings is dependent on the functions which are being summed over.

The final output of the computer program is the average root mean square error normalized to the standard deviation of the power density spectrum, and this output is printed in the T-table format of Romberg's Quadrature method.

We may capitalize upon the fact that lattice sums are involved in the integration in order to transform the integration from an infinite to a finite domain without any appreciable increase in complexity. This is done simply by making the integrand a lattice sum and restricting the domain of the integration to one sample cell. Further simplification is effected by taking notice of the evenness of certain functions involved. A functional block

diagram of the program is displayed in Figure 3-4.

3.3.3 Image Power Spectral Densities

Figure 1-8c shows a power spectral density obtained from a discrete Fourier transform of the farmland scene of Fig. 1-8a, digitized into a 128 x 128 array of pixels with sample spacings corresponding to 50 meters. This result is plotted as a function of $|\underline{\omega}|$ in Figure 3-5, the data having been averaged circularly about the origin in the Ω plane. Since the mean square error in image reconstruction depends directly on the spatial high frequency components, this curve must be extrapolated analytically to be useful for these studies. We therefore attempt to fit to this plot a density of the form:

$$\Phi(\underline{\omega}) = \frac{4\pi\sigma^2 D_c^2 (M-1)}{\left(1 + D_c^2 |\underline{\omega}|^2\right)^M} \quad (3-16)$$

The roll off factor M is easily seen to be $3/2$. The correlation distance D_c for best fit was judged to be about 679 meters. This curve is also plotted in Figure 3-5. For a sample interval to be used as the standard of distance as is done in the computer simulation, the number of samples per correlation distance is

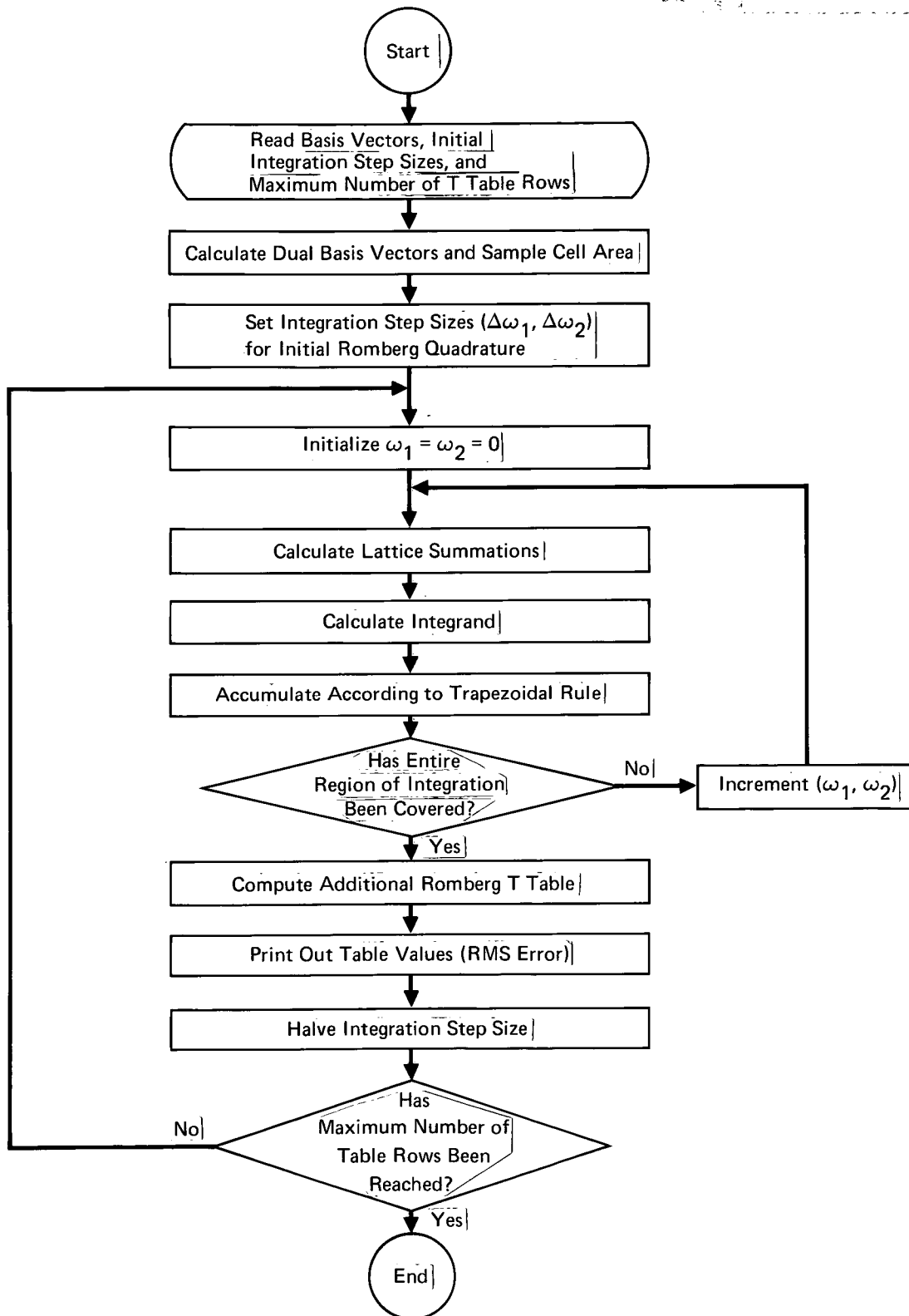
$$D = \frac{D_c}{\Delta x} = \frac{679 \text{ meters/interval}}{25 \text{ ft. sample} \cdot .3048 \text{ meters/ft.}} = \frac{89 \text{ samples}}{\text{correlation interval}} \quad (3-17)$$

for the 1 sample/58.06 sq meter (625 sq ft) case

and $D = \frac{679}{200(.3048)} = 11 \text{ samples/correlation interval}$

for the 1 sample/3716 sq meters (40,000 sq ft) case

Urban area, mountains, and forest regions were also investigated. These had roll off factors of $M = 1.02, 1.54, \text{ and } 1.37$ respectively. M cannot be less than unity or the integrals may not exist. This can be seen by constructing a two-dimensional Parseval relation to obtain the mean squared image intensity from its spectrum. This suggests that the urban scene may require a very high sample density for reconstruction or that higher order representation need be made for its spectral representations. These latter will require a more



GP72-0450-40

FIGURE 3-4
ROOT MEAN SQUARED RECONSTRUCTION ERROR FLOW DIAGRAM

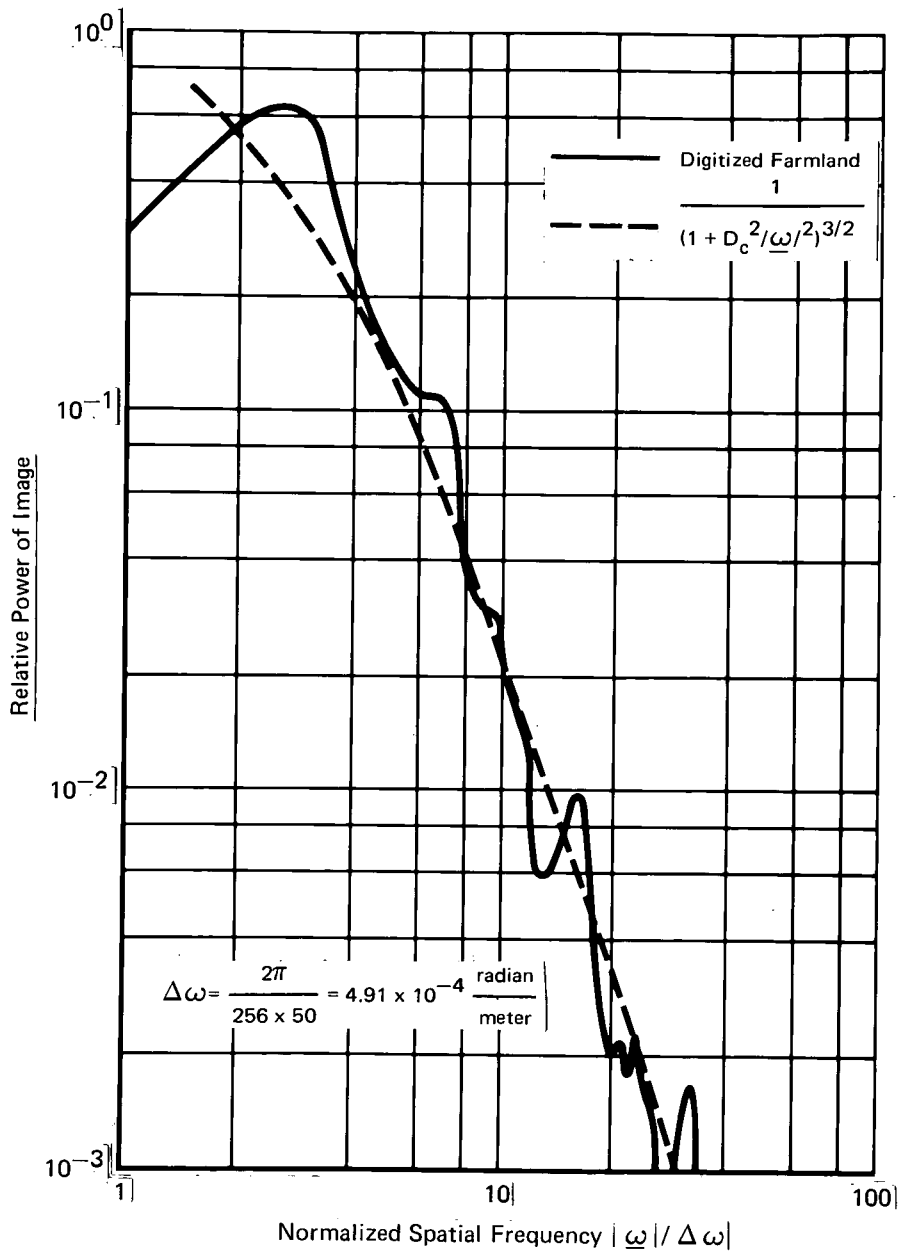


FIGURE 3-5
POWER SPECTRAL DENSITY OF FARMLAND

extensive processing of real image statistics.

Comparison of the above results does show a possibility for the classification of terrain types by their spectral characteristics.

3.4 QUANTITATIVE RESULTS

With computer implementation of the averaged mean squared error expression, sample densities and lattice shapes, sample aperture overlaps and shapes, and recording device characteristics were then evaluated. The comparison of alternate strategies is emphasized since absolute quantitative specification of rms error is not entirely meaningful except for very specific applications. The following sections discuss these effects.

3.4.1 Influence of Image Spatial Frequency Content

The average mean squared error obtained from any specific application depends strongly on the image power spectral density $\Phi(\omega)$. For band limited functions, it is possible to eliminate reconstruction error entirely if the sample density is high enough. It would follow, therefore, that image roll off M (see Section 3.3.3) is an important parameter. Figure 3-6 illustrates the effects of varying M . The optimal reconstruction algorithm was selected in order to isolate the effect under consideration. Subsequent analysis was performed using the $M = 3/2$ value. Other values of roll-off are expected to shift the results in the manner indicated by the figure. Note that an overlap of about .6 will give near optimal results. This is about the overlap required to leave no area of the image unrepresented. Larger overlaps than .6 are seen to be non-detrimental.

3.4.2 Sample Density

Sample density variation was investigated using two basic sample densities of one sample per 58.06 square meters (625 sq ft) and one sample per 3716 square meters (40,000 sq ft). Figures 3-7 and 3-8 show that overlap characteristics are little affected. A circular aperture with the rhombic sampling lattice was selected as being representative enough to display these effects since lattice shapes are not very influential.

Rhombic Sampling Lattice
Uniform Circle Sampling Aperture
Optimal Reconstruction

$$\Phi(\omega) = \frac{4\pi\sigma^2 D^2 (M-1)}{(1 + D^2/\omega^2) M}$$

Sample Density = 1 Sample/58.06 sq meters (625 sq ft) D = 89

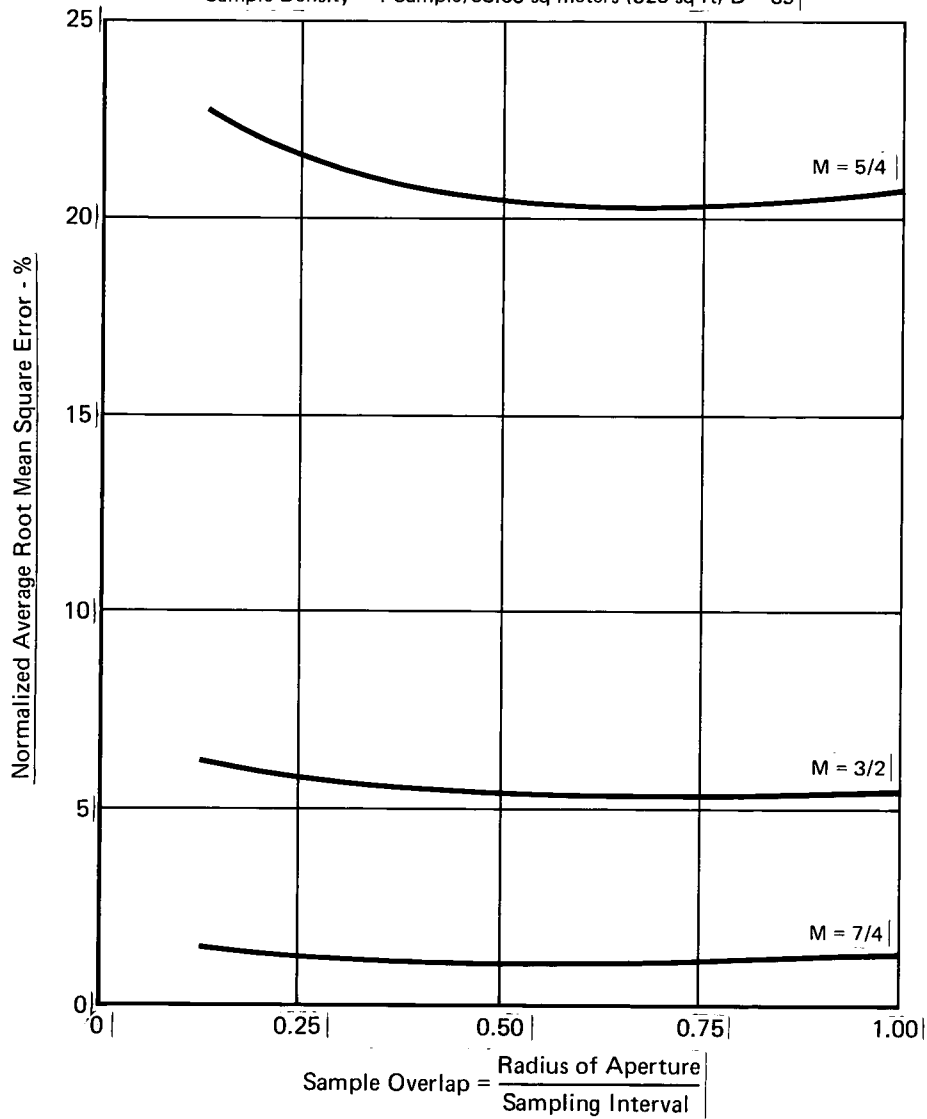


FIGURE 3-6
EFFECTS OF IMAGE SPATIAL FREQUENCY ROLL-OFF

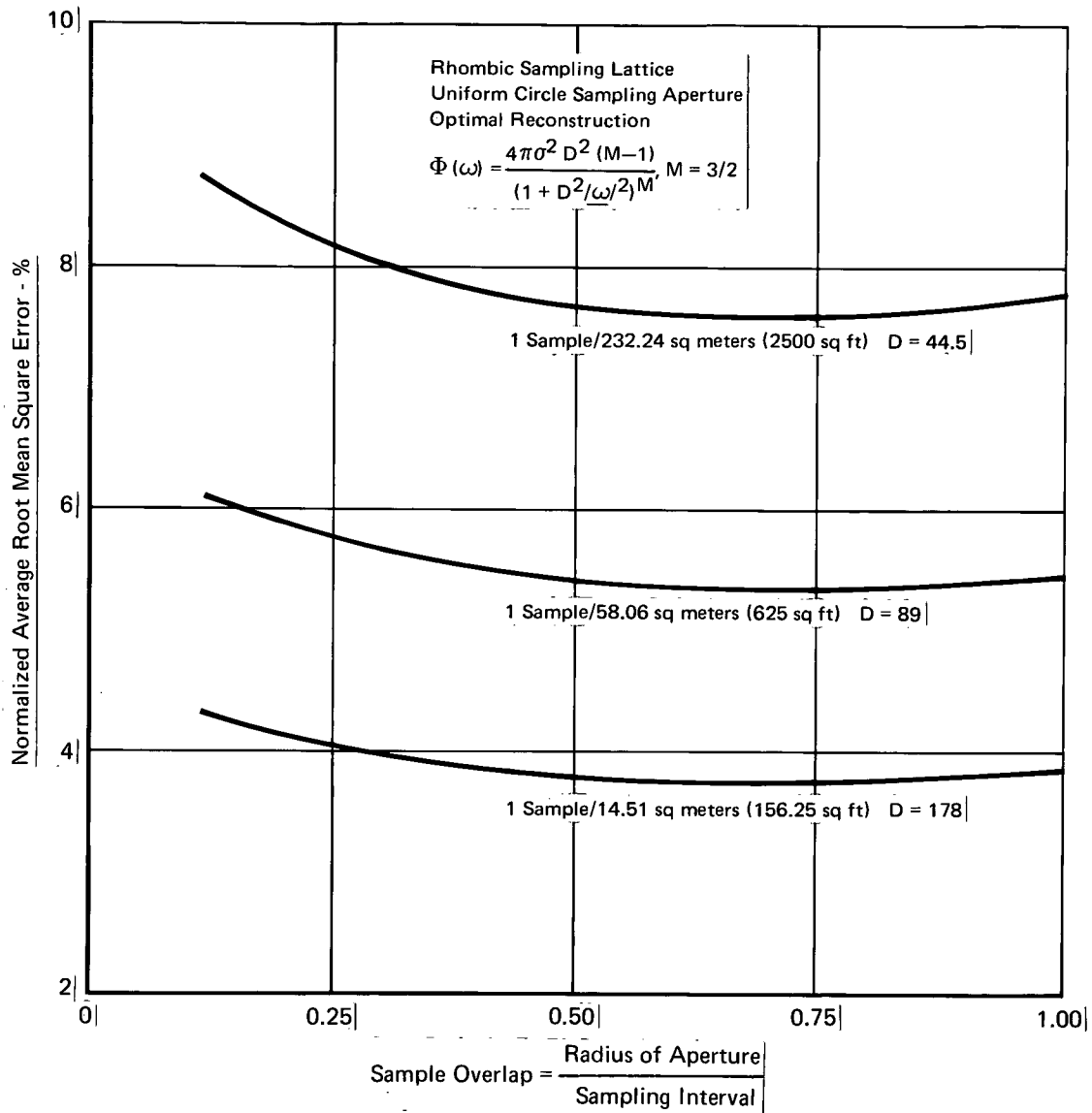


FIGURE 3-7
EFFECTS OF IMAGE SAMPLE SPACING

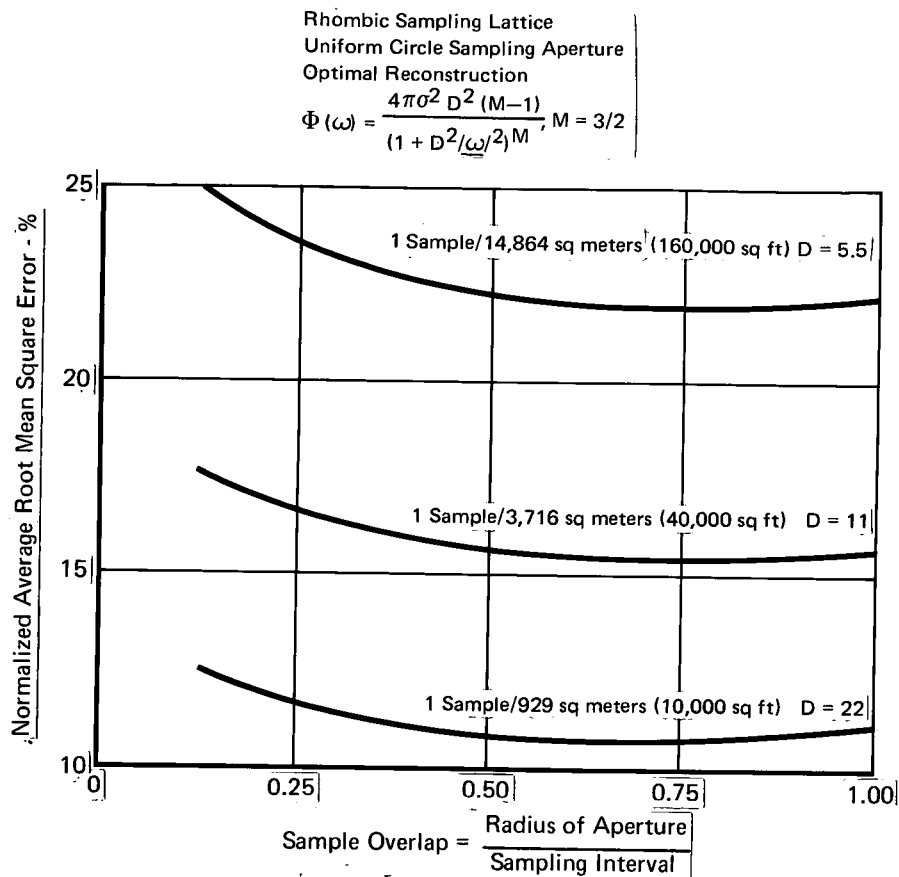


FIGURE 3-8
EFFECTS OF IMAGE SAMPLE SPACING

GP72-0450-52

3.4.3 Sampling Lattice Effects

Peterson and Middleton (Reference 10) have shown that, for band limited functions, the densest lattices obtainable without overlap are optimal. Thus, the rhombic lattice is best for circular and hexagonal aperture cases, and either the square or rhombic lattice is equally good for the square apertures. These results are carried over to the non-band limited case by examining the circular aperture case. Figure 3-9 shows a comparison of the square lattice with the rhombic lattice. These lattices have equal spacing in the x_1, x_2 directions. In the rhombic lattice, the samples in adjacent scans are out of phase, so to speak. As can be seen from the Figure, the effect is slight from mean squared error considerations.

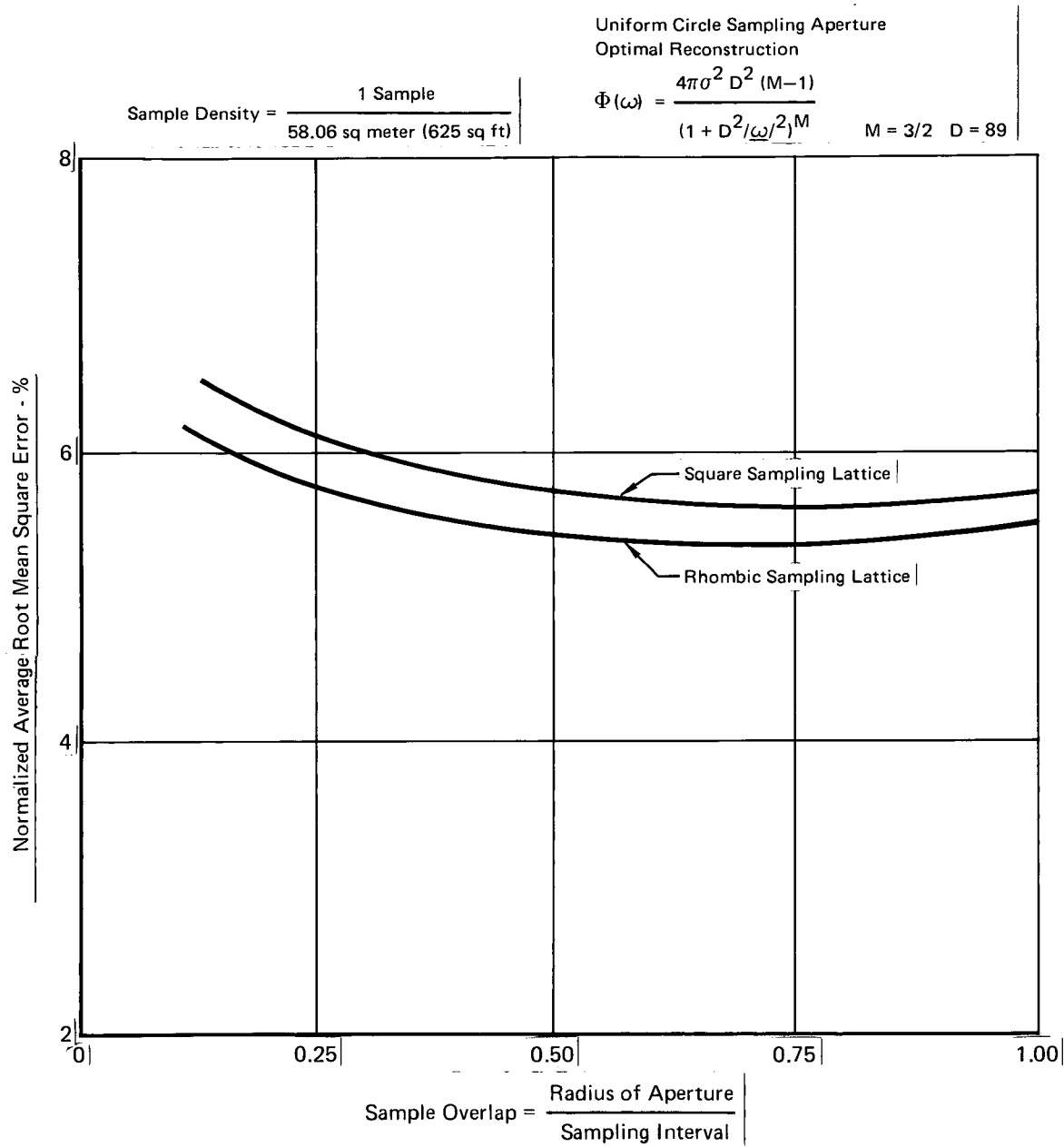


FIGURE 3-9
SAMPLING LATTICE COMPARISON

3.4.4 Comparison of Reconstruction Methods and Aperture Shapes

A comparison of the reconstruction methods discussed in Section 3.2.4 has been made for the apertures described in Section 3.2.2. This was done for the sample density of one sample per 58.06 square meters (625 square feet). Since the definition of sample overlap is different for each aperture shape, the various apertures were considered separately. Figures 3-10 through 3-13 show these results. The differences between the circle, hexagon and square are seen to be minor. The gaussian aperture difference can also be judged as small if overlap for that case is modified to be twice the aperture standard deviation divided by sampling interval. These results indicate that efforts to improve reconstructed image quality would be better spent on interpolation technique improvement rather than aperture shape optimization.

3.4.5 Effects of Continuous Scan (Video)

Continuous scanning and reconstruction of the continuous record can be represented by allowing the sample density in the scan direction to become infinite. This, as was mentioned before, is equivalent to a dual lattice becoming sparse. Allowing the sample density in the scan direction to become infinite transforms the integration over a lattice cell into an integral over an infinite domain. To avoid program modifications and to also gain insight into this limiting procedure, cases with increasing scan direction density were investigated.

Figure 3-14 shows the rms error for the case of a gaussian aperture with two different overlaps between scan lines. The .5 overlap represents the situation in which the one sigma circles are contiguous between successive scans. The 0.14 overlap represents the condition existing for the McDonnell Digital Image Processing System (DIPS) for which the distance between scan lines is 1.5×10^{-3} inches and the one sigma radius of the scanning aperture is $.21 \times 10^{-3}$ inches.

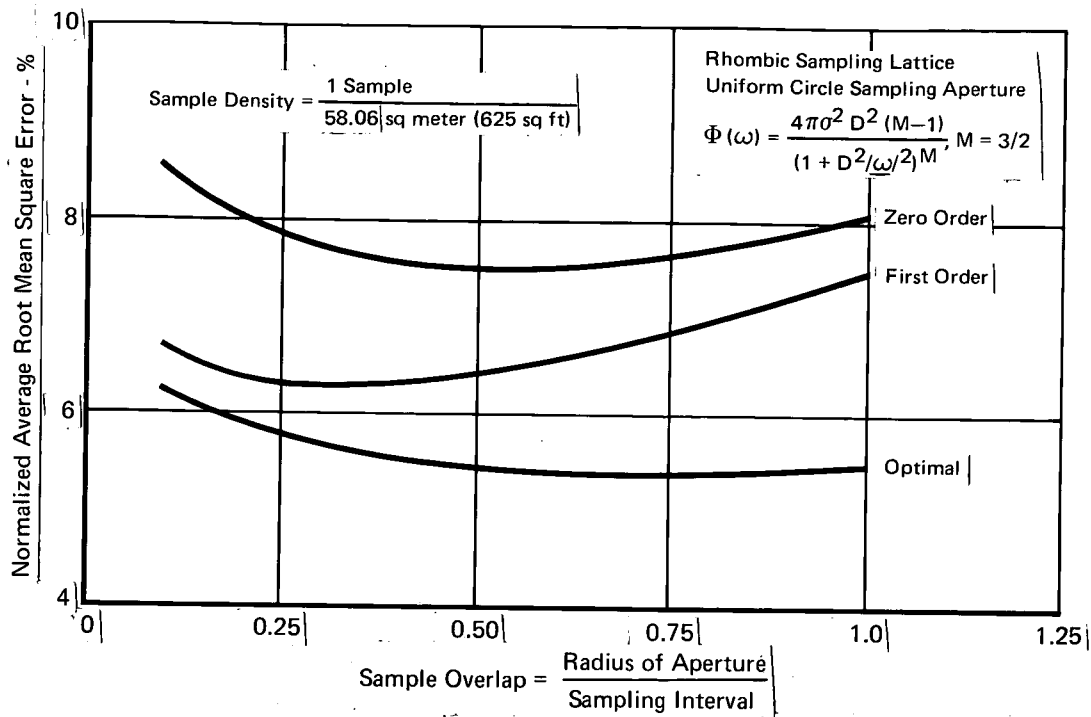


FIGURE 3-10
INTERPOLATION TECHNIQUE COMPARISON FOR CIRCULAR SAMPLING APERTURE

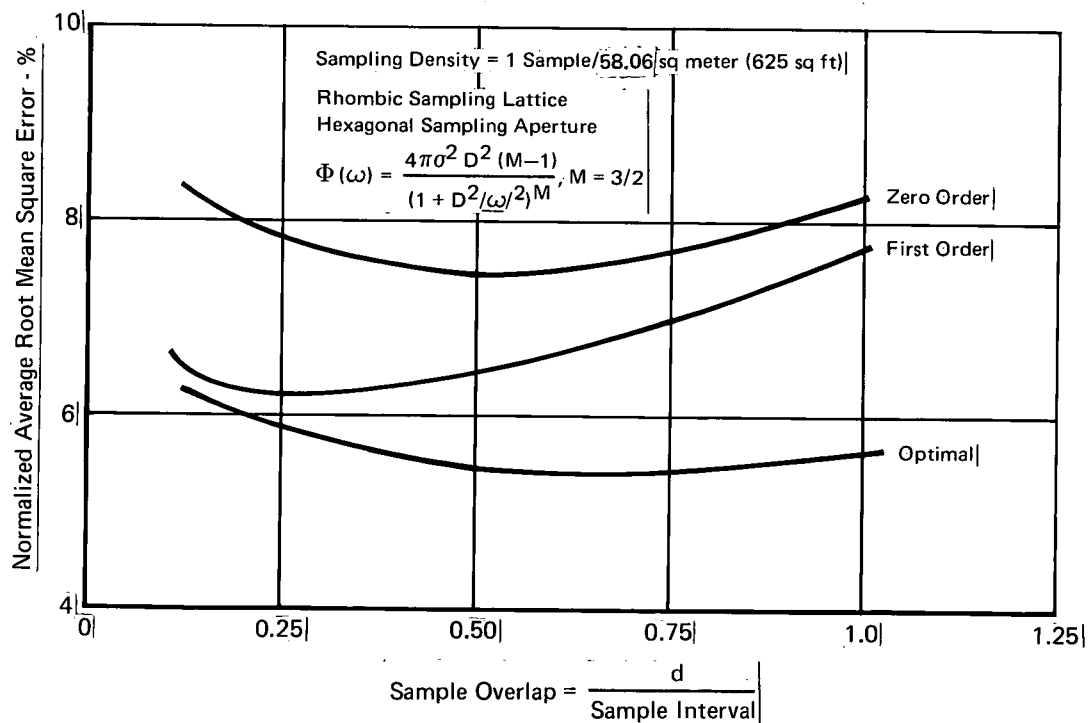


FIGURE 3-11
INTERPOLATION TECHNIQUE COMPARISON FOR
HEXAGONAL SAMPLING APERTURE

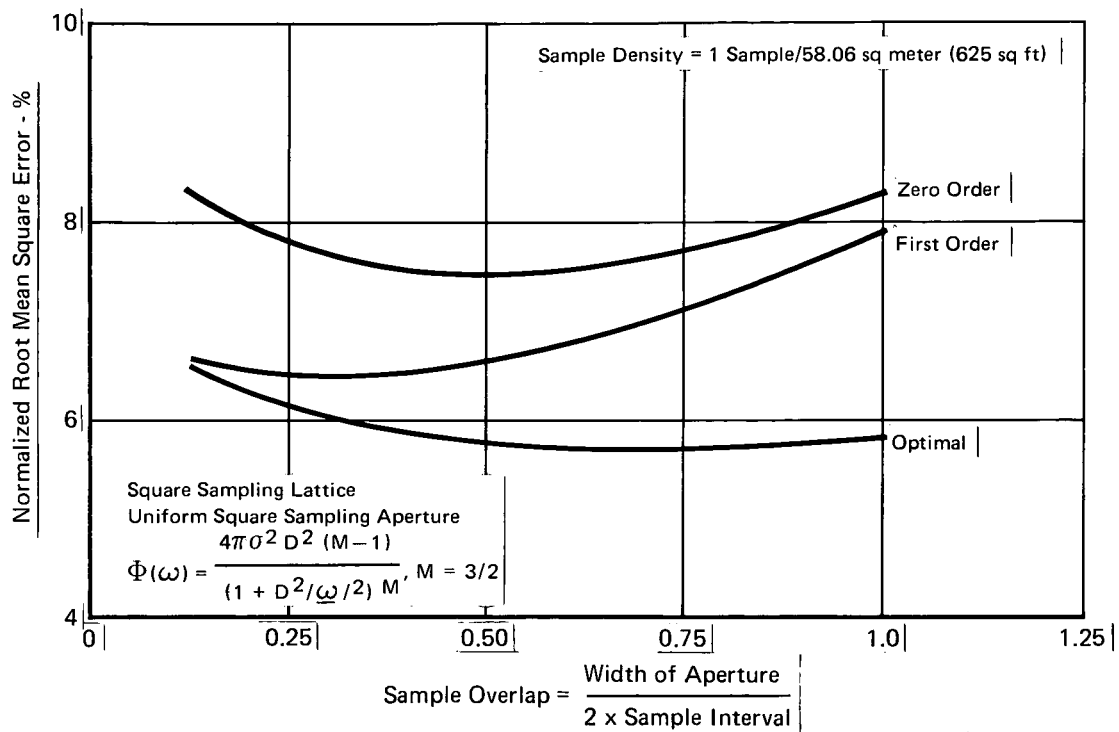


FIGURE 3-12
INTERPOLATION TECHNIQUE COMPARISON FOR
SQUARE SAMPLING APERTURE

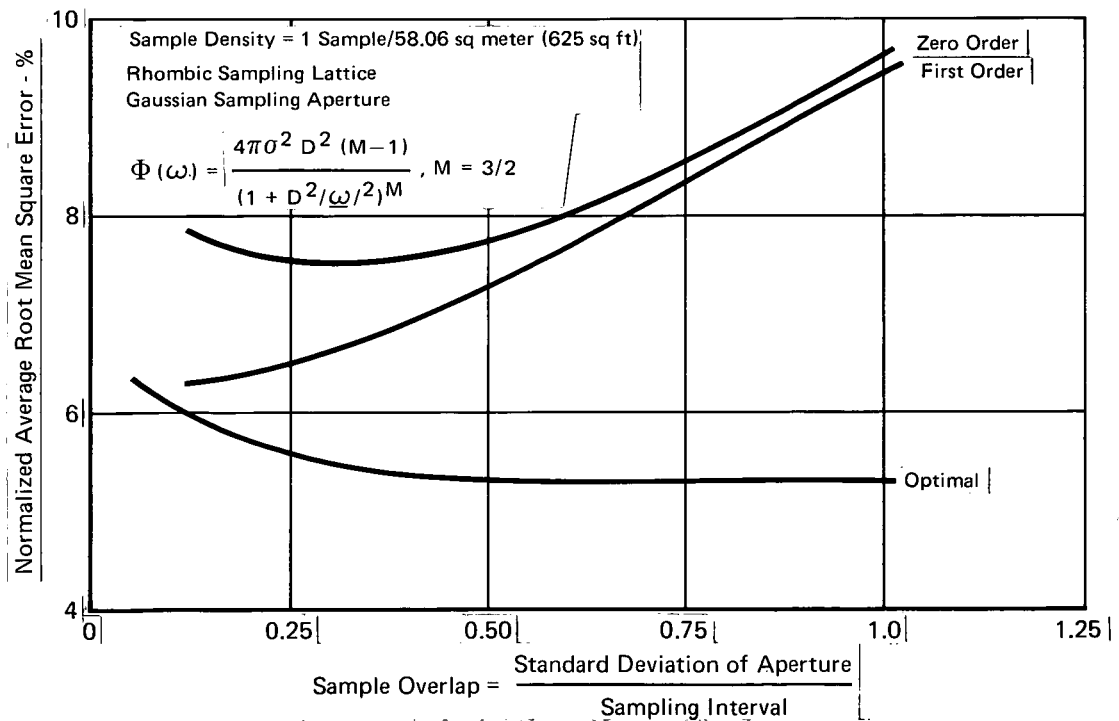


FIGURE 3-13
INTERPOLATION TECHNIQUE COMPARISON FOR
GAUSSIAN SAMPLING APERTURE

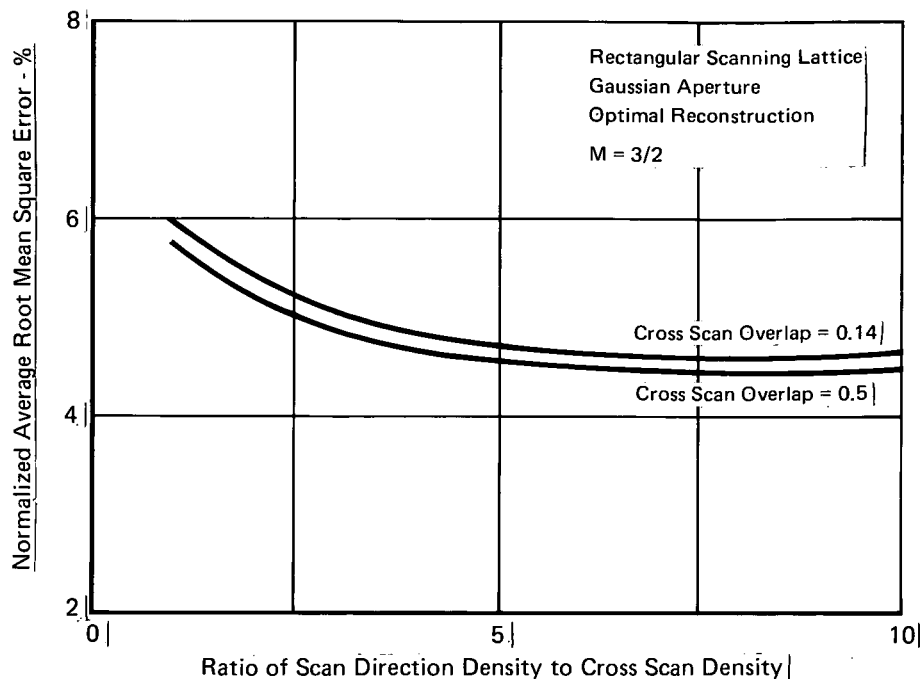


FIGURE 3-14
CONTINUOUS SCAN CHARACTERISTICS

Apparently, an increase in sample density (along the scan direction) by a factor of seven is equivalent to continuous processing. An approximate twenty-five percent improvement results from processing video rather than equally spaced samples.

Figure 3-15 illustrates the effect of varying the interscan distance as the scan direction sampling density increases while the two dimensional sample density is held constant. (i.e. 1 sample/625 sq. ft.). The sampling apertures were assumed to be Gaussian such that their two dimensional spot is a one sigma ellipse whose axis are in a ratio corresponding to the ratio of the scanning densities. For the example shown, the ellipses were assumed to be contiguous (i.e. the overlap is 1/2). This curve illustrates the image degradation caused by aliasing errors in the absence of any presampling filtering.

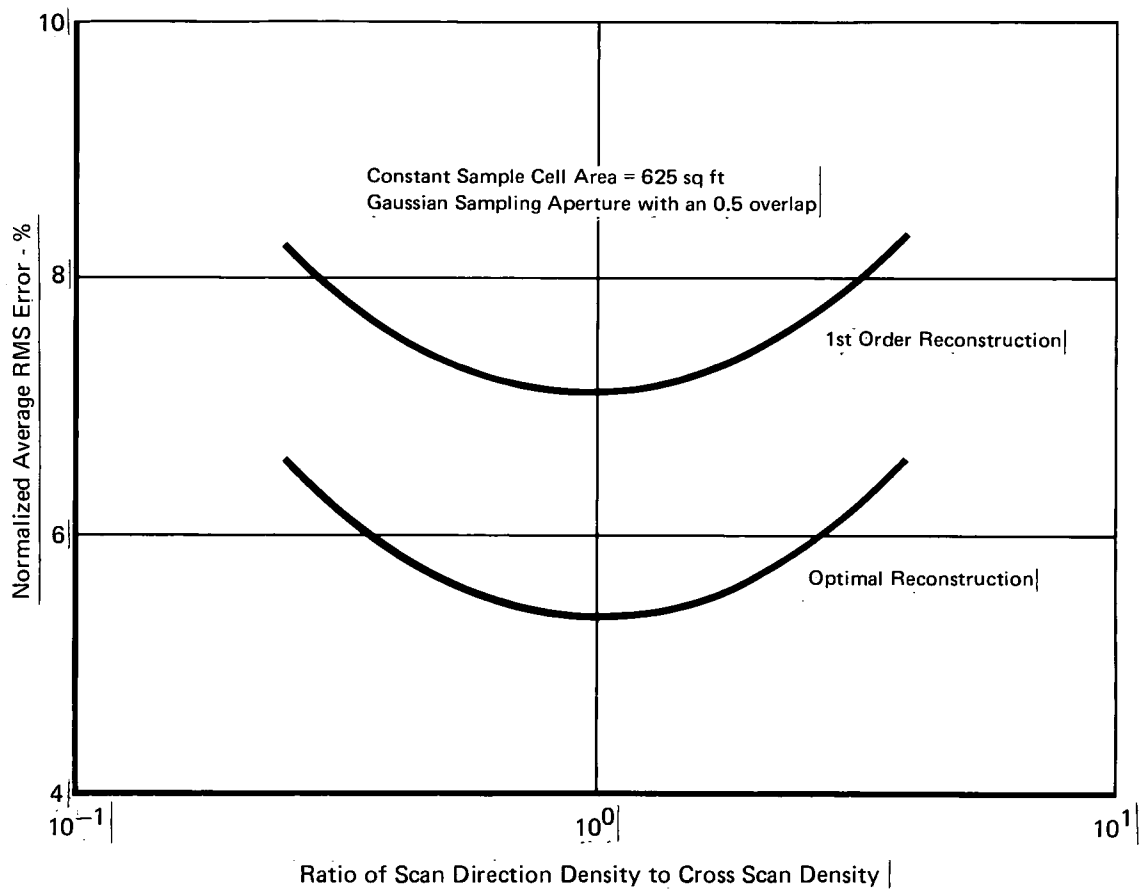


FIGURE 3-15
EFFECTS WITH CONSTANT SAMPLE CELL AREA

3.4.6 Image Recorder Effects

An expression for mean squared reconstruction error including the recording device characteristics is derived in Appendix D. Two cases were investigated with this expression; 1) a Gaussian sampling aperture with a rhombic lattice and a Gaussian recording spot characteristic, and 2) a rectangular sampling aperture with a rectangular lattice and recording spot characteristic.

The results for the first case, shown in Figure 3-16, indicate that the recording spot spacing need only be one-tenth of the sample spacing to effectively have a continuous recording situation. The rms error is approximately doubled by using no interpolation at all.

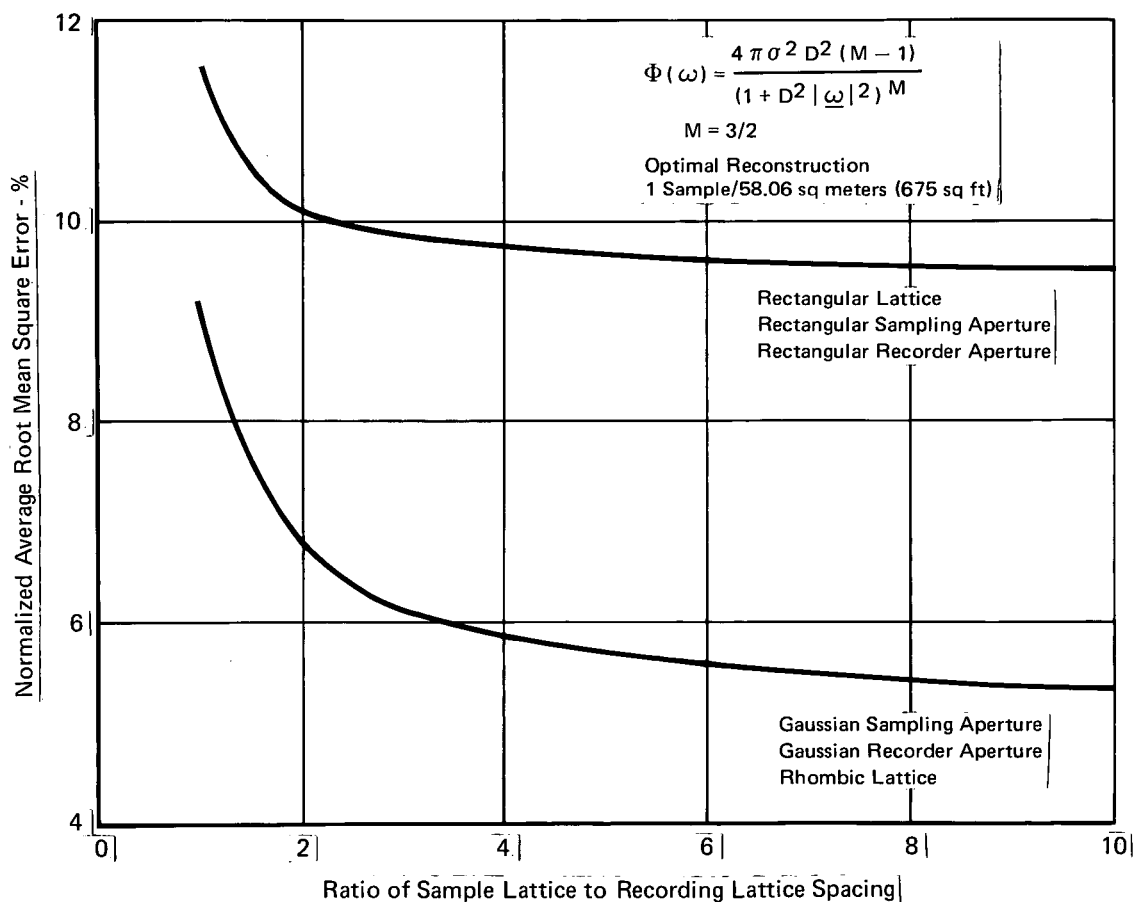


FIGURE 3-16
RECONSTRUCTION ERROR AS FUNCTION OF IMAGE
RECORDING DEVICE CHARACTERISTICS

For the second case, the rectangular sampling lattice has the same spacing as the rhombic in one direction but the spacing normal to this is four times as large so that the sample density is $3/8$ or .2165 times the density for the Gaussian case. The aperture was rectangular in shape with this same 4:1 ratio of sides, was uniform, and of a size to make the sampled FOV contiguous. The recording characteristics had these same features. The error resulting from this situation is also shown in Figure 3-16. Apparently only about five recording spots between every pair of sample points is sufficient to give the same performance as a continuous recording device.

3.4.7 Presampling Filtering Effects

A simple instructive example of filtering effects which may occur before sampling is a first order time delay acting on the video before sampling. Figure 3-17 illustrates the added degradation incurred as a result of the time delay times scan speed being various fractions θ of the interscan distance. The situation depicted is the same as for the .5 overlap continuous scan examined in Section 3.4.5. This was analyzed according to the

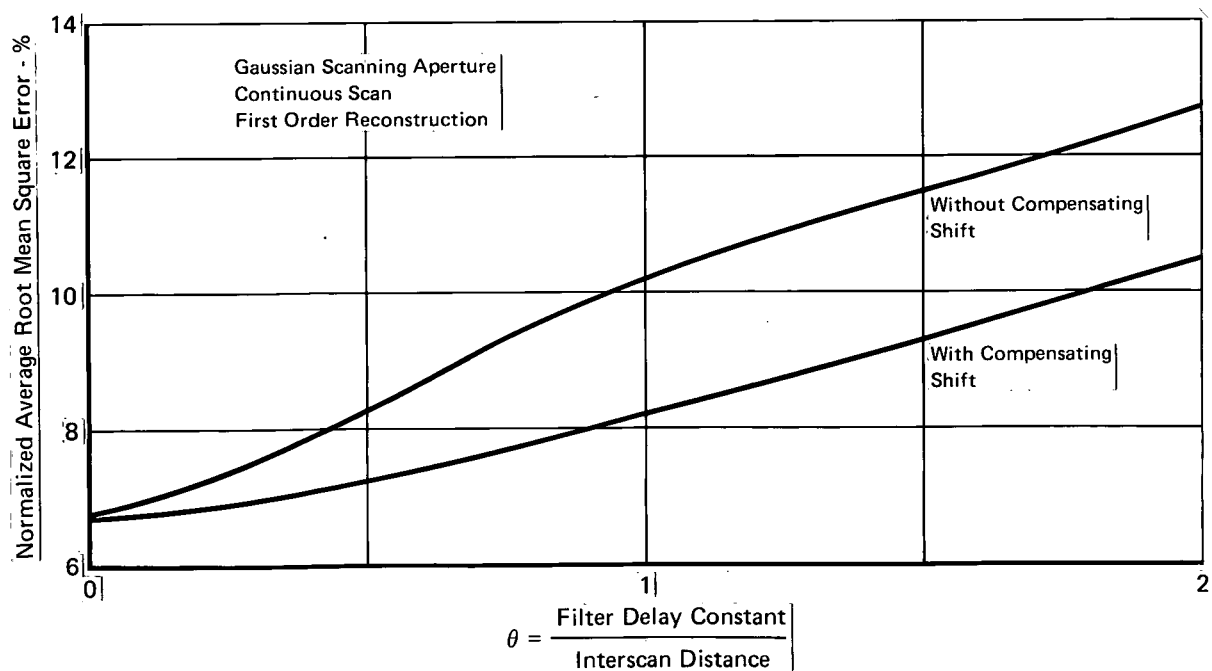


FIGURE 3-17
EFFECT OF FIRST ORDER DELAY PREFILTER

methods described in Appendix G. First order reconstruction is displayed since the optimal reconstructor would remove nearly all of the effects of the filter. The mean square error is shown for those cases with and without an anticipated time shift in the reconstructed image. The amount of the shift used was equal to the spatial delay of the first order filter. This shift is not optimum, but is a reasonable value. To be optimum, the shift would be selected as a function of the scene spatial frequency spectrum, scanning aperture, and reconstruction method used.

3.5 IMAGE SAMPLING STRATEGY SPECIFICATION

The sampling strategy to be selected will depend upon the applications envisaged for the reconstructed imagery. The results discussed so far are based on the unequivocal minimums rms error criterion. This is desirable for most purposes, and if a comparison of apertures and lattices is required, this is the most natural and general approach. However, special applications can take advantage of more specialized techniques. Some of the requirements on sampling and reconstruction imposed by special user applications are discussed in the following section. We begin however, by pointing out some of the conclusions obtained from the rms error criterion.

3.5.1 Minimum RMS Error

For the cases examined in this study, we may conclude the following: 1) The sampling lattice should be rhombic for the circular, gaussian or hexagonal sampling apertures. The lattice can be either square or rhombic for the square or rectangular aperture (the error difference is approximately three percent); 2) Varying aperture overlap within the range of .125 to 1.0 results in fifteen percent variation in rms reconstruction error; 3) The most significant tradeoff parameter appears to be the interpolation reconstruction technique which, between the extremes of zero order reconstruction and optimal reconstruction, contributes thirty percent to the rms error.

These considerations indicate that sampling strategy has less effect than reconstruction considerations, at least for cases in which the sampling pro-

cedure is unconstrained. The constrained situation (such as sample densities in the x_1 , x_2 , being quite different) is expected to impose significant requirements on the aperture shape, but this evaluation has not yet been performed. One would select a rhombic sampling lattice if no mission requirements counteract this choice. Also, no requirement for other than a simple gaussian aperture was demonstrated unless the sampling procedure is quite anisotropic.

3.5.2 Position Location

Position Location is defined as the spatial registration of two images. These images may differ due to different sun angles, different FOV, and seasonal changes. Sampling and reconstruction of these images must be weighted toward features which are of comparable dimension to the required registration error bound. Figure 3-18 shows a proposed procedure for selecting sample densities and weighting functions. First, the image power spectral density and the noise impose a resolution limit which must be

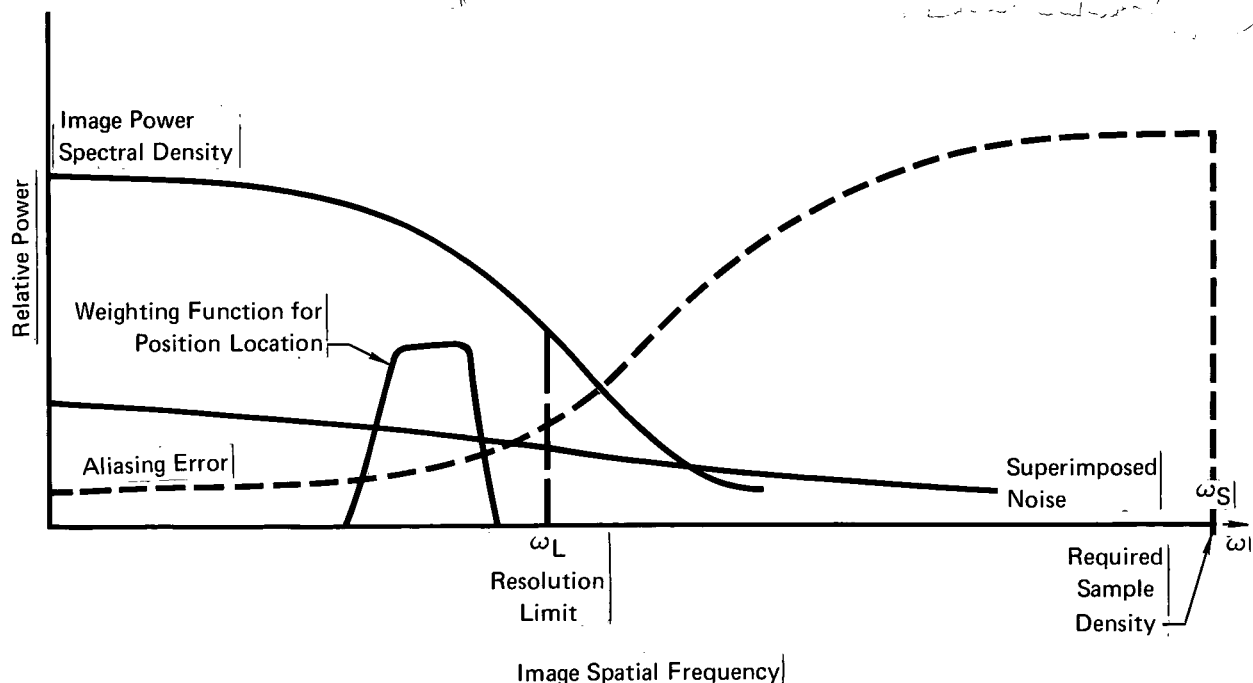


FIGURE 3-18
POSITION LOCATION CONSIDERATIONS

GP72-0450-43

greater than $2\pi/(\text{registration requirement})$ if the registration accuracy is to be met. Secondly, the sample density must be set at a density high enough to reduce the effect of aliasing at this frequency to be within acceptable bounds (say .1 of image power at that frequency). Finally a weighting function is selected for image reconstruction which passes only those frequencies useful for registration.

3.5.3 Feature Extraction

Feature extraction is such a general term that only selected examples can be discussed. As far as sampling and reconstruction are concerned, only those aspects of feature extraction which pertain to image spatial properties are of interest. An important concept in feature extraction is multispectral species identification. This concept involves the recording of imagery in several spectral bands, and the investigation of the intensity relationship of the various electromagnetic frequencies which determines a point in a feature space (Ref. 14). Usually, high spatial resolution is not of great concern, but this is a choice to be made on the part of the user. An important consideration is that the intensity reconstruction error be of comparable or less magnitude than the natural variation expected within a species class. This is necessary to keep the point from varying beyond the limits of the appropriate species identification procedure.

Boundary detection is another aspect of feature extraction. This can be investigated by restricting the region of the spatial frequency domain to the band (annulus in the two-dimensional case) occupied by the boundaries of interest. In addition, aperture shape may be used to advantage in boundary detection if the orientation of the boundaries is fixed relative to the scan direction. This particular effect could be analyzed in the rms error sense by means of an anisotropic image power spectral density which represents the orientation of the boundary lines.

3.5.4 Random Sampling

Random sampling of band limited functions theoretically can be used to advantage for power spectral density determination. Beutler (Reference 15) shows that the power spectral densities of such functions are determined by samples taken randomly at an average sample density lower than the Nyquist density. The demonstration of this does not, however, provide a constructive method of determining the power spectral densities from the samples. Reconstruction of the actual signal rather than its statistics is a more difficult problem. The practicality of such signal recovery at less than the Nyquist density is questionable from "stability" considerations. Landau (Reference 16) defines stable sampling as sampling with the property that small changes in the sample values produce correspondingly small changes in the recovered signal. Thus, stability in this context is a type of continuity property. Such a stability requirement is present in an earth reconnaissance program.

Quantitative results for certain types of random sampling situations have been obtained. Leneman and Lewis (Reference 17) have exhibited mean squared reconstruction errors for certain types of one dimensional random sampling of signals which need not be band limited. The sampling procedures considered were Poisson sampling and periodic sampling with skips. The reconstruction methods were rather restrictive but some generalization may be possible to two dimensions and higher order interpolation methods. This approach could give results of some practical importance, however the systematic utilization of random sampling for channel bandwidth reductions is an open question.

3.6 CONCLUSIONS

The intent of this study was to obtain quantitative evaluation of some of the basic features of sampling and reconstruction rather than draw specific conclusions from these evaluations. We have, in terms of rms reconstruction errors, quantitatively described the effects of parametric variation of such things as sample density, terrain type, discreteness of recording device and presample filtering. It is inappropriate to draw specific conclusions from these, however in trade off areas such as sample lattice, sample aperture size and shape, we can say the following. The mean squared error criterion does not impose stringent requirements upon aperture shape or size as a function of sampling lattice unless the sampling is very anisotropic. Also, we may generally conclude that interpolation to a refinement of about five recording device spots (in each direction) per pair of sample values is sufficient. That is, no further refinement will improve the reconstruction.

It is best to allow mission constraints or instrumentation considerations determine the sampling procedure and then use the criteria discussed in this report to evaluate the consequences of adopting or adapting that sampling method. The study has shown how these criteria can be expanded to include very specialized applications.

3.7 AREAS FOR FURTHER STUDY

This study has suggested several interesting areas which merit further investigation. For example, more anisotropic sampling lattice configurations (preferably those compatible with advanced mission or instrumentation constraints expected in earth surveys) should be examined. Also, adaptation of the rms error criterion to specialized tasks such as boundary detection, registration, or feature extraction may provide useful results.

Noise superimposed on the image, either before or after sampling, is a limiting factor in many image sensing applications. This can be easily included into the present rms error formulation. Optimal reconstruction formulae incorporating this superimposed noise does not appear to add any significant computational complexities.

Another area needing further development is in the derivation of better reconstruction methods. This has been shown to be a promising area of investigation which allows meaningful improvement in image reconstruction. For example, development of practical suboptimal reconstruction formulae based upon judicious truncation of the optimal formulae warrants consideration. A computer simulation of image reconstruction which can represent interpolation of up to the fourth order would be an invaluable extension to the present study. Certainly the implementation problem must be of immediate concern. If there are practical limitations to any of the reconstruction methods, it is best to have these identified as early as possible.

The addition of real imagery to supplement any of the above mentioned areas of investigation is a desirable feature to include. The illustration of an image actually displaying a five or ten percent reconstruction error will provide a valuable addition to the study.

REFERENCES

1. Mission 131 Screening and Indexing Report, NASA Earth Resources Aircraft Program, September, 1970
2. Mission 129 Screening and Indexing Report, NASA Earth Resources Aircraft Program, September, 1970
3. Mission 158 Screening and Indexing Report, NASA Earth Resources Aircraft Program, September, 1970
4. Image Interpretation Handbook, TM 30-245, NAVAIR 10-35-685, AFM 200-50, Volume I, December, 1970, pp 325
5. Anuta, P. E., "Spatial Registration of Multispectral and Multitemporal Digital Imagery Using Fast Fourier Techniques," IEEE Transactions On Geoscience Electronics, Vol. GE-8, No. 4, October, 1970, pp 353-368
6. Richards, P. I., "Computing Reliable Power Spectra," IEEE Spectrum, January, 1967, pp 83-90
7. Bingham, C., Godfrey, M. D., and J. W. Tukey, "Modern Techniques of Power Estimation," IEEE Transactions On Audio and Electroacoustics, Vol., AU-15, No. 2, June, 1967, pp 56-66
8. Schwartz, M., Information, Transmission, Modulation and Noise, McGraw-Hill, 1959, pp 239
9. Barnea, D. I. and H. F. Silverman, The Class of Sequential Similarity Detection Algorithms for Fast Digital Image Registration, IBM Research Report RC 3356, May 1971
10. Peterson, D. P. and Middleton, D., "Sampling and Reconstruction of Wave-Number-Limited Functions in N-Dimensional Euclidean Spaces," Information and Control 5, 1962
11. Montgomery, W. D., Shields, P. C. and Alward, J. L., Summary of Mathematical Work Related to Infrared Radiation Data Processing, Michigan, U. of, (I&OSL) RPT. 6054-4-7, March 1966
12. McRae, D. D., "Interpolation Errors," Advanced Telemetry Study, Technical Report Part 1, Radiation Incorporated, 15 Feb. 1961 (Revised 18 May 1961)
13. Bauer, F. L., Rutishauser, H., and Stiefel, E., "New Aspects in Numerical Quadrature," Proceedings of Symposia in Applied Mathematics, Vol. IV, 1963
14. Bond, A. D., "Notes on Computer Aided Data Processing of Earth Resources Imagery," Presented at a Short Course on Remote Sensing of Environment, University of Tennessee Space Institute, Tullahoma, Tennessee, 8 March 1972

15. Beutler, F. J., "Alias-Free Randomly Timed Sampling of Stochastic Processes," IEEE Trans. on Information Theory, Vol. II-16, No. 2, March 1970
16. Landau, H. J., "Sampling, Data Transmission and the Nyquist Rate," Proc. IEEE, Vol. 55, No. 10, October 1967
17. Leneman, O. A. and Lewis, J. B., "Random Sampling of Random Processes: Mean-Square Comparison of Various Interpolators," IEEE Transactions on Automatic Control, Vol. AC-11, No. 3, July 1966
18. Levi, L., Applied Optics, Vol. I, Wiley, New York, 1968

Appendix A

DERIVATION OF MEAN SQUARED ERROR EXPRESSIONS

These derivations essentially follow Peterson and Middleton (Reference 10) taking just the parts which are of interest in deriving the required expressions. The condition that the scene spectrum be band-limited has been omitted as not being general enough for real applications.

Let A denote the set of sampling points in the image plane X . Thus if $\underline{a}_1, \underline{a}_2$ are the basis vectors for the sampling lattice,

$$A = \{n_1 \underline{a}_1 + n_2 \underline{a}_2 : n_1, n_2 \text{ integers}\}. \quad (\text{A-1})$$

Let B denote the set of points in the frequency plane Ω which is dual to A in the sense that

$$B = \{m_1 \underline{b}_1 + m_2 \underline{b}_2 : m_1, m_2 \text{ integers}\}, \quad (\text{A-2})$$

and

$$\underline{a}_i \cdot \underline{b}_j = 2\pi \delta_{ij}. \quad (\text{A-3})$$

Let $f(\underline{x})$ denote the image to be sampled. Assume this image is adjusted so that the average value of the intensity is zero. (i.e., $E\{f(\underline{x})\} = 0$) and an auto-covariance function is given,

$$E\{f(\underline{x})f(\underline{x}+\underline{z})\} = K(\underline{z}). \quad (\text{A-4})$$

Denote the sample aperture function by $\gamma(\underline{x})$. The ℓ th sample is then

$$\psi(\underline{v}_\ell) = \int_X f(\underline{y}) \gamma(\underline{v}_\ell - \underline{y}) d\underline{y}, \quad \underline{v}_\ell \in A. \quad (\text{A-5})$$

If $g(\underline{x})$ is the reconstruction (interpolation) function, the reconstructed image function $f^*(\underline{x})$, is given by

$$f^*(\underline{x}) = \sum_{\underline{v}_\ell \in A} g(\underline{x} - \underline{v}_\ell) \psi(\underline{v}_\ell). \quad (\text{A-6})$$

The mean squared error in the reconstruction is

$$\begin{aligned} E\{[f(\underline{x}) - f^*(\underline{x})]^2\} &= E\{f^2(\underline{x}) - 2f(\underline{x})f^*(\underline{x}) + f^{*2}(\underline{x})\} = K(0) - 2 \sum_{\underline{v}_\ell \in A} g(\underline{x} - \underline{v}_\ell) \\ &\times \int_X K(\underline{x} - \underline{y}) \gamma(\underline{v}_\ell - \underline{y}) d\underline{y} + \sum_{\underline{v}_\ell \in A} \sum_{\underline{v}_m \in A} g(\underline{x} - \underline{v}_\ell) g(\underline{x} - \underline{v}_m) \int_X \int_X K(\underline{y} - \underline{z}) \gamma(\underline{v}_\ell - \underline{y}) \gamma(\underline{v}_m - \underline{z}) d\underline{y} d\underline{z}. \end{aligned} \quad (\text{A-7})$$

In the single integral make the substitution $\underline{z} = \underline{x} - \underline{y}$, $d\underline{z} = d\underline{y}$, and in the double integral make the substitutions $\underline{\sigma} = \underline{y} - \underline{v}_\ell$, $\underline{\tau} = \underline{z} - \underline{v}_\ell$, $d\underline{\sigma} = d\underline{y}$, $d\underline{\tau} = d\underline{z}$. Then

$$\begin{aligned} E\{[f(\underline{x}) - f^*(\underline{x})]^2\} &= K(0) - 2 \sum_{\underline{v}_\ell \in A} g(\underline{x} - \underline{v}_\ell) \int_X K(\underline{z}) \gamma(\underline{z} - (\underline{x} - \underline{v}_\ell)) d\underline{z} \\ &+ \sum_{\underline{v}_\ell \in A} \sum_{\underline{v}_m \in A} g(\underline{x} - \underline{v}_\ell) g(\underline{x} - \underline{v}_\ell + \underline{v}_\ell - \underline{v}_m) \int_X \int_X K(\underline{\sigma} - \underline{\tau}) \gamma(-\underline{\sigma}) \gamma(\underline{v}_m - \underline{v}_\ell - \underline{\tau}) d\underline{\sigma} d\underline{\tau} \\ &= K(0) - 2 \sum_{\underline{v}_\ell \in A} g(\underline{x} - \underline{v}_\ell) \int_X K(\underline{z}) \gamma(\underline{z} - (\underline{x} - \underline{v}_\ell)) d\underline{z} \\ &+ \sum_{\underline{v}_\ell \in A} \sum_{\underline{v}_k \in A} g(\underline{x} - \underline{v}_\ell) g(\underline{x} - \underline{v}_\ell - \underline{v}_k) \int_X \int_X K(\underline{\sigma} - \underline{\tau}) \gamma(-\underline{\sigma}) \gamma(\underline{v}_k - \underline{\tau}) d\underline{\sigma} d\underline{\tau}. \end{aligned} \quad (\text{A-8})$$

Let a bar over the expression denote the expectation uniformly averaged over a sampling cell Ψ . Let Q denote the area of Ψ so that

$$Q = |\underline{a}_1 \times \underline{a}_2|, \quad (\text{A-9})$$

then

$$\begin{aligned} \overline{E\{[f(\underline{x}) - f^*(\underline{x})]^2\}} &= K(0) - \frac{2}{Q} \int_{\Psi} \sum_{\underline{v}_\ell \in A} g(\underline{x} - \underline{v}_\ell) \int_X K(\underline{z}) \gamma(\underline{z} - (\underline{x} - \underline{v}_\ell)) d\underline{z} d\underline{x} \\ &+ \frac{1}{Q} \int_{\Psi} \sum_{\underline{v}_\ell \in A} \sum_{\underline{v}_k \in A} g(\underline{x} - \underline{v}_\ell) g(\underline{x} - \underline{v}_\ell - \underline{v}_k) \int_X \int_X K(\underline{\sigma} - \underline{\tau}) \gamma(-\underline{\sigma}) \gamma(\underline{v}_k - \underline{\tau}) d\underline{\sigma} d\underline{\tau} d\underline{x}. \end{aligned} \quad (\text{A-10})$$

A summation over a sampling lattice repeats the integration over all the sample cells in the plane so we may drop the summation and integration over the entire plane. Thus

$$\begin{aligned} \overline{E\{[f(\underline{x}) - f^*(\underline{x})]^2\}} &= K(0) - \frac{2}{Q} \int_X g(\underline{x}) \int_X K(\underline{z}) \gamma(\underline{z} - \underline{x}) d\underline{z} d\underline{x} \\ &+ \frac{1}{Q} \int_X \sum_{\underline{v}_k \in A} g(\underline{x}) g(\underline{x} - \underline{v}_k) \int_X \int_X K(\underline{\sigma} - \underline{\tau}) \gamma(-\underline{\sigma}) \gamma(\underline{v}_k - \underline{\tau}) d\underline{\sigma} d\underline{\tau} d\underline{x}. \end{aligned} \quad (\text{A-11})$$

Denote the lattice of delta functions corresponding to the sample points by

$$\Delta(\underline{x}) = \sum_{\underline{v}_\ell \in A} \delta(\underline{x} - \underline{v}_\ell). \quad (\text{A-12})$$

The Fourier expansion of this is

$$\Delta(\underline{x}) = \sum_{\substack{\underline{u} \in B \\ \underline{m}}} c_m e^{\underline{i}\underline{x} \cdot \underline{u}_m} \quad (\text{A-13})$$

The nth Fourier coefficient can be obtained in the usual way.

$$\begin{aligned} \int_{\Psi} e^{\underline{i}\underline{x} \cdot \underline{u}_n} \Delta(\underline{x}) d\underline{x} &= \sum_{\substack{\underline{u} \in B \\ \underline{m}}} c_m \int_{\Psi} e^{-\underline{i}\underline{x} \cdot \underline{u}_n} e^{\underline{i}\underline{x} \cdot \underline{u}_m} d\underline{x} \\ &= \sum_{\substack{\underline{u} \in B \\ \underline{m}}} c_m \int_{\Psi} e^{-\underline{i}\underline{x} \cdot (\underline{u}_n - \underline{u}_m)} d\underline{x} \\ &= \sum_{\substack{\underline{u} \in B \\ \underline{m}}} c_m \int_0^1 \int_0^1 e^{-i(\xi \underline{a}_1 + \eta \underline{a}_2) \cdot (\underline{u}_n - \underline{u}_m)} Q d\xi d\eta \\ &= \sum_{\substack{\underline{u} \in B \\ \underline{m}}} c_m Q \left(\int_0^1 e^{-i \underline{a}_1 \cdot (\underline{u}_n - \underline{u}_m) \xi} d\xi \right) \left(\int_0^1 e^{i \underline{a}_2 \cdot (\underline{u}_n - \underline{u}_m) \eta} d\eta \right). \end{aligned} \quad (\text{A-14})$$

Representing \underline{u}_n , and \underline{u}_m as

$$\begin{aligned} \underline{u}_n &= n_1 \underline{b}_1 + n_2 \underline{b}_2 \\ \underline{u}_m &= m_1 \underline{b}_1 + m_2 \underline{b}_2. \end{aligned} \quad (\text{A-15})$$

with n_1, n_2, m_1, m_2 integers we have

$$\int_0^1 e^{-i a_1 (\underline{u}_n - \underline{u}_m) \xi} d\xi = \int_0^1 e^{-i 2\pi (n_1 - m_1) \xi} d\xi \quad (A-16)$$

$$= \begin{cases} 1 & , n_1 = m_1 \\ \left(\frac{e^{-i 2\pi (n_1 - m_1)} - 1}{-i 2\pi (n_1 - m_1)} \right) / \left(\frac{e^{-i 2\pi (n_1 - m_1)} - 1}{-i 2\pi (n_1 - m_1)} \right) & , n_1 \neq m_1 \end{cases}$$

$$= \delta_{n_1 m_1}.$$

Similarly $\int_0^1 e^{-i a_2 (\underline{u}_n - \underline{u}_m) \eta} d\eta = \delta_{n_2 m_2}$

hence

$$\int_{\Psi} e^{-i \underline{x} \cdot \underline{u}_n} \Delta(\underline{x}) d\underline{x} = \sum_{\substack{\underline{u}_m \in B}} c_m Q \delta_{n_1 m_1} \delta_{n_2 m_2} \quad (A-17)$$

$$= \sum_{\substack{\underline{u}_m \in B}} c_m Q \delta_{nm} = c_n Q$$

$$c_n = \frac{1}{Q} \int_{\Psi} e^{-i \underline{x} \cdot \underline{u}_n} \Delta(\underline{x}) d\underline{x}$$

$$= \frac{1}{Q} \int_{\Psi} e^{-i \underline{x} \cdot \underline{u}_n} \sum_{\substack{\underline{v}_\ell \in B}} \delta(\underline{x} - \underline{v}_\ell) d\underline{x} \quad (A-18)$$

$$= \frac{1}{Q};$$

$$\Delta(\underline{x}) = \frac{1}{Q} \sum_{\substack{\underline{u}_m \in B}} e^{i \underline{x} \cdot \underline{u}_m}, \quad (A-19)$$

Using this expression the averaged mean squared error becomes

$$\begin{aligned} \overline{E\{[f(\underline{x}) - f^*(\underline{x})]^2\}} &= K(\underline{0}) - \frac{2}{Q} \int_X g(\underline{x}) \int_X K(\underline{z}) \gamma(\underline{z} - \underline{x}) d\underline{z} d\underline{x} \\ &+ \frac{1}{Q^2} \sum_{\underline{u} \in B} \int_X \int_X g(\underline{x}) g(\underline{x} - \underline{\rho}) \int_X \int_X K(\underline{\sigma} - \underline{\tau}) \gamma(-\underline{\sigma}) \gamma(\underline{\rho} - \underline{\tau}) e^{i\underline{\rho} \cdot \underline{u}} d\underline{\sigma} d\underline{\tau} d\underline{x} d\underline{\rho}. \end{aligned} \quad (A-20)$$

Let $\Phi(\underline{\omega})$, $G(\underline{\omega})$ and $\Gamma(\underline{\omega})$ denote the Fourier transforms of $K(\underline{x})$, $g(\underline{x})$ and $\gamma(\underline{x})$ respectively so that for the transform $F_1(\underline{\omega})$ of a transformable function $f_1(\underline{x})$ we have

$$F_1(\underline{\omega}) = \int_X f_1(\underline{x}) e^{-i\underline{\omega} \cdot \underline{x}} d\underline{x}, \quad (A-21)$$

and also

$$f_1(\underline{x}) = \frac{1}{(2\pi)^2} \int_{\Omega} F_1(\underline{\omega}) e^{i\underline{\omega} \cdot \underline{x}} d\underline{\omega}. \quad (A-22)$$

We shall make use of a Parseval theorem which states that

$$f_1(\underline{0}) = \frac{1}{(2\pi)^2} \int_{\Omega} F_1(\underline{\omega}) d\underline{\omega}. \quad (A-23)$$

Now consider the function $h(\underline{y})$ defined by

$$\begin{aligned} h(\underline{y}) &= K(\underline{y}) - \frac{2}{Q} \int_X g(\underline{x} - \underline{y}) \int_X K(\underline{z}) \gamma(\underline{z} - \underline{x}) d\underline{z} d\underline{x} \\ &+ \frac{1}{Q^2} \sum_{\underline{u} \in B} \int_X g(\underline{x} - \underline{y}) \int_X g(\underline{x} - \underline{\rho}) e^{i\underline{\rho} \cdot \underline{u}} \int_X \gamma(\underline{\rho} - \underline{\tau}) \int_X K(\underline{\sigma} - \underline{\tau}) \gamma(-\underline{\sigma}) d\underline{\sigma} d\underline{\tau} d\underline{\rho} d\underline{x}. \end{aligned} \quad (A-24)$$

Then

$$\overline{E\{[f(\underline{x}) - f^*(\underline{x})]^2\}} = h(\underline{0}). \quad (A-25)$$

Rewriting the expression we obtain

$$\begin{aligned}
 h(\underline{y}) = & K(\underline{y}) - \frac{2}{Q} \int_X \left[\int_X K(\underline{z}) \gamma(-(\underline{x}-\underline{z})) d\underline{z} \right] g(-(\underline{y}-\underline{x})) d\underline{x} \\
 & + \frac{1}{2} \sum_{\substack{\underline{u} \in B \\ \underline{u}_m}} \int_X \left[\int_X \left[\int_X \left[\int_X \gamma(-\underline{\sigma}) K(\underline{\tau}-\underline{\sigma}) d\underline{\sigma} \right] \gamma(\underline{\rho}-\underline{\tau}) d\underline{\tau} \right] g(\underline{x}-\underline{\rho}) e^{\frac{i\underline{\rho} \cdot \underline{u}_m}{m}} d\underline{\rho} \right] g(-(\underline{y}-\underline{x})) d\underline{x}.
 \end{aligned} \tag{A-26}$$

We now derive the Fourier transform of a convolution of the form

$$f_3(\underline{x}) = \int_X f_1(\underline{y}) f_2(\underline{x}-\underline{y}) e^{\frac{i\underline{y} \cdot \underline{z}}{m}} d\underline{y}. \tag{A-27}$$

$$\begin{aligned}
 F_3(\underline{\omega}) &= \int_X f_3(\underline{x}) e^{-i\underline{\omega} \cdot \underline{x}} d\underline{x} \\
 &= \int_X \int_X f_1(\underline{y}) f_2(\underline{x}-\underline{y}) e^{\frac{i\underline{y} \cdot \underline{z}}{m}} e^{-i\underline{\omega} \cdot \underline{x}} d\underline{y} d\underline{x} \\
 &= \int_X \int_X f_1(\underline{y}) e^{-i(\underline{\omega}-\underline{z}) \cdot \underline{y}} f_2(\underline{x}-\underline{y}) e^{-i\underline{\omega} \cdot (\underline{x}-\underline{y})} d\underline{y} d(\underline{x}-\underline{y}) \\
 &= \int_X f_1(\underline{y}) e^{-i(\underline{\omega}-\underline{z}) \cdot \underline{y}} d\underline{y} \int_X f_2(\underline{\rho}) e^{-i\underline{\omega} \cdot \underline{\rho}} d\underline{\rho} \\
 &= F_1(\underline{\omega}-\underline{z}) F_2(\underline{\omega}).
 \end{aligned} \tag{A-28}$$

The Fourier transform $H(\underline{\omega})$ of $h(\underline{x})$ is obtained by repeated application of the above formula.

$$\begin{aligned}
 H(\underline{\omega}) = & \Phi(\underline{\omega}) - \frac{2}{Q} \Phi(\underline{\omega}) \Gamma(-\underline{\omega}) G(-\underline{\omega}) \\
 & + \frac{1}{2} \sum_{\substack{\underline{u} \in B \\ \underline{u}_m}} \Gamma(-(\underline{\omega}-\underline{u}_m)) \Phi(\underline{\omega}-\underline{u}_m) \Gamma(\underline{\omega}-\underline{u}_m) G(\underline{\omega}) G(-\underline{\omega}).
 \end{aligned} \tag{A-29}$$

A Parseval relation then furnishes the desired expression for the average mean squared error.

$$\overline{E\{[f(\underline{x}) - f^*(\underline{x})]^2\}} = \frac{1}{(2\pi)^2} \int_{\Omega} \left[\Phi(\underline{\omega}) - \frac{2}{Q} \Phi(\underline{\omega}) \Gamma(-\underline{\omega}) G(-\underline{\omega}) \right. \\ \left. + \frac{1}{Q^2} \sum_{\underline{u}_m \in B} \Phi(\underline{\omega} - \underline{u}_m) \Gamma(\underline{\omega} - \underline{u}_m) \Gamma(-(\underline{\omega} - \underline{u}_m)) G(\underline{\omega}) G(-\underline{\omega}) \right] d\underline{\omega}. \quad (A-30)$$

Since the sampling lattice is infinite, this expression can be written as

$$\overline{E\{[f(\underline{x}) - f^*(\underline{x})]^2\}} = \frac{1}{(2\pi)^2} \int_{\Omega} \Phi(\underline{\omega}) \left[1 - \frac{2}{Q} \Gamma(-\underline{\omega}) G(-\underline{\omega}) \right. \\ \left. + \frac{1}{Q^2} \Gamma(\underline{\omega}) \Gamma(-\underline{\omega}) \sum_{\underline{u}_m \in B} G(\underline{\omega} + \underline{u}_m) G(-(\underline{\omega} + \underline{u}_m)) \right] d\underline{\omega}. \quad (A-31)$$

Appendix B

APERTURE TRANSFORMS

Determination of the Fourier Transforms of the sampling apertures is a straightforward application of the necessary integral formulae. A few of the cases will be listed in this appendix for reference purposes. Each of the apertures $\gamma(\underline{x})$ has been normalized so that the volume under the surface they represent is unity. Some of the apertures are depicted pictorially in Figure B-1.

Gaussian Aperture:

$$\gamma(\underline{x}) = \frac{1}{2\pi\sigma^2} e^{-\left(\frac{\underline{x} \cdot \underline{x}}{2\sigma^2}\right)} \quad (B-1)$$

It should be remembered that this is a two dimensional situation so that the volume inside a 1σ cylinder is 39.3% of the total. 2σ and 3σ represent 86.4% and 98.80% respectively. The transform of this function is also gaussian.

$$\Gamma(\underline{\omega}) = e^{-\left(\frac{\sigma^2 \underline{\omega} \cdot \underline{\omega}}{2}\right)} \quad (B-2)$$

Uniform Disk of Radius R:

$$\gamma(\underline{x}) = \begin{cases} \frac{1}{\pi R^2}, & |\underline{x}| < R, \\ 0, & |\underline{x}| \geq R. \end{cases} \quad (B-3)$$

$$\Gamma(\underline{\omega}) = \frac{2J_1(|\underline{\omega}|R)}{|\underline{\omega}|R} \quad (B-4)$$

Here $J_1(\)$ is the Bessel function of the first kind of the first order and $|\underline{\omega}|$ is the vector magnitude of $\underline{\omega}$ (i.e. $|\underline{\omega}| = \sqrt{\underline{\omega} \cdot \underline{\omega}}$).

Square with edge 2d:

$$\gamma(\underline{x}) = \begin{cases} \frac{1}{4d^2}, & \underline{x} \in \text{square}, \\ 0, & \underline{x} \notin \text{square}. \end{cases} \quad (\text{B-5})$$

$$\Gamma(\underline{\omega}) = \frac{\sin \omega_1 d}{\omega_1 d} \frac{\sin \omega_2 d}{\omega_2 d} \quad (\text{B-6})$$

ω_1 and ω_2 are the coordinates of $\underline{\omega}$ (i.e. $\underline{\omega} = (\omega_1, \omega_2)$).

Hexagon of altitude d:

$$\gamma(\underline{x}) = \begin{cases} \frac{1}{2\sqrt{3} d^2}, & \underline{x} \in \text{hexagon}, \\ 0, & \underline{x} \notin \text{hexagon}. \end{cases} \quad (\text{B-7})$$

$$\Gamma(\underline{\omega}) = \begin{cases} \frac{1}{3} \frac{1}{u+v} \left[\sin(u+2v) \frac{\sin u}{u} + \sin(2u+v) \frac{\sin v}{v} \right], & u \neq 0 \text{ and } v \neq 0, \\ & \text{and } u+v \neq 0, \\ \frac{1}{3} \left[\frac{\sin 2v}{v} + \left(\frac{\sin v}{v} \right)^2 \right], & u=0 \text{ and } v \neq 0 \\ \frac{1}{3} \left[\frac{\sin 2u}{u} + \left(\frac{\sin u}{u} \right)^2 \right], & u \neq 0 \text{ and } v=0, \\ \frac{1}{3} \left[2 \cos v + \frac{\sin v}{v} \right] \frac{\sin v}{v}, & u+v=0, v \neq 0 \\ 1, & u=v=0, \end{cases} \quad (\text{B-8})$$

where

$$\begin{aligned} u &= \frac{1}{2} \left(\frac{\omega_2}{\sqrt{3}} - \omega_1 \right) d, \\ v &= \frac{1}{2} \left(\frac{\omega_2}{\sqrt{3}} + \omega_1 \right) d. \end{aligned} \quad (\text{B-9})$$

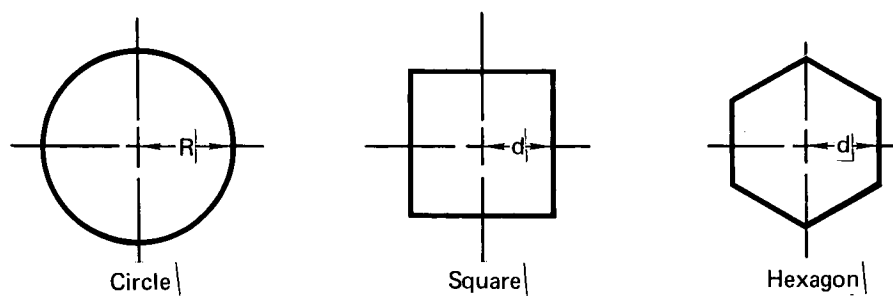


FIGURE B-1
SAMPLING APERTURES

Appendix C

RECONSTRUCTION TRANSFORMS

The simplest reconstruction in one dimension is step type interpolation in which the value of the reconstructed function is equal to the value of the nearest sample. This "one-point" reconstruction has a simple generalization to two dimensional reconstruction. This is defined by specifying that the reconstructed image f^* as a function of the samples ψ be

$$f^*(\underline{x}) = \psi(\underline{v}_\ell) \quad (C-1)$$

with \underline{v}_ℓ being the closest sample point in A to \underline{x} in the metric determined by the sample lattice basis vectors $\underline{a}_1, \underline{a}_2$. More specifically if a point \underline{x} is represented by

$$\underline{x} = \alpha \underline{a}_1 + \beta \underline{a}_2 \quad (C-2)$$

then its "distance" from the origin is

$$\|\underline{x}\| = (\alpha^2 + \beta^2)^{1/2} \quad (C-3)$$

so that

$$\|\underline{x}\| = [(\underline{x} \cdot \underline{b}_1)^2 + (\underline{x} \cdot \underline{b}_2)^2]^{1/2} \quad (C-4)$$

in terms of the dual basis vectors $\underline{b}_1, \underline{b}_2$.

It is easily verified that for this case the reconstruction function $g(\underline{x})$ is defined by

$$g(\underline{x}) = \begin{cases} 1, & |\underline{x} \cdot \underline{b}_1| < \pi \text{ and } |\underline{x} \cdot \underline{b}_2| < \pi \\ 0, & \text{otherwise,} \end{cases} \quad (C-5)$$

in other words $g(\underline{x}) = 1$ on a rhombic figure determined by $\underline{a}_1, \underline{a}_2$ as shown in Figure C-1.

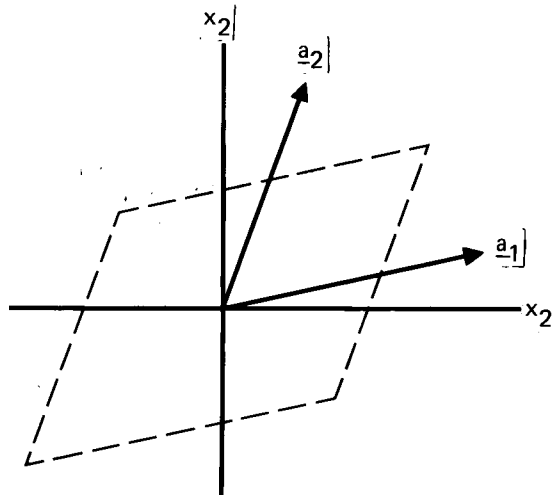


FIGURE C-1 |
ONE POINT RECONSTRUCTION GEOMETRY|

GP72-0450-81|

In transforming the function $g(\underline{x})$ we change coordinates from x_1, x_2 to α, β . The Jacobian of this transformation is easily seen to be

$$J = \begin{vmatrix} \frac{\partial x_1}{\partial \alpha} & \frac{\partial x_1}{\partial \beta} \\ \frac{\partial x_2}{\partial \alpha} & \frac{\partial x_2}{\partial \beta} \end{vmatrix} = Q = \text{area of sample cell.} \quad (\text{C-6})$$

Thus the Fourier Transform of $g(\underline{x})$ is

$$\underline{G}(\underline{\omega}) = Q \int_{-1/2}^{1/2} \int_{-1/2}^{1/2} e^{-\underline{\omega} \cdot (\alpha \underline{a}_1 + \beta \underline{a}_2)} d\alpha d\beta = Q \frac{\sin \frac{1}{2} \underline{\omega} \cdot \underline{a}_1}{\frac{1}{2} \underline{\omega} \cdot \underline{a}_1} \frac{\sin \frac{1}{2} \underline{\omega} \cdot \underline{a}_2}{\frac{1}{2} \underline{\omega} \cdot \underline{a}_2}. \quad (\text{C-7})$$

A two dimensional generalization of one dimensional linear interpolation is the bilinear form

$$g(\underline{x}) = \begin{cases} (1-|\alpha|)(1-|\beta|), & \text{for } |\alpha| \text{ and } |\beta| < 1 \\ 0, & \text{otherwise.} \end{cases} \quad (C-8)$$

For this case $g(\underline{x})$ depends upon the four nearest points, that is, the four points contained by the rhombic figure determined by the sample basis vectors as shown in Figure C-2.

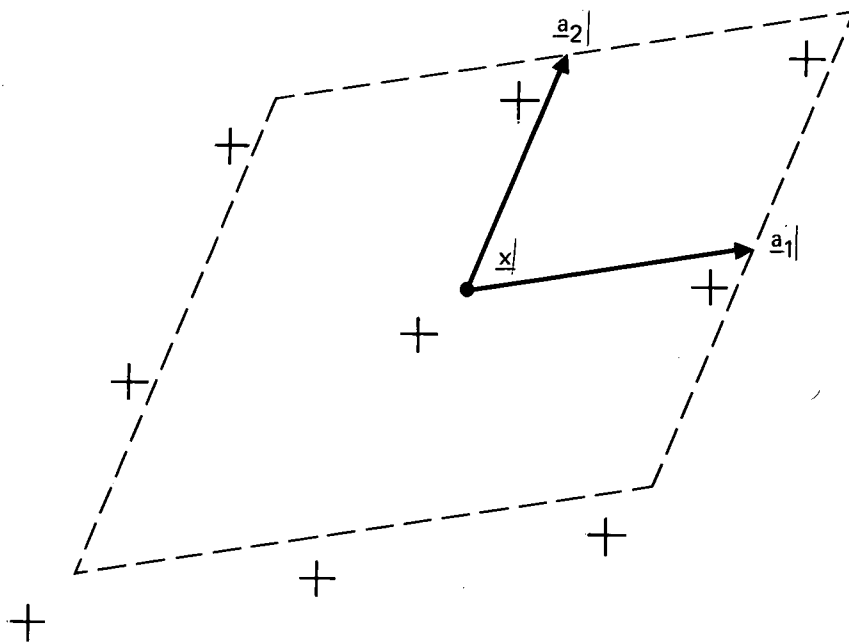


FIGURE C-2
FOUR POINT RECONSTRUCTION GEOMETRY

GP72-0450-78

In this case

$$G(\underline{\omega}) = Q \left(\frac{\sin \frac{1}{2} \underline{\omega} \cdot \underline{a}_1}{\frac{1}{2} \underline{\omega} \cdot \underline{a}_1} \right)^2 \left(\frac{\sin \frac{1}{2} \underline{\omega} \cdot \underline{a}_2}{\frac{1}{2} \underline{\omega} \cdot \underline{a}_2} \right)^2 \quad (C-9)$$

These results bear an obvious similarity to the one dimensional case. Further generalization along these lines is possible. Also mixture between basis vector directions of different interpolation methods is easily done.

Appendix D

DERIVATION OF MEAN SQUARED ERROR EXPRESSION WHICH INCLUDES
THE RECORDER SPOT CHARACTERISTIC

To include the recording characteristics into the formulation let $\hat{f}(\underline{x})$ be the recorded image function. Then

$$\hat{f}(\underline{x}) = \sum_{\underline{v}_q \in C} f^*(\underline{v}_q) p(\underline{x} - \underline{v}_q), \quad (D-1)$$

where $p(\underline{x})$ is the recorder characteristic; that is, the recorder, if printing a unit value at $\underline{x}=0$, will produce an image $p(\underline{x})$. C is the set of points at which the recorder prints. This set is assumed to form a periodic lattice. Inserting the expression for the reconstructed image f^* as a function of the sample values ψ we have

$$\begin{aligned} \hat{f}(\underline{x}) &= \sum_{\underline{v}_q \in C} \left[\sum_{\underline{v}_\ell \in A} g(\underline{v}_q - \underline{v}_\ell) \psi(\underline{v}_\ell) \right] p(\underline{x} - \underline{v}_q) \\ &= \sum_{\underline{v}_\ell \in A} \left[\sum_{\underline{v}_q \in C} g(\underline{v}_q - \underline{v}_\ell) p(\underline{x} - \underline{v}_q) \right] \psi(\underline{v}_\ell) \\ &= \sum_{\underline{v}_\ell \in A} \left[\sum_{\underline{v}_q \in C} g(\underline{v}_q - \underline{v}_\ell) p((\underline{x} - \underline{v}_\ell) - (\underline{v}_q - \underline{v}_\ell)) \right] \psi(\underline{v}_\ell). \end{aligned} \quad (D-2)$$

Assuming that the lattice C is a refinement of the lattice A , ($A \subset C$), we can write

$$\hat{f}(\underline{x}) = \sum_{\underline{v}_\ell \in A} \left[\sum_{\underline{v}_r \in C} g(\underline{v}_r) p((\underline{x} - \underline{v}_\ell) - \underline{v}_r) \right] \psi(\underline{v}_\ell). \quad (D-3)$$

Define

$$g^*(\underline{x}) = \sum_{\underline{v}_r \in C} g(\underline{v}_r) p(\underline{x} - \underline{v}_r). \quad (D-4)$$

Writing this as a convolution we have

$$\begin{aligned} g^*(\underline{x}) &= \sum_{\underline{v}_r \in C} \int_X g(\underline{y}) p(\underline{x} - \underline{y}) \delta(\underline{y} - \underline{v}_r) d\underline{y} \\ &= \sum_{\underline{u}_s \in D} \int_X g(\underline{y}) p(\underline{x} - \underline{y}) \frac{1}{S} e^{i\underline{y} \cdot \underline{u}_s} d\underline{y}, \end{aligned} \quad (D-5)$$

where S is the area of a cell of the printing lattice C , and D is the lattice in the Ω plane with basis vectors reciprocal to those of C . Taking the Fourier transform of this expression we obtain

$$G^*(\underline{\omega}) = \frac{1}{S} \sum_{\underline{u}_s \in D} G(\underline{\omega} - \underline{u}_s) P(\underline{\omega}) \quad (D-6)$$

where $G^*(\underline{\omega})$ and $P(\underline{\omega})$ are the transforms of $g(\underline{x})$ and $p(\underline{x})$ respectively. Noticing that

$$\hat{f}(\underline{x}) = \sum_{\underline{v}_\ell \in A} g^*(\underline{x} - \underline{v}_\ell) \psi(\underline{v}_\ell), \quad (D-7)$$

whereas

$$f^*(\underline{x}) = \sum_{\underline{v}_\ell \in A} g(\underline{x} - \underline{v}_\ell) \psi(\underline{v}_\ell), \quad (D-8)$$

we find that the averaged mean square error in the total reconstruction including the recorder characteristics can be obtained by substituting $g^*(\underline{x})$ for $g(\underline{x})$ so that

$$\overline{E\{[f(\underline{x}) - \hat{f}(\underline{x})]^2\}} = \frac{1}{(2\pi)^2} \int_{\Omega} \Phi(\underline{\omega}) \left[1 - \frac{2}{Q} \Gamma(-\underline{\omega}) G^*(-\underline{\omega}) + \frac{1}{Q^2} \Gamma(\underline{\omega}) \Gamma(-\underline{\omega}) \sum_{\substack{\underline{u}_m \in B}} G^*(\underline{\omega} + \underline{u}_m) G^*(-(\underline{\omega} + \underline{u}_m)) \right] d\underline{\omega} \quad (D-9)$$

where

$$G^*(\underline{\omega}) = \frac{1}{S} \sum_{\substack{\underline{u}_s \in D}} G(\underline{\omega} - \underline{u}_s) P(\underline{\omega}) \quad (D-10)$$

For a realistic recording situation the overlap characteristics of the printing spots is not a parameter which may be varied but depends upon the spacing so that the average intensity in any area represents the scene being reproduced. To determine this relationship we consider the limiting case in which $p(\underline{x})$ becomes narrow and the density of printer spots becomes large (i.e., C becomes dense, D becomes sparse and S becomes small).

Recalling that the reconstructed image is

$$\hat{f}(\underline{x}) = \sum_{\substack{\underline{v}_q \in C}} f^*(\underline{v}_q) p(\underline{x} - \underline{v}_q) \quad (D-11)$$

then if $f^*(\underline{v}_q) = 1$ for all $\underline{v}_q \in C$ we require that the average value of $\hat{f}(\underline{x})$ be 1 so that

$$\frac{1}{S} \int_Y \hat{f}(\underline{x}) d\underline{x} = 1 \quad \text{where } Y \text{ is a recorder cell and } S \text{ is its area} \quad (D-12)$$

thus

$$\int_{\underline{y}} \sum_{\substack{\underline{v} \in C \\ \underline{q}}} p(\underline{x} - \underline{v} - \underline{q}) d\underline{x} = S. \quad (D-13)$$

This requirement sets the "gain" for the recorder. This can also be written as

$$\int_{\underline{x}} p(\underline{x}) d\underline{x} = S \quad (D-14)$$

or as

$$P(\underline{0}) = S. \quad (D-15)$$

Appendix E

OPTIMAL LINEAR INTERPOLATION FOR NON-BAND LIMITED FUNCTIONS

For certain non-band limited functions an optimum linear interpolation can be identified similar to a Wiener filter except that for two dimensional applications the causality requirement is not as meaningful so that spectral factorization is not involved. The approach is by a variational procedure as was Peterson and Middleton's with the exception that their prefiltering considerations are not used. Consider the formula given in Appendix A for the mean squared error (not averaged) as a functional of $g(\underline{x})$.

$$E[g(\underline{x})] = K(\underline{0}) - 2 \sum_{\underline{v}_\ell \in A} g(\underline{x} - \underline{v}_\ell) \int_X K(\underline{z}) \gamma(\underline{z} - (\underline{x} - \underline{v}_\ell)) d\underline{z} \quad (E-1)$$

$$+ \sum_{\underline{v}_\ell \in A} \sum_{\underline{v}_\kappa \in A} g(\underline{x} - \underline{v}_\ell) g(\underline{x} - \underline{v}_\ell - \underline{v}_\kappa) \int_X \int_X K(\underline{\sigma} - \underline{\tau}) \gamma(-\underline{\sigma}) \gamma(\underline{v}_\kappa - \underline{\tau}) d\underline{\sigma} d\underline{\tau}.$$

We simply require that for all admissible $h(\underline{x})$

$$\lim_{\epsilon \rightarrow 0} \frac{\partial E}{\partial \epsilon} [g(\underline{x}) + \epsilon h(\underline{x})] = 0. \quad (E-2)$$

This gives

$$\begin{aligned} & -2 \sum_{\underline{v}_\ell \in A} \int_X K(\underline{z}) \gamma(\underline{z} - (\underline{x} - \underline{v}_\ell)) d\underline{z} h(\underline{x} - \underline{v}_\ell) \\ & + \sum_{\underline{v}_\ell \in A} \sum_{\underline{v}_\kappa \in A} g(\underline{x} - \underline{v}_\ell - \underline{v}_\kappa) \int_X \int_X K(\underline{\sigma} - \underline{\tau}) \gamma(-\underline{\sigma}) \gamma(\underline{v}_\kappa - \underline{\tau}) d\underline{\sigma} d\underline{\tau} h(\underline{x} - \underline{v}_\ell) \\ & + \sum_{\underline{v}_\ell \in A} \sum_{\underline{v}_\kappa \in A} g(\underline{x} - \underline{v}_\ell) \int_X \int_X K(\underline{\sigma} - \underline{\tau}) \gamma(-\underline{\sigma}) \gamma(\underline{v}_\kappa - \underline{\tau}) d\underline{\sigma} d\underline{\tau} h(\underline{x} - \underline{v}_\ell - \underline{v}_\kappa) = 0. \end{aligned} \quad (E-3)$$

Rearranging terms in summations this becomes

$$\begin{aligned}
 & -2 \sum_{\underline{v}_\ell \in A} \int_X K(\underline{z}) \gamma(\underline{z} - (\underline{x} - \underline{v}_\ell)) d\underline{z} h(\underline{x} - \underline{v}_\ell) \\
 & + \sum_{\underline{v}_\ell \in A} \sum_{\underline{v}_\kappa \in A} g((\underline{x} - \underline{v}_\ell) - \underline{v}_\kappa) \int_X \int_X K(\underline{\sigma} - \underline{\tau}) \gamma(-\underline{\sigma}) \gamma(\underline{v}_\kappa - \underline{\tau}) d\underline{\sigma} d\underline{\tau} h(\underline{x} - \underline{v}_\ell) \\
 & + \sum_{\underline{v}_\ell \in A} \sum_{\underline{v}_\kappa \in A} g((\underline{x} - \underline{v}_\ell) - \underline{v}_\kappa) \int_X \int_X K(\underline{\sigma} - \underline{\tau}) \gamma(-\underline{\sigma}) \gamma(-\underline{v}_\kappa - \underline{\tau}) d\underline{\sigma} d\underline{\tau} h(\underline{x} - \underline{v}_\ell) = 0.
 \end{aligned} \tag{E-4}$$

Implying that we must have

$$\int_X K(\underline{z}) \gamma(\underline{z} - \underline{x}) d\underline{z} = \sum_{\underline{v}_\kappa \in A} g(\underline{x} - \underline{v}_\kappa) \int_X \int_X K(\underline{\sigma} - \underline{\tau}) \gamma(-\underline{\sigma}) \frac{\gamma(\underline{v}_\kappa - \underline{\tau}) + \gamma(-\underline{v}_\kappa - \underline{\tau})}{2} d\underline{\sigma} d\underline{\tau}. \tag{E-5}$$

In terms of a summation over the B lattice,

$$\int_X K(\underline{z}) \gamma(\underline{z} - \underline{x}) d\underline{z} = \frac{1}{Q} \sum_{\underline{u}_m \in B} \int_X \int_X \int_X e^{i\underline{z} \cdot \underline{u}_m} g(\underline{x} - \underline{z}) K(\underline{\sigma} - \underline{\tau}) \gamma(-\underline{\sigma}) \frac{\gamma(\underline{z} - \underline{\tau}) + \gamma(-\underline{z} - \underline{\tau})}{2} d\underline{\sigma} d\underline{\tau} d\underline{z}. \tag{E-6}$$

The Fourier transformation of this is

$$\Phi(\underline{\omega}) \Gamma(-\underline{\omega}) = \frac{1}{Q} \sum_{\underline{u}_m \in B} \frac{1}{2} [\Phi(\underline{\omega} + \underline{u}_m) + \Phi(-\underline{\omega} - \underline{u}_m)] \Gamma(\underline{\omega} + \underline{u}_m) \Gamma(-\underline{\omega} - \underline{u}_m) G(\underline{\omega}) \tag{E-7}$$

so that the optimal condition is given by

$$G_{\text{opt}}(\underline{\omega}) = \frac{\Phi(\underline{\omega}) \Gamma(-\underline{\omega})}{\frac{1}{Q} \sum_{\underline{u}_m \in B} \frac{1}{2} [\Phi(\underline{\omega} + \underline{u}_m) + \Phi(-\underline{\omega} - \underline{u}_m)] \Gamma(\underline{\omega} + \underline{u}_m) \Gamma(-\underline{\omega} - \underline{u}_m)} \tag{E-8}$$

provided that the denominator does not vanish which is rarely the case for non band limited functions and if this expression is inverse Fourier transformable.

In any practical situation the scene power spectral density $\phi(\underline{\omega})$ is an even function so that

$$G_{\text{opt}}(\underline{\omega}) = \frac{\phi(\underline{\omega})\Gamma(-\underline{\omega})}{\frac{1}{Q} \sum_{\substack{\underline{u} \in B \\ \underline{m}}} \phi(\underline{\omega} + \underline{u}_{\underline{m}})\Gamma(\underline{\omega} + \underline{u}_{\underline{m}})\Gamma(-\underline{\omega} - \underline{u}_{\underline{m}})} \quad (\text{E-9})$$

Inserting this into the expression for the average mean squared error (Appendix A) we have

$$\begin{aligned} \overline{E\{[f(\underline{x}) - f_{\text{opt}}^*(\underline{x})]^2\}} &= \frac{1}{(2\pi)^2} \int_{\Omega} \left[\phi(\underline{\omega}) - \frac{2}{Q} \phi(\underline{\omega})\Gamma(-\underline{\omega})G_{\text{opt}}(-\underline{\omega}) \right. \\ &\quad \left. + \frac{1}{Q^2} \sum_{\substack{\underline{u} \in B \\ \underline{m}}} \phi(\underline{\omega} + \underline{u}_{\underline{m}})\Gamma(\underline{\omega} + \underline{u}_{\underline{m}})\Gamma(-\underline{\omega} - \underline{u}_{\underline{m}})G_{\text{opt}}(\underline{\omega})G_{\text{opt}}(-\underline{\omega}) \right] d\underline{\omega} \\ &= \frac{1}{(2\pi)^2} \int_{\Omega} \phi(\underline{\omega}) \left[1 - \frac{1}{Q} \Gamma(-\underline{\omega})G_{\text{opt}}(-\underline{\omega}) \right] d\underline{\omega} \\ &= \frac{1}{(2\pi)^2} \int_{\Omega} \phi(\underline{\omega}) \left[1 - \frac{\phi(\underline{\omega})\Gamma(\underline{\omega})\Gamma(-\underline{\omega})}{\sum_{\substack{\underline{u} \in B \\ \underline{m}}} \phi(\underline{\omega} + \underline{u}_{\underline{m}})\Gamma(\underline{\omega} + \underline{u}_{\underline{m}})\Gamma(-\underline{\omega} - \underline{u}_{\underline{m}})} \right] d\underline{\omega}. \end{aligned} \quad (\text{E-10})$$

This is the formula to be used in calculating the optimal reconstruction error. Note that for band limited scenes (support of $\phi(\underline{\omega})$ is restricted to a finite region of the Ω plane) and high enough sample density, then the summation appearing in the expression will consist of evaluation at the point $\underline{u}_{\underline{m}} = \{0\}$ only and the expression reduces to 0.

Appendix F

MODULATION TRANSFER FUNCTIONS

The modulation transfer function concept in common usage for optical systems (Reference 18) can be adapted to spatial frequency applications in image analysis. In this way the resolution of reconstructed images can be predicted using communications engineering methods for introducing any of the image degradations or enhancements encountered in a space data retrieval situation.

This procedure is based upon the transformation properties of power spectral densities. If $\Phi_i(\underline{\omega})$ is the (two dimensional) power spectral density of the input of a linear system with weighting function $\gamma(\underline{x})$ and $\Gamma(\underline{\omega})$ is the Fourier transform of $\gamma(\underline{x})$ then the output power spectral density $\Phi_0(\underline{\omega})$ is given by

$$\Phi_0(\underline{\omega}) = \Gamma(\underline{\omega})\Gamma(-\underline{\omega})\Phi_i(\underline{\omega}) \quad (\text{F-1})$$

It will be seen that $|\Gamma(\underline{\omega})\Gamma(-\underline{\omega})|^{1/2}$ may be thought of as a modulation transfer function. It can represent optical systems, atmospheric attenuation or electrical filtering in a scanning situation (see Appendix G).

A sampled and reconstructed image requires a further sophistication which is in common usage in communications engineering. If A is the set of sample points forming a periodic lattice (with cell area Q), and if B is the frequency lattice dual to A, and if $g(\underline{x})$ with transform $G(\underline{\omega})$ is the interpolation formula as in Appendix A, then the reconstructed image power spectral density $\Phi^*(\underline{\omega})$ is given by:

$$\Phi^*(\underline{\omega}) = \frac{G(\underline{\omega})}{Q} \frac{G(-\underline{\omega})}{Q} \sum_{\substack{\underline{u} \in B \\ -\underline{m}}} \Phi(\underline{\omega} + \frac{\underline{u}}{Q}) \quad (\text{F-2})$$

The summation represents the folding frequencies introduced by the sampling. One reservation must be made in introducing the power spectral density of the sampled and reconstructed image because of the following considerations. The local frequency content of the reconstructed image will depend upon the position within a sample cell. This is because the covariance, $E[f^*(\underline{x})f^*(\underline{z})]$,

is not a function of $\underline{z-x}$ only. If we consider this as a function of $\underline{z-x}$ and \underline{z} , then the \underline{z} dependence is periodic with the sample lattice. If this \underline{z} dependence of the covariance function is averaged uniformly over a sample cell the resulting function of $\underline{z-x}$ can be transformed to give an "average" power spectral density. This is the procedure needed to give the above result for $\Phi^*(\underline{\omega})$.

The modulation M of a scene is defined in terms of the darkest intensity D and the lightest intensity L by

$$M = \frac{L-D}{L+D} \quad (F-3)$$

so that there is a simple relationship between modulation and power spectral density. The intensity I at a spatial frequency $\underline{\omega}$ is $I = \frac{L-D}{2}$.

The average intensity Ξ (zero frequency) of the scene is $\Xi = \frac{L+D}{2}$, hence

$$M = \frac{I}{\Xi} \quad (F-4)$$

whence

$$M(\underline{\omega}) = \sqrt{\frac{\Phi(\underline{\omega})}{\Phi(0)}} \quad (F-5)$$

This is a two dimensional modulation figure. Resolution in photographic applications is frequently expressed in terms modulation by empirically setting the limit of the human eye at a modulation of .01. Thus resolution can be expressed in terms of spatial frequency bandwidth which may differ depending upon angular orientation due to anisotropic behavior introduced by the scanning or data processing.

The optical considerations such as atmospheric attenuation and optical system modifications can be done in terms of modulation transfer functions modifying the modulation as usual or translated into communications theory terms involving power spectral densities.

Appendix G

ANALOG SCANNING AND FILTERING

Analog scanning can be represented as a limiting case of a rectangular sampling lattice in which the sample density in one direction becomes infinite thus turning the sampling pattern from an array of points into a pattern of parallel lines. The scanning aperture giving coupling between scan lines can thus be taken into account by retaining the two dimensional formulation.

The formulation is actually simpler in this case since the dual lattice B becomes sparse in one direction and in the limit is nothing but a linear string of isolated points representing the line scan frequency and its multiples. Thus fewer terms need to be retained in the lattice sums involved in mean squared error calculations.

Electrical filtering of a scanned image acts upon only one scan line at a time and can be represented as an aperture function involving a delta function for its cross scan spatial dependence. This function can then be cascaded with the actual aperture function acting before the sampling (scanning) takes place. As an example consider a first order time lag. This has the weighting function

$$w(\underline{x}) = \begin{cases} \frac{1}{\theta} e^{-\frac{x_1}{\theta}} \delta(x_2), & x_1 \leq 0 \\ 0 & , x_1 > 0 \end{cases} \quad (G-1)$$

where the distance θ is the product of the time constant and the scan speed. The coordinate x_1 is in the direction of a scan line. The Fourier transform of this is

$$W(\omega) = \frac{1}{1+i\omega_1\theta} \quad (G-2)$$

which is complex but will only appear in the formulae as

$$\text{Re } \{W(\omega)\} = W(\omega)W(-\omega) = \frac{1}{1+\omega_1^2\theta^2} \quad (G-3)$$

The mean squared error formula as modified to accommodate this is

$$\begin{aligned} \overline{E\{[f(\underline{x}) - f^*(\underline{x})]^2\}} &= \frac{1}{(2\pi)^2} \int_{\Omega} \Phi(\underline{\omega}) \left[1 - \frac{2}{Q} \Gamma(-\underline{\omega}) G(\underline{\omega}) \frac{1}{1 + \omega_1^2 \theta^2} \right. \\ &\quad \left. + \frac{1}{Q^2} \Gamma(\underline{\omega}) \Gamma(-\underline{\omega}) \frac{1}{1 + \omega_1^2 \theta^2} \sum_{\substack{\underline{u} \\ \underline{m} \in B}} G(\underline{\omega} + \underline{u}_{\underline{m}}) G(-\underline{\omega} - \underline{u}_{\underline{m}}) \right] d\underline{\omega}. \end{aligned} \quad (G-4)$$

Appendix H \

NEW TECHNOLOGY

There were no reportable items during the performance of this contract.